TUM School of Engineering and Design

Mechanical characterization of biological materials with laser-Doppler vibrometry

Sascha Schwarz

Vollständiger Abdruck der von der TUM School of Engineering and Design der Technischen Universität München zur Erlangung des akademischen Grades eines Doktors der Ingenieurwissenschaften genehmigten Dissertation.

Vorsitz: Prof. Dr. rer. nat. Oliver Lieleg

Prüfer*innen der Dissertation:

1. Prof. Dr. ir. Daniel J. Rixen

2. Prof. Dr. rer. nat. Hauke Clausen-Schaumann

3. Prof. Alessandra Moretti, Ph.D.

Die Dissertation wurde am 15.06.2021 bei der Technischen Universität München eingereicht und durch die TUM School of Engineering and Design am 08.11.2021 angenommen.

If you want to find the secrets of the Universe,
think in terms of energy, frequency and vibration.
Nikola Tesla

To my beloved family and the love of my life, Julia.

Acknowledgment

It is a privilege to carry out one's Ph.D. studies, follow one's research interest, and satisfy the appetite for knowledge. However, this privilege is often not clearly visible during the studies, with all the problems and concerns, revealing this privilege rather towards the end during thesis writing. Consequently, I want to thank ***Dr. Stefanie Sudhop*** for initiating this project and allowing me to pursue my interest in Bioprinting and Biofabrication, believing in my skills, and encouraging and supporting me throughout my Ph.D. project.

I also want to thank both my supervisors, ***Prof. Dr. Hauke Clausen-Schaumann*** and ***Prof. Dr. Daniel J. Rixen***, for making this highly interdisciplinary work possible by their own efforts, interests, and time. Mentors also play an important role in such a scientific project, and I was lucky enough to call ***Prof. Dr. Alfred Fuchsberger*** and ***Prof. Dr. Rainer Burgkart*** my mentors.

Without ***Prof. Dr. Alessandra Moretti, Dr. Christine Poch,*** and ***Anna Meier***, I would not have been able to work with cardiomyocytes, from my perspective, the most interesting type of cells. Thank you very much for always being supportive and open for discussion. My thanks also goes to all the numerous collaborators who made this interdisciplinary work possible and are not mentioned here. Thank you!.

Huge thanks goes to ***Bastian Hartmann*** for fruitful and patient discussions about physical principles and for conducting all the IT-AFM measurements included in this study. Nearly from the beginning, I was lucky enough to have ***Benedikt Kaufmann*** as a colleague of mine. He is one of the most patient listeners I can imagine, and his patience has been challenged many times by me. I was also happy to be always surrounded by students, patiently following my ideas and visions and pushing them to the next level.

This work also would not have been possible without the people from Polytec, always helping me with expertise, material, and devices. Special thanks goes to ***Jörg Sauer***, ***Dennis Berft***, ***Marco Fritzsche***, ***Dr. Stefan König***, and ***Robert Moerl***.

I want to send my gratitude and love to my wife ***Julia*** for always being so understanding and supportive during the last years. I have the incredible luck of having a loving person at my side, understanding my deep passion for my work. Without her support, I would not have succeeded in this endeavor. My son ***Adrian*** and my daughter ***Paula*** showed me the real importance and beauty of life and what really matters. Finally, yet importantly, I want to thank my mother, ***Andrea,*** for always believing in me and supporting me in any decision during my whole life.

Thank you all!

Sascha Schwarz
Munich, June 2021

Abstract:

With its high-sensitivity, non-intrusive, and contactless measurement characteristics, laser-Doppler vibrometry (LDV) allows for a detailed insight into the vibrational dynamics of technical systems, regardless of their fragility and structural characteristics. Concerning the label-free measurements of transparent materials, such as biological hydrogels relevant in Tissue Engineering and Biofabrication, the full potential of this technology never has been fully investigated. Currently, the standard mechanical characterization methods for biological materials rely on physical contact with the sample. However, in Tissue Engineering, such contacts inherently pose the risk of sample contamination or sample damage. For this reason, new methods, which are capable of measuring and monitoring mechanical properties in a contactless manner, are urgently needed. This exploratory study, therefore, investigates whether and how LDV can be used for the mechanical characterization of transparent biological materials, such as hydrogels, living cells, and cellular aggregates, as well as native and engineered tissues.

Using an LDV device with a near-infrared (NIR) laser wavelength, the frequency spectra of gelatin hydrogel disks with different polymer concentrations were investigated in a label-free and free-hanging setup. Based on analytical and numerical models, the mechanical properties of the gels were deduced from the LDV data, and the results were compared to measured Young's moduli obtained by indentation-type atomic force microscopy (IT-AFM) and unconfined compression testing, two established methods for the mechanical characterization of biological samples, as well as to literature values. The Young's modulus values determined by LDV show good agreement with the confined compression testing results, while the IT-AFM results seem to underestimate the Young's, which could be due to strain stiffening effects of the gelatin material. In addition, the concentration-dependent damping ratio of gelatin determined by LDV and the scaling of the Young's modulus with gelatin concentration agree reasonably well with literature values. Additionally, the elastic properties were deduced by measuring the dynamics of a bi-clamped beam structure on which the gelatin sample was cast. Here, a similar trend compared to the direct measurement of the gelatin disk was discovered, but due to a non-permanent contact between the sample and the cantilever structure, the results are not that significant and reliable. Measuring the dynamics of living cells submerged in culture medium using a 532 nm laser wavelength LDV device was also investigated and did not render results linkable to the cell's mechanical properties due to poor reflectivity at the used wavelength. The contraction activity of cardiomyocytes and cardiomyocyte spheroids and their modulation by drugs was measured using LDV and compared to the results of particle imaging velocimetry analysis. While no LDV signal could be recorded on cardiomyocyte monolayers fully covered by cell culture medium, the natural and the drug-enhanced contraction of partially submersed cardiomyocyte spheroids could be recorded by LDV, and the results agreed well with the particle imaging velocimetry analysis. The analysis of bovine cartilage plugs did not show any difference between treated and untreated samples through enzymatic digestion. Finally, engineered tissue in a shape of a free-hanging sheet exposed to air was analyzed, and its dynamics were successfully measured using a NIR-LDV device.

As an initial attempt, this exploratory study indicates and evaluates the feasibility of using LDV as a novel mechanical characterization method for transparent biological materials and can be seen as a guideline, proposing the next important steps and research directions developing future applications in this field.

Zusammenfassung

Die Laser-Doppler Vibrometrie (LDV) ermöglicht mit ihren hochempfindlichen, zerstörungsfreien und kontaktlosen Messeigenschaften detaillierte Einblicke in die Schwingungsdynamik technischer Systeme. Das volle Potential dieser Technologie im Bereich des Tissue Engineerings und der Biofabrikation, wurde noch nicht vollständig untersucht. Etablierte Methoden für die mechanische Charakterisierung von biologischen Materialien sind häufig kontaktbasiert, sofern eine kontaktbasierte Methode aufgrund der fragilen Probeneigenschaften überhaupt möglich ist. Im Tissue Engineering ist allerdings eine kontakt-basierte Messung immer mit dem Risiko der Kontamination oder Beschädigung der Probe verbunden, so dass letztendlich ein Bedarf an neuen Methoden besteht, welche eine kontaktlose Messung und Überwachung der mechanischen Eigenschaften ermöglichen können. Wie und ob LDV für die mechanische Charakterisierung von solchen transparenten biologischen Materialien, wie beispielsweise Hydrogele, lebende Zellen, Sphäroide und natives sowie künstliches Gewebe verwendet werden können, wird in dieser Arbeit als grundlegende Fragestellung untersucht.

Unter Verwendung eines Nahinfrarot (NIR) LDV-Gerätes wurden die Frequenzspektren von Gelatinescheiben analysiert und basierend auf mathematischen Modellen wurden deren mechanischen Eigenschaften aus den erhobenen LDV-Daten abgeleitet. Es folgte ein Vergleich der Ergebnisse mit Literaturwerten sowie mit gemessenen Elastizitätsmodulen die mittels indentations-basierter Rasterkraftmikroskopie (IT-AFM) und einaxialen Druckversuchen, zwei etablierten Methoden zur mechanischen Charakterisierung biologischer Proben, gewonnen wurden. Die mittels der LDV Daten ermittelten Elastizitätsmodule zeigen eine gute Übereinstimmung mit den experimentellen Ergebnissen der Druckprüfung, während die IT-AFM-Ergebnisse den Elastizitätsmodul zu unterschätzen scheinen, was auf belastungsabhängige Versteifungseffekte des Gelatinematerials zurückzuführen sein könnte. Zusätzlich wurden die elastischen Eigenschaften durch die Messung der Dynamik einer doppelt eingespannten Balkenstruktur, auf welche die Gelatineprobe gegossen wurde, abgeleitet. Im Vergleich zur direkten Messung wurde hierbei ein ähnlicher Trend festgestellt, aber aufgrund des nicht-permanenten Kontakts zwischen der Probe und der Balkenstruktur sind die Ergebnisse nicht allzu belastbar. Die Messung der Dynamik von lebenden Zellen, welche komplett mit Kulturmedien bedeckt sind, wurde mit einem 532 nm LDV-Gerät untersucht und lieferte aufgrund der geringen Reflektivität der Zellmembran keine verwertbaren Ergebnisse, die mit den mechanischen Eigenschaften der Zelle in Verbindung gebracht werden könnten. Die Kontraktionsaktivität von Kardiomyozyten und Kardiomyozyten-Sphäroiden, sowie deren Beeinflussung durch Medikamente, wurde mittels LDV gemessen und mit den Ergebnissen der Particle Imaging Velocimetry Analyse verglichen. Während an Kardiomyozyten-Monolayern, die vollständig mit Zellkulturmedium bedeckt waren, kein LDV-Signal aufgezeichnet werden konnte, konnte die natürliche und die medikamentenverstärkte Kontraktion von teilweise bedeckten Kardiomyozyten-Sphäroiden analysiert werden. Die Analyse von Rinderknorpelproben zeigte keinen Unterschied zwischen enzymatisch verdauten und unverdauten Proben. Zuletzt konnte künstliches Gewebe in Form einer an der Luft frei hängenden, zellbeladenen Kollagenstruktur erfolgreich mit einem NIR-LDV-Gerät analysiert.

Die Ergebnisse dieser Studie zeigen erstmals die Machbarkeit der LDV-Methode als neuartige mechanische Charakterisierungsmethode für transparente biologische Materialien auf und können als Leitfaden für zukünftige Studien verwendet werden.

Acronyms

AFM	Atomic force microscopy
BPM	Beats per minute
CAD	Computer-aided design
CO_2	Carbon dioxide
ECM	Extracellular matrix
FDM	Fused deposition modeling
fps	Frames per second
FRF	Frequency response function
HEPES	4-(2-hydroxyethyl)-1-piperazineethanesulfonic acid buffer solution
hMSCs	Human mesenchymal stem cells
iPS	Induced pluripotent stem-cells
IT-AFM	Indentation-type atomic force microscopy
LDV	Laser-Doppler vibrometry
NIR	Near-infrared region ($\sim$790 – 2,500 nm)
NIR-SLDV	Near-infrared scanning laser-Doppler vibrometry
O_2	Oxygen
PBS	Phosphate buffered saline
PIV	Particle imaging velocimetry
PLA	Polylactide
RPM	Rounds per minute
SLA	Stereolithography
SLDV	Scanning laser-Doppler vibrometry
STL	Surface tessellation language

Symbols

A	area
a	nodal diameter
c	damping constant
b	nodal circle
d	distance
D	plate bending stiffness
E	Young's modulus
F	force
f_D	Doppler frequency
f_d	damped resonance frequency
f_n	undamped resonance frequency
$F(\omega)$	input force
h	thickness
$H(\omega)$	transfer function
I	intensity
k	structural stiffness
l	length
m	structural mass
n	refractive index
r	radius
R	reflected energy
$X(\omega)$	output response
α	absorption coefficient
β	half opening angle to an edge of the AFM cantilever tip
γ	damping constant
ρ	density
κ	optical extinction coefficient
λ	wavelength
ν	Poisson's ratio
ω	circular frequency
ζ	damping ratio

Contents

1

Introduction

In nature, as well as in technology, functionality often results from the combination of a system's geometrical structure and mechanical material properties. In many cases, the structure itself can be evaluated by optical measurement methods on different scales. However, the material properties are not easy to determine, and their characterization often requires complex, contact-based measuring methods. Such contact-based methods often rely on defined sample geometries, and their integration into existing manufacturing or production processes can be challenging. Tissue engineering (TE) and the emerging field of biofabrication, aiming to provide functional three-dimensional tissue replacement materials in the future, would benefit from a contactless mechanical characterization regarding process integration. The structure and mechanical material properties of native tissues could then be analyzed contactless, serving as a blueprint for fabricating new functional tissue equivalents. Relevant building blocks for such fabrication processes are soft biological materials, like hydrogels and living cells. However, if these materials do not match those native mechanical properties, functionality can hardly be achieved during subsequent tissue cultivation.

Instead of using contact-based methods, such as indentation or compression testing, potentially harming or contaminating the biological sample, contactless methods can be used for non-invasive mechanical characterization. Many of these methods characterize the mechanical vibrations of structures when subjected to external dynamic forces. Such mechanical vibrations can be observed everywhere around us in our daily lives: whether it is the beating of our heart, the buzzing of bees, or earthquakes shaking large areas of our planet. Entire buildings and bridges can slowly but steadily be excited into vibration by the wind, sometimes even to their point of failure. Everyday technologies, like microphones and loudspeakers, only function due to vibrations, just like the mechanisms of hearing and speaking in humans. Mechanical vibrations can be defined as a repetitive movement around a point of equilibrium and a permanent change between kinetic and potential energy, capable of traveling through three-dimensional structures with ease in the form of a wave. The way the vibration is modulated while passing through the structure allows to draw conclusions about the structure's inherent mechanical properties.

In vibrational analysis, engineers study exactly this reaction of physical structures and their components when subjected to dynamic external loads and forces [1]. By analyzing the system's response to an external input, parameters like resonance frequencies, damping and modes shapes can be identified, enabling the parametrization of the vibration: If the geometry and mass of a geometrical structure are known, the elastic and viscoelastic material properties can be deduced from the measured vibrational data by using suitable

mathematical models and methods, such as continuum mechanics or the finite element method (FEM).

Analyzing such vibrating systems requires a sufficiently sensitive, non-destructive and ideally contactless measurement method capable of measuring a broad range of sample structures regardless of their size and geometrical complexity. As an optical measurement method, laser-Doppler vibrometry (LDV) completely fulfills these requirements. LDV uses the optical Doppler-effect to determine the velocity amplitudes of oscillating surfaces and can therefore be used to measure vibrations contactless without altering the inherent dynamics of the investigated object. Today, LDV is a well-established method for a broad range of industrial applications, ranging from the automotive industry [2] to the characterization of rotating systems like wind power plants [3] and turbine blades [4]. Monitoring the structural integrity of large components in civil engineering and the in-line quality control of manufacturing processes by the analysis of vibration signatures are also common applications [5-7]. Besides these established industrial applications of LDV, also more unconventional applications have been investigated, like the determination of fruit ripeness [8-10], the communication between insects [11-13], or the walking dynamics of crabs [14]. In the medical field, LDV has been used to determine the structural health of teeth and bone [15, 16], detect aneurysms [17], and monitor the beating of the heart, also known as optical vibrocardiography [18]. LDV has also helped to define and understand the role of ligaments and tendons in the human body and human locomotion [19-21]. The characterization of the human hearing apparatus [22, 23], a better understanding of the tympanic membrane [22-24], and the ossicles could be achieved using LDV. Knowledge gained from such experiments enabled improved middle ear implants [25, 26] and ossicular prostheses [27]. Nevertheless, a lot of potential applications of LDV in the medical field have not been investigated yet. Especially when it comes to the mechanical analysis of biological materials used in TE and biofabrication [28].

This is the underlying motivation and the aim of this thesis: Evaluating if and how LDV can be used to analyze the mechanical material properties of various biological materials like hydrogels, living cells, native and engineered tissues and thereby contribute to the overall goal of TE to develop three-dimensional, functional replacement tissue or whole organs. The fact that most biological hydrogels, as well as mammalian cells, are optically transparent and reflect only a small percentage of the incoming laser intensity constitutes a major technological challenge, making a label-free measurement difficult. By establishing and applying appropriate experimental procedures, this work proposes new concepts for measuring these materials with LDV, always having future applications in mind, enabling a contactless and non-intrusive mechanical characterization of such materials.

2

Theoretical background

Laser-Doppler vibrometry: the fundamental physical principle

Trying to explain the motion of binary stars and the associated red and blue shift when observing them, Christian Doppler discovered the Doppler effect in 1842, the basic physical principle of LDV. The Doppler effect occurs when a wave, here an electromagnetic wave with a defined wavelength λ, is reflected by a moving surface with the velocity v resulting in a frequency shift (Doppler frequency) f_D of the reflected light [29]:

$$f_D = 2 \cdot \frac{v}{\lambda} \qquad (1)$$

In the LDV device, a laser beam is split into two beams, a measurement beam focused onto the sample surface and a reference beam, which never leaves the device. After the measurement, the laser beam experiences the frequency shift at the sample surface, and a Mach-Zehnder interferometer is used to create an interferogram by superimposing the reference beam and the measurement beam (see Figure 1). Via the interferogram, the frequency shift f_D and thus, the absolute value of the sample velocity can be determined.

To not only get the absolute value of the velocity but also the direction of the sample movement, the reference beam frequency is typically shifted by $\Delta f_R = 40$ MHz using a Bragg cell. The signal frequency f_S determined through the interferogram, representing the difference between the reference beam shift Δf_R and the Doppler frequency f_D, can then be used to calculate the surface velocity v:

$$f_S = \Delta f_R - f_D = 40\ MHz - \frac{2v}{\lambda} \qquad (2)$$

In this setup, a motionless sample generates a modulation frequency f_S of 40 MHz. If the sample moves towards the interferometer, f_S is higher than 40 MHz, and during a sample motion away from the interferometer, the modulation frequency is below 40 MHz.

The resulting intensity I_{res} of the interferogram is not equal to the sum of the two intensities of the measurement and reference laser but can be calculated using this equation [29-31]:

$$I_{res} = I_1 + I_2 + 2\sqrt{(I_1 I_2)}\cos\left[\frac{2\pi(r_1 - r_2)}{\lambda}\right] \quad (3)$$

The total intensity I_{res} results from the superposition of the two beams (I_1 and I_2) and the lengths of the two light paths r_1 and r_2 (r_1 for the measuring beam and r_2 for the reference beam). Equation (3) can be used to measure the displacement very precisely for amplitudes smaller than the used laser wavelength. If the displacement amplitude is larger than the laser wavelength, the oscillation cycles of the interferogramm have to be taken into account additionally.

The interferogram is analyzed using a photodetector, converting the optical pattern into an electrical signal. From a technical point of view, the frequencies at which the bright and dark fringes of the interferogram are oscillating is determined, being directly proportional to the velocity of the measured object and equals the difference between the reference shift Δf_R and the Doppler frequency f_D. Nevertheless, this velocity measurement mode is especially suitable for high sample oscillation velocities since a comparably high and well measurable Doppler frequency occurs. For oscillations below 1 Hz, it is often better to analyze changes of the interferogram's intensity, since in this case, only low velocity amplitudes and, therefore, a low frequency shift f_D are given.

As an optical measurement method, LDV relies on a sufficient amount of signal being reflected or scattered back from the investigated surface. This implies that materials with low reflectivity and scattering intensity typically do not reflect or scatter back enough signal at the applied wavelength. Besides, in such a case, light could potentially be reflected by surfaces behind the sample and superimpose with the signal originating from the sample's surface. If this is the case, results eventually are dominated by signals originating from behind the sample, masking the relevant dynamics of interest.

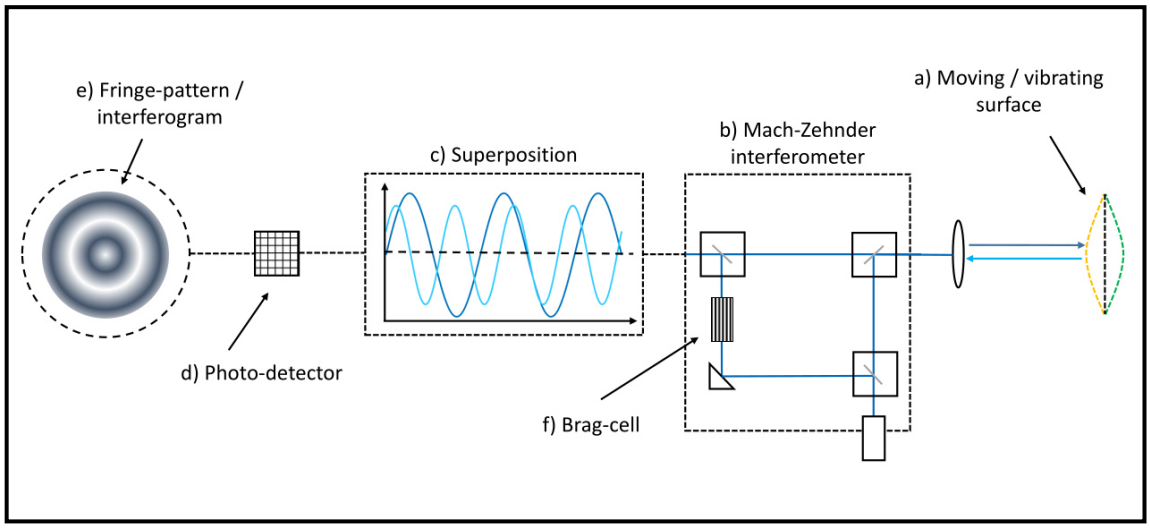

Figure 1 | Basic principle of LDV. *Focused light reflected from a moving surface (a) is superimposed with the original laser through a Mach-Zehnder interferometer (b). The two superimposed beams form a fringe-pattern on the photodetector, transforming the optical information into an electrical signal (d). A change in the oscillation frequency of the pattern directly correlates with the velocity amplitude, and changes in the interferogram intensity are linked to the vibration's displacement amplitude. Due to the 40 MHz modulation by the Bragg cell (f), the directionality of the vibration can be determined.*

Measuring transparent materials with LDV

Many biological materials are optically transparent dielectric materials, reflecting only a small percentage of the incoming laser intensity, making label-free LDV measurements challenging. The reflectance R can be calculated using the Fresnel equations. For dielectric materials and an incidental angle of $\theta = 0°$ with respect to the surface normal, as it is typically encountered in LDV measurements, the reflectance R is given by [29]:

$$R = \left|\frac{n_1 - n_2}{n_1 + n_2}\right|^2 \qquad (4)$$

Here n_1 and n_2 are the refractive indexes of two dielectric materials. As a consequence, only 2.01% of incoming laser intensity is reflected by the interface between air ($n_1 = 1$) and a material with high water content ($n_2 \approx 1.33$) [30, 32] at normal incidence in the visible range of the optical spectrum ($\sim 380 - 780$ nm) (see Equation (4)). For such a small amount of reflected signal, proper focusing becomes essential to ensure a maximum amount of light being applied to a single spot on the sample's surface, increasing the available signal onto the photodetector.

To overcome the challenge of low reflectivity, different approaches have been developed. The application of titanium dioxide powder can increase the reflectivity, but with aqueous materials, there is a risk of surface stiffening due to additional drying through the powder [33, 34]. Furthermore, the powder particles are making the surface rougher increasing diffraction and scattering effects. Another approach is the application of reflective adhesive tapes onto the sample's surface [16, 35]. This often alters the mechanical properties, especially of the surface area, which is not ideal regarding surface measurement methods such as LDV. Incorporating reflective particles in transparent materials also improves the

signal quality and measurement results [36, 37]. Nevertheless, each inserted material possessing different mechanical properties compared to the sample affects its behavior when subjected to external forces. This mainly accounts for lightweight and soft samples, like hydrogels, tissues, and living cells: the biological materials examined in this exploratory study.

In addition to the problem of low reflectivity regarding transparent materials possessing a high-water content, like mammalian cells or biological hydrogels, most of the light passes through the material, and only a small amount is reflected at its surface. If and how much of the applied laser energy can pass entirely through the sample depends on the absorption coefficient α and the sample thickness. The material- and wavelength-specific absorption coefficient α is defined as the decay length of the intensity as light travels through a material and the relation between the intensity I_0 before entering the material and the intensity I after traveling a distance d through the material is described by Lambert-Beer's law [30]:

$$I = I_0 e^{-\alpha d} \qquad (5)$$

Consequently, if the material-specific absorption coefficient α is known, the intensity I available behind the sample can be calculated. This ensures that no signal entirely passing the sample is back-reflected, superimposing with the signal originating from the surface of interest. This study used this formula to determine the optimal thickness for testing the gelatin samples (see Chapter 6.1).

Biological materials: building blocks for tissue engineering

The functionality of tissues and organs may be impaired from time to time due to accidents, illness, or aging. Such a reduced functionality continuously increases the currently unmet demand for donor organs and functional tissue substitute materials. The long-term goal of TE is to provide engineered, functional tissue replacement materials capable of mimicking the complexity of native tissues and contributing to the restoration of functionality in the patient's body. The three main constituents for achieving this goal are cells, growth factors, and biocompatible substrate materials, acting as a supporting framework for cellular growth and tissue generation by providing mechanical and biochemical cues guiding the cell-driven formation of structures and functions [38, 39]. In the ideal case, such engineered tissues are entirely produced out of biological materials, such as extracellular matrix (ECM) proteins, as these have a high degree of biocompatibility and cellular acceptance due to their natural origin. The relevant biological materials used in this thesis are collagen type I, gelatin, living mammalian cells, and native tissue. Furthermore, engineered tissues fabricated using a self-developed novel method combining living cells and collagen type I, referred to as biomolding (see Figure 24), have been analyzed in this study (see Figure 2).

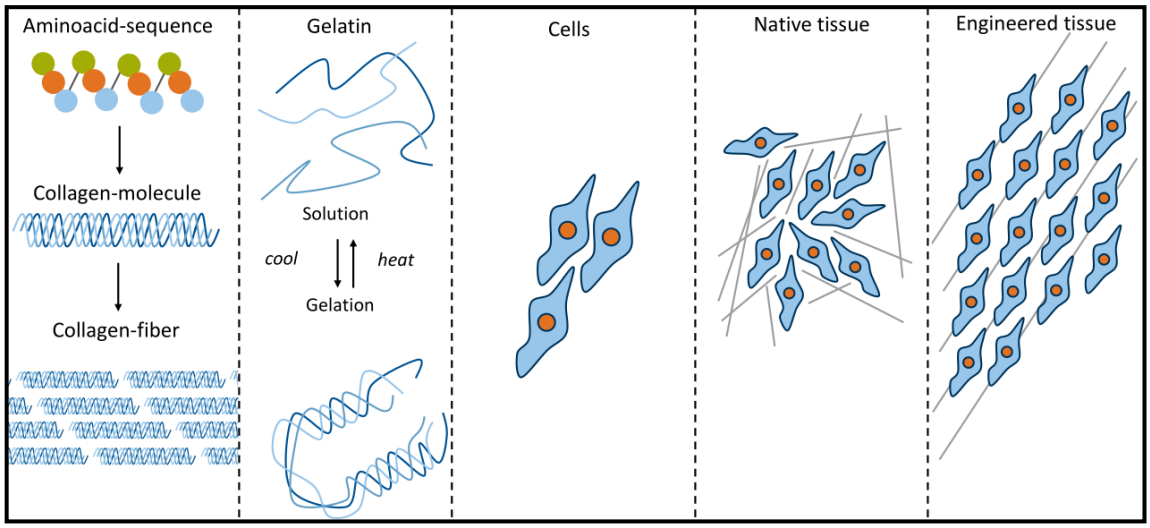

Figure 2 | Relevant biological materials used in this study. Collagen type I: *Structural protein consisting of triple-helical molecules self-organizing into bigger fibers through fibrillogenesis.* ***Gelatin:*** *Acidic treatment of collagen type I disintegrates its fibrillar structure. The resulting gelatin shows a thermoresponsive behavior, forming a solid gel when cooled down and a viscous solution when heated up. Solidification is achieved through entanglement and local triple-helical formations.* ***Cells:*** *Basic building unit of living organisms consisting of a membrane (dark blue contour), cytosol (light blue), and nucleus (orange).* ***Native tissue:*** *Material structured out of living cells and ECM proteins like collagen type I fibers (grey lines).* ***Engineered tissue:*** *Combining living cells and ECM proteins like collagen type I, engineered tissue can be fabricated using different bioprinting and biofabrication methods. Its structure can either follow the structure of native tissue or be altered regarding the patient's needs.*

Cells stabilize and adapt to their environment by producing and secreting three-dimensional ECM consisting of large proteins, such as collagen, enzymes, and glycoproteins [40, 41]. The most relevant ECM protein for this study is collagen type I, the most abundant structural protein in the human body. Collagen type I mainly consists of three monomers forming a 204.8 nm long triple helix. These procollagens are packed into oriented collagen fibrils and crosslinked with each other [42, 43]. Proper fibrillogenesis and network formation depend on several parameters, including pH-value, ionic strength, temperature, and protein concentration [44]. Using type I collagen has the great advantage that cells like fibroblasts and human mesenchymal stem cells (hMSCs) possess all the relevant enzymatic tools for proper fibrillogenesis and reformation of the collagen network [45]. Thus, using these tools, cells can reform their environment and tune its mechanical properties to achieve proper and functional tissue development. Finally, this connection between ECM and cells results in functional tissues and organs [46, 47].

Acidic denaturation of collagen type I disrupts its structure and leads to a thermoresponsive hydrogel known as gelatin [48]. When heated up, entangled gelatin molecules disengage and can slide past each other, forming a viscous solution. In this state, the material can be easily processed. Upon cooling down, the solution gels again in a reversible manner. Because of its good processibility and good biocompatibility, gelatin is often used in a broad range of applications ranging from the food industry [49] to ballistics [50, 51], as well as applications in medical sciences as a soft tissue substitute and tissue phantoms [52-56]. Those polymer networks often possess a high-water content similar to the human body and are categorized as hydrogels. When consisting of natural polymers, such hydrogels are perfectly suited for cellular incorporation and, thanks to their adjustable mechanical properties, can mimic a broad range of human tissues [57, 58].

Biological hydrogels like collagen type I and gelatin can be used as a growth substrate for cells, the smallest living unit in the human body. Initially, every cell in the human body

starts from a pluripotent stem cell, which has the unique potential to differentiate into all types of cells and organs [40]. Human body stem cells play an important role in regeneration processes, making them important for therapeutic approaches in medicine [59-61]. Because in the human body, pluripotent stem cells capable of differentiating into different types of cells are only present during the embryonic stage, a novel method was developed by Shinya Yamanaka in 2006 [62]. With this method, somatic cells can be reprogrammed with the help of viral vectors to possess pluripotency again. Originating, for example, from endothelial skin cells available in huge amounts, iPS-cells offer the potential of providing a sufficient amount of patient-specific stem cells for future applications in TE and regenerative medicine.

One early approach in TE was the printing of scaffolds using suitable biocompatible and biodegradable thermoplastic materials, and cells were seeded rather randomly in a thin layer on the scaffold surface [38, 63]. However, the thermoplastic materials used in this approach are not bioactive, meaning that they cannot be reformed by the cells according to their needs. As a result, the printed scaffold cannot be adapted in its mechanical properties by the cells and due to its structural stability and high elastic modulus of these thermoplastic materials are well-suited for bone and cartilage applications [64-66], but not for softer tissues like tendon, muscle, and lung, where this stiff material would impair maturation and reformation process, thus hindering the flexibility required for organ development and mobility. For such soft tissues, the decellularization of intact organs and the recellularization with patient-derived stem cells is a more suitable approach [67, 68]. Here, recellularization is often achieved through the vascular system into the decellularized organ. Often, the decellularized ECM between the existing vascular structure is reseeded irregularly and incompletely with the patient's cells. The flow required for pushing the cells into the organ matrix potentially harms the cells, impairing full functionality [69-71]. In recent years, the interdisciplinary combination of additive manufacturing and TE methods advanced the fabrication of three-dimensional tissue replacement materials, leading to new and promising approaches in the emerging field of biofabrication.

Tissue engineering meets additive manufacturing: the evolving field of biofabrication

Biofabrication can be defined as the fabrication of complex biological structures using living cells, molecules, ECM, and biomaterials [72, 73]. Biofabrication is located at the interface between developmental biology, material sciences, and mechanical engineering and includes the fabrication together with the subsequent maturation to deliver functional tissue equivalents [73]. Considered part of TE, biofabrication as a term was first mentioned describing the biomineralization processes of pearls [74] and the enamel deposition on mammalian teeth [75]. Cell sheet technology [76-78], the casting of cell-laden materials into molds [79-81], and the seeding of cells onto a porous, often 3D-printed, biodegradable scaffold structure [64, 82, 83] have long been among the main biofabrication approaches relevant in TE. With additive manufacturing, a new method called bioprinting has been developed to fabricate such living constructs. In bioprinting a cell-laden hydrogel, a so-called bioink, is used and the desired geometry is produced in a layer-by-layer approach [84, 85]. Thereby, the material is selectively placed where required, thus enabling the fabrication of complex, organic geometries. This freedom-of-design aspect is the main reason why bioprinting holds such high potential for TE and the future development of tissue replacement materials based on an entirely new workflow (see Figure 3). Now, the fabrication process uses not only the patient’s cells but also his highly complex geometry.

This advantage also includes cavities necessary for the perfusion of the artificial organ, and the supply of nutrients and oxygen are as easy to implement as the complex internal structures of bones, capable of bearing the entire weight of a human body [85].

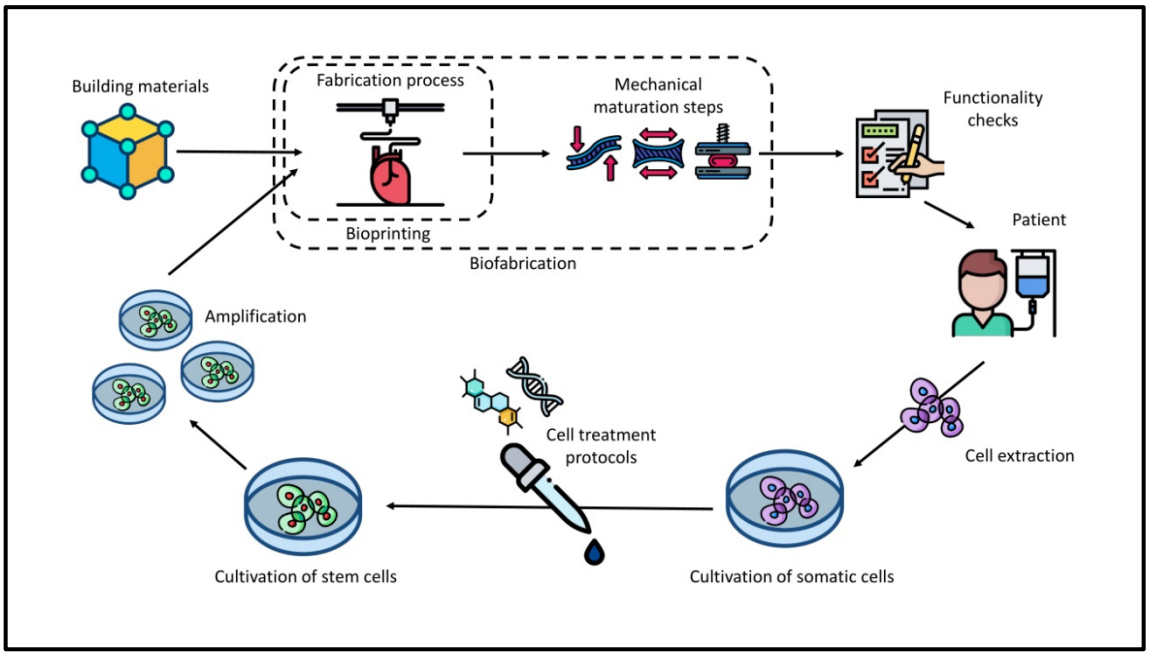

Figure 3 | Tissue Engineering workflow supported by biofabrication and bioprinting. *Cells extracted from the patient are transformed into pluripotent stem cells through specific treatment protocols. Subsequent cultivation increases the available amount of cells for tissue fabrication. Suitable bioinks for printing are obtained by combining living cells and relevant building materials, like natural and synthetic polymers. Using techniques such as extrusion-based bioprinting, three-dimensional, cell-laden structures can be manufactured. During cultivation, mechanical stimuli are applied by external forces enabling the development and maturation towards functional tissue equivalents. After a successful assessment of the relevant functionality, the engineered tissue can be transferred into the patient restoring the initially impaired function.*[1]

Among various bioprinting methods developed in recent years, extrusion-based printing is a widely used technique in academia and industry [87]. Like every manufacturing method, extrusion-based bioprinting imposes specific printing materials requirements, the bioinks [88, 89]. These cell-laden materials should have a low viscosity during extrusion through the printer nozzle to minimize harming shear forces exerted on the cells. After the extrusion process, the same material should be as rigid as possible to maintain the desired geometry after fabrication and during subsequent cultivation. These conflicting requirements often are reconciled by introducing high-crosslinker densities [90], synthetic polymers with tuneable rheological properties ensuring a high shape fidelity [91, 92], or a high overall polymer concentration [93]. However, a high polymer concentration can be a restrictive environment for cell growth, cell proliferation, and cell migration, thus hindering functional tissue formation [94, 95]. Natural polymers, such as collagen or other ECM-based materials, are particularly attractive for bioprinting applications because cells have the tools to work with them, like crosslinking or hydrolyzing enzymes, and can thus reform the printed structures according to their requirements internally. Furthermore, these materials have been evolutionarily optimized to the needs of cells over millions of years. Unfortunately, most ECM-based materials are challenging for the use in extrusion-based bioprinting. This is due to their self-assembly and polymerization mechanisms leading to a fibrillary network. Before fibrillogenesis, the monomeric starting solution is too liquid for maintaining a three-

[1] The single pictures have been taken from the image database *flaticon* [86].

dimensional printed geometry and after fibrillogenesis, the gel is too solid for printing, likely to clog the printer nozzle [96-98]. One possible way to overcome these limitations is to use so-called support-baths maintaining the printed geometry until fibrillogenesis is completed, by matching the viscous properties of the printing material [96, 99].

Within the scope of this project, a novel method for the production of cell-laden, three-dimensional constructs fabricated using natural ECM proteins has been developed, here referred to as the biomolding approach. In this approach, a synthetic Pluronic F127 sacrificial ink well-suited for extrusion-based printing and TE applications [100-103] is used for printing a temporary casting mold. This material can be washed away after the casting and solidification through fibrillogenesis of the cell-laden ECM-hydrogel without harming the engineered tissue. Similar casting approaches have already shown promising results for fabricating engineered tissue equivalents entirely made out of natural materials [81, 104-106]. We have integrated a fixation for the engineered tissue in our approach, capable of guiding its growth according to its geometrical design facilitating maturation (see Chapter 5.8). In both bioprinting and biomolding approaches, single cells are mixed with one or more suitable carrier polymers. High cell densities can be printed but also change the rheological properties of the bioink, eventually impeding the fabrication process [107]. Cell concentration can be too low, and the resulting distance between the single cells is too high for enabling a fast and reliable tissue formation process and, therefore, important cell-cell interactions [108, 109]. In our biomolding approach, the casting of high cell density materials does not pose any problem.

One way to increase the cellular concentration in engineered constructs without affecting the rheological properties of the printing material are cellular aggregates, so-called spheroids. Such spheroids can be generated by seeding cells into a non-adherent round-shaped geometry, resulting in a fusion of the single cells into one spheroid driven by gravitational forces [110]. Furthermore, by incorporating spheroids into bioinks or the direct printing of spheroids as building blocks, a higher degree of functionality can be achieved [111]. Compared to two-dimensional biological systems, three-dimensional assays show a higher level of authenticity regarding drug testing [112]. Consequently, spheroids are often used for studying cell-cell interactions and drug testing [113, 114]. Combining different cell types in one spheroid creates an organoid, often possessing characteristics of the target organ [115]. Due to their fusing capabilities, spheroids are often used as building blocks in organ printing, following the principle of directed tissue self-assembly [116-118]. These benefits make spheroids interesting for TE and biofabrication applications and therefore are also considered in this study.

Nevertheless, such engineered constructs still rely on applying chemical and mechanical stimuli after their fabrication to achieve complete functionality of the target tissue and organ through a guided maturation. In recent years, especially the importance of mechanical stimuli and their incorporation into tissue cultivation through mechanical maturation devices to facilitate maturation became increasingly important [119-124].

The importance of mechanical properties in tissue development

Regarding the development of functional tissue, the incorporated cells need further information through biochemical and mechanical stimuli after the bioprinting process in order to differentiate into the required cell type of the target tissue. Through the printing process itself, only a cell-laden three-dimensional geometry can be achieved. Organ or

tissue-specific functionality has to be obtained and guided through the subsequent maturation processes. Recent studies have shown a strong linkage between cell fate and the mechanical properties of the cellular microenvironment [125-127]. Cells can sense their environment's mechanical properties and receive mechanical stimuli from neighboring cells and the extracellular matrix [128-131]. Gradients in the Young's modulus guide cell migration and other processes like neuron growth and vascular tube formation [132-136]. Pathological processes, such as cancer growth and the formation of metastases, are influenced by the mechanics of the cancerous cells and their surrounding ECM [137-140]. Studies show that for each type of tissue and organ, specific mechanical properties can be defined for the healthy and functional state [130]. Deviations from this expected state indicate potential disease progression, structural damage, and functionality loss [125].

Taking all this knowledge into account, the relevance of biological materials being able to mimic the mechanical properties of their native template is shown [141]. Furthermore, in addition to the different tissue types, also the tissue-specific cells themselves have specific mechanical properties [139]. Consequently, in order to obtain functional tissue substitute material, the material properties after the fabrication process are crucial, as they initiate maturation of the artificial, engineered tissue towards a more functional state. This is especially important for tissues that have to sustain high mechanical loads like cartilage, muscles, and tendons. Thus, it is necessary to continually monitor the mechanical properties during fabrication and maturation processes for obtaining functional tissue substitute material. Such in-situ mechanical properties monitoring of printed tissue constructs could be realized using LDV.

State of the art in measuring the mechanical properties of soft biomaterials

The high water content of biological materials is the reason for their intrinsic viscoelasticity leading to time-dependent mechanical behavior. The capability to mimic native tissue properties makes hydrogels highly interesting for TE applications in science and industry. Hydrogels can be described as highly hydrated and swollen polymer networks [142]. Their elastic properties arise from the crosslinked polymer network, and the viscous, time-dependent behavior arises from the trapped water within the network, which is relocated when external forces are applied [143, 144].

Depending on the method used for testing, both the elastic and the viscous properties or only one of the two can be measured. The mechanical characterization of biological materials is often done using contact-based methods, where an indenter is pushed into the sample or where the entire sample is compressed, determining the stress-strain relation [143-145]. In indentation testing, a probe of a defined geometry indents the sample while the force and indentation depth are measured. Using an elastic model, which accounts for the probe geometry, the elastic modulus can be deduced from the recorded force-indentation curve. Because of their limited mechanical stability, soft samples like biological materials can be damaged or even punctured during testing if too high strains are applied. Depending on the indenter's size, the results are referred to as the nano- and micro-regime of the material. By distributing the load over the whole sample surface and compressing the entire sample, the bulk properties of the sample material are revealed through compression testing. This can either be done in a confined or unconfined experimental setup [144].

For probing soft biological samples, such as cells, hydrogels, and native or engineered tissues, indentation-type AFM (IT-AFM) is a standard modality for spatially high resolved

mechanical indentation testing [128, 135, 146-149]. This high spatial resolution is achieved using a micrometer-sized cantilever spring with a small pyramidal tip with a curvature radius in the nanometer range (~20 nm) at its end. With this setup, forces from the piconewton up to the nanonewton regime (~10 pN – 10 nN) can be applied to the sample. The deflection of the cantilever is measured with an optical lever arm, i.e., a laser beam, which is reflected at the backside of the cantilever onto a segmented photodiode (see Figure 4 a)). Thus, a displacement of the laser spot generates a position-sensitive photocurrent. AFM was initially designed to create high-resolution topographic images by scanning the tip over the sample's surface (see Figure 4 b)). However, IT-AFM can also be used to mechanically characterize microscopic structures and their Young's modulus with submicrometer spatial resolution. Compared to optical techniques, AFM imaging and IT-AFM are comparatively slow since they rely on mechanical contact. Multiple data points have to be acquired to obtain statistically reliable datasets by scanning the sample surface since, at this small-scale, obtained data will possess higher variations. Thus, it is not the single measurement point but the multiple contacting of the sample surface that slows this method down. This is not the case with indentation measurements at the macro- or microscale, where often only a few measurements are sufficient for obtaining statistically reliable data.

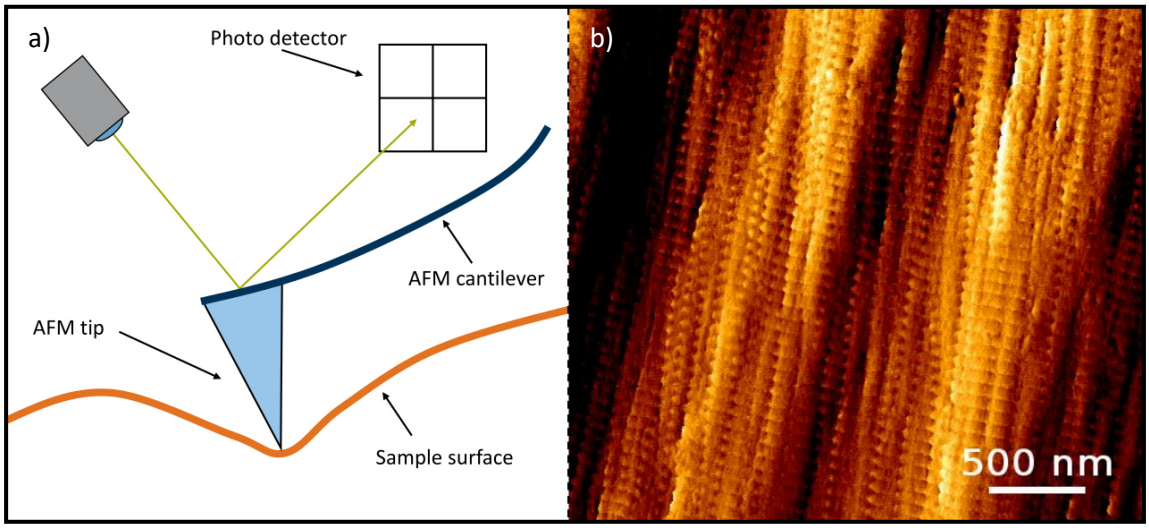

Figure 4 | AFM working principle. a) *By indenting the AFM tip into or scanning it over a surface, the AFM cantilever is deflected from its normal position. The tip displacement can be directly deduced from the position of the reflected laser beam on the photodetector. Because the cantilever's spring constant is known, the applied force can be calculated from the measured displacement, and from the resulting force-indentation curve, the Young's modulus can be deduced.* ***b)*** *AFM image (3 x 3 µm) of a mouse achilles tendon cryo-section. Collagen type I fibrils with the typical 67 nm D-band pattern can be seen in a highly aligned orientation, and collagen fibrils clustering to bigger fiber bundles. This image was kindly provided by Bastian Hartmann.*

Methods like indentation and compression testing are typically carried out in a quasi-static low-frequency mode for probing the elastic material properties. To determine the material viscosity, dynamic excitation schemes termed dynamic mechanical analysis (DMA) has been developed, where the sample is dynamically excited with increasing frequencies. Originally, DMA was used to determine the glass transition temperature of solid polymers by step-wise heating up the samples during the dynamic testing [150]. Usually, samples are placed between two circular plates. A sinusoidal stress is applied to the sample on one side, and the resulting sinusoidal deformation is measured on the opposite side for determining the strain. An in-phase response between input stress and output strain often accounts for a purely elastic material, a phase-shift of 90° for viscous material, and a phase-shifted

response for a visco-elastic material. [151]. Although the DMA method can characterize both viscous and elastic material properties, it is not optimally suited for biological materials since it often requires a defined sample geometry. Besides, a contact loss between the plates caused by the high water content and slippery surfaces can occur, making measurements challenging.

In contrast to contact-based methods, which usually require placing the samples on or in the measurement device, contactless methods can be used to investigate the sample from a distance and allow measurements of biological samples in a sterile environment. In addition, most contact-based methods exert substantial strain on the samples, while contactless methods can probe the samples exerting significantly smaller deformations. Such contactless testing is often implemented in the clinical field by using already available technologies like magnetic resonance imaging (MRI). A strong external magnetic field in MRI polarizes the spin of protons in hydrogen atoms and measures the relaxation times back to their equilibrium after shutting down the magnetic field. The relaxation time constants are different for hydrogen atoms bound by collagen molecules and differ with the hydration state of collagen, which can then be linked to its mechanical properties and disease progression [152-154], such as the detection of tissue fibrosis [155].

Another non-invasive mapping method for soft tissue elastic properties is shear-wave elastography (SWE) [56, 156-158]. In SWE, an ultrasound transducer is used for inducing shear waves traveling through the whole sample using an acoustic pushing pulse as excitation. The same device can then be used to track wave propagation, altered by the elastic sample properties, using the ultrasound echo [159-162]. Because the propagation velocity is strongly dependent on the fiber orientation in the sample, this technique can also be used to characterize the grade of anisotropy in biological materials [163]. Most of the described SWE approaches are minimally invasive. However, they cannot be fully considered contactless since the ultrasonic probe still requires surface contact to minimize signal loss due to the additional air interface. For samples with a defined geometry and constant distance to the sensor, a contactless measurement based on ultrasound can be realized [164]. Wave detection can also be realized using a focused ultrasound beam for exciting a more defined sample region and measuring the response using a hydrophone, making this method applicable in water and, therefore, also in physiological conditions [158, 165]. Ultrasound can be too weak to sufficiently exciting the sample. To overcome this problem, a probe attached to a linear actuator can be connected to the sample's surface and can be used to introduce surface waves, so-called Rayleigh-waves, which can then be analyzed with high precision using LDV [33, 34]. The previously described methods work with the echo of the excitation signal, increasing dispersive effects due to longer traveling paths, consequently lowering the signal quality. The spatial resolution can be increased using a laser for the excitation, as done in photoacoustic imaging. Here, the absorbed laser energy is internally converted to thermal energy resulting in a volumetric expansion. By switching the laser on and off periodically, the exposed sample position acts as a wave generator, and the emitted mechanical waves can be detected using an ultrasound probe [166, 167].

It should be noted that all the methods described above only probe a particular point or small area of the sample. Only by scanning over the entire sample surface it is possible to analyze thoroughly the structure of interest and its material properties. This can be time-consuming and requires expensive equipment. Instead, full-field methods can analyze the sample structure in one run without scanning or subsequent time-consuming stitching of

the data using digital imaging techniques. For example, particle image velocimetry (PIV) algorithms can measure the movement of speckle patterns on surfaces or the flow of particles in liquids [168]. Correlating the analyzed displacement with the material properties of the sample enables the calculation of strains, also known as digital image correlation and tracking [169, 170]. Nevertheless, especially for higher frequencies, expensive high-framerate cameras are required to generate a lot of data, making data analysis further time-consuming. LDV directly measures the desired physical value faster, with a beam at a micrometer-sized point and more reliably, since full-field methods such as PIV and DIC need to analyze a region to determine the displacement and subsequent extensive imaging analysis. An intensive and multi-step data analysis is often accompanied by the risk of higher variations, since several setting choices have to be made at each step.

All previously described contactless measurement methods analyze a system response resulting from a known input, often an impulse or dynamic force excitation. If input and output are known, the sample's inherent material properties can be determined by such a vibrational analysis using elastic theory and analytic or numerical modeling. As an input signal, the excitation energy is modulated according to those properties when passing through the sample towards the output location.

Vibrational analysis

In vibrational analysis, the oscillation of a system due to internal or external dynamic excitation is measured, and following the gathered information, the desired information about the system can be deduced. This methodology is most frequently used to monitor machinery and its structural health conditions [171-175]. All structures possessing mass and finite stiffness can vibrate through a periodic exchange between potential and kinetic energy. Mechanical vibration is an oscillating response of elastic bodies to disturbances with respect to their equilibrium position. Four categories of mechanical vibration can be defined based on the way energy is supplied to the system [176]:

- Free vibration: Pendulum, tuning fork, piano string
- Self-excited vibration: Wing flutter, violin string
- Forced vibration: Rotor unbalances, uneven road
- Parameter-excited vibration: Gear transmission

Free vibration occurs when a body is displaced from its equilibrium position by an external force, like an impact, possessing any kind of return force to its original position. The system vibrates at its undamped natural frequency f_n, and the oscillation amplitude decays over time due to internal and external friction. A single-degree-of-freedom mass-spring system is an example of free vibration with small damping. Its undamped natural frequency f_n, with the overall structural mass m and spring constant k can be calculated as follows [176]:

$$f_n = \frac{1}{2\pi}\sqrt{\frac{k}{m}} \tag{6}$$

Once deflected from its original position, such an undamped system will vibrate forever. Nevertheless, most real systems are undergoing damping effects. Through damping, energy stored in the vibration is partly dissipated by external or internal friction, both decreasing the oscillation amplitude over time. External friction originates from the interaction of the vibrating system with its environment, and internal friction arises from the system's molecules resisting the motion of the complete structure. Depending on the amount of damping, vibration can be reduced in its amplitude or even prevented, accounting for an overdamped system. The damped natural frequency f_d of a linear mass-spring-damper system with structural mass m, spring constant k, and the damping coefficient ζ is [176]:

$$f_d = f_n\sqrt{1-\zeta^2} \tag{7}$$

$$\zeta = \frac{actual\ damping}{critical\ damping} = \frac{c}{c_c} = \frac{c}{2\sqrt{km}} \tag{8}$$

In contrast, self-excited vibration arises from the modulation of a steady input force into a vibration near the structure's natural frequency, mostly due to friction effects. Compared to a free vibration, here, a long-term external force must be present. For example, this is the case in aviation when the steady airflow over the airplane's wings is modulated into vibration near thewing's natural frequency and results in flutter effects [176]. Exciting structures by a time-varying external force results in forced vibration. The system's resonances or natural modes of vibration will be excited if the external driving frequency matches the structure's natural frequencies. If parameters of the excited structure can be changed during operation, it is called parameter-excited vibration. This is, for example, the case when the gears in the transmission of a car are changed.

Modal analysis studies the dynamic properties of a system in the frequency-domain and is primarily concerned with the determination of modal parameters like the natural frequency, damping, and mode shapes [177]. Typically, experimental modal testing is done in a single input, multiple output configuration using one excitation point with known force and multiple measurement locations on the structure [178]. The input force is typically measured using a force sensor, and numerous output points are measured using accelerometers. The excitation can be realized by impact hammer testing or by using a shaker. An impact hammer generates an impulse measured by a force sensor at the tip of the hammer and results in all modes of the structure being excited. This method is ideal for small, lightweight structures. Electromechanical shakers amplify the signal generated by a signal generator, and compared to an impact hammer, more energy can be supplied to the system over a longer period [178]. An impedance force sensor, measuring both input force and acceleration at that driving point between the shaker and the structure, is installed. In both excitation schemes, the structure responds by attenuating some and amplifying other frequencies.

Because vibrating structures cannot be seen as single-degree-of-freedom systems and possess multiple degrees of freedom, excitation results in a spatial amplitude distribution over the whole vibrating structure. The overall shape of the vibration at the resonance

frequency is defined by the mode shape, meaning that all parts of the system move sinusoidally with the same frequency in a defined pattern of motion [178]. Unlike a free vibration, which usually is analyzed in the time domain, forced vibration is often described in the frequency domain as a function of the forcing frequency. This can be achieved using a fast Fourier transform (FFT) algorithm converting the measured time signal into a frequency-dependent representation of the amplitude. The Fourier transform decomposes the signal into its frequency components and treats the original signal as a sum of sine or cosine functions with different frequencies [30].

The inherent dynamic properties of structures like resonances frequencies, damping, and mode shapes can be obtained from the frequency-response-function (FRF). This transfer function describes the relationship between the input force and the output response as a function of frequency (see Figure 5). Modal parameters can be analyzed by curve fitting the calculated transfer function. In general, the FRF represents the summation of responses from multiple modes. Nevertheless, in the proximity of a resonance frequency, the FRF will be dominated by the response of the respective mode if the eigenfrequencies are well-separated and the damping is not too big [179]. The width of the resonance peak, also known as the full width at half maximum (FWHM) or full-width-at-half-power, holds information about the system's damping properties at the relevant frequency, also known as modal damping [30, 180]. The geometrical vibration pattern occurring near a resonance frequency is the mode shape. It can be analyzed using multiple sensors at different locations, or a scanning LDV (SLDV), enabling a fast characterization of surfaces. Such SLDV devices have various applications determining the spatial characteristics of mode shapes, even of very light structures without contact [2, 4, 181]. The resonance frequency is located at the peak of the resonance curve.

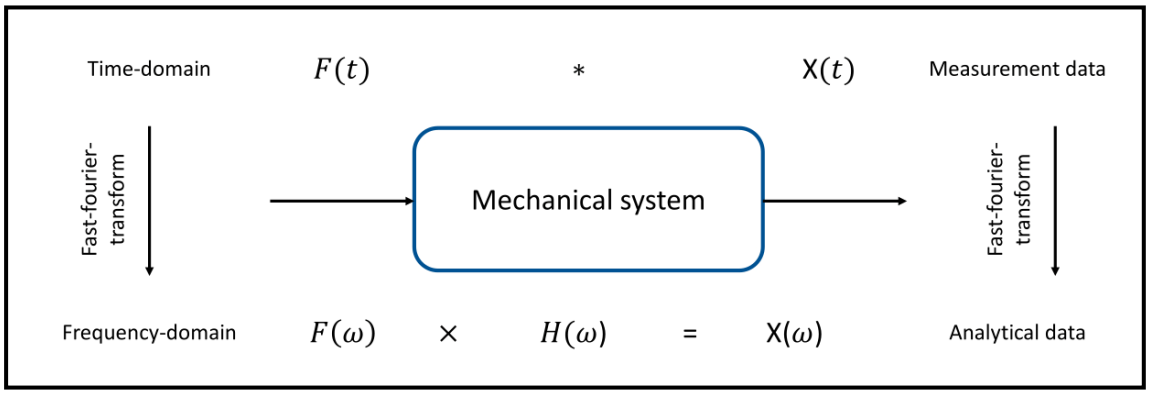

Figure 5 | Calculation of the FRF. *By applying a known force* $\boldsymbol{F(\omega)}$ *to a mechanical system and measuring its response* $\boldsymbol{X(\omega)}$*, the FRF* $\boldsymbol{H(\omega)}$ *can be calculated. The multiplication in the frequency domain corresponds to a mathematical convolution in the time-domain (*).*

For a single-input single-output system possessing linear time-invariant properties, the FRF can be calculated as follows and is described by different names depending on the physical values measured [182]:

$$H(\omega) = \frac{Output\ response}{Input\ force} = \frac{X(\omega)}{F(\omega)} \tag{9}$$

$$Receptance = \frac{Displacement\ response}{Force\ excitation}$$

$$Mobility = \frac{Velocity\ response}{Force\ excitation}$$

$$Accelerance = \frac{Acceleration\ response}{Force\ excitation}$$

$$Transmissibility = \frac{Velocity\ response}{Velocity\ excitation}\ (or\ ratio\ of\ accelerations\ or\ displacements)$$

The transfer function relevant for this study is the transmissibility and defines the relation between input and output measured in the same unit. Transmissibility greater than one implies an input amplification and the presence of resonances at the respective frequency.

Like accelerometers and impedance sensors, force sensors always add additional mass to the system affecting modal parameter estimation and require space for proper installation [183]. Furthermore, they rely on a sufficient amount of energy being introduced by the shaker to be able to measure with a good signal-to-noise ratio. Because this study mainly considers the measurement of soft and fragile samples, the input energy generated using a piezo was always relatively low to protect the samples. Moreover, the experimental setups were often lighter than the commercially available force sensors themselves. Especially for such applications, LDV is well-suited, and therefore, input and output are both measured as velocity data.

Putting it all together: using LDV for the vibrational analysis of biological materials

The proper development of functional tissue requires well-defined mechanical properties guiding tissue growth and maturation, also accounting for the fabrication of engineered tissue. Compared to contact-based mechanical testing methods, vibrational analysis using LDV enables a contactless and non-intrusive measurement. By analyzing the system's output related to a defined input, its inherent dynamics can be measured. If the mass and geometry of a vibrating system are constant, a change in its vibrational spectrum indicates a change in its mechanical properties. Through the calculation of the FRF, here the transmissibility, parameter identification of the measured structure can be made. By comparing the results of the LDV investigation with the mechanical data obtained from contact-based reference methods, a correlation between the frequency data and the mechanical properties of the samples can be realized. The expected mechanical properties can be deduced using analytical or numerical models if available for the used experimental setup, geometry, and

material. This is the basic methodology used in this study to perform vibration analysis on biological materials. Besides many other areas that could benefit from this new application of LDV, the evolving field of biofabrication is examined in detail as the key motivation of this thesis.

3

Objective and outline

Can LDV be used to characterize the mechanical properties of transparent biological materials without additional markers or coatings?

Motivated by the steadily increasing demand for tissue replacement materials and the resulting need for suitable mechanical testing methods, this currently unanswered question stated above is addressed in this thesis. The introduction of additive manufacturing technologies expanded the TE workflow leading to new techniques and strategies for providing personalized, tissue-imitating replacements adapted to the patient's needs, both in geometry and material, being developed (see Figure 3). Many materials used in TE are rather soft and fragile, and contact-based measuring methods are unsuitable for a direct process integration posing the risk of harming the sample during testing and often requiring an intricate sample preparation. Additionally, the contact between sample and measurement poses the risk of sample contamination. Because LDV is a high-resolution, contactless and non-destructive testing method, it can be integrated into the biofabrication process. Figure 6 shows the biological materials relevant to the TE-workflow, on which the applicability of LDV was tested.

In this study, various attempts have been made to evaluate the feasibility of LDV to characterize biological materials. This work focuses on measuring mechanical properties guiding cellular growth and tissue maturation, eventually leading to organotypic functionality. In a first approach, bovine cartilage samples, human cells, and cellular constructs like spheroids were investigated (see Figure 6). The developmental state of cells is directly linked with cellular mechanics, and therefore a contactless, non-invasive measurement of these properties using LDV can be a helpful assessment tool. Spheroids, tightly packed cell aggregates, can be used to introduce high cell densities in artificial, engineered tissues. By studying their reaction to changing environmental conditions, new insights into feasible fabrication processes of tissue analogs can be gained. In many aspects, spheroids can even be seen as small functional units. In this thesis, the contraction activity of cardiomyocyte spheroids and the changes caused by applying drugs like isoprenaline were analyzed (see Chapter 6.5). Besides their mechanical properties, the contraction activity is also an important marker regarding the viability and functionality of cardiomyocytes. Measurements on native tissues, such as bovine cartilage, provide information about the mechanical properties of healthy tissues, which is required for the fabrication of future engineered tissues (see Chapter 6.7). Knowing the change in stiffness of native tissues during an ongoing disease progression can be simulated through digestive enzymes during the experiment and can help to develop novel diagnostic methods in the clinical field.

Among the countless suitable building materials for such applications, collagen type I and its denatured from gelatin (see Chapter 2) are a frequent component of bioinks used in extrusion-based bioprinting [54, 184, 185]. Because gelatin is a thermo-reversible hydrogel, gelating below a concentration-dependent temperature, it is easier to handle and process than collagen type I. Therefore, gelatin was investigated more extensively in this study (see Chapter 6.2). Additionally, an experimental setup to monitor the mechanical properties of printed hydrogels, which potentially can be integrated into such processes, was investigated (see Chapter 6.3). At last, the application of LDV to engineered tissues was evaluated (see Chapter 6.7). For this purpose, a biomolding approach for the generation of three-dimensional, cell-laden structures was developed. Through a critical discussion of the results, the author deduces and recommends future experiments and directions for this interdisciplinary application of LDV in the area of TE and biofabrication.

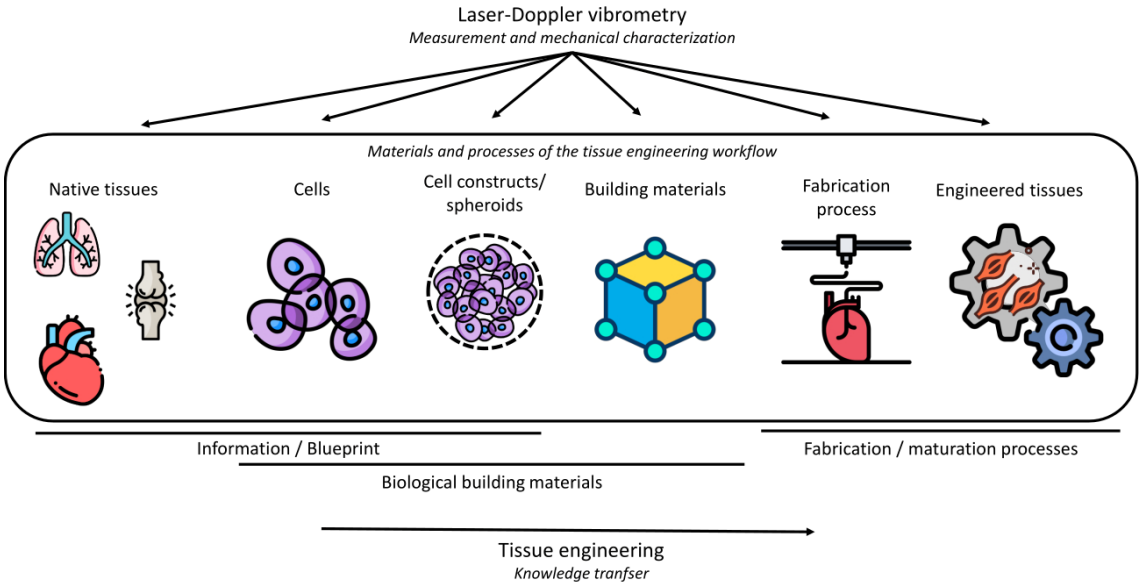

Figure 6 | Scope of this thesis: applicability of LDV on biological materials. *Experiments with native tissues and living cells can give clues and information about building up new, engineered tissue following its native structure and mechanical properties. This also accounts for cells and cell-aggregates like spheroids. Measurements on building materials, like hydrogels, ensure the right mechanical properties already during the fabrication process. Here, characterizing the mechanical properties through vibrational analysis can give clues about the developmental state of the cells. Direct monitoring of fabrication processes like bioprinting helps to standardize and adjust the properties of the engineered tissues. LDV can help monitor tissue growth and development during the maturation of engineered tissue, ensuring the desired functionality.*[2]

[2] The single pictures have been taken from the image database *flaticon* [86].

Various experiments have been designed and performed to evaluate the benefit of LDV for the mechanical characterization of biological materials. Each of them has their **motivation**, **goals**, and **results**, shortly presented in the **following abstracts**:

Optical transmission of gelatin samples

All mammalian cells and almost all biological hydrogels are transparent in the visible range of the optical spectrum (~ 380 – 780 nm). Besides, because of the comparatively low refractive index (n ~ 1.33) of mammalian cells and biological hydrogels, only a small percentage of the incoming light is reflected at their surface (see Chapter 2). Consequently, LDV measurements suffer from a weak signal, and light reflected from behind the sample may potentially interfere with the signal originating from the surface of interest and obscure the measurement (see Figure 7). To avoid such an undesired effect, a near-infrared (NIR) laser with a wavelength of 1550 nm was used, and the absorption coefficient of gelatin at $\lambda = 1550$ nm was determined by measuring the transmission through gelatin samples of different thicknesses. A material and wavelength-specific absorption coefficient could be calculated, and a sample thickness of 3 mm was chosen for the subsequent experiment, in which a circular clamped gelatin disk was investigated in its dynamics and mechanical properties. At this thickness, only a negligible proportion of the laser intensity passes through the sample, and the sample preparation process is still feasible. This experiment's results are presented in chapter 6.1 and published in Schwarz et al. [186].

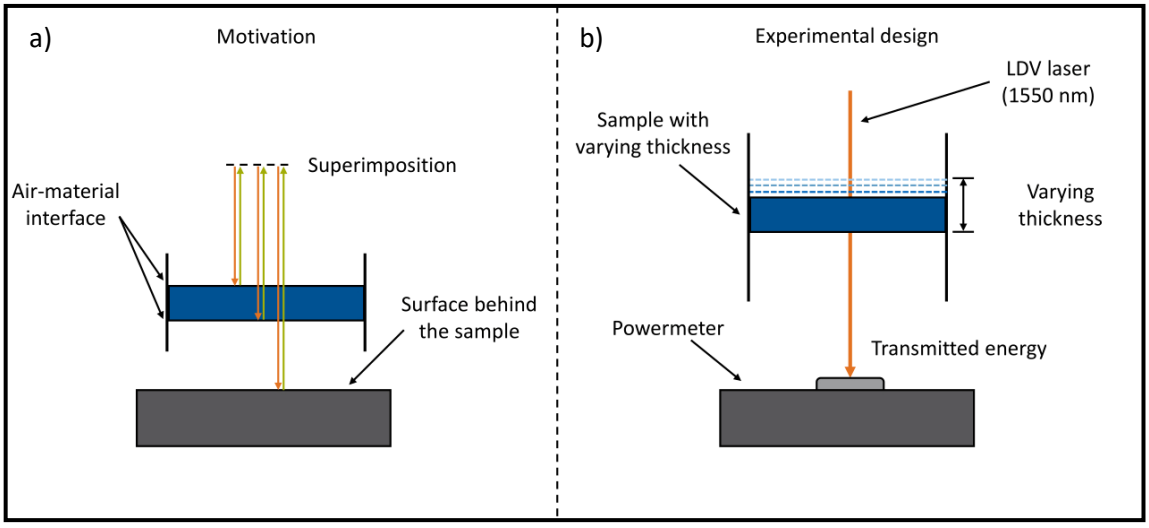

Figure 7 | Optical properties of gelatin. ***a)*** *This experiment helps to understand how much laser intensity can pass through the sample since a fraction of this reflected light could superimpose with the signal originating from the surface of interest, falsifying the results. The overall goal of this experiment was the experimental determination of the optimal sample thickness for subsequent experiments.* ***b)*** *Measuring the transmitted amount of laser energy at different sample thicknesses (blue rectangle and blue dashed lines) for a wavelength of 1550 nm, a material-specific absorption coefficient can be calculated, helping to deduce the proportion of transmitted laser intensity.*

Direct measurement of gelatin samples

This experiment investigated if the elastic properties of gelatin hydrogels can be determined using the LDV method. Here, the sample thickness was set to 3 mm, as determined by the optical transmission experiment described in the previous section. A suitable experimental design was developed for testing gelatin samples with different polymer concentrations, and a circularly clamped disk setup was chosen (see Figure 8). Correlation of LDV data and the mechanical properties were achieved by comparing the LDV results to IT-AFM and unconfined compression testing results. The results of these experiments are presented in chapter 6.2 and published in Schwarz et al. [186]. They show that the Young's moduli of the gelatin samples can be deduced from the LDV measurements, using both analytical and numerical methods.

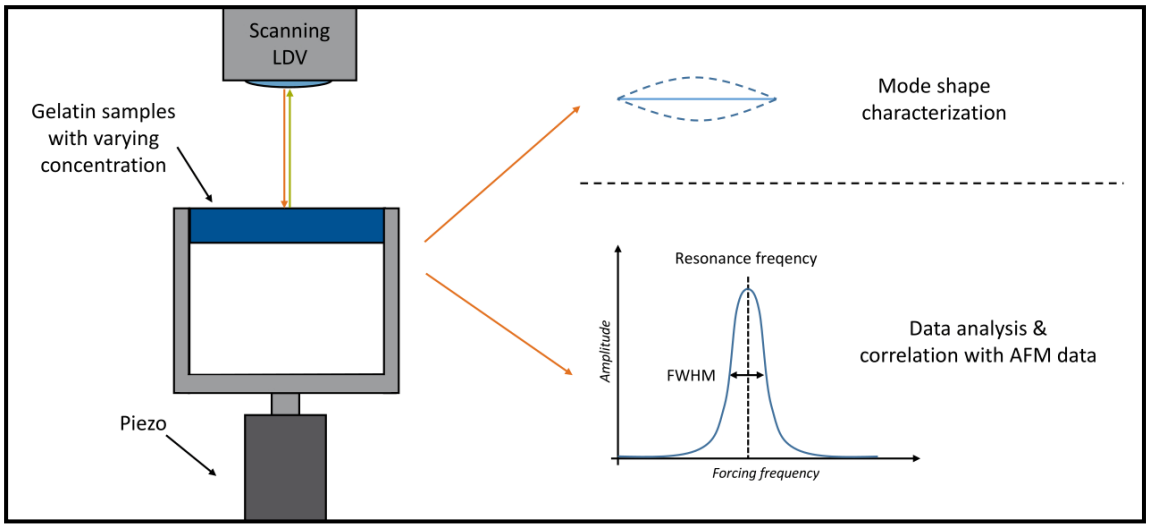

Figure 8 | Direct measurement of gelatin samples. *Using an SLDV device and a freely-suspended gelatin disk, the resonance frequencies and the mode shapes could be analyzed with the chosen experimental setup. A change in the resonance curves regarding peak frequency and FWHM could be detected by measuring different samples with varying polymer concentrations and different mechanical properties. This approach enables the characterization of soft and fragile materials.*

Cantilever-assisted measurement of gelatin samples

With the approach described in the previous paragraph, one can directly measure the response of the externally excited sample using LDV. Nevertheless, such a setup relies on time-intensive sample preparation and a defined sample geometry, rendering this approach unsuitable for direct implementation into bioprinting, biofabrication, or other processes. Therefore, a concept was developed where the hydrogel sample was placed on a bi-clamped beam (see Figure 9), which performs characteristic oscillations when dynamically excited by external forces. Through the interaction of this sensing geometry with the sample, the response of the sensing structure to the dynamic excitation is modulated according to the mechanical properties of the sample. While the properties are known and defined, a change in the system's response can be linked with the elastic properties of the sample being placed on top of the beam. One advantage of this approach is that difficult-to-handle samples, such as hydrogels, can directly be cast or printed onto the sensing geometry without any further preparation, thereby minimizing the required testing time. For correlating LDV data to the mechanical properties of the sample, IT-AFM measurements were again carried out. Possible applications of such probing structures could be the monitoring of critical process parameters in the production and processing of viscous materials. For example, an array of such bi-clamped beam structures integrated into the printing bed of a bioprinter could determine the properties of the printed hydrogel strands during the process [187]. The results presented in chapter 6.3 and published in Schwarz et al., show a decreasing displacement amplitude of the bi-clamped beam at its resonance frequency with increasing gelatin concentration, i.e., increasingYoung's modulus [188].

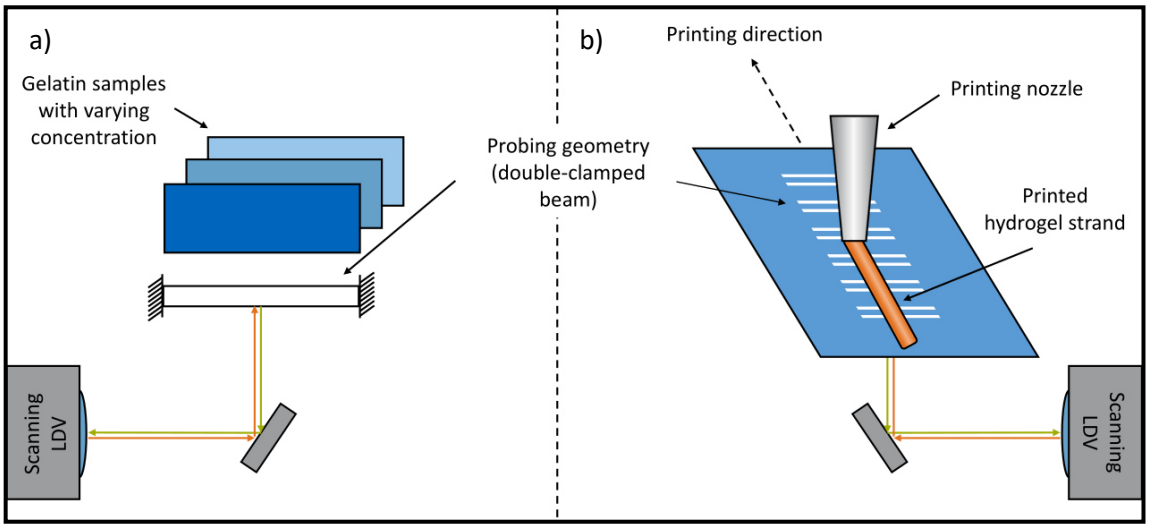

Figure 9 | Indirect measurement of hydrogels. a) *In addition to the direct measurement of the surface of a transparent sample, the measurement can also be performed using probe geometries, here a bi-clamped beam. For this purpose, the dynamics of this bi-clamped beam were measured from below, while different gels of different strengths were cast on its upper side. The vibration of the beam was then measured, modulated by the mechanical properties of the gel samples placed on top of it, and results were compared with Young's moduli from IT-AFM measurements.* ***b)*** *Compared to direct LDV measurement described in the previous paragraph, this approach can be integrated much easier into existing processes, like extrusion-based bioprinting.*

Vibrational analysis of living cells

Except for tissues such as cartilage and bone, possessing a high extracellular matrix (ECM) content, cells are the main building blocks of natural and artificial tissues. Their mechanical properties can give clues about ongoing cellular processes such as differentiation and disease progression. In these experiments, a microscope-based LDV setup with a wavelength of 532 nm was used, capable of analyzing microscopic structures. A monolayer of adherent murine fibroblast cells cultured in a Petri dish was used to investigate the direct measurement of the cells in a culture medium using a 20x water immersion objective (see Figure 10). The results of these experiments are presented in chapter 6.4 and published in Schwarz et al. [189]. Due to the low reflectivity of the cell membrane at this wavelength in an aqueous environment, no cell dynamics could be measured. Instead, only the vibration of the Petri dish surface below the cell was characterized due to its high refractive index and thus high reflectivity at the used wavelength. Originally, it was also planned to study and compare LDV data taken from cells possessing different mechanical properties, specifically induced through genetic modifications. This experiment could not be done since the chosen approach did not work.

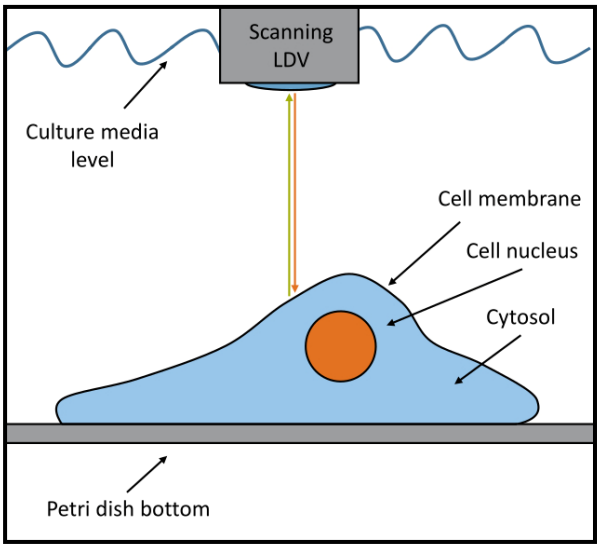

Figure 10 | Measurement of living cells. *The feasibility of characterizing cellular dynamics using a microscope-based LDV setup (wavelength of 532 nm) and water-immersion objective directly dipping into the culture medium was evaluated in these experiments. This is relevant for assessing the mechanical properties of cells and their deviation during disease progression or drug application.*

Characterization of cardiomyocytes and their contractility

Because the measurement of cells at a wavelength of 532 nm was problematic due to their low reflectivity at this wavelength, a new experimental setup was designed and investigated using an instrument again with a 1550 nm laser wavelength. For this wavelength, no LDV device with a microscope objective was available. However, because with a diameter of 60 μm at a focal length of 54.9 cm, the laser spot size of the 1550 nm scanning LDV is larger than a single cell, larger cell-spheroids were used for these experiments. By lowering the liquid level of the culture medium in the multiwell plate, it was possible to measure directly on the surface of the cardiomyocyte spheroids with the LDV, without the need for using a water-immersion objective (see Figure 11). To validate this new approach, a series of microscope images were recorded simultaneously to the LDV measurement using an inverted optical microscope, positioned underneath the multiwell plate containing the cell-spheroids. The contraction motions were extracted by analyzing the recorded images using PIV algorithms. Instead of probing differences in cellular mechanics, like in the previous experiments, the cardiomyocyte spheroids possess spontaneous contractility, which can be analyzed by the LDV device. The results of these experiments are presented in chapter 6.5. When the spheroids are partly exposed to air, their contraction activity can be directly monitored via LDV, and changes due to the application of drugs can be detected. Future applications of this concept could be the simultaneous monitoring of contraction rates and amplitudes of multiple spheroids, speeding up drug development, and the assessment of new, personalized treatment methods.

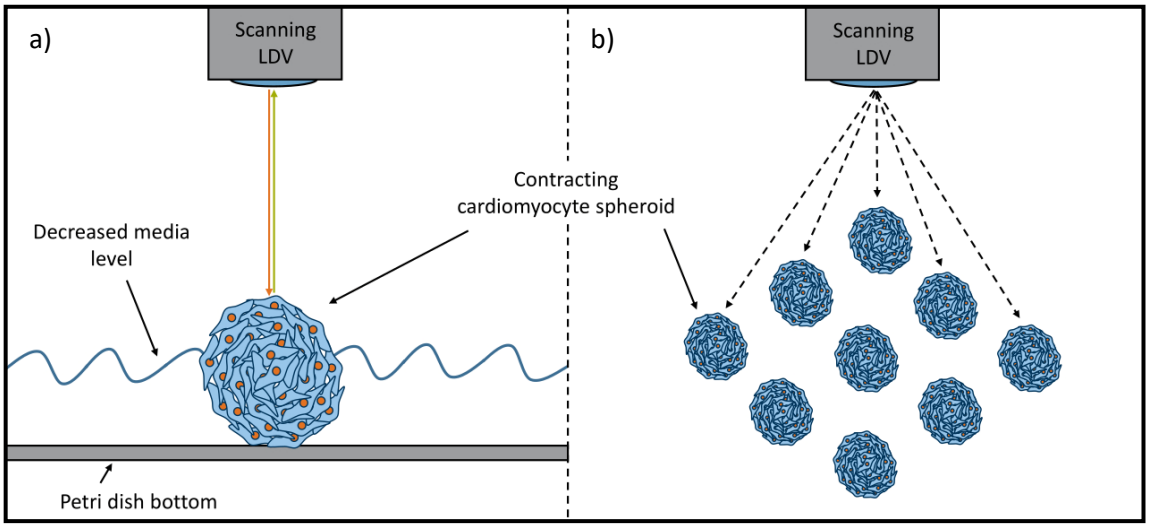

Figure 11 | Characterization of cardiomyocytes-spheroids. ***a)*** *This experiment evaluates whether the contractions of cardiomyocyte spheroids can be measured and detected with LDV. Due to the high absorption of water at 1550 nm, the level of the culture medium is reduced below the surface of the spheroids.* ***b)*** *Regarding future applications, LDV is well suited for high-throughput applications in drug development and the simultaneous characterization of the cardiomyocyte contractility.*

Measurement of native and digested tissue

Native tissues are the blueprint, revealing how to fabricate functional tissue equivalents. For the fabrication of engineered tissues. Their mechanical properties need to match a narrow window to ensure proper functionality. A deviation of these properties usually leads to a loss of functionality and often is one of the first hints for starting disease progression. Diseases of the cartilage, such as osteoarthritis, also lead to a disintegration of the collagen network during its progression, ultimately resulting in a functional disruption of the entire affected joint [190, 191]. With the progressive disappearance of the cartilage, the subchondral bone is increasingly exposed to mechanical impacts, and severe damage occurs. To test the applicability of LDV for analyzing pathological changes in tissues, measurements on bovine cartilage samples were carried out. Cartilage mainly consists of collagen type II and can be partially disrupted and disintegrated using the digestive enzyme collagenase. According to the literature, the Young's modulus decreases with increasing treatment time [192-195]. The sample was dynamically excited by directly contacting a piezo on the cartilage surface (see Figure 12). The reaction due to this input energy and its change resulting from the enzymatic digestion was analyzed using a near-infrared scanning laser-Doppler vibrometry (NIR-SLDV) device. Results of the LDV measurement were compared with data acquired from an indentation experiment. For both experiments, the same indentation geometry for mechanical probing and excitation was used. Between each set of measurements, the sample was further digested using the enzyme collagenase. This approach could help identify the small changes in the cartilage layer's mechanical properties using an endoscopic setup, indicating a starting disease progression. The results of this experiment are presented in chapter 6.6. The cartilage surface can be characterized using a NIR LDV device, but no significant change in the mechanical properties of the cartilage due to its enzymatic digestion could be detected.

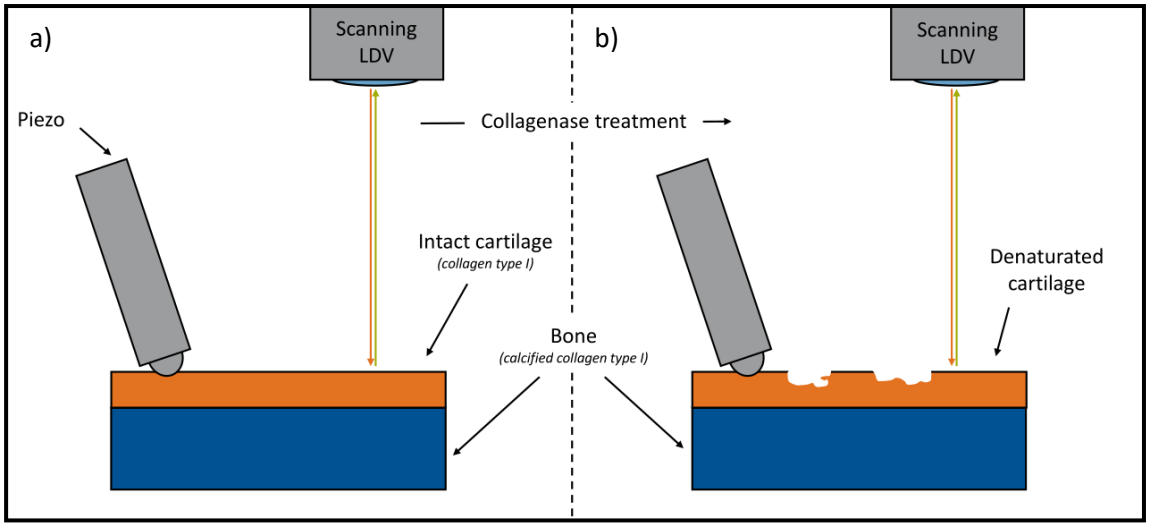

Figure 12 | Vibrational analysis of bovine cartilage samples. a) *The cartilage sample is excited by a piezo-driven probe on its surface. Using the LDV, the system's response to this input energy is measured.* ***b)*** *By applying the enzyme collagenase, especially the superficial collagen layers are denatured and disintegrated, changing the cartilage's mechanical properties. Because this process is also similar to the disease progression of osteoarthritis, LDV could potentially be used as a diagnostic method in orthopedics in the future.*

Measurement of engineered tissue

The biomolding approach developed during this study can produce cell-laden structures with a defined three-dimensional geometry. However, to obtain the desired biological functionality, these constructs must be cultivated and maturated before transplanted into the patient's body. During this tissue maturation, the mechanical properties of such a tissue undergo specific changes that can be used as an indicator revealing the success and progression of such a process. In these experiments, the biomolding approach was used to generate three-dimensional, cell-laden collagen constructs, and it was evaluated if the mechanical properties can be analyzed using LDV. Unlike cardiomyocytes, the hMSC used in this experiment do not contract periodically, but they actively reform their surrounding collagen network, also known as mesenchymal condensation [196-200]. This phenomenon's driving mechanism is the tensional homeostasis of cells, maintaining an equilibrium between internal and external cellular forces [201]. With increasing cultivation time, the constructs shrink and become denser, also changing their mechanical properties. Besides, the cells increasingly align themselves in one direction, creating an anisotropic structure, also altering its mechanical properties. This growing tension and anisotropy are necessary to produce mechanically active tissues such as muscles and tendons. In these experiments (see Figure 13), the question, whether LDV is suitable for detecting these morphological and mechanical changes in the tissue constructs is clarified in a first attempt, only addressing the measurability of such constructs. Future applications for this approach could be the high-throughput characterization of engineered tissue samples during their maturation and cultivation in pharmaceutical production lines. The results of this experiment are presented in chapter 6.7 and show that the first resonance frequency and its first bending mode of the engineered tissue can be detected.

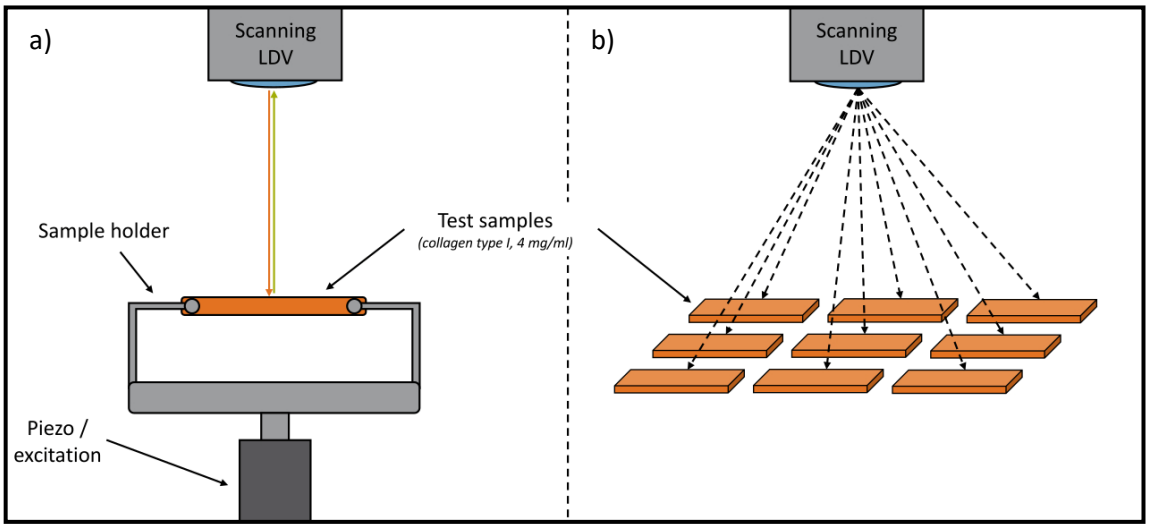

Figure 13 | Characterization of engineered tissue constructs. a) *The depicted initial experiment should clarify if it is possible to measure the resonances of three-dimensional collagen constructs using LDV. Over the time of cultivation, potential changes in the sample's mechanical properties could be detected.* ***b)*** *The potential of LDV lies in the parallelization of measurements. This will be mandatory as soon as three-dimensional engineered tissues are used in the pharmaceutical industry, where contact-based methods could be too risky in terms of contamination and sample integrity during measurement procedures. This concept is not evaluated in this thesis.*

4

Thesis contributions

This thesis contributes to the poorly investigated potential of using LDV for the non-destructive and contactless mechanical characterization of biological materials, relevant in the field of TE (see Figure 14). Like living cells and biological hydrogels, those materials are transparent in the visible range of the light, making optical measurements even more challenging. The main challenge is to find a proper experimental setup addressing and combining the individual requirements of two scientific disciplines, TE and vibrational analysis, with LDV. Before this study, these two fields were mainly unconnected. Bringing those two scientific fields one step closer to each other has been successfully mastered in this work, laying the fundamentals for new and interdisciplinary innovations.

So far, only labeled biological materials have been investigated with LDV. Such markers or reflective coatings can alter the mechanical properties of these often soft and fragile samples. A label-free measurement is mandatory regarding applications in the medical field since materials and components used in the medical field have to fulfill strict regulations. Consequently, every new component introduced into a process can be another potential source of failure regarding successful medical approval. Furthermore, samples should not be destroyed during testing and should be further cultivated after the experiment without contamination. This was the case for all experimental workflows and living materials used in this study.

Testing the mechanical properties of transparent biological hydrogels can be challenging to analyze due to their poor intrinsic reflectivity and low structural stability. The experimental workflow presented in this study allows for the non-destructive and contactless testing of elastic hydrogel properties. Furthermore, it was ensured that the laser signal reflected from behind the sample does not interfere with the measurement signal. As a sample geometry, a freely suspended disk was chosen. Furthermore, generating such a sample geometry can be challenging, is not always suitable for each type of material and this concept is not that easy to integrate into existing processes. Therefore, a workflow was investigated, which uses a bi-clamped beam cantilever for probing the sample. On top of this beam, the sample can be positioned. The change of the beam's dynamics due to the mechanical properties of the sample is measured. Since the reflectivity of the beam material can be adjusted according to the measuring laser's wavelength, the optical sample properties are no longer important. This approach can be well integrated into existing processes, where the mechanical properties of viscous materials and their monitoring are important, but contact-based testing is not feasible. This is, for example, the case for bioprinting (see Figure 14).

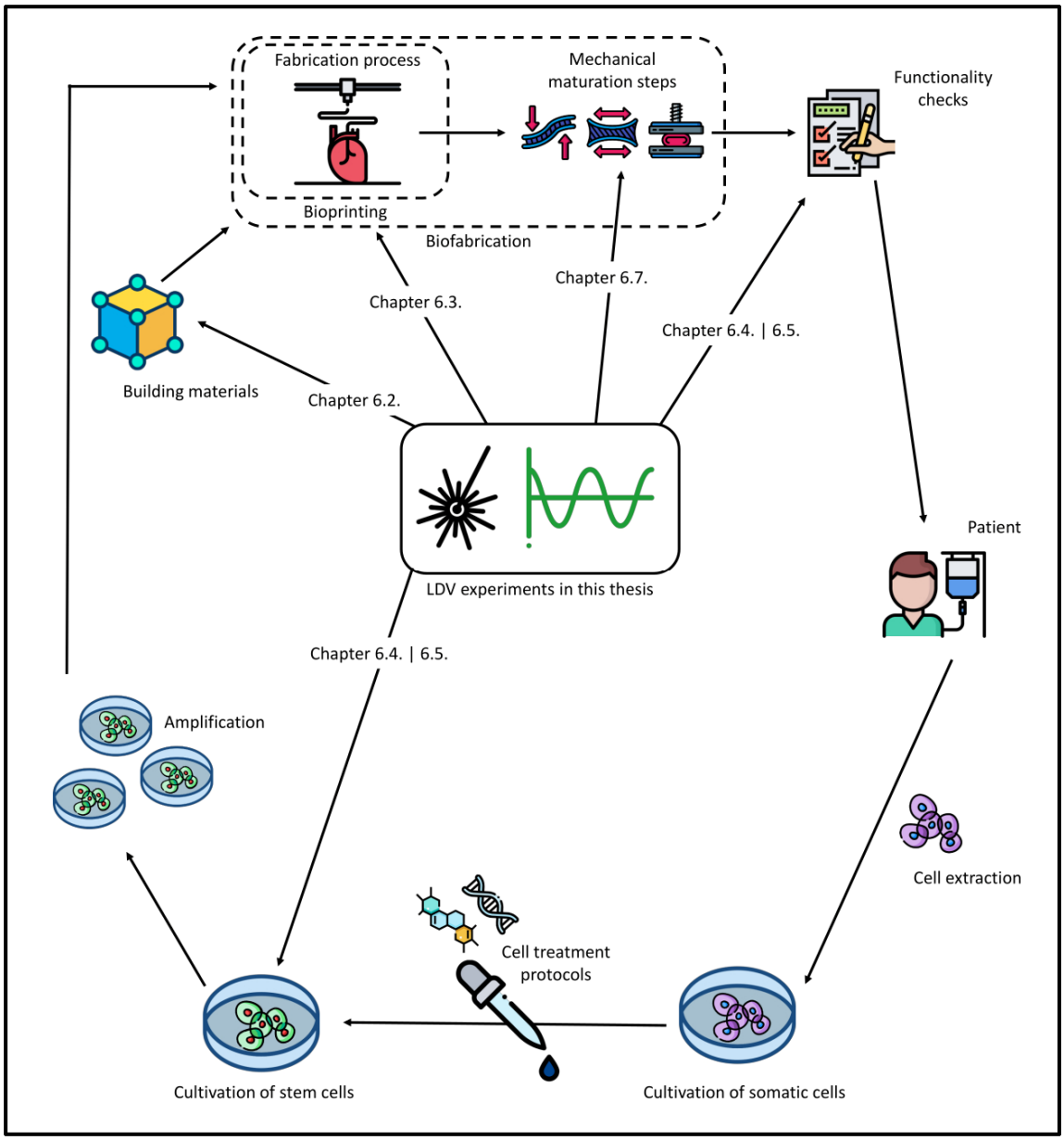

Figure 14 | Contribution of this thesis: applications of LDV regarding biological materials and fabrication processes relevant to the TE workflow. *This study answers the question, if and how LDV can be used for the mechanical characterization of biological materials. Therefore, LDV has been tested on different living and non-living materials, like gelatin, cells, spheroids, native and engineered tissues.*[3]

Besides biological hydrogels such as gelatin, this study also examined living cells. Measuring an adherent monolayer of living fibroblast cells, no signal could be recorded from their membrane surface but from the Petri dish bottom underneath them. In this experiment, an LDV device with a laser wavelength of 532 nm was used to analyze the cells submersed in a culture medium. The culture medium could not be removed since such a monolayer of cells is too thin for being partially exposed to air and possible drying out of the cells has to be prevented. Here, the NIR laser could not be used due to the high laser absorption of water at this wavelength of 1550 nm. However, this was the case with cellular aggregates, beating cardiomyocyte spheroids. Those were large enough to be partially exposed to air and analyzed in their contraction movement using a NIR-SLDV device. Also, the change of

[3] The single pictures have been taken from the image database *flaticon* [86].

the contraction activity due to the application of drugs could successfully be tested. Such a concept could help evaluate the functionality during quality control (see Figure 14)

Regarding tissue, native bovine cartilage and engineered tissue sample could be examined. The cartilage surface dynamics could be measured using the NIR-SLDV device, but the mechanical properties analyzed by indentation testing could not be derived from the LDV measurement data. In this experiment, only the basic question of whether a cartilage surface exposed to air can be measured is answered. This also accounts for the engineered tissue experiment results, which have been manufactured using the self-developed biomolding approach. Here, not only the dynamics of such a fabricated construct can be measured using a NIR-SLDV, but also its first bending mode. Regarding the workflow presented in figure 14, this proposed concept could help monitor engineered tissues during mechanical maturation steps directly after fabrication.

This work contributes to the field of TE, bringing it one small step closer to its future goal of fabricating functional tissue equivalents (see Figure 14). During this fabrication process, the measurement and monitoring of mechanical material properties are crucial. As a contactless and non-invasive optical measurement method, LDV is a suitable method for being integrated into this context. For evaluating this statement, various experimental designs for the mechanical characterization of transparent, biological materials using LDV have been proposed and investigated (see Figure 14).

Such living tissue replacement constructs will be first used as a more native model system for drug development and as a replacement for animal testing. This will be the entry point from purely academic and proof-of-concept science towards more industrial applications. One important missing piece for bringing TE and the fabrication of engineered tissues one step closer to such industrial and clinical applications is the lack of automatization and standardization. The more experiments can be carried out, the more representative the drug testing will be, and the more likely the decreased need in animal experiments becomes. The future goal of fabricating tissue equivalents for human patients can only be achieved by meeting regulations and increasing reproducibility, ensuring consistent product qualities. Currently, fabricated constructs do possess many variations regarding shape accuracy and later functionality. Additional to those mentioned variations, in medical sciences there is also the personalization regarding each individual patient, ultimately demanding for a standardized and personalized product at the same time.

In the future, the process presented in figure 14 needs to develop towards a more controllable and adjustable process. The approaches presented in this thesis for the LDV integration can help to narrow the gap between science and industry by proposing new strategies to standardize the often difficult characterization of biological samples in their mechanical properties and their batch-to-batch variations. The findings from the experiments conducted within this study can provide proofs-of-concept regarding different applications of LDV in the field of biological materials and contribute to integrating LDV as a measurement method to many applications in this field. Based on this study's results and experiences, new and better experiments can be planned and carried out to get an additional step closer towards this goal (see Chapter 9).

Short overview of thesis contributions[4]:

Elastic properties of gelatin hydrogel disks (label-free): *The presented concept enables the label-free and contactless characterization of gelatin and other hydrogels in their elastic properties.*

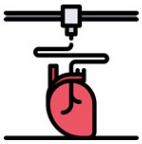

Elastic properties of gelatin hydrogels (probing structure): *With this approach, soft materials can be characterized in their elastic properties already during a fabrication process. This was done by measuring the dynamics of a bi-clamped beam and its changes due to sample contact using LDV.*

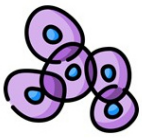

Living, adherent fibroblast cells: *Assessing the mechanical properties of adherent mammalian cells, submersed in culture media, could be a helpful monitoring tool in future cell culture. With an LDV laser wavelength of 532 nm used in this experiment, it was not possible to measure the dynamics of the unlabeled cell surface.*

Beating cardiomyocyte spheroids: *Using a NIR-SLDV, the contraction of cardiomyocytes partially exposed to air can be analyzed. This setup can especially be helpful in future high-throughput screenings in drug development for cardiac diseases impairing the contraction activity of the heart.*

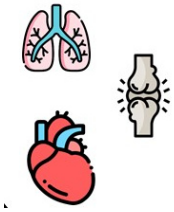

Native tissue: *In this experiment, the dynamics of the cartilage surface can be analyzed using a NIR-SLDV device. Nevertheless, the chosen excitation technique was insufficient for drawing conclusion about the sample's mechanical properties. In the future, this approach could be used, for detecting mechanical changes in the patient's cartilage via arthroscopic LDV.*

Engineered tissue: *The future monitoring of engineered tissue and its mechanical properties can be done with this approach. Here, the dynamics of an engineered tissue exposed to air were measured using a NIR-SLDV device.*

[4] The single pictures have been taken from the image database *flaticon* [86].

As part of the research work in this study, the following scientific contributions have been published by the author:

- Markus Krane, Martina Dreßen, Gianluca Santamaria, Ilaria My, Christine M. Schneider, Tatjana Dorn, Svenja Laue, Elisa Mastantuono, Riccardo Berutti, Hilansi Rawat, Ralf Gilsbach, Pedro Schneider, Harald Lahm, **Sascha Schwarz**, Stefanie A. Doppler, Sharon Paige, Nazan Puluca, Sophia Doll, Irina Neb, Thomas Brade, Zhong Zhang, Claudia Abou-Ajram, Bernd Northoff, Lesca M. Holdt, Nora Lang, Christian Kupatt, Connie Bezzina, Rüdiger Lange, Neil E. Bowles, Matthias Mann, Bruce D. Gelb, Lia Crotti, Lutz Hein, Thomas Meitinger, Sean Wu, Daniel Sinnecker, Peter J. Gruber, Karl-Ludwig Laugwitz, Alessandra Moretti
  Sequential defects in cardiac lineage commitment and maturation cause hypoplastic left heart syndrome
  Circulation, 2021
  DOI: 10.1161/CIRCULATIONAHA.121.056198

- **S. Schwarz**, B. Hartmann, J. Sauer, R. Burgkart, S. Sudhop, D. J. Rixen, H. Clausen-Schaumann
  Contactless vibrational analysis of transparent hydrogel structures using laser-Doppler vibrometry
  Experimental Mechanics, 2020
  DOI: 10.1007/s11340-020-00626-0
  The core of this paper was also presented at the IMAC-XXXIX digital conference 2021, IMAC-XXXVI conference 2018 (Orlando, USA), and GAMM 89th annual meeting 2018 (Munich, Germany).

- **S.Schwarz**, S. Kiderlen, R. Moerl, S. Sudhop, H. Clausen-Schaumann, D.J. Rixen
  Investigating the feasibility of laser-Doppler vibrometry for vibrational analysis of living mammalian cells
  Di Maio D., Baqersad J. (eds) Rotating Machinery, Optical Methods & Scanning LDV Methods, Volume 6. Conference Proceedings of the Society for Experimental Mechanics Series. Springer, 2020
  DOI: 10.1007/978-3-030-47721-9_4
  The core of this paper was also presented at the IMAC-XXXVIII conference 2020 (Houston, USA).

- **S. Schwarz**, B. Hartmann, R. Moerl, S. Sudhop, H. Clausen-Schaumann, D. J. Rixen
  Vibrational analysis of biopolymer-based hydrogels using 3D-printed test structures for applications in bioprinting
  Mechanics of biological systems and materials & micro- and nanomechanics. Proceedings of the 2019 annual conference on experimental and applied mechanics, Springer, 2019
  DOI: 10.1007/978-3-030-30013-5_6
  The core of this paper was also presented at the SEM Annual Meeting 2019 (Reno, USA).

- J. Schmid, **S. Schwarz**, M. Fischer, S. Sudhop, H. Clausen-Schaumann, M. Schieker, R. Huber
  A laser-cutting-based manufacturing process for the generation of three-dimensional scaffolds for tissue engineering using Polycaprolactone/Hydroxyapatite composite polymer
  Journal of Tissue Engineering, 10, 1 – 11, 2019
  DOI: 10.1177/2041731419859157

- J. Schmid, **S. Schwarz**, R. Meier-Staude, S. Sudhop, H. Clausen-Schaumann, M. Schieker, R. Huber
  A perfusion bioreactor system for cell seeding and oxygen-controlled cultivation of three-dimensional cell cultures
  Tissue Engineering: Part C, 24, 585 – 595, 2018
  DOI: 10.1089/ten.tec.2018.0204

5

Experimental methods

In the following sections, the experimental methods used in this study are described in detail. To improve the overall readability, detailed product descriptions such as the article number and manufacturer details can be found in chapter 10.1.

5.1. LDV-Measurements

5.1.1. Direct measurement of Hydrogels

In this experiment, the dynamics of a circular clamped hydrogel disk were examined using LDV. Therefore, an already prepared sample holder (see Chapter 5.4) was placed in a top-down orientation onto a piece of Parafilm™ via a standard adhesive tape (see Figure 28 a)). A defined volume of warm gelatin hydrogel, here 222 μl, was pipetted through one of the two lateral holes into the sample holder, resulting in a circular 3 mm thick gelatin disk (see Figure 28 b)). After five minutes at room temperature (22.3 °C), the sample was carefully transferred into the fridge and stored for another five minutes at 4 °C. Subsequently, the Parafilm™ could be removed manually without destroying the smooth surface of the hydrogel disk (see Figure 28 c)). The same sample holder was used for all experiments, and all resting times were the same among all samples. Measurements were done using a NIR-SLDV with a laser wavelength of 1550 nm. A close-up unit was used to achieve a higher resolution, decreasing the focal length to about 20 cm.

Starting an experimental run was done by screwing the sample directly onto the piezo stack. Here, the sample was allowed to rest for another 6 minutes for room temperature equilibration. Using the software interface, the laser was focused on the sample holder's rim (see Figure 15) since focusing on a solid, non-transparent surface was less error-prone. Because the experimental design results in a gelatin sample surface equal to the sample holder's surface, both are in the same focal plane, and consequently, the same focal value was set in the LDV system. A total of 20 measurement points were circularly defined onto the sample holder's rim and 31 measurement points on the gelatin disk's surface (see Figure 28 d)). With a HiFi-amplifier and the piezo stack, the sample was excited using a periodic chirp from 0 to 2.5 kHz (linear sweep with 1.56 Hz frequency resolution, 640 ms sweep time, 3906.25 Hz/s sweep speed) using the in-built signal generator of the SLDV device.

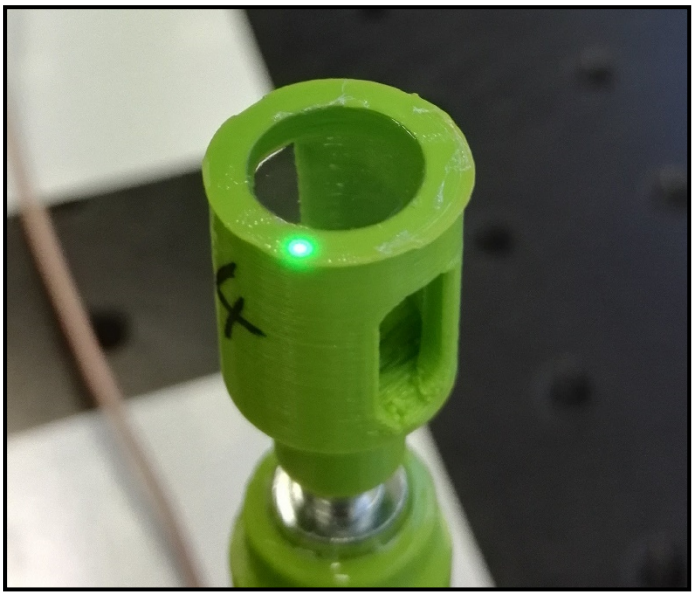

Figure 15 | Hydrogel sample during the measurement. *Focusing was done on the non-transparent rim of the sample holder (bright green spot of the pilot laser) and the determined focal value was also used for the transparent hydrogel sample. The sample holder was directly screwed onto the piezo stack.*

Analyzing measurement data and calculating the transmissibility was done using Matlab™ software. Taking the obtained velocity amplitude at each measurement point on the sample holder's edge, its mean velocity amplitude was calculated and used as an input signal for the transmissibility calculation. Transmissibility was then calculated by dividing the velocity amplitude (FFT) data acquired from the hydrogel disk's central point by the mean velocity amplitude (FFT) of the 20 sample holder measurement points. Analysis of the first resonance frequencies, here also described as (0,1) mode, and the corresponding FWHM was done using Matlab™ and the *findpeaks* function. The damping constant γ and the damping ratio ζ were derived from the FWHM of the squared transmissibility $\Delta f_{FWHM}(Transmissibility^2)$ following Equation (10) and (11) [180]:

$$\gamma = \pi \cdot \Delta f_{FWHM}(Transmissibility^2) \tag{10}$$

and

$$\zeta = \frac{\gamma}{2\pi \cdot f_{0,1}} = \frac{\Delta f_{FWHM}(Transmissibility^2)}{2 f_{0,1}} \tag{11}$$

where $f_{0,1}$ is the resonance frequency of the (0,1) mode.

5.1.2. Cantilever-assisted measurement of hydrogels

Instead of measuring the dynamics of a circular clamped disk directly at its surface and being therefore highly dependent on the sample's optical material properties, here, the sample was probed using a cantilever. The response of this geometry was then analyzed using an SLDV. The 3D-printed sample holder was directly screwed onto the piezo stack (see Figure 36 a)). A silver mirror was positioned through the lateral openings at an angle of 45°, reflecting the LDV laser beam directly onto the backside of the bi-clamped beam structure (see Figure 36 b)). The piezo was fixed with a standard double-adhesive tape onto the table, and vibrational decoupling of the setup was realized by placing the breadboard onto an 8 mm thick Sorbothane dampening sheet (see Figure 16 a)). When pouring the still warm and liquid hydrogel sample onto the cantilever, there is a risk of sample material flowing through the two slits beside the cantilever, consequently changing sample mass and volume. Those gaps were sealed using Pluronic™ F127 (0.33 g/ml, see Chapter 5.3 for preparation) to prevent this undesired effect. The cold, liquid material was introduced manually into the slits with a 10 ml standard syringe and a 0.33 mm standard nozzle. Shortly after extrusion into the slits, the material solidifies and closes the gap (see Figure 36, c)). For sample preparation, the warm gelatin hydrogel is directly cast into the sealed cylindrical cavity on top of the sample holder, afterward placed into the fridge at 4 °C for 6 minutes. The hydrogel solidifies and the sacrificial material liquefies in this step, releasing the lateral gaps beside the beam again. Afterward, everything was carefully screwed onto the piezo stack and tightened. Before starting an experiment, the sample was given another 8 minutes of resting time to adapt to the room temperature (23.8 °C), avoiding possible thermal equilibration processes affecting the measurement. For all measurements, the same sample holder was used. It was thoroughly cleaned in-between measurements using warm water (50 °C) to remove the remaining gelatin and dried using pressurized air.

For this experiment, an SLDV device with a wavelength of 1550 nm, a standard piezo stack, and a standard HiFi amplifier were used. It was the same setup as already used in the direct measurement of gelatin hydrogel disks (see Chapter 5.1.1). Using the in-built signal generator, a periodic chirp from 0 to 25 kHz (linear sweep with 0.98 Hz frequency resolution, 1024 ms sweep time, 24,414.06 Hz/s sweep speed) was generated and used as an excitation signal. In total, twenty measurement points were placed circularly around the beam (see Figure 38, green spheres and Figure 16, green dots) at the bottom of the cylindrical cavity. For avoiding undesired vibrations of the sample holder, the cavity for positioning the mirror directly under the beam was as small as possible. Hence, the experimental design only allowed the laser to be focused on the center of the beam without much variation. Therefore, as an input signal for calculating the transmissibility, the mean values of the amplitude velocity from the twenty measurement points of the empty sample holder were taken (see green dots in Figure 16 b) and Figure 38, blue line).

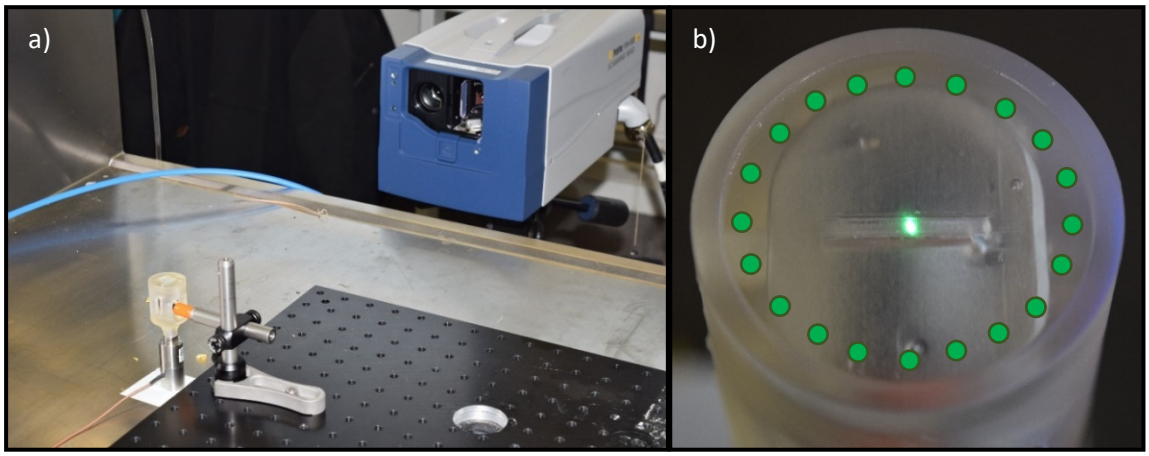

Figure 16 | Complete experimental setup. a) *The mirror reflecting the measurement laser onto the beam's backside was positioned using optical posts screwed onto a metal plate. This experimental breadboard was placed onto a Sorbothane dampening sheet to prevent the piezo's vibrations, possibly exciting the mirror into undesired dynamics.* ***b)*** *A transparent gelatin is cast on top of the cantilever structure. The green pilot laser on the backside of the beam can be recognized as it shines through the sample holder's transparent resin material. Here, the green dots symbolize the measurement points positioned in the software for characterizing the sample holder around the beam geometry.*

5.1.3. Measurement of fibroblast cells

In this experiment, a microscope-based LDV setup was used for characterizing living fibroblast cells growing in a Petri dish. With this setup, microscopic structures can be analyzed since standard microscope objectives can directly be integrated. In contrast to the NIR-SLDV devices used in previous experiments, this device uses a green laser with a wavelength of 532 nm instead of a NIR laser with a 1550 nm wavelength. Therefore, to avoid undesired reflections and a loss of signal intensity at the interface between air and culture medium, a 25x water immersion lens was used. Such an objective can be immersed directly into the culture medium, allowing the laser to be easily focused onto the sample surface. Here, a monolayer of cells cultured in a Petri dish was used. Fixation of the Petri dish without cover was done using a 3D-printed sample holder. For the measurement, a region was selected where both the cell body and uncovered Petri dish bottom were visible in the same microscope image. Thanks to the scanning function, both areas could be measured in one measurement procedure. Samples were stored in an incubator at 37 °C and 10% CO_2 between measurements. Due to the lack of incubation during the LDV measurement, the experimental time was limited to around 5 minutes, avoiding possible damage to the cells. Vibrational excitation was done by placing an electrodynamic exciter directly onto the sample table of the LDV and using a periodic chirp sweep from 0 to 800 Hz (linear sweep with 3.13 Hz frequency resolution, 320 ms sweep time, 2500 Hz/s sweep speed) as an excitation signal. Because the whole setup was excited to vibrate, the cell's inherent material properties were extracted, calculating the transmissibility. This was done by dividing the velocity amplitude signal from the cell surface as output through the velocity amplitude data obtained from the neighboring Petri dish surface as input.

5.1.4. Measurement of iPS-cardiomyocytes

Because the measurement of unlabelled cells with a 532 nm LDV setup was not feasible, a NIR-SLDV device was used in the next step since it could analyze transparent hydrogel samples (see Chapter 6.2). At the time of the experiment, no LDV device with an integrated microscopic setup and a laser wavelength of 1550 nm was available. Therefore, the LDV was positioned directly over a microscope to determine the exact measurement position on the cell surface (see Figure 46 a) and b), and Figure 17). In the current setup, no incubation unit was integrated and consequently, the experiment's duration needed to be as short as possible since otherwise, the cells could die due to non-physiological conditions. Furthermore, the living cells were partially exposed to air during the experiment resulting in an undersupply of nutrients. Due to the sub-Hertz contraction rate, the displacement amplitude in the time-domain was recorded with the LDV device using the built-in displacement decoder. Simultaneously, a 100 fps video was recorded with the microscope camera from below the cells and spheroid. This acquired data was then analyzed using a PIV algorithm. Both measurements were started manually simultaneously but on different computers resulting in a slight time shift, which was corrected manually during data analysis.

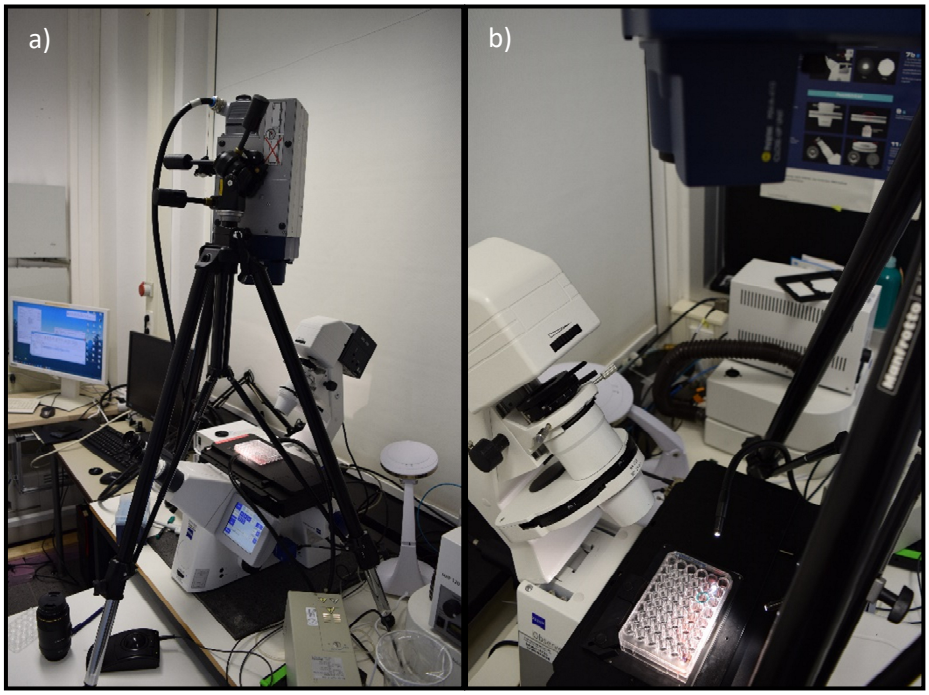

Figure 17 | Experimental setup for the cardiomyocyte experiment. *The LDV device was placed on top of the microscope and an additional light source was used for proper sample illumination. The measurements of spheroids were done in 48 multiwell plates.*

Besides spheroids, also a monolayer of cardiomyocyte cells was analyzed to determine the smallest sample size still being measurable. All samples were measured with and without a cover for testing its influence regarding the results and if enclosed measurements are feasible. During the experiment, it was already apparent that the measurement works best for spheroids since, due to their bigger size, they can cope better with the removal of the culture medium than single cells (see Figure 18). Therefore, the effect of isoprenaline, also known as adrenaline, was only investigated on spheroids. For this purpose, after a short

measuring time of 15 seconds, in which the normal contraction rate was recorded, 100 μl of a 100 nM isoprenaline solution was pipetted directly onto the spheroids.

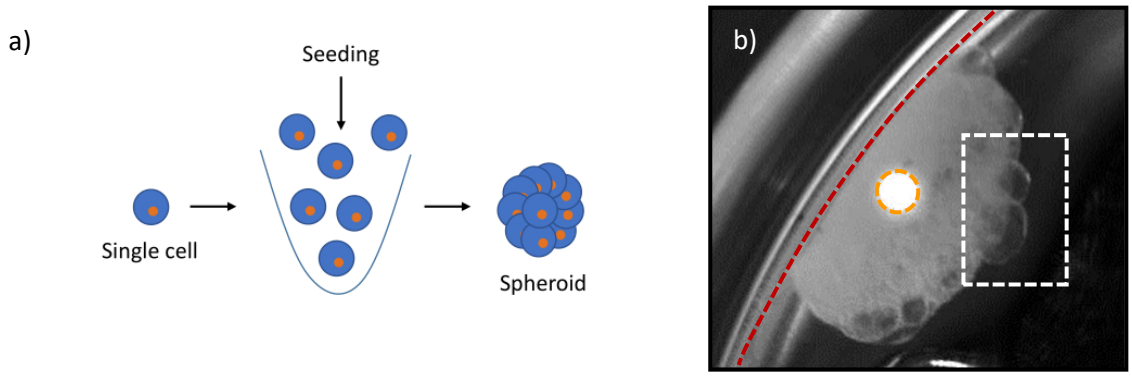

Figure 18 | Cardiomyocyte spheroid formation and experimental view during measurement. a) *By seeding single cells into a non-adherent cavity, a round spheroid with high cell density can be generated. Cells fuse into a sphere driven by gravity since the individual cells cannot adhere to the well's round surface.* ***b)*** *Microscope image of a spheroid from below. The pilot laser can be seen as a small white spot shining through the spheroid (orange dashed circle). This picture already shows that the light-dark patterns required for PIV image analysis are not very well defined, reducing the quality of the PIV results. Therefore, the PIV analysis window (white dashed rectangle) must be placed in an area where a good bright-dark pattern is present. The spheroid's (red dashed line) slightly oval shape results from the fact that it was sucked to the edge of the multiwell plate when the culture medium was pipetted out.*

5.1.5. Measurement of native tissue

Besides the mechanical characterization of single cells and cellular aggregates with LDV, the investigation of native tissues in their mechanical properties is of interest. Therefore, articular cartilage and the changes in its mechanical properties caused by treatment with collagenase were examined. Using a laboratory stand with a clamp, the piezo used for exciting the sample was fixed. The probe for contacting the sample surface was screwed on the piezo and brought in contact with the sample (see Figure 19, a)). The tip of the probe was a cylinder with a diameter of 1 mm. The cartilage plug itself was fixed with tissue glue (Hystoacryl) on the 3D-printed sample holder (see. Figure 19), which was in turn fixed with double-sided adhesive tape (see Figure 19) on a metal plate. Using the LDV-software, a measuring grid was positioned on the sample surface. As the LDV was positioned directly above the sample, it was not possible to measure directly at the probe's contact point, as the laser beam was blocked by it. For this reason, the measuring points were positioned as close as possible to the excitation point. A periodic chirp signal from 0 to 12.5 kHz (linear sweep with 3.91 Hz frequency resolution, 256 ms sweep time, 48,828.13 Hz/s sweep speed) was used as an excitation signal.

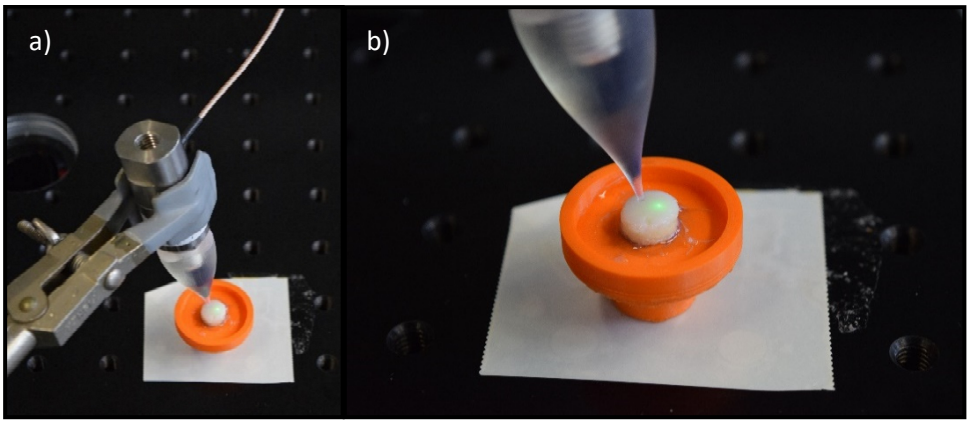

Figure 19 | Experimental setup for the vibrational analysis of bovine cartilage. a) *Using a clamp, the piezo was fixed above the sample and the 3d-printed indentation geometry was contacted with the sample surface.* ***b)*** *The 3D-printed orange sample holder was fixed with double-sided adhesive tape. The fixation of the cartilage plug into the sample holder was done using hystoacryl glue.*

5.1.6. Measurement of engineered tissue

The information gained from the analysis of native tissues and their structural properties can be used to build engineered tissue from scratch. Here, also their mechanical properties need to be monitored. In this experiment, the feasibility of using LDV for this task was evaluated. Because the fabrication of engineered tissue is both time and cost-intensive, contamination must be prevented. Therefore, a measuring chamber was developed in order to avoid possible contamination of the sample during the experiments (see Figure 56). The chamber was closed using a transparent cover sealed with a dampening silicon layer and its position was fixed with magnets. The piezo stack was inserted into the chamber from below through an opening at the bottom side to ensure a vibrational decoupling between the excitation signal and the chamber.

Engineered tissue was manufactured as later described in chapter 5.8. Before the sample was manually positioned into the measuring chamber, the whole chamber was sterilized using 80% ethanol. The sample holder was directly screwed onto the piezo stack and the sample was fixed onto this sample holder using two magnets (see Figure 20). The sheet itself was fixed on a sheet holder and thanks to the magnetic fixation, it could easily be removed without damage and be transferred back to the incubator. As an excitation signal for this piezo, a periodic chirp from 0 to 2.5 kHz (linear sweep with 1.56 Hz frequency resolution, 640 ms sweep time, 3906.25 Hz/s sweep speed) was used. The measuring grid was placed on all structures with the LDV-software (see Figure 58). Analyzed structures were the two magnets, the sheet itself, the sheet holder and the sample holder.

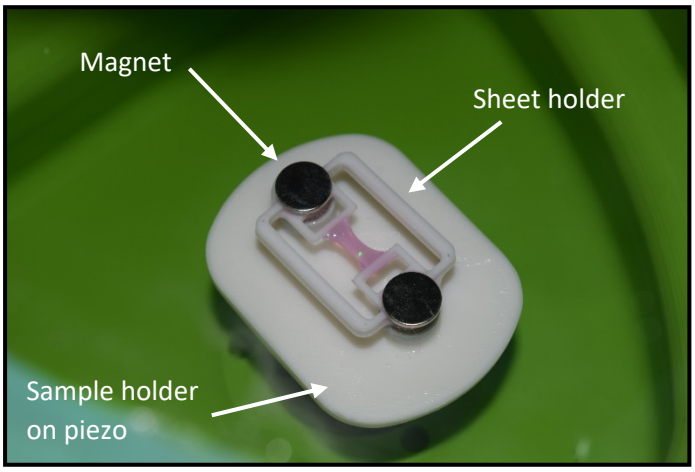

Figure 20 | Engineered tissue in the measurement chamber (green) fixed with two magnets on the sample holder (white). *The picture is taken through the transparent chamber cover.*

5.2. Mechanical characterization experiments

5.2.1. Nanoindentation measurements

IT-AFM measurements on gelatin samples and bovine cartilage samples were carried out by Bastian Hartmann as previously described [128, 186, 188, 192]. Briefly, a NanoWizard I AFM device with silicon nitride cantilevers was used. The cantilevers had a nominal spring constant of 0.1 N/m and a pyramidal tip with a nominal radius of 20 nm. Tip velocity during indentation was set to 12 μm/s, and spring constant calibration was done using the thermal noise method [202]. The Young's modulus E was extracted from the obtained force curves by fitting the modified Hertz model for a pyramidal indenter, giving the force F as a function of the indentation depth d [203]:

$$F(d) = \frac{E}{(1-\nu^2)} \cdot \frac{\tan\beta}{2} \cdot d^2 \qquad (12)$$

Whereas ν is the Poisson's ratio set to 0.5 for incompressible materials [194], β is the half opening angle to an edge of the tip, here 17.5°. Force curves were analyzed from the contact point up to 1 μm indentation depth using the JPK Data Processing software. The maxima of the Gaussian distribution in the summarized stiffness histogram was determined using the Igor Pro software.

5.2.2. Indentation measurements

For correlating the LDV measurement results with the mechanical properties of the cartilage samples, indentation measurements were done. Therefore, the *MACH-1™* with a multiaxial load cell (70 N, force resolution of 2.5 mN) was used. *MACH-1™* indentation measurement of cartilage samples was done using a flat-ended cylindrical indenter with a radius r of

0.5 mm (see Figure 21 b)). This was the only available and printable indentation geometry for the *MACH-1™* testing device in the lab. With a smaller tip radius, damage to the cartilage surface could not be ruled out. First, the contact point was defined and afterward, the force-displacement data was recorded with an indentation depth d of 800 μm. Young's modulus E was extracted using the Hertz fit as a model [203]:

$$F(d) = \frac{2 \cdot E}{(1 - \nu^2)} \cdot r \cdot d \qquad (13)$$

Directly after each LDV measurement, the indentation measurements were done. The digestive enzyme collagenase type II was used to gradually denature the cartilage surface, consisting mainly of collagen type II and hyaluronic acid. After each measurement (LDV and *MACH-1™*), the plug was incubated for 15 minutes in 0.5 mg/ml collagenase type II dissolved in PBS at 37 °C. For the last measurement, the complete denaturation time was 75 minutes, and six measurement cycles, including five digestion steps, were completed.

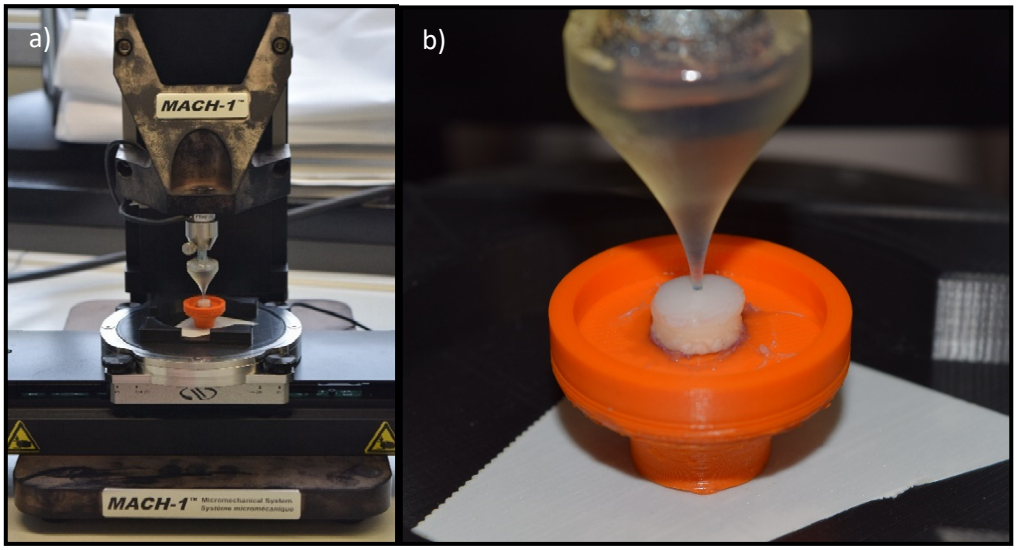

Figure 21 | Measurement setup for indentation measurements of the cartilage plug. a) *MACH-1™ testing device with the 3D-printed indentation geometry attached to the load cell. The sample was fixed on the movable stage, enabling multiple measurement points.* ***b)*** *Cartilage plug during indentation measurement. The orange sample holder is fixed with double-sided adhesive tape and can be directly screwed onto the piezo stack with the integrated thread.*

5.2.3. Unconfined compression testing

Unconfined compression testing of a gelatin cylinder with different concentrations was done using a flat indenter with a 12.5 mm diameter and the *MACH-1™* testing machine. This experiment's results are required for correlating the results from the LDV measurement with the mechanical sample properties. Gelatin samples with a 7.7 mm diameter and a mean height h of 6.2 mm have been fabricated by casting them into a 3D-printed sample holder. For each sample, the height was measured using a digital caliper ruler. For each gelatin concentration, five samples were measured with a total compression length Δl of 927 μm and a compression rate of 139 µm/s, corresponding to a maximum strain of 15% and a strain

rate of 2.3%/s. Taking the slope of the stress-strain curves, respectively the linear part between 10 and 15% strain, the Young's modulus E was calculated [30]:

$$E = \frac{\Delta F \cdot h}{\Delta l \cdot A} \tag{14}$$

5.3. Hydrogel preparation

Gelatin hydrogel

Crystallized gelatin powder was dissolved in warm, deionized water using a heated magnetic stirrer. The temperature was set to 55 °C, and after 8 minutes of stirring, the completely dissolved and melted gelatin formed a clear, honey-liked solution ready for pouring into the relevant sample holder. For example, to obtain a 0.1 g/ml concentration stock solution, 1 g of gelatin powder was mixed with 10 ml of deionized water. The speed of the magnetic stirrer was set to approximately 30 RPM. Higher speeds result in bubbles that are later hard to remove and can decrease the smoothness of the sample surface. The beaker with the stock solution was sealed with a piece of Parafilm™ during and after production to minimize possible evaporation effects. The stock solution was stored in an incubator set to 37 °C and 80% relative humidity until needed for an experiment.

Cell-laden collagen type I hydrogel

The buffer solution for neutralizing the acidic collagen type I stock solution was obtained by mixing a 7 M NaOH and 1 M HEPES buffer solution with 10x DMEM mediumin a 1:1 ratio. The final pH value of the buffer was adjusted to a pH value of 8±0.3. Cells are resuspended in 100 μl warm collagen buffer solution by gently pipetting up and down. Afterward, the final cell concentration was determined by counting them using a Neubauer counting chamber. Acidic collagen stock solution with a 5 mg/ml concentration was pipetted directly into the cell-laden buffer solution, and everything was mixed gently. The mixing ratio was 4:1, and the final collagen concentration in the cell-laden hydrogel was 4 mg/ml.

Sacrificial ink for casting mold printing

3.3 g of *Pluronic*™ F-127 powder was dissolved in 10 ml of deionized water to produce a 0.33 g/ml stock solution. Everything was mixed manually using a spatula until a white and wax-like consistency was obtained. The beaker was sealed with a piece of Parafilm™ and put into the fridge at 4 °C for at least 12 hours, forming a transparent and liquid solution.

5.4. Fabrication of sample holders and support structures

Fabrication of sample holder for optical transmission experiment

The sample holder for the optical transmission experiment was printed using the *Ultimaker™ 2+* FDM 3D printer, standard PLA filament, a layer height of 0.1 mm, and 100%

infill (see Figure 22 a)). The design was developed using the computer-aided design (CAD) software *SolidWorks™*.

Fabrication of gelatin disk holder for direct LDV measurement

Custom-made sample holder (see Figure 22 b)), in which the gelatin hydrogel was directly pipetted to create a circular fixed disk, was 3D-printed using an *Ultimaker™ 2+* and PLA filament. The CAD model designed in *SolidWorks™* was prepared for printing using the *Cura™* slicing software. Layer height was set to 0.1 mm, and the model was printed solid with an infill of 100%. This setting was selected to avoid undesired resonances of the sample holder, possibly interfering with the dynamics of the hydrogel disk sample.

Fabrication of the cantilever geometry for indirect LDV measurement

A high-resolution manufacturing method was essential for this experiment since the beam's geometry needs to be printed very precisely. The test structure containing the cantilever geometry should only consist of one part, which can be screwed directly onto the piezo stack (see Figure 22 c)). Therefore, the stereolithography (SLA) system *Form™ 2* and the transparent resin were chosen. Here, the layer height was set to 25 μm. After printing, the model was processed in a washing station with isopropyl and afterward cured in a curing station for 30 minutes at 60 °C. The thread was cut manually into the sample holder for fixation onto the piezo stack during experiments. The dimensions of the beam were 12 mm in length and both 1 mm in height and width. Smaller beam sizes resulted in poor shape accuracy and deformation of the beam after post-processing since the curing process introduces certain internal stress, which can lead to deformations of filigree structures. The smallest possible gap size still feasible without clogging was 0.4 mm.

Fabrication of sample holder for LDV cell measurement

The sample holder was designed for a standard Petri dish with a 35 mm diameter, directly fixed onto the microscope-based LDV system (see Figure 22). Printing was done using an *Ultimaker™ 2+* FDM 3D printer and PLA filament. The layer height was set to 0.1 mm in the slicing software *Cura™*. To increase the overall stability of the sample holder, wall thickness was set to 1.2 mm.

Fabrication of *MACH-1™* and piezo indentation geometry for cartilage measurement

Both the indenter for the *MACH-1™* device and the indenter for the piezo stack (see Figure 22 e)) were designed using *SolidWorks™* CAD software. The diameter of the flat-ended, cylindrical tip was set to 1 mm. Printing was done using the *Form™ 2* SLA printer with a clear standard resin and a layer height of 25 μm. The head side of a screw (1/4 inch – 28 x 5/8) was glued directly into the indenter geometry with epoxy resin so that the cylindrical tip can be fixed via the thread of the screw on the force sensor of the *MACH-1™*. Regarding the indenter geometry for the piezo, the required M8 thread was cut manually.

Design and fabrication of support structures for engineered tissue

The baseplate geometry (see Figure 22 g)) was printed with an *Ultimaker™ 3* and high-temperature PLA. Layer height was set to 0.1 mm, infill percentage to 100% to avoid floating. For better shape accuracy, a print nozzle with a diameter of 250 μm was used. The print job was paused at the height of 1.4 mm to insert cylindrical neodymium magnets (3 mm in diameter and 1.5 mm in height) into cavities. After the magnets were placed in

the corresponding cavities, the print job was continued, encapsulating the magnets completely in PLA. This prevents possible cell damage through corrosion products caused by an interaction between the magnetic material and the culture medium. Preliminary tests have shown that the corrosion products will lead to complete cell death. The magnets are necessary to fix the baseplate onto the bioprinter's printing bed during the mold printing process. The posts for fixing the sheet holder onto the baseplate (see Figure 55, bottom row) are the same (blunt tip) syringe needles (inner diameter 0.33 mm, outer diameter 0.63 mm) used for printing the sacrificial ink. These are pre-formed and carefully melted into the base plate using a soldering iron tempered to 300 °C. The thin sheet holders, designed to carry the engineered tissue, were also manufactured using an *Ultimaker™ 3* and *Volcano* PLA (see Figure 22 f)). Compared to a standard PLA filament, this material has a higher glass transition temperature of 90 °C, making it more suitable for applications in a warm environment.

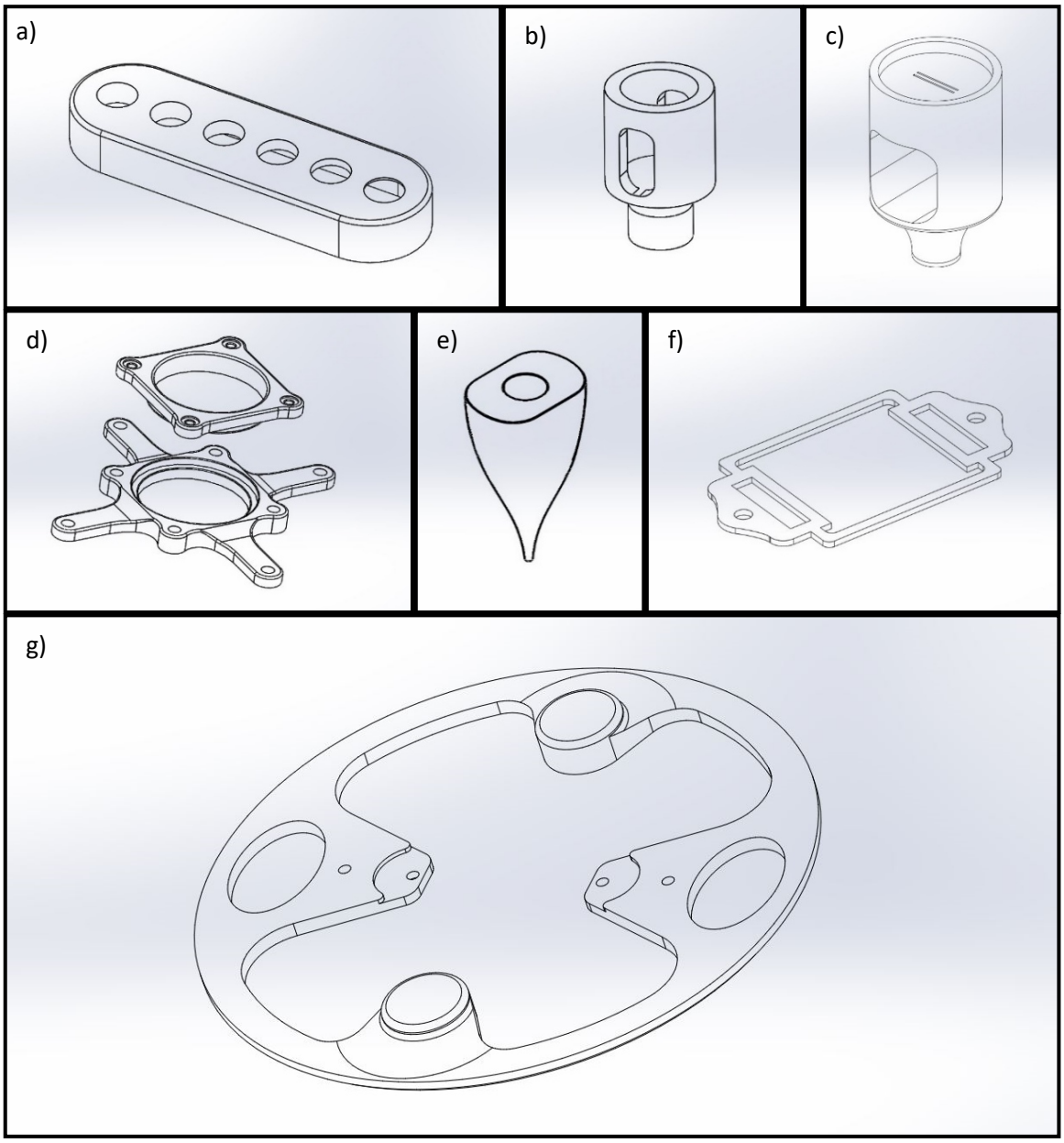

Figure 22 | Sample holder and support geometries. a) *Sample holder for the optical transmission testing.* ***b)*** *Sample holder for the direct measurement of gelatin disks.* ***c)*** *Sample holder for the indirect measurement with an integrated cantilever beam geometry.* ***d)*** *For the cell measurement required Petri dish fixation.* ***e)*** *Indentation geometry for the cartilage experiment.* ***f)*** *Thin sheet holder for engineered tissue.* ***g)*** *Baseplate unit for fixing the sheet holder geometry.*

Design and concept of the measurement chamber for engineered tissue

The chamber's main part was printed using the *Ultimaker™ 2+* FDM 3D printer and standard PLA filament (see Figure 23, green part). Layer height was set to 0.1 mm and, to ensure proper sealing, inner and outer wall thickness was adjusted to 1.2 mm. The transparent cover (polycarbonate, *Makrolon™*) was cut with a laser cutter, and cylindrical neodymium magnets were glued into the corresponding holes using epoxy resin. For vibration damping, a suitable 1 mm thick silicone membrane was made using a silicone suitable for casting (see Figure 23, turquoise part). The FDM 3D printer Ultimaker 2+ was also used for this purpose. The silicone component was glued to the cover with epoxy resin. For making the magnetic fixation work, neodymium magnets were glued in the corresponding position on top of the chamber.

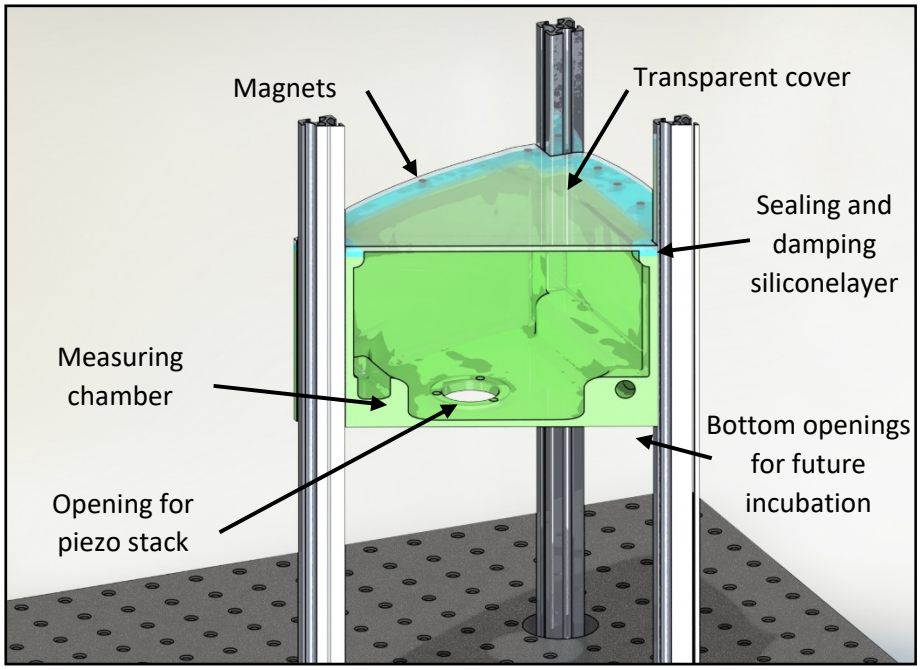

Figure 23 | Rendering of the measuring chamber concept. *Through the opening in the bottom of the chamber (green), a piezo stack can be inserted, fixed onto the baseplate (black). Through three circular openings in this plate, the chamber was positioned and stood on three vertical alloy beams. A Sorbothane mattress was placed below the metal plate to ensure a vibrational decoupling from the excitation source. Otherwise, the transparent cover would also vibrate during the measurement, influencing the results. In the lower rear area, two openings are available for connecting the in- and output of an external incubation unit not available yet.*

5.5. Cell-culture

Cultivation of human mesenchymal stem cells

hMSCs were cultivated using DMEM supplemented with 10% FCS, 1% *GlutaMax*™ and 1% Penicillin/Streptomycin. The temperature in the humidified cell culture incubator was set to 37 °C and CO_2 concentration to 10%. Cells were kindly provided by Böcker et al. [204].

Cultivation of murine fibroblasts

Murine NIH3T3 fibroblast wild-type cells were cultivated using DMEM supplemented with 10% FCS, 1% *GlutaMax*™, and 1% Penicillin/Streptomycin. The temperature in the humidified cell culture incubator was set to 37 °C and CO_2 concentration to 10 %. Cells were kindly provided by Prof. Christof Hauck and Timo Baade (University of Konstanz).

Cultivation of cardiomyocytes

IPS-cardiomyocytes spheroids were kindly provided by Anna Meier and Prof. Dr. Alessandra Moretti (professorship for regenerative medicine in cardiovascular disease, TUM School of Medicine, Klinikum Rechts der Isar). Cultivation was done using DMEM supplemented with 2% FCS, 1% non-essential amino acids, 1% Penicillin/Streptomycin, and 0.1 mM mercaptoethanol as a maintenance medium.

Cell preparation for sheet fabrication

The culture medium was removed entirely from a confluent hMSCs culture, and dead cells and other residues were washed away using 10 ml of warm PBS solution. Afterward, 2 ml

of Trypsin/EDTA solution (0.25%/0.02% (w/v)) were pipetted into the culture flask and left to react for a total of 5 minutes at 37 °C and were gently agitated every minute manually. This solution digests the cells' attachment proteins, causing them to detach from the culture dish and separate the cells from each other. After 5 minutes, 2 ml of warm DMEM culture medium was added to inhibit the detachment process and prevent severe damage to the cells. The cell suspension was centrifuged in a 10 ml falcon tube for 3 minutes at 500 rpm forming a cell pellet at the bottom of the tube, ready for further process steps.

5.6. Preparation of bovine cartilage plugs

Cartilage plugs were prepared from Bastian Hartmann, as previously described in Kahlarodi et al. [205].

5.7. Optical transmission of gelatin

Optical transmission of gelatin hydrogel disks with varying thicknesses was investigated using a high-sensitivity thermopile sensor, converting the thermal energy from laser absorption into an electrical signal. This is important since laser light being able to pass the transparent sample completely can be reflected and interfere with the signal originating from the surface sample. For this experiment, a 0.20 g/ml gelatin hydrogel solution was prepared (for preparation, see Chapter 5.3) and cast into the support holder as described in chapter 5.4 for the gelatin disk. To measure the absorption of gelatin concerning the sample thickness at a wavelength of 1550 nm, the sample holder with the gelatin disk was positioned directly over the thermophile sensor (see Figure 26). The LDV device was positioned perpendicular to the surface of the sample. In total, 12 different values of thickness between 0.75 and 5.77 mm were measured. Following measurement data and using Lambert-Beer's law (see Equation (5)), the material-specific absorption coefficient α was calculated [30]. Here, I was the intensity measured by the sensor, I_0 was the energy of the measurement laser of the LDV device (8.92 mW at a wavelength of 1550 nm), and d was the thickness of the corresponding samples.

5.8. Fabrication of engineered tissue

The biomolding approach

The biomolding approach was developed especially to fabricate engineered tissue made out of ECM-based hydrogels like collagen type I. Here these materials are cast into a printed casting mold instead of being extruded through a nozzle. Often, manufactured geometries dissolve directly after extrusion, or the printing nozzles are already clogged during extrusion [96-98]. Complete fibrillation from the liquid stock solution to a gel often takes a certain time, making this type of material more suitable for casting processes [206-209]. Compared to classical casting approaches of natural hydrogels in TE, this approach involves printing the casting mold using a sacrificial material. Such materials, like Pluronic™ F127, can be

printed with a high-shaped fidelity, and the removal can be realized without harming the fragile construct [100, 101]. Studies have shown that ECM-based hydrogels often undergo strong shrinking without a fixation [210-212]. This problem can be solved either by adding other hydrogels like hyaluronan [213, 214] or by introducing small fixation geometries, which can be specifically designed regarding the shape of the constructs (see Figure 24). Furthermore, since they prevent shrinkage in certain areas, controlled forces can be generated, guiding and facilitating maturation processes. The first results of such casting approaches demonstrate promising results regarding engineered vascular grafts and heart valves [79, 80].

Design and fabrication of casting mold

The casting mold was designed and exported as an stl file using *SolidWorks™* CAD software. Afterward, this file was prepared for printing using *Simplify 3D™* slicing software. As a printing material, the sacrificial ink described before was used and extruded with a pressure of around 1.8 bar and a standard nozzle with an inner diameter of 0.33 mm at a temperature of 37 °C. Thanks to the experimental design, the desired geometry was printed directly into a standard Petri dish and around the support structures (see Figure 24). The whole procedure was conducted under a laminar flow hood ensuring sterile conditions to prevent contamination.

Preparation of the cell-laden constructs

After the printing process, the required volume of cell-laden collagen type I hydrogel was pipetted directly into the casting mold (see Figure 24). The whole setup was then transferred into an incubator for one hour at 37 °C and 80% relative humidity, so the collagen's fibrillogenesis process can occur. After 60 minutes, warm nutrient media was pipetted into the Petri dish until the casting mold was covered about 1 mm high. After being submerged and incubated for about 6 hours, the casting mold is completely dissolved, and the cell-laden collagen type I structure is released.

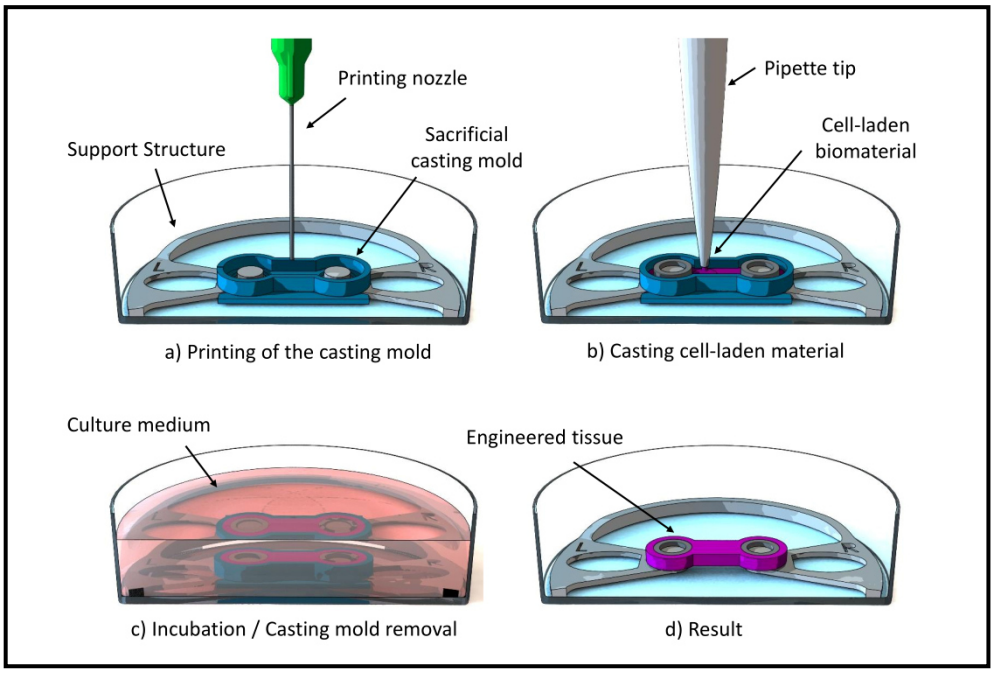

Figure 24 | Fabrication of a cell-laden engineered tissue. a) *In the first step, the mold was printed using Pluronic™ F127 (dark blue) as a sacrificial ink. Printing was done using an in-house developed bioprinting platform. The desired geometry was printed around a magnetically fixed support structure placed in a standard Petri dish.* ***b)*** *After printing the mold geometry, a cell-laden biomaterial, here collagen type I (4 mg/ml, purple), was directly pipetted into the mold.* ***c)*** *The natural fibrillogenesis process of collagen type I takes place under physiological conditions (37 °C, 80% relative humidity) and needs at least one hour in the incubator unit. The sacrificial mold was then removed by gently pipetting warm culture medium into the Petri dish and incubating the setup for at least 12 hours.* ***d)*** *After the removal, a cell-laden and three-dimensional construct is obtained.*

5.9. Particle imaging velocimetry analysis

PIV allows for the optical investigation of particle flow, characterizing its velocity and direction [215]. Here, not the movement of particles in a liquid has been examined, but the movement of bright-dark areas in a bright field video for extracting the contracting cell's velocity. Because many studies already proof the feasibility of analyzing cardiomyocyte contractility with PIV, it is used in this study as a reference method for LDV. Videos were recorded at 100 fps, using a frame grabber card and the open-source μ-Manager software [216, 217]. The used camera was an ORCA-Flash camera installed at a Zeiss Axiovert microscope with a 10x magnification lens. The analysis was done using the PIVlab plug-in library for Matlab™ [218-220].

5.10. Analytical calculation of the gelatin disk Young's modulus

Besides measuring the gelatin disk's mechanical properties using nano-indentation and unconfined compression testing, the mechanical properties can also be calculated from the measured LDV frequency data following a suitable analytical model. Therefore, using a mathematical model, the expected Young's modulus for the measured resonance frequency measured with the LDV device and FWHM can be calculated for a thin gelatin disk. The

resonance frequency is the damped resonance frequency f_d and can be transformed into the undamped resonance frequency f_n following Equation (15) [176]:

$$f_d = f_n\sqrt{1-\zeta^2} \tag{15}$$

For a circular, thin clamped disk, the first modal frequency f_{01} can be calculated as follows [179]:

$$f_{ab} = \frac{\omega_{ab}}{2\pi} \tag{16}$$

$$\omega_{ab} = {\beta_{ab}}^2\sqrt{\frac{D}{m}} \tag{17}$$

The number of nodal lines regarding the mode shape is defined by the number of nodal diameters a and the number of nodal circles b. Following the boundary conditions and diameter of the disk, the coefficient β_{ab} can be calculated. Because, in the direct measurement of the gelatin disk, only the (0,1) mode is of interest, the solution for the first mode ω_{01} can be used by setting the disk's radius to 4.85 mm [179]:

$$\omega_{01} = 1.015^2\frac{\pi^2}{a^2}\sqrt{\frac{D}{m}} \tag{18}$$

The plate bending stiffness D can be calculated using the Young's modulus E, the sample thickness h, and the Poisson's ratio ν [179]:

$$D = \frac{Eh^3}{12(1-\nu^2)} \tag{19}$$

whereas m is the mass per unit of the surface [179]:

$$m = \int_{-\frac{h}{2}}^{\frac{h}{2}} \rho\, dz \tag{20}$$

The Young's modulus *E* can be calculated following this final equation:

$$E = \frac{\left(\frac{f_n \times 2\pi}{1.015^2 \frac{\pi^2}{a^2}}\right)^2 \cdot m \cdot 12(1-\nu^2)}{h^3} \quad (21)$$

For a thick gelatin disk, as it was used for the experiment presented in chapter 5.1.1, the results can be adapted following the published work of Zhou et al. [221]. Following a 9.7 mm diameter and a height of 3 mm, a thickness to radius ratio of 0.61 can be calculated. Extrapolation from the data presented in the paper renders for this ratio a correction factor of 0.59, changing Equation (18) to the following equation:

$$\omega_{01} = 0.59 \cdot 1.015^2 \frac{\pi^2}{a^2}\sqrt{\frac{D}{m}} \quad (22)$$

One underlying assumption for applying this calculation is that the Young's modulus is independent of the frequency, often not true regarding visco-elastic materials [222-224]. Still, in this study, we derive the Young's modulus from dynamic frequency data and compare it with IT-AFM and unconfined compression data, both determined quasi-statically. This has to be kept in mind, and in future experiments, the Young's modulus should also be probed dynamically.

5.11. Finite element method analysis

5.11.1. Analysis of a thick gelatin disk

A three-dimensional solid mechanics model was used for the modal analysis of a thick gelatin disk in *COMSOL Multiphysics*™ FEM software. A fine physics-controlled mesh size was set to "finer", density and Young's modulus were set to 1. The value 0.49 was used as Poisson's ratio. Using the first modal frequencies $f_{0,1}^{FEM}$ obtained from the FEM analysis, the first resonance frequencies determined with the direct LDV measurement $f_{0,1}$ (see Supplementary Table 1) and the experimentally determined gelatin density ρ (see Table 1), the expected Young's modulus *E* can be calculated:

$$E = \left(\frac{f_{0,1}}{f_{0,1}^{FEM}}\right)^2 \cdot \rho \quad (23)$$

This can be deduced from the fact that for linear dynamic problems with the same material and the same geometry, the eigenfrequency is proportional to $\sqrt{\frac{E}{\rho}}$:

$$f_n = \frac{{\beta_{ab}}^2}{2\pi}\sqrt{\frac{Eh^3}{12(1-\nu^2)}} \qquad (24)$$

Removing all shape-related parameters, one gets the following proportional dependence:

$$f_n \propto \sqrt{\frac{E}{\rho}} \qquad (25)$$

Because $f_{0,1}$ from the LDV measurement and $f_{0,1}^{FEM}$ from the FEM analysis should be the same, the following equation can be formed, leading to the equation already shown above:

$$f_{01} = f_{01}^{FEM}\sqrt{\frac{E}{\rho}} \qquad (26)$$

5.11.2. Analysis of a beam geometry

Eigenfrequency analysis of a beam geometry covered with a gelatin layer was done using *COMSOL Multiphysics*™ software and a two-dimensional solid mechanics model. The analyzed geometry resembles a cross-section of the experimental setup for the indirect hydrogel analysis shown in chapter 5.1.2 (see Figure 25). The four lateral edges were defined as fixed constraints for the analysis, and the interface between the two rectangles was defined as a union with a relative repair tolerance of $1e^{-6}$. Mesh size was set to the option *extremely coarse* since otherwise, the algorithm finds too many non-relevant modes, especially for the soft upper geometry, and it was challenging to find the relevant modes of the lower geometry resembling the stiff beam.

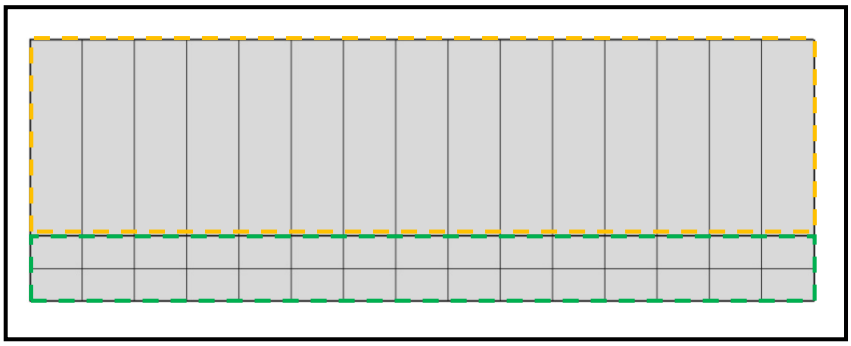

Figure 25 | Geometry and meshing used for the FEM analysis. *The upper beam (3 x 12 mm, yellow dashed line) represents the gelatin hydrogel layer placed upon the beam, here a rectangle (1 x 12 mm, green dashed line). All lateral edges were defined as fixed.*

A linear elastic material model was chosen, requiring density, Poisson ratio, and Young's modulus as material input data for analysis. The polymerized SLA printing resin density was determined by printing six cubes with an edge length of 10 mm using the Form 3 printer. After washing print results for 10 minutes in isopropanol and UV-light post-curing for 30 minutes at 60 C, each sample weight was measured and the resulting density calculated. The density of different gelatin concentrations was also determined experimentally by weighting a defined volume of 10 ml. The Poisson ratio of the SLA resin was set to 0.25 as no information is available from the manufacturer, and the material here is assumed as an isotropic linear elastic material. Regarding the incompressible gelatin material, the Poisson ratio was set to 0.49, as 0.50, indicating a perfectly incompressible material would lead in practice to a division by zero during the numerical calculations. Young's modulus data for the resin can be found in the manufacturer's datasheet, and the mechanical properties of the gelatin samples were measured using IT-AFM. All material properties used in the FEM analysis are listed in Table 1.

Table 1 | For the FEM analysis, used material data.

Material	Density $\left(\frac{kg}{m^3}\right)$	Poisson ratio	Young's Modulus (kPa)
Cured SLA resin	1150.00	0.25	$2.8e^6$
Gelatin 0.10 g/ml	1005.80	0.49	5.48
Gelatin 0.15 g/ml	1017.30	0.49	13.27
Gelatin 0.20 g/ml	1028.80	0.49	27.23
Gelatin 0.25 g/ml	1040.30	0.49	47.62
Gelatin 0.30 g/ml	1051.80	0.49	60.49
Gelatin 0.35 g/ml	1063.30	0.49	80.60
Gelatin 0.40 g/ml	1074.80	0.49	68.23
Gelatin 0.45 g/ml	1086.30	0.49	93.93
Gelatin 0.50 g/ml	1097.80	0.49	125.35

6

Results

6.1. Optical transmission of gelatin hydrogels

One important aspect to consider when characterizing transparent materials using optical methods is the potential reflection of the measurement laser from behind the sample. Many studies use reflective markers or coatings to prevent such reflection from behind the sample and increase the reflected signal from the surface of interest [16, 36]. Consequently, the transmitted amount of laser energy for different gelatin sample thicknesses was investigated. This data was then used to determine an optimal sample thickness at which only a negligible amount of laser energy is being transmitted. In total, twelve different gelatin disk heights ranging from 0.75 mm to 5.70 mm, with a polymer concentration of 0.20 g/ml, have been investigated. The transmitted laser power was measured using a thermophile power sensor. As expected, the results show an exponential decrease in transmitted energy with increasing sample thickness (see Figure 27).

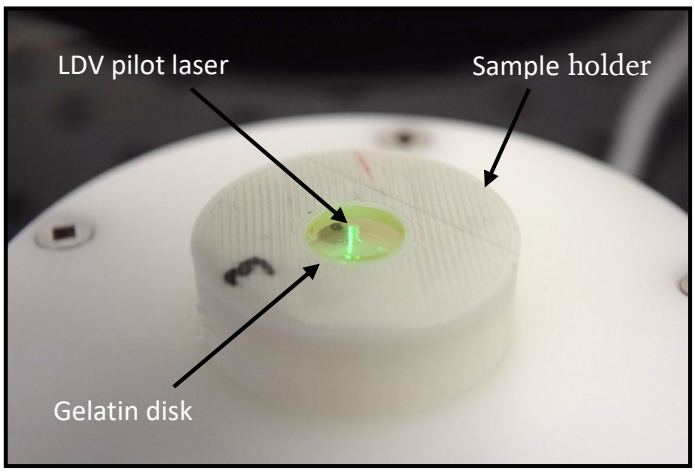

Figure 26 | Measurement of optical transmission. 3D-printed sample holder directly placed over the power meter's measurement window. In the center, the green pilot laser of the LDV device and the hydrogel disk with 3 mm in thickness and a diameter of 9.7 mm can be seen.

By fitting Lambert's law to the data (see Equation (5)), an absorption coefficient α of 1.012 mm^{-1} was derived for a 0.20 g/ml gelatin hydrogel and a wavelength of 1550 nm. For the following LDV measurement of gelatin disks, a sample thickness of 3 mm was chosen.

For this thickness, the sample preparation was reproducible, and at the same time, less than 0.23% of the incident laser power reach the LDV detector if a 100% reflective surface is positioned behind the gelatin disk. For the initial laser power of 8.92 mW, less than 21 μW get back to the LDV device, much less than the signal originating from the sample surface.

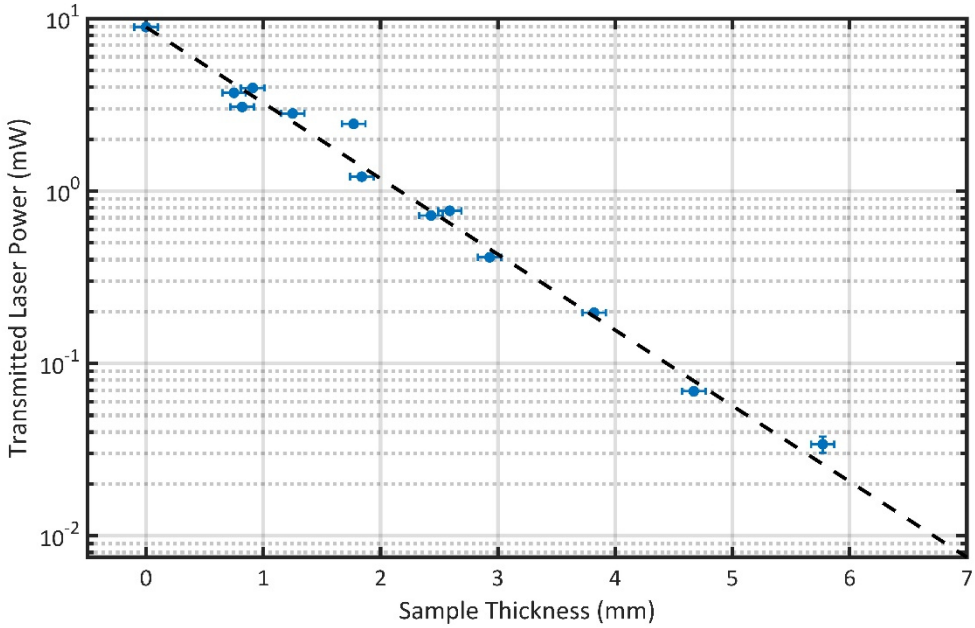

Figure 27 | Absorption data of gelatin hydrogels regarding the LDV laser. *Semi-logarithmic representation of transmitted laser power for sample thicknesses ranging from 0.75 to 5.7 mm of a 0.20 g/ml gelatin hydrogel. The black dashed line represents the transmitted power in respect of the sample thickness following the calculated absorption coefficient* $\boldsymbol{\alpha} = 1.012\ mm^{-1}$. *Taken from Schwarz et al. [186].*

6.2. Direct, label-free measurement of gelatin disks

To evaluate the feasibility of LDV as a tool to characterize the elastic properties of transparent hydrogels, an appropriate measurement setup and experimental procedure were developed (see Chapter 5.1.1). Free-hanging gelatin disks, which were circularly fixed in a sample holder, were fabricated (see Figure 28). For excitation, the sample holder was screwed onto a piezo stack, and a frequency sweep from 0 to 2.5 kHz was used for excitation. At different locations on the gelatin surface and the sample holder's rim, the frequency-dependent velocity amplitudes were determined using the scanning LDV, enabling the analysis of the resonance frequencies and the corresponding mode shapes (see Figure 28 d)). The Young's moduli of the different gels were calculated based on their first resonance frequencies (the 0,1 mode) using two different analytical models as well as FEM analysis. To compare these results to conventional indentation and compression testing, the Young's moduli of the gelatin samples were also determined by IT-AFM and unconfined compression testing.

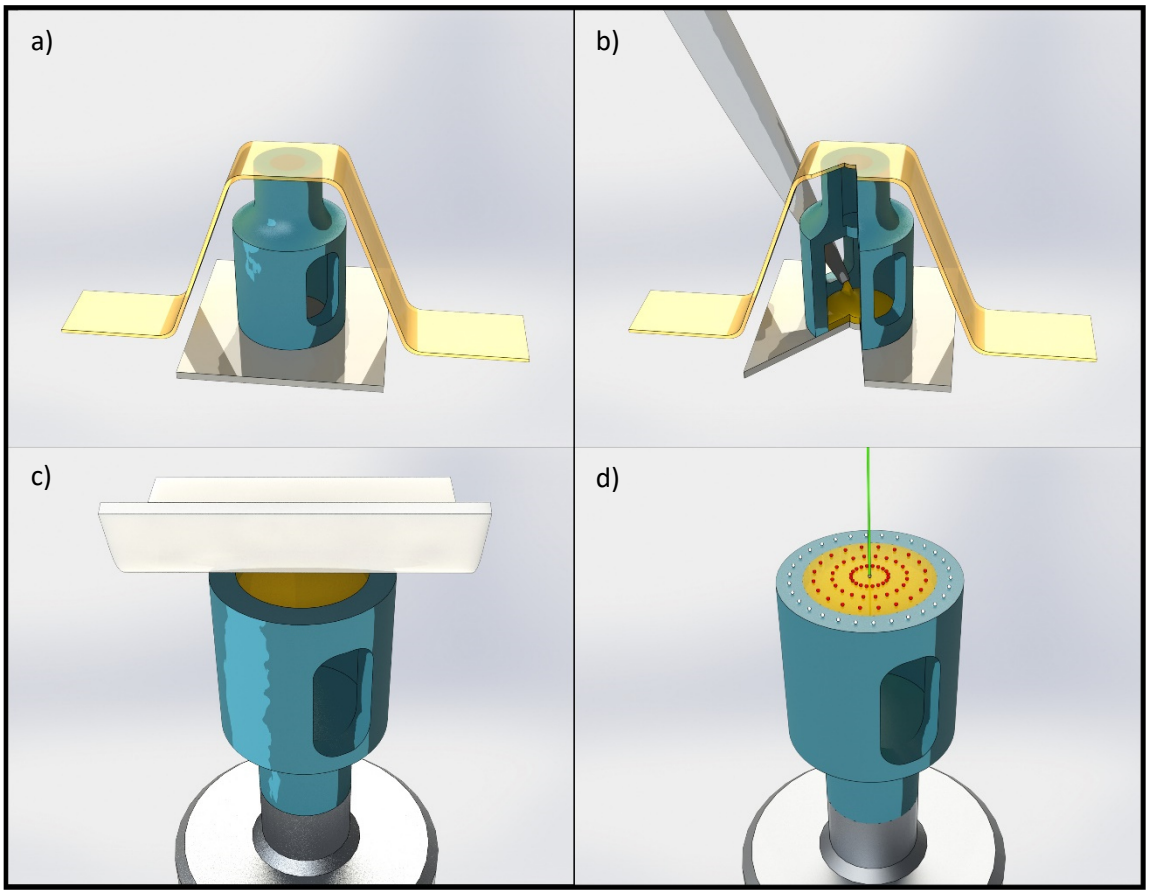

Figure 28 | Preparation of hydrogel disk samples. a) *The 3D-printed sample holder (blue) was placed top-down onto a piece of Parafilm™ (white), a wax-based tape with a smooth surface and low adhesion to the hydrogel. Fixation was done using standard adhesive tape (yellow).* ***b)*** *A defined volume of the warm, viscous gelatin hydrogel (orange) was pipetted into the cavity and stored in a fridge at 4 °C for five minutes* ***c)*** *After this cooling period, the Parafilm™ was carefully removed without destroying the smooth surface or the structure itself of the sample. The sample holder was screwed onto the piezo stack (grey).* ***d)*** *Using the operating software of the SLDV device, a measurement grid was placed onto the sample's surface (red and white dots). Red dots symbolize the measurement positions on the hydrogel's surface, and white dots represent measurement points on the sample holder's surface. Taken from Schwarz et al. [186].*

Using the scanning feature of the NIR-SLDV device, the mode shapes of the gelatin disks were analyzed. Figure 29 shows the (0,1) mode of a 0.20 g/ml gelatin disk. The (0,1) mode could be observed for all gelatin samples. Mode shapes of higher resonances are shown in the Supplementary Figure 1.

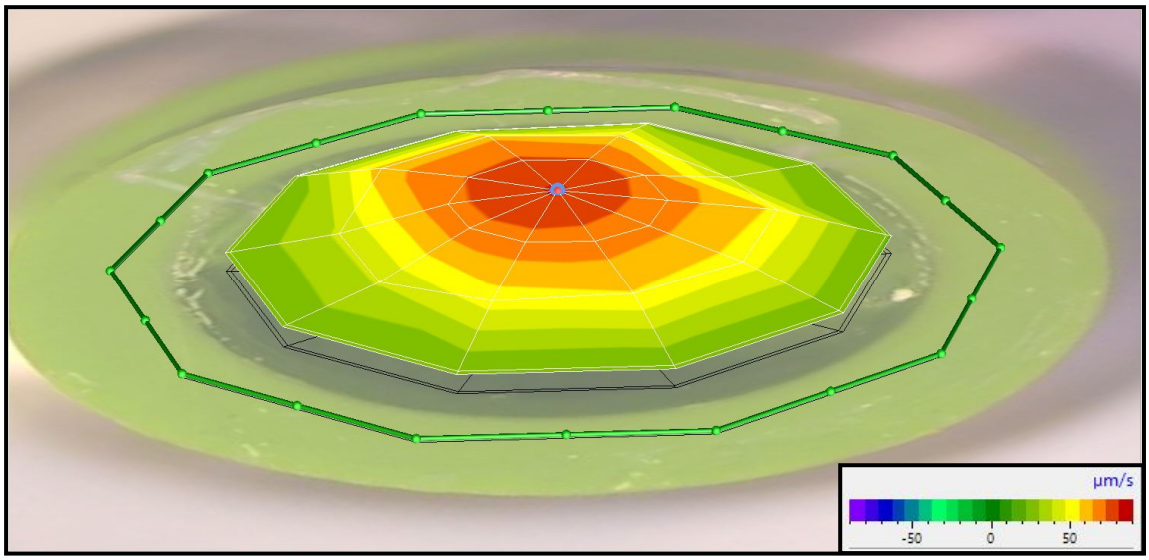

Figure 29 | Shape of the (0,1) mode of a 0.20 g/ml gelatin disk at 223 Hz. *The false-color scale indicates the local velocity amplitude perpendicular to the disk surface.*

In the LDV signals recorded at the center of the 0.20 g/ml gelatin disk (see Figure 30, blue line) and at the rim of the sample holder (see Figure 30, orange line), resonances of both structures, the gelatin disc, and the sample holder rim can be observed. For the gelatin hydrogel, in total, four resonances can be recognized between 0 and 1500 Hz. The first resonance of the gelatin disc, located at 223.4 Hz, corresponds to the (0,1) mode shown in Figure 29. As expected, the velocity amplitude of the rim signal increases with increasing frequencies. The sample holder's first resonance can be observed at around 926 Hz, which is well above the first resonance of the 20 g/ml gelatin disk (see Figure 30), ensuring that the first resonance of the gelatin sample is not affected by resonances of the sample holder. This is the case for the (0,1) modes of all investigated gelatin samples but not for the higher resonances of the gelatin samples. Therefore, for further analysis, only the first resonances, i.e., the (0,1) modes and their FWHM, were used.

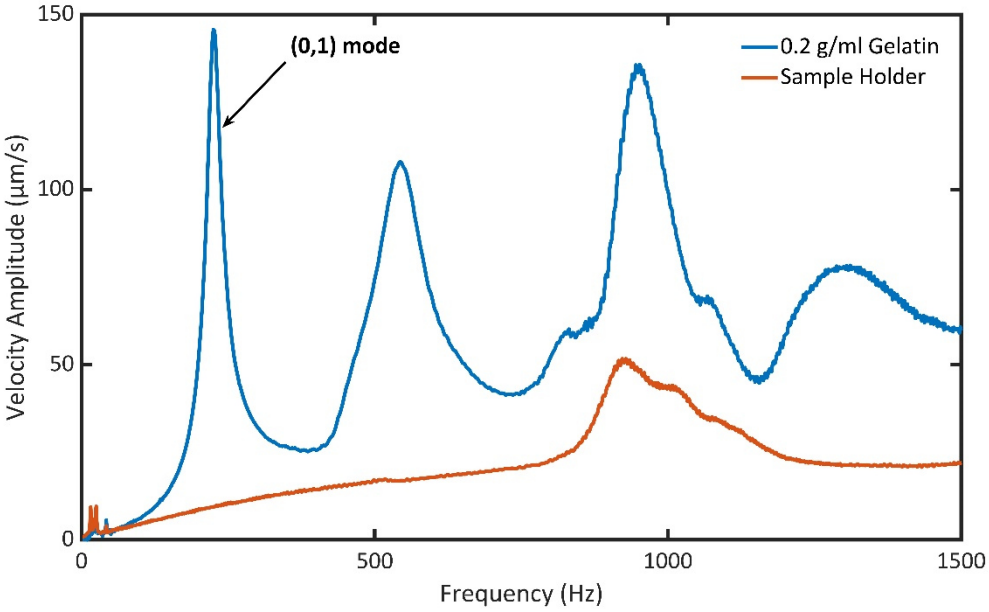

Figure 30 | Obtained velocity amplitude from an 0.20 g/ml gelatin disk and sample holder. *Velocity amplitude of the sample holder's rim (orange line, mean value) and the central point of the gelatin disk (blue line). The first resonance peak of the (0,1) mode is located at 223.4 Hz. Taken from Schwarz et al. [186].*

Figure 31 shows the transmissibility, the ratio between the velocity amplitude (FRF) measured at the output, and the velocity amplitude (FRF) obtained at the input location of all investigated gelatin samples. With increasing polymer concentration, the resonance peaks slowly shift towards higher frequencies. A continuous increase in the FWHM of the resonance peaks can also be observed for higher polymer concentrations, accounting for increased modal damping.

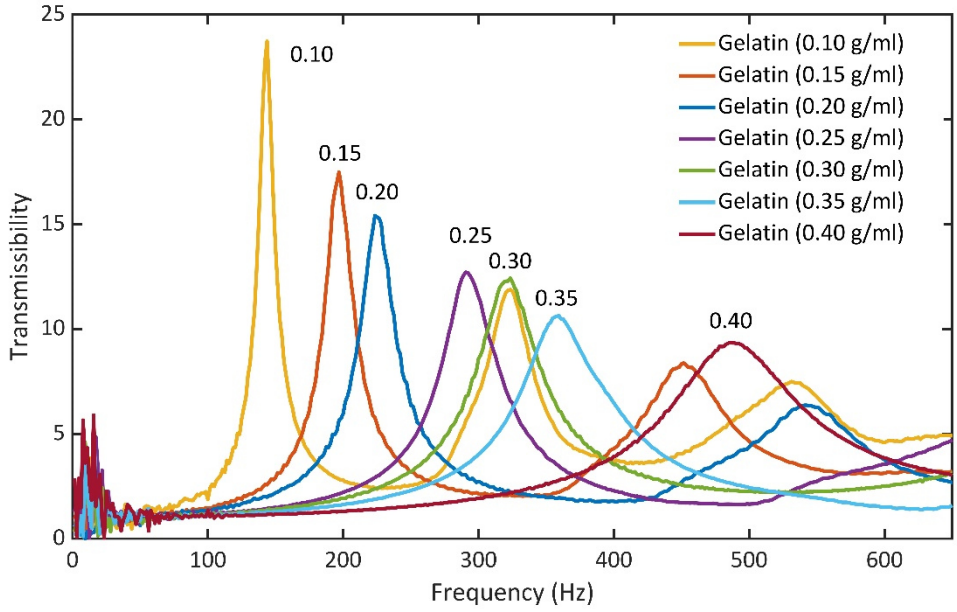

Figure 31 | Transmissibility of different gelatin samples. *Transmissibility of seven different gelatin samples with a concentration ranging from 0.10 g/ml to 0.40 g/ml. For each sample, the first resonance peak can clearly be determined, as well as its shift towards higher frequencies with increasing gelatin concentration. The same effect can be observed for the FWHM. Taken from Schwarz et al. [186].*

IT-AFM testing was done to link the obtained LDV data to the Young's modulus of each gelatin sample (see Chapter 5.2.1). As expected, with increasing gelatin concentration, the Young's modulus increases in the IT-AFM measurements (see Figure 32, orange dots). Within error limits, there is an almost linear increase of Young's moduli with the gelatin concentration, which agrees with literature observations [225, 226]. The measured Young's moduli start at 2.06 kPa for the 0.10 g/ml sample and reach 34.88 kPa for the 0.35 g/ml sample in the IT-AFM experiment. However, the last data point at 0.40 g/ml seems to be an outlier because, with 33.95 kPa, its Young's modulus is lower than the Young's modulus observed at 0.35 g/ml. This could be caused by the small air bubbles which were frequently observed within the gelatin disc at this gelatin concentration, suggesting that the measurements at 0.40 g/ml were possibly recorded on or near such an air bubble. Therefore, the last data point at 0.40 g/ml was excluded from the linear fit (see Figure 32, orange dashed line). The blue dots in Figure 32 represent the first resonance frequencies obtained from LDV measurements, which are also plotted against gelatin concentration. Similar to the Young's moduli, the frequencies of the first resonances increase with higher polymer concentration. Here, the first resonance frequency of the 0.40 g/ml gelatin sample also increases with higher gelatin concentration, even exhibiting a slight upward jump, compared to the 0.35 g/ml sample. This jump points to an increase in the Young's modulus also at 0.40 G/ml and underlines the hypothesis of an air bubble near the location where the IT-AFM was recorded.

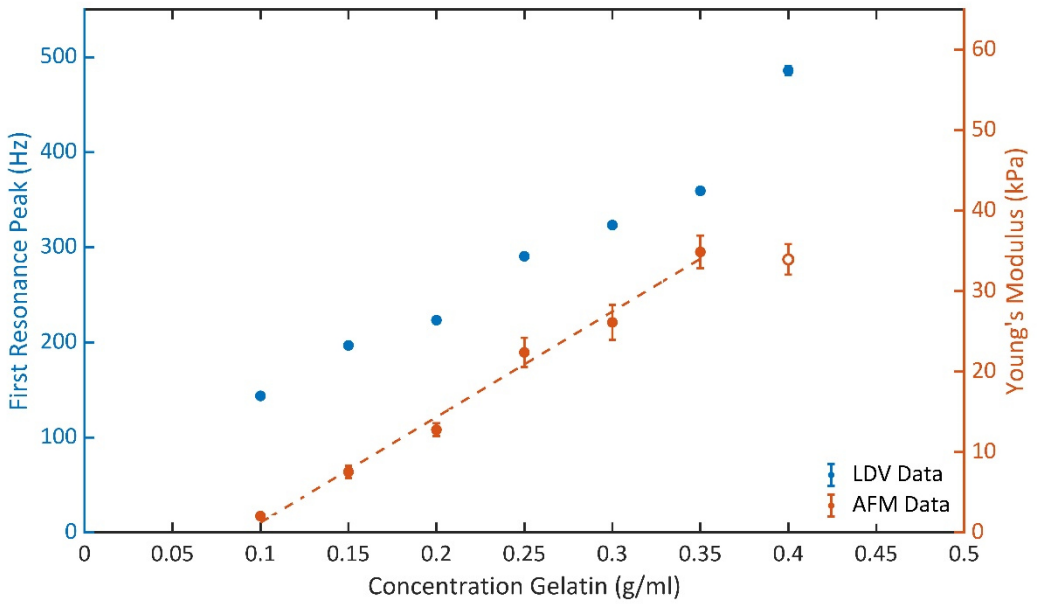

Figure 32 | First resonance frequencies and Young's moduli in dependency of the gelatin concentration. *Resonance frequencies (blue dots, right axis) of the gelatin samples. As a standard deviation for the measured value (error bars blue dots, not visible), the measuring inaccuracy of the device was used here, which is 1% of the measured value. Young's moduli of the different samples (orange dots, right axis) as measured from the IT-AFM. The measured value of the 0.4 g/ml samples is declared as an outlier. The error bars symbolize the calculated standard deviation from the mean value out of in total five force maps, each consisting of 100 measurement points. Taken from Schwarz et al. [186].*

Figure 33 shows a direct comparison between the first resonance frequency and the square root of the Young's moduli (see blue dashed line). As expected for a circular clamped disk, the resonance frequency of the (0,1) mode exhibits a nearly linear increase with the square root of the Young's modulus (see Equation (18)). Here again, the outlier at 0.40 g/ml does not follow the trend of the other gelatin concentrations.

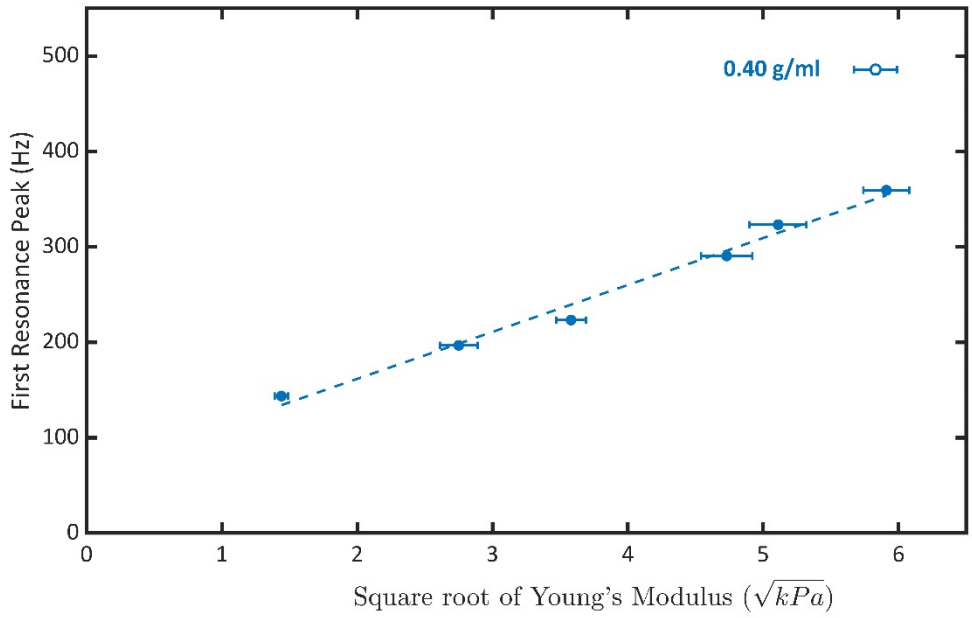

Figure 33 | Eigenfrequency plotted versus the square root of Young's modulus determined by IT-AFM. *A linear increase of the first resonance frequency with increasing Young's modulus can be recognized. Taken from Schwarz et al. [186].*

In addition to the elasticity, which correlates with the frequency of the first resonance, the transmissibility spectra displayed in Figure 31 also contain information about the material's viscosity, which correlates with the FWHM of the resonance. Therefore, a closer look at the modal damping was taken, and the damping ratio ζ was calculated using the FWHM of the relevant resonance peaks (see Equation (10) and Equation (11)). Figure 34 reveals an exponential increase of the damping constant with gelatin concentration, matching with data presented in the literature [227-229]. The damping constant γ is shown in the Supplementary Figure 2.

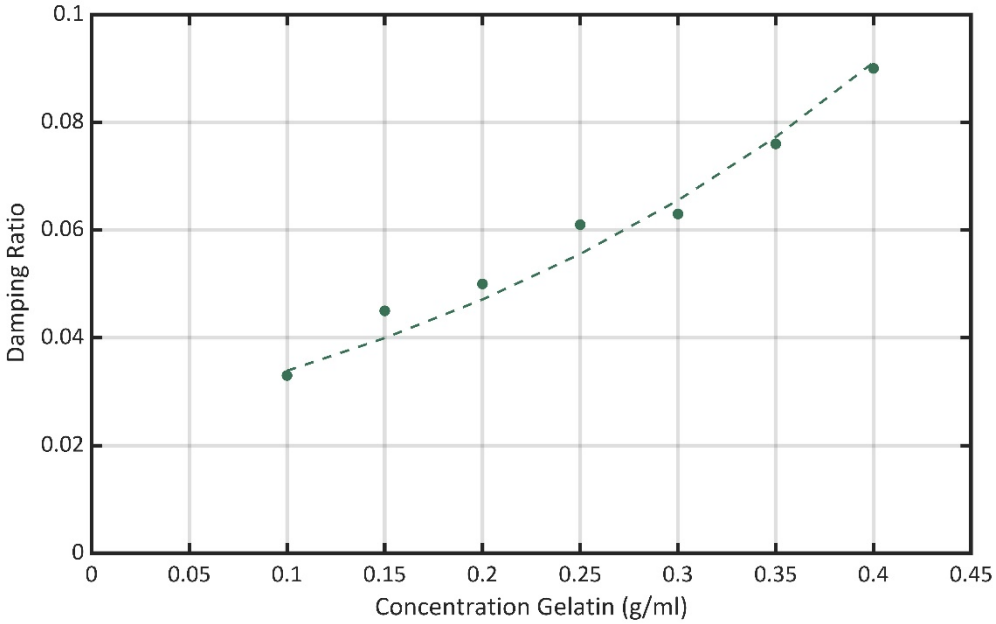

Figure 34 | Damping ratio ζ of the (0,1) mode for each tested gelatin concentration. *Taken from Schwarz et al. [186].*

The Young's modulus can also be derived from the resonance frequencies using numerical or analytical mathematical methods. Following Equation (18) to (21), this was using a thin gelatin disk model following classical plate theory, not accounting for shear forces since these models are mostly applicable on thin plates where shear forces can be neglected. The resulting Young's moduli (see Figure 35, blue dots) match the experimental IT-AFM values (see Figure 35, orange dots) well considering also the experimental error (see Figure 35 and Supplementary Table). However, the results from the FEM study do not show such a good agreement with the IT-AFM data and render significantly higher Young's moduli (see Figure 35, green dots). This difference between IT-AFM results and FEM modeling might be caused by the fact that IT-AFM only probes the sample surface. Regarding the FEM analysis, the entire sample is deformed and bent, thus taking the entire sample thickness into account and also shear forces. IT-AFM measurements, as well as the thin disk model, may therefore underestimate the Young's modulus. The dimensions of the gelatin disk used in this experiment require models suitable for thick plates, and following the data presented in the work of Zhou et al. [221], introducing a correction factor for thin plate models when applied onto thick plates, renders higher Young's modulus values (see Figure 35, yellow dots). These results were more consistent with the FEM analysis but deviated markedly from the IT-AFM results. In order to assess the elastic modulus of the whole gelatin sample, unconfined, quasi-static compression testing was performed (see Figure 35, purple dots). Here, the entire samples are compressed up to a strain of 15%, and the results now fit much better concerning the thick plate model and the FEM analysis results, and a linear relationship between Young's modulus and gelatin concentration can be confirmed for all data. Although the experimental, numerical, and analytical results compare well among each other, they only indicate and do not prove a certain trend. This aspect will be highlighted and discussed in more detail in the discussion chapter.

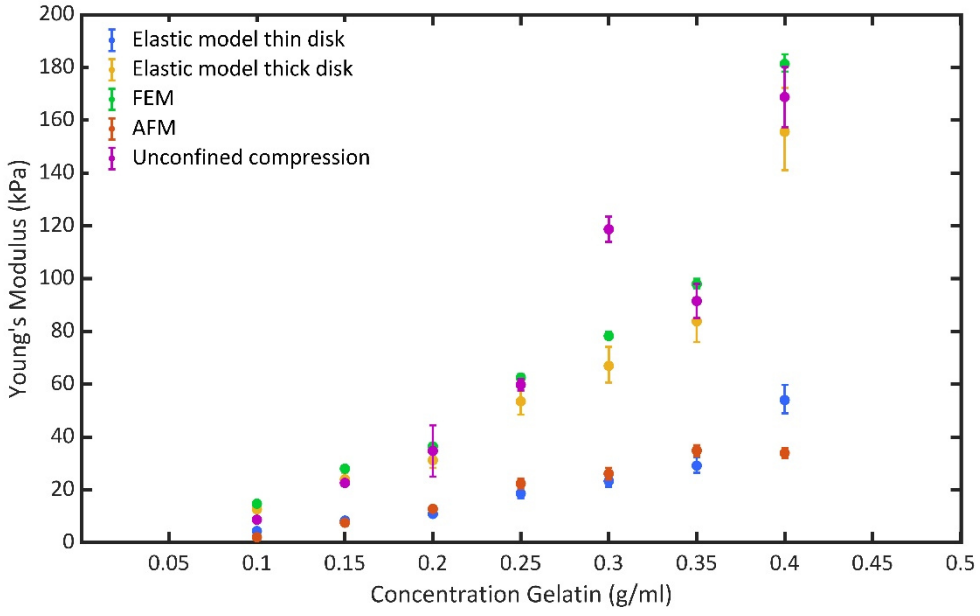

Figure 35 | Experimentally and analytically determined Young's moduli values. *Comparison between the Young's moduli measured using the AFM (orange dots) and the unconfined compression testing (purple dots). Calculating the expected Young's modulus values using the measured frequency data following the elastic model for a thin disk (blue dots) results in similar data as the AFM experiment (orange dots). Unconfined compression testing (purple dots), FEM analysis (green dots), and the analytical solution for a thick disk (blue dots) agree very well but differ from the AFM results and the thin disk model. Taken from Schwarz et al. [186].*

6.3. Cantilever-assisted measurement of gelatin hydrogel

The previous chapter shows how LDV can provide qualitative and quantitative information about the elastic properties of transparent hydrogels. The presented concept strongly relies on a defined sample geometry, and sample preparation can be challenging since a circular clamped disk geometry is required for testing and a potential detachment from the sample holder's rim needs to be prevented. An integration of this approach into existing processes can be difficult. Therefore, a setup was developed, allowing for direct integration of the LDV technique into processes like extrusion-based bioprinting. The hydrogel is positioned onto a solid surface in such processes, preventing a direct measurement in a free-hanging setup. The experimental design was adapted in a way that the sample could be placed on a mechanical probing structure, here a bi-clamped beam. Instead of directly measuring the surface of the transparent biological material and being highly dependent on its optical properties, the backside of the bi-clamped beam is measured using a mirror (see Figure 36). By placing a sample on top of this cantilever, a change in the sample's mechanical properties can be detected, since they modulate the measured dynamics of the beam if physical contact is given. For the experiment, the 3D-printed test structure was screwed onto the piezo stack (see Figure 36 b), blue part). The bi-clamped beam dynamics can be measured via a mirror on its backside using the LDV device. The still liquid sample is cast on top of the beam. After sample solidification, measurements can be done.

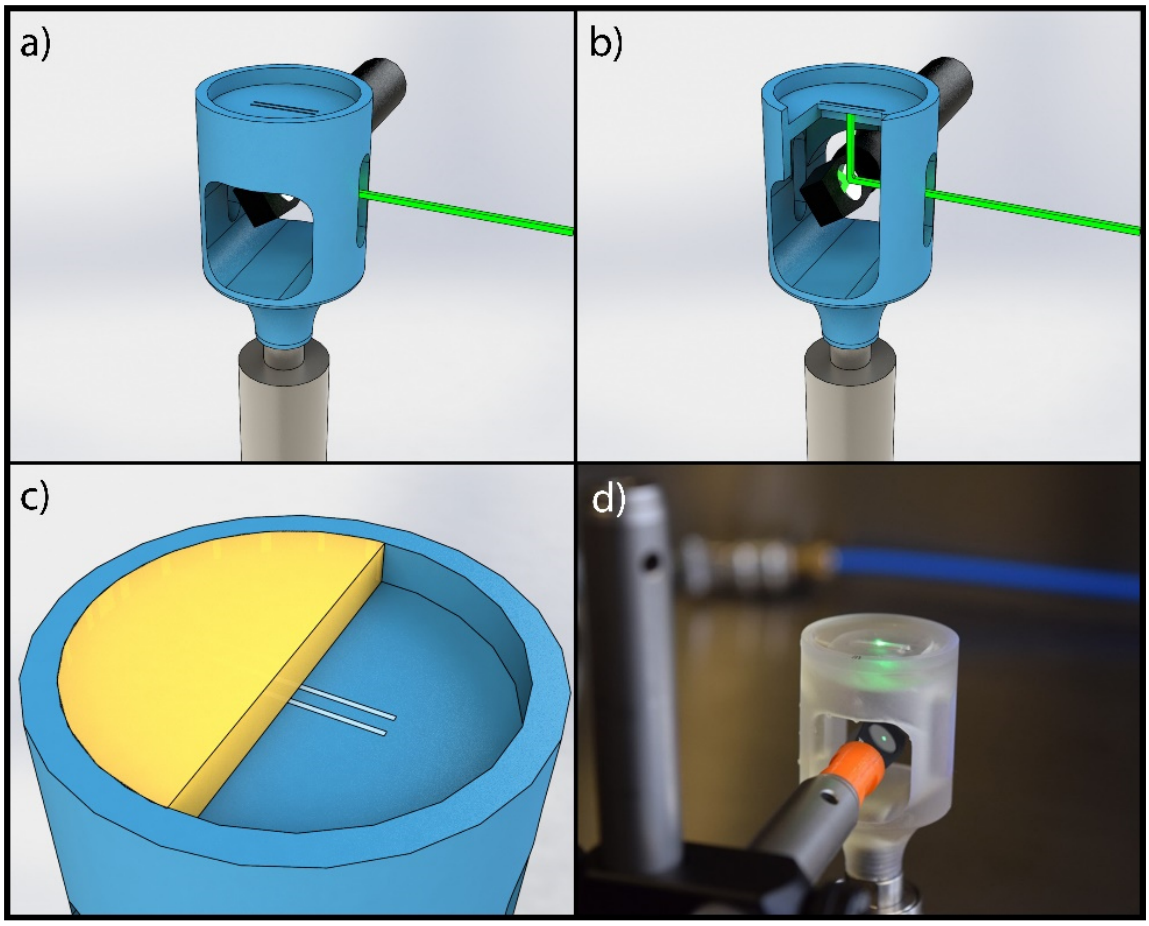

Figure 36 | Sample preparation process. **a)** 3D-printed sample holder (blue) screwed onto a piezo stack (grey). **b)** Through lateral cavities, the LDV laser (green) was reflected on the beam structure's backside via a silver mirror. The fixation of the mirror was vibrationally decoupled to avoid any disturbance of the measurement. **c)** A sacrificial ink, *Pluronic*™ F127 (light blue), was used for sealing the lateral cavities beside the beam to avoid leakage of the warm and, at this time, liquid hydrogel sample (sectional view, orange) directly pipetted into the sample holder. **d)** Complete experimental setup. Taken from Schwarz et al. [188].

Similar to the gelatin disk experiment, also here the scanning feature of the NIR-SLDV device enables the characterization of the mode shapes (see Figure 37). At 16.4 kHz, the bi-clamped beam possesses its first resonance frequency, and a bending mode can be observed as mode shape. The displacement amplitude of the beam's center raises near this resonance frequency from 43 pm up to 1.42 nm.

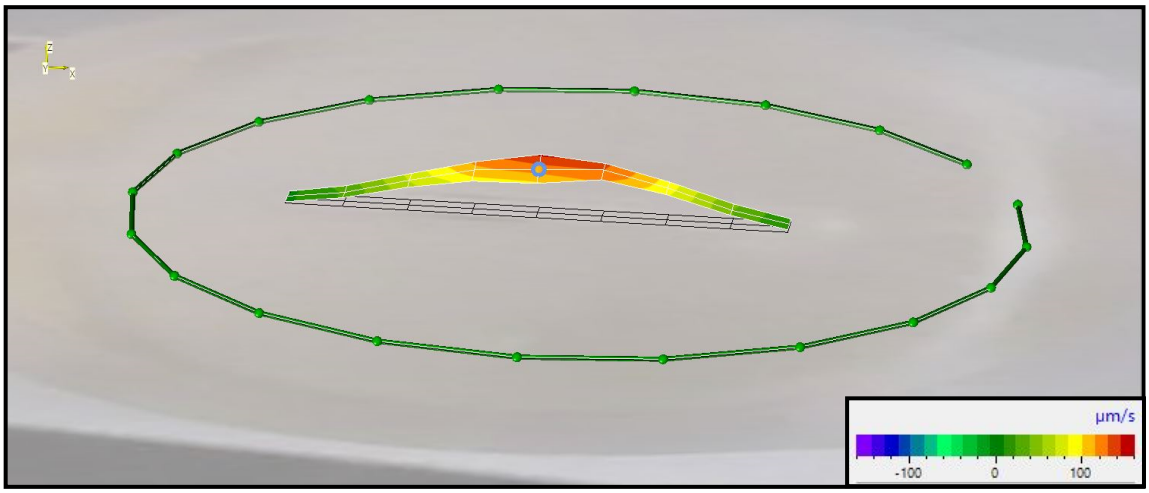

Figure 37 | First bending mode of the bi-clamped beam structure at 16.4 kHz. *At this resonance frequency, the amplitude displacement is 1.42 nm. Compared to this value, the average displacement apart from resonances is relatively small, with only 43 pm. The false-color scale shows the local velocity perpendicular to the scanned beam surface.*

If the mirror holder shown in Figure 36 d) would also be excited during testing, results would be falsified, and the relevant resonances of the beam could eventually not be revealed. The signal taken from the mirror holder shows no significant dynamics (see Figure 38, red line), indicating the successful vibrational decoupling of the experimental setup. Data measured on the top of the empty beam shows multiple resonances (see Figure 38, blue line). The mode shape shown in Figure 37 can be attributed to the resonance frequency of the empty beam located at 16.4 kHz with a velocity amplitude of 146.6 µm/s and a displacement amplitude of 1.42 nm. The purple line in Figure 38 shows the dynamics of the bi-clamped beam with a hydrogel sample on top of it, measured from its backside. Resonances are recognizable, and compare to the empty beam, resonances are decreased in their amplitudes. A slight shift of the resonances towards lower frequencies is possibly due to the additional sample mass. In all signals, except the one from the mirror holder, the resonance of the whole sample holder at 4.3 kHz is present. However, since it is below the relevant dynamics of the beam at 16.4 kHz, they do not influence the measurement results.

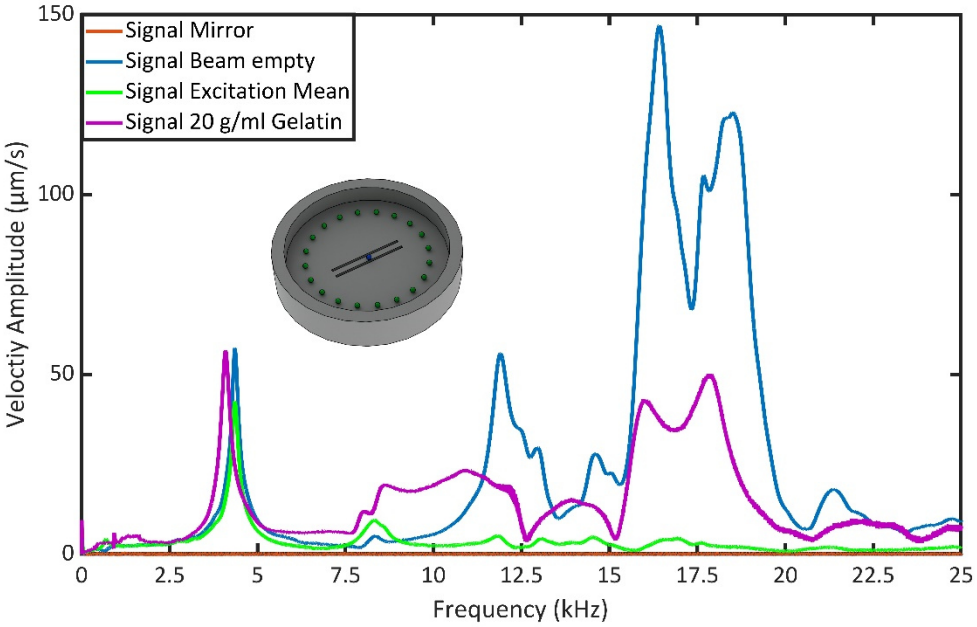

Figure 38 | Experimental amplitude velocity data of the cantilever structure measured using the NIR-SLDV device. *The red line indicates the vibration of the mirror holder during the measurement. No relevant dynamics occur during testing, indicating a successful vibrational decoupling of the setup. The blue line represents the dynamics of the unladen beam (blue point), and the green data shows the vibration of the empty sample holder (mean value, green points), possessing a single resonance at 4.3 kHz. The blue and green lines represent the vibrations without and with a gelatin sample. The signal taken from the sample holder (green line) shows no resonance frequencies in the relevant frequency region between 15 and 20 kHz. Taken from Schwarz et al. [188].*

The transmissibility was calculated by dividing the data taken from the back of the laden bi-clamped beam as output data through the mean value of the empty sample holder (see Figure 39, green line and green dots). Comparing the transmissibilities of the different gelatin concentrations with each other, two resonance peaks between 15 and 20 kHz can be identified, present for all gelatin concentrations. As mentioned before, the slight shift of the peaks, especially the one at 16.4 kHz, is due to the transmissibility being calculated using data taken from the sample holder with and without a gelatin sample on top of it. This had to be done since the sample holder's dynamics could only be measured from above and, therefore, without a gelatin sample (see Figure 38, green dots). Because the sample holder was designed as compact as possible, the cavity for placing the mirror was also very small. Consequently, it was only possible to focus the measurement on the beam's backside and not beside it for measuring the dynamics of the sample holder. Looking at the two resonances peaks, both decrease in amplitude with increasing polymer concentration, but only the first one can be analyzed properly. For data analysis, the first resonance peak was chosen.

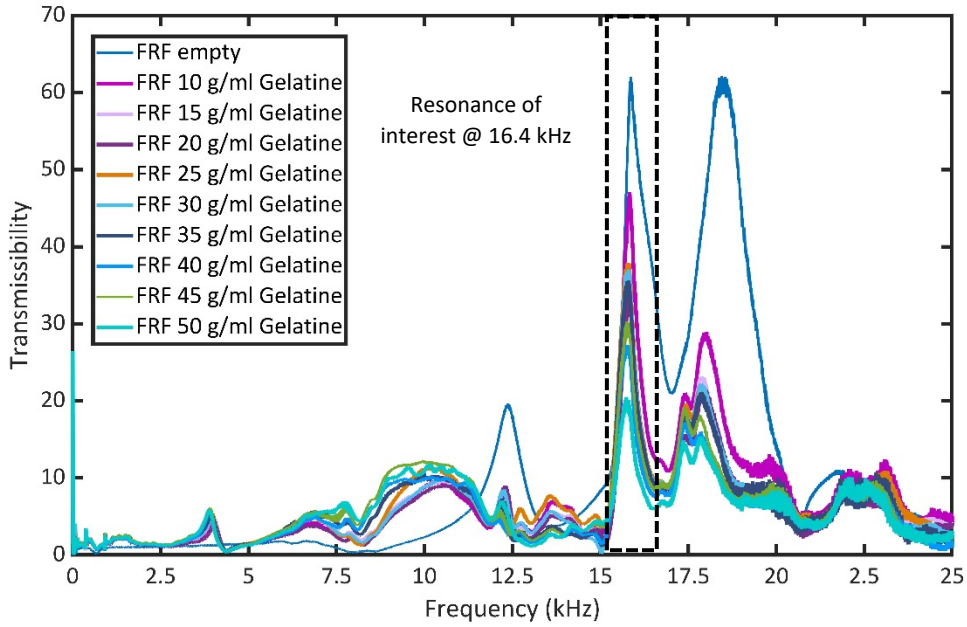

Figure 39 | Transmissibility comparison for different gelatin concentrations. *The blue line indicates the transmissibility of the beam without a sample on top of it. The other lines show the transmissibility for different polymer concentrations, implying a decrease in peak heights with increasing gelatin concentrations. For further analysis, the decreasing peak height of the resonance located at 16.4 kHz (black dashed rectangle) was taken into account. Taken from Schwarz et al. [188].*

The Young's modulus of each sample was measured using IT-AFM (see Figure 40, blue dots) and compared with the peak height of the resonance peak located at 16.4 kHz. The measured Young's moduli increased linearly with increasing gelatin concentration, similar to the data presented in the previous chapter 6.2. Plotting the peak height of the resonance curve at 16.4 kHz for each gelatin concentration against the respective Young's modulus determined with IT-AFM measurements shows an apparent decrease in the peak height with increasing Young's modulus (see Figure 40). Here the linear fit (orange dashed line) does not match the data and the IT-AFM results.

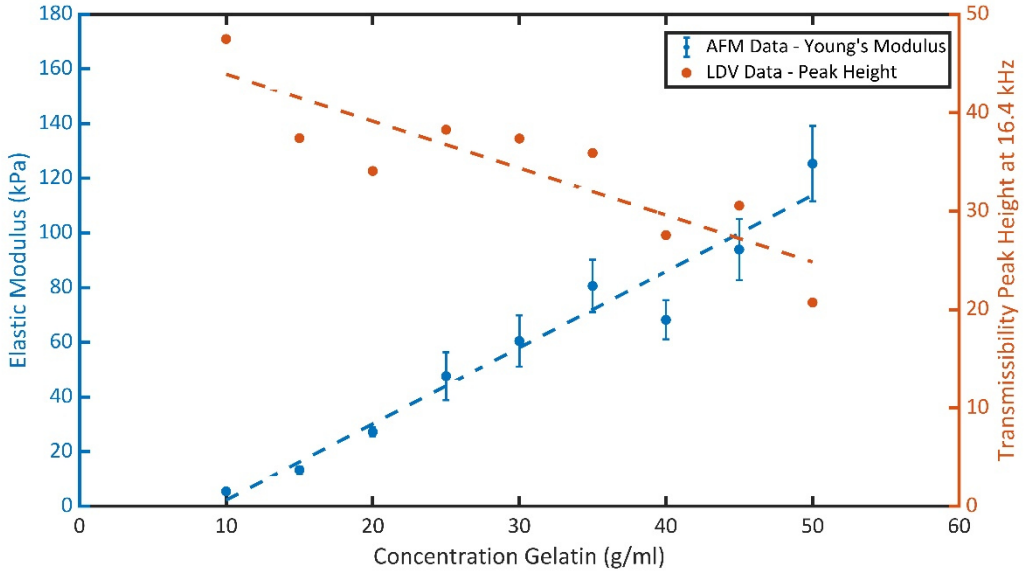

Figure 40 | Young's modulus compared to the peak height of the resonance frequency of different hydrogel concentrations. *With increasing gelatin concentration and increasing Young's modulus of the investigated samples, the amplitude transmissibility of the resonance frequency at 16.4 kHz decreases. Error bars for AFM data represent the standard deviation from the acquired force maps, three maps with 100 measurement points each. Taken from Schwarz et al. [188].*

Directly comparing LDV and the IT-AFM data indicates a slight decrease in the peak height with an increasing Young's modulus (see Figure 41). Performing a correlation analysis between the Young's modulus and the peak height renders a negative Pearson correlation factor of -0.82, indicating a dependence between these two data sets. This correlation was calculated using the *corrcoef* function in Matlab™. The decrease of the displacement amplitude with increasing polymer concentration is displayed in Supplementary Figure 4.

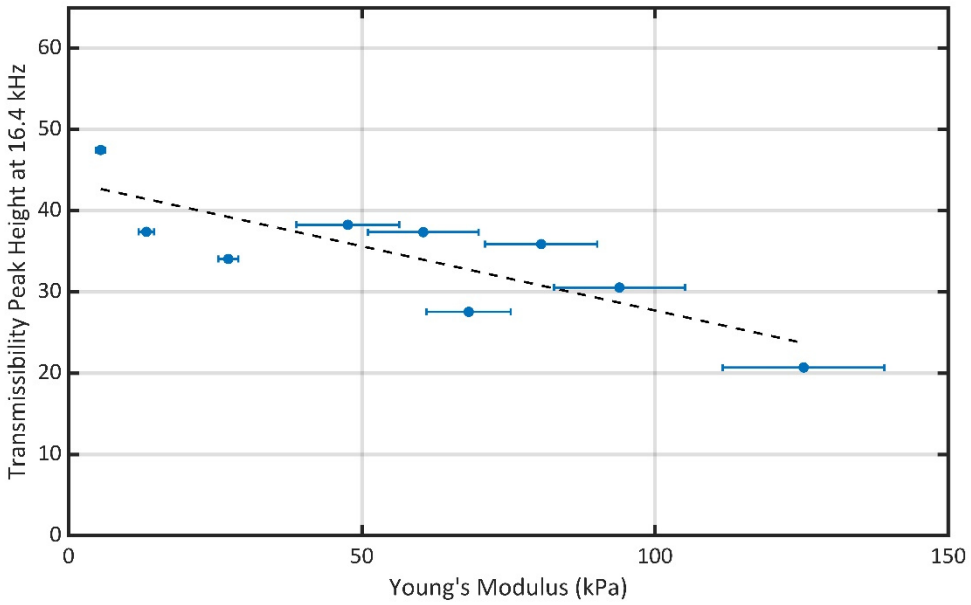

Figure 41 | Direct comparison of the resonance's peak height at 16.4 kHz and the Young's modulus of the samples. *Shown are the amplitude of the calculated FRF transmissibility located at 16.4 kHz (see Figure 39) and the measured Young's modulus. A slight decrease in the transmissibility amplitude with increasing Young's modulus can be observed. The Pearson correlation factor between the Young's modulus and the transmissibility peak height at 16.4 kHz is -0.82.*

Resonance peaks located at 16.4 kHz do not seem to change in their FWHM, which does not suggest a change in the damping ratio ζ and, therefore, also in the damping constant γ of the sample. Calculating the damping ratio ζ confirms this observation and shows no significant change across all gelatin concentrations (see Figure 42). This result suggests that both the viscous and the structural damping do not change with increasing gelatin concentration. This finding does not agree with the results of the direct measurement in chapter 6.2. All the data presented here can be found in more detail in the Supplementary Table 3.

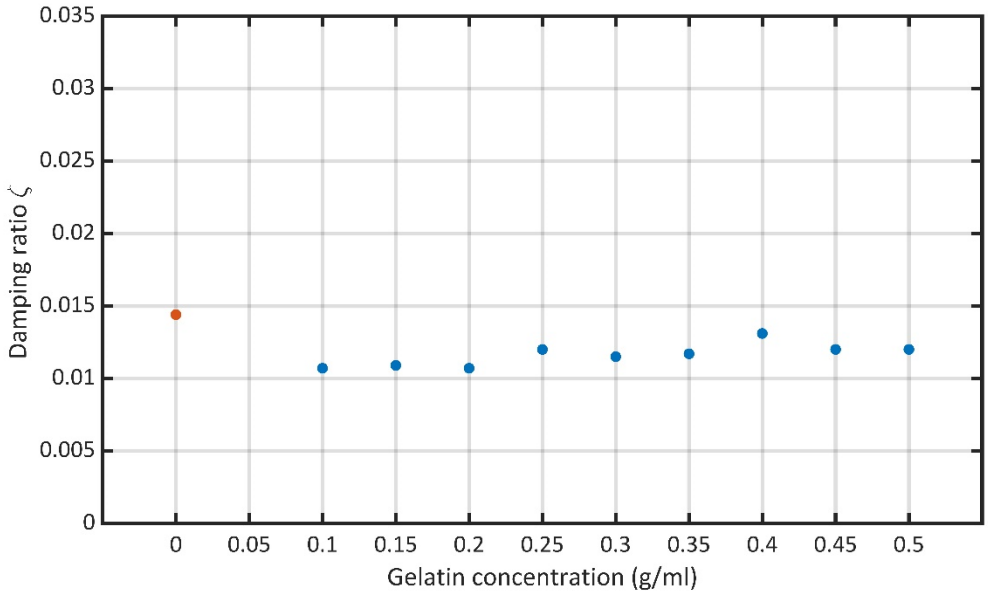

Figure 42 | Damping ratio ζ calculated for the empty beam (orange dot) and the laden bi-clamped beam (blue dots). *Despite the different gelatin concentrations and their different Young's moduli (see Figure 40), no significant change in the damping ratio can be detected.*

Two possible reasons for a constant damping ratio ζ among all gelatin concentrations can be identified: either no permanent contact exists between the sample and beam, or the beam is too stiff for being influenced in its dynamics by the sample material properties. An FEM analysis was performed to investigate which results could be expected for such an experimental setup (see Figure 43). Here, in the model, a solid contact between the gelatin layer and the beam is defined. For a non-laden beam geometry, in the FEM simulation, the first resonance appears at 11.05 kHz, and when the hydrogel layer is added, this first modal frequency initially drops to 9.83 kHz due to the additional mass of the investigated system. With an increase in the Young's modulus of the gelatin sample, the natural frequency of the first mode increases. The lower beam's Young's modulus of 2.8 GPa is much higher than the Young's modulus of the gelatin layer ranging from 5.5 to 125.4 kPa. This implies that changes in the hydrogel layer only have a minimal effect on the modal frequency of the entire structure. All mode shapes from the FEM analysis are shown in Supplementary Figure 5.

Following the FEM analysis results, IT-AFM, and LDV measurement, it is likely that no fixed contact existed between the surface of the probing geometry and the gelatin sample on top of it, enabling a sliding of the two structures against each other, and consequently, the modal parameters do not change with the increasing Young's modulus. Only in the vertical direction an interaction due to the increased displacement amplitudes was present, which can be observed in the amplitude decrease with increasing gelatin concentration. A further study should be a FEM analysis with a defined sliding contact between the gelatin sample and the bi-clamped beam surface to investigate this hypothesis further.

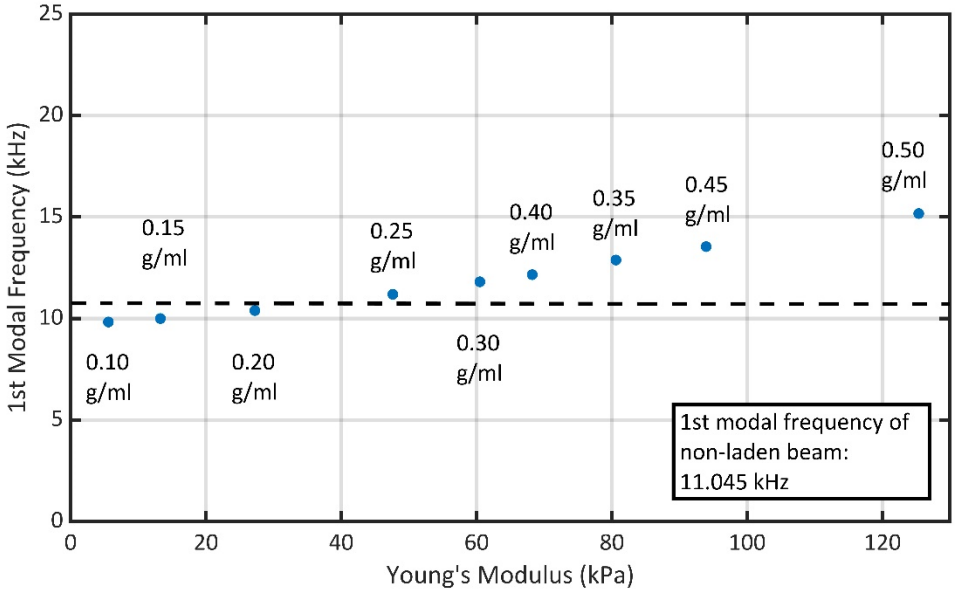

***Figure 43 | First modal frequencies calculated using FEM software plotted against the measured* Young's modulus.** *In the experimental results, no change in the resonance frequency with increasing Young's modulus can be seen. Performing a FEM analysis shows that with increasing Young's modulus, the 1st modal frequency should also increase. Due to the additional mass through the gelatin sample placed on top of the beam, the frequency dropped from 11.05 kHz to 9.83 kHz.*

6.4. Fibroblast cell measurement

After successfully using LDV to analyze transparent hydrogels, the feasibility of probing the biomechanical properties of cells was investigated. In cell culture, most mammalian cells are grown adherent on a surface. Each cell is tightly attached to the surface of a Petri dish or cell culture flask. The Young's modulus of cells changes depending on cell activity, differential state, and disease progression, making cell mechanics a quality marker for the fabrication of functional engineered tissues and TE applications, ensuring later functionality. To evaluate the possibility of analyzing the mechanical properties of cells by LDV, murine fibroblasts cultured in an adherent 2D-culture were chosen as a model system. An LDV setup integrated into an upright optical microscope setup with a water-immersion objective was used. The LDV measurement laser was focused onto the cell membrane and the Petri dish bottom directly underneath the cell, measuring the response to an external excitation (see Figure 44).

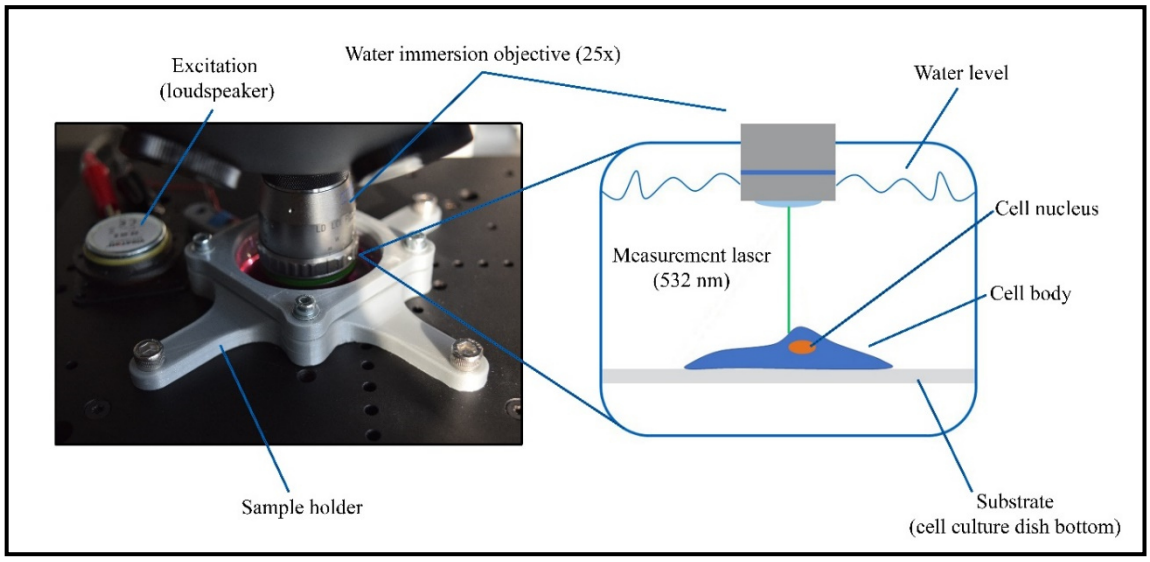

Figure 44 | Experimental setup for cell measurements. *The Petri dish was directly fixed onto the LDV setup using the 3D-printed sample holder. Excitation was generated using the in-built signal generator and an* electrodynamic exciter. The laser was focused directly onto the cell membrane and the blank Petri dish surface. Taken from Schwarz et al. [189].

After immersing the objective into the culture medium, the murine fibroblasts were first identified and located (see Figure 45, blue contour). A measuring grid was defined onto and around a chosen cell (see Figure 45, left side). Figure 45 shows the LDV data recorded on the apical cell membrane exposed to the surrounding fluid and the Petri dish surface, as well as the calculated transmissibility. Several resonances can be observed between 23 and 500 Hz, leading to the conclusion that excitation by the electrodynamic exciter was sufficient. However, no differences between the two data sets recorded on the cell membrane and the Petri dish can be detected. In the relevant frequency range between 23 and 500 Hz, the transmissibility is close to 1. Outside of this range, the measured velocity amplitude is only a few nanometres per second, which is probably background noise and results in erratic transmissibility values. With this setup, measuring the mechanical parameter of living mammalian cells seems not possible. In this experiment, the amount of reflected signal behind the sample is higher than the signal originating from the sample surface, dominating results.

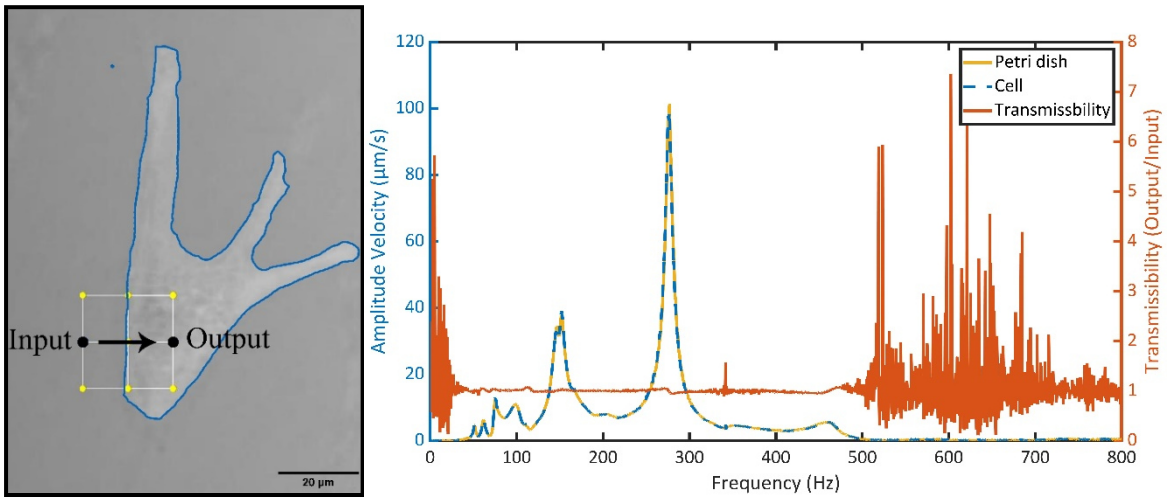

Figure 45 | Bright field image of the measured murine fibroblast, measured signals, and calculated transmissibility. Left: *Single fibroblast cell (inside the blue contour line) growing on the Petri dish surface. Using the software interface, a measurement grid can be defined at the edge of the cell for measuring areas representing the bare Petri dish surface and the apical cell membrane.* ***Right:*** *Signal data acquired at the cell surface (blue dashed line, left axis), from the Petri dish surface (green line, left axis), and the resulting transmissibility (orange line, right axis). Taken from Schwarz et al. [189].*

6.5. Human cardiomyocyte contraction measurement

In contrast to the murine fibroblasts used in the previous experiment, cardiomyocytes (heart muscle cells) possess the ability of spontaneous contraction, which is an essential marker of their functionality and viability [230-232]. To evaluate the monitoring of this contraction movement, a NIR-SLDV device, as used in the hydrogel experiments, was used (see Chapter 5.1.1 and Chapter 5.1.2). Because of the lack of an integrated microscopic imaging setup, there was no information about the exact measurement location during the experiment available, and the LDV device was positioned directly above an inverted optical microscope, where the LDV pilot laser position could be determined through the microscope image (see Figure 46). Furthermore, the cell contraction was also recorded from below through a recorded video signal from the microscope camera and by using PIV analysis. PIV is an established measurement method for monitoring cardiomyocyte contraction [233-236]. Here, the PIV analysis was used as a control method for evaluating the LDV results. Because water absorbs most of the applied laser energy due to the high extinction coefficient for the used laser wavelength of 1550 nm [32], the culture media was removed during the measurement, until the sample's surface was partially exposed to air and could be analyzed via the NIR-LDV measurement laser.

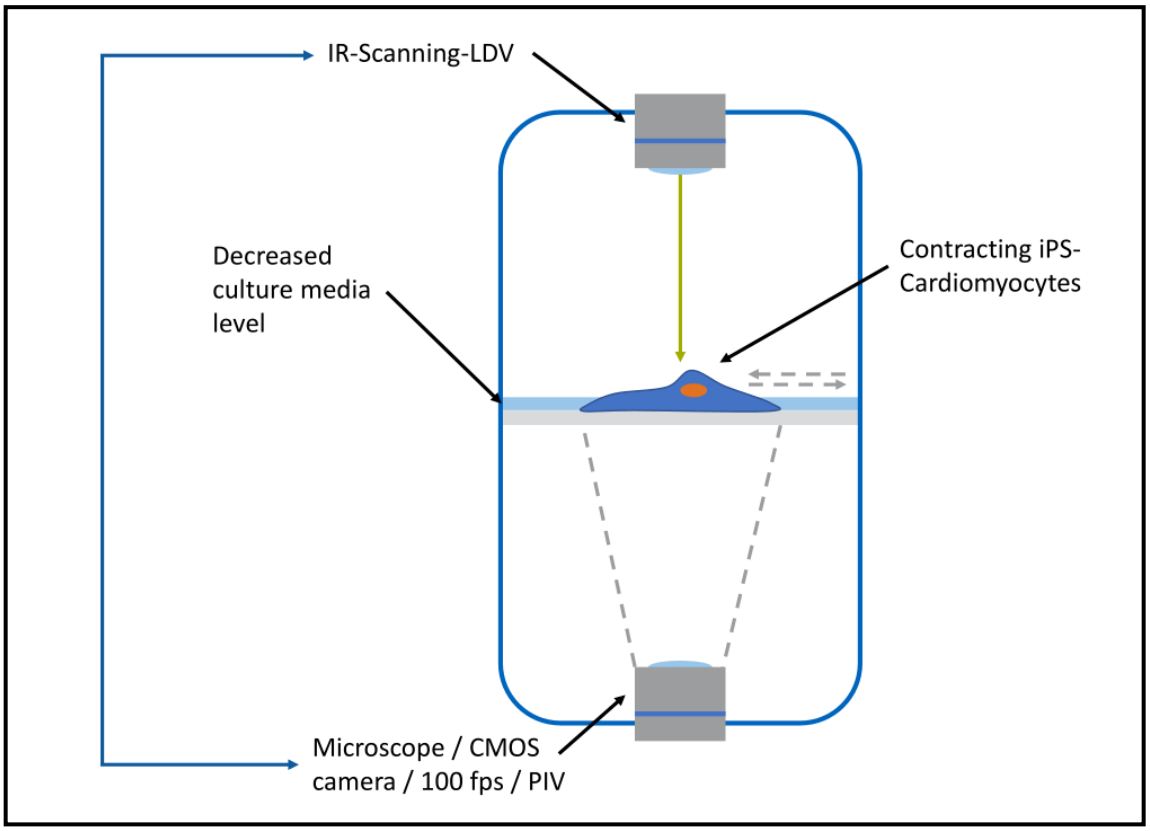

Figure 46 | Experimental setup for cardiomyocyte contraction measurement. a) *On top of the microscopic setup, a NIR-SLDV was positioned. For measuring the cell surface and since the aqueous culture medium absorbs the laser, the liquid level was decreased until the cell surface was exposed to air. From below, the standard imaging setup from the microscope was used, images were recorded with 100 fps and later analyzed using a PIV algorithm.*

When measuring a monolayer of contracting cells covered with a thin layer of cell culture medium, contractions can be roughly detected in the LDV data, but the signal-to-noise ratio is too low for reliable data analysis (see Figure 47 a)). This is probably caused by the thin non-removable culture medium layer, preventing the cells from drying out during the experiment. PIV results show a high signal-to-noise ratio across all experiments. This is mainly because the sample shows a random bright and dark pattern in the brightfield microscope images, enabling the PIV algorithm to better track and analyze the lateral contraction movement through the displacement of this pattern. During the cultivation of cardiomyocytes, the contraction movement partially detaches the cell monolayer from the growth substrate. As a result, the detached areas shrink due to the contraction movements and growth processes, leading to small cell accumulations being higher than the surrounding cell monolayer and, therefore, could be measured and analyzed using the NIR-LDV laser (see Figure 47 b), blue line). Here, a contraction can be detected better but still not optimally compared to the spheroid measurement. The PIV analysis results show nearly no contraction, which is basically due to the decreased contraction activity and speed resulting from the lack of physical conditions and culture media supply (see Figure 47 b), orange line). Despite the reduced contraction activity, individual peaks can be detected in the LDV data not being present in the PIV data, underlying the high sensitivity of the LDV method.

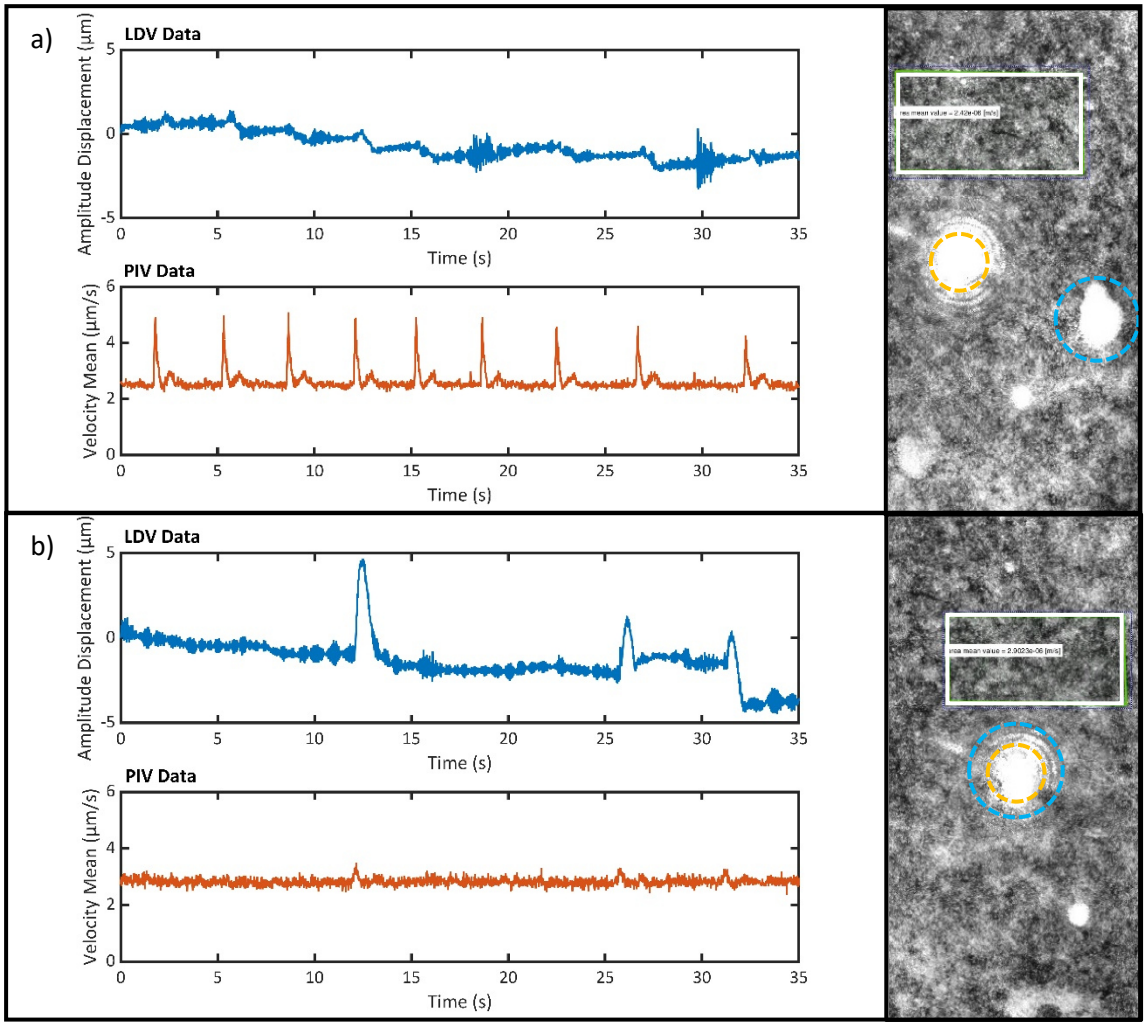

Figure 47 | Results for cell monolayer and cellular elevation measurement. a) *LDV measurement data (blue line) allows roughly to recognize repetitive patterns that may be correlated with cardiomyocyte contraction, but not reliably due to the low signal-to-noise ratio. On the opposite, PIV results (orange line) have a high signal-to-noise ratio, and repetitive patterns can be recognized very well, which is due to the nice speckle pattern in the brightfield image and the analysis window (white rectangle).* ***b)*** *Positioning the LDV measurement laser directly over a cellular elevation (yellow and blue dashed circle) results in better identifiable patterns since the cellular structure protrudes from the culture medium. With the lack of physiological conditions and nutrient supply, the contraction activity decreases, and only a few contraction events could be detected. This lowered cardiomyocyte activity can also be observed in the PIV data (orange line).*

Compared to the cell monolayer, cardiomyocyte spheroids can be exposed to air much easier due to their bigger size, improving measurement results. Measuring contractions without a multiwell plate cover, both signals show a repetitive sequence from which the beats per minute (BPM) can be deduced (see Figure 48 a)). Because only small amplitude velocities are present for the sub-Hertz contractions, the LDV device directly measures the displacement amplitude. This helps explain the slight increase of the baseline during the measurement, which can be traced back to the slipping of the whole spheroid onto the remaining thin water film during the measurement. Because its surface is not smooth, the distance of the LDV device to the sample's surface changes, and, therefore, the baseline resembles the spheroid's topology. The results from the PIV analysis represent the velocity of the movement in the plane of the Petri dish. Here, the baseline lies at around 10 μm/s indicating the slipping velocity of the spheroid. Besides the measurement without a cover, it was also evaluated whether LDV can analyze the contractions through a transparent cover. Experiments have been performed without a resting period, and consequently, the cells suffer from a lack of nutrient supply and adequate temperature control, reducing

contraction strength and rate over time. Contractions still can be identified but not reliably. Nevertheless, BPM values deduced from LDV and PIV data show a good agreement (see Supplementary Figure 7).

In both datasets, LDV and PIV data, a low level of noise can be recognized. These results in more detail revealed that the noise frequencies in both datasets are similar (see Figure 48 b)). Taking a closer look reveals a frequency of around 20 Hz. This frequency of 20 Hz represents 1200 rounds per minute (rpm), which is a relatively common operation velocity for computer fans. The only component of this experiment, possibly introducing this disturbing parameter, is the fan of the data acquisition card responsible for recording the 100 images per second. Unfortunately, the fan is not adjustable in its rpm value and can not be turned off during the experiment.

If the corresponding BPM is calculated for each time interval between two contractions individually, a decrease over the increasing number of contractions becomes apparent (see Figure 48 c)). Again, this can be explained by a lack of temperature control and nutrient supply. The individual values were evaluated manually according to the individual contraction events (see Figure 48 a), black dashed lines). Calculating the mean value and standard deviation for all recorded contractions, a BPM value of 30.46 ± 5.80 min^{-1} for the LDV data and a value of 30.46 ± 5.81 min^{-1} for the PIV data was obtained. Calculating the mean value and the corresponding standard deviation for all clearly defined BPM values resulted in a good agreement between LDV and PIV (see Supplementary Figure 4).

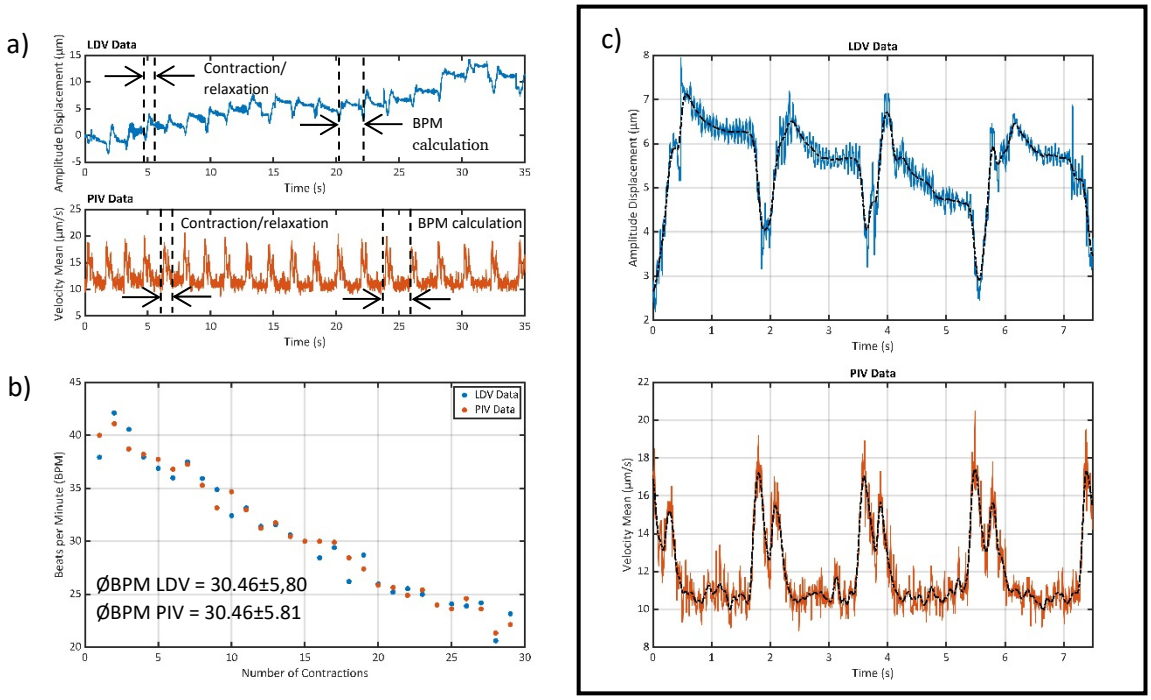

Figure 48 | Results from cardiomyocyte measurement without a multi-well plate cover. a) *Both LDV data (top, blue dots) and PIV data (bottom, orange dots) show repetitive patterns allowing to determine the contraction and relaxation phases of each contraction event. Furthermore, the time between two contractions can be extracted for calculating the BPM values.* ***b)*** *For each time interval between two consecutive contractions, the contraction rate in one minute was calculated (beats per minute, BPM). The spheroid activity decreases continuously over time due to a lack of nutrient supply and temperature control.* ***c)*** *Zooming into the data reveals the disturbing vibration with a frequency of around 20 Hz. The black dashed line represents the measurement data smoothed by a Gaussian filter (factor 0.20 for the LDV data, factor 0.50 for the PIV data).*

By calculating the velocity amplitude out of the smoothed LDV data (see Figure 49), LDV and PIV results can be compared directly. However, a minor time shift between PIV and LDV measurements has occurred, as they have been started manually on two different computer systems, resulting in an unsynchronized start of the measurements. Therefore, the PIV results were shifted forward in time by 0.2 seconds. The contraction and relaxation phases of both curves can be identified clearly. Because the PIV algorithm calculates the absolute mean value of the target area, the information about the direction of the movement is lost. This is not the case for LDV, as it can determine the direction of the movement with the help of the integrated Bragg cell. The maximum values of the contraction and relaxation phases match quite well when comparing the values from the PIV and the LDV measurement. A complete match is not expected because the two methods were not applied precisely to the same regions of the spheroid (see Figure 49 b)).

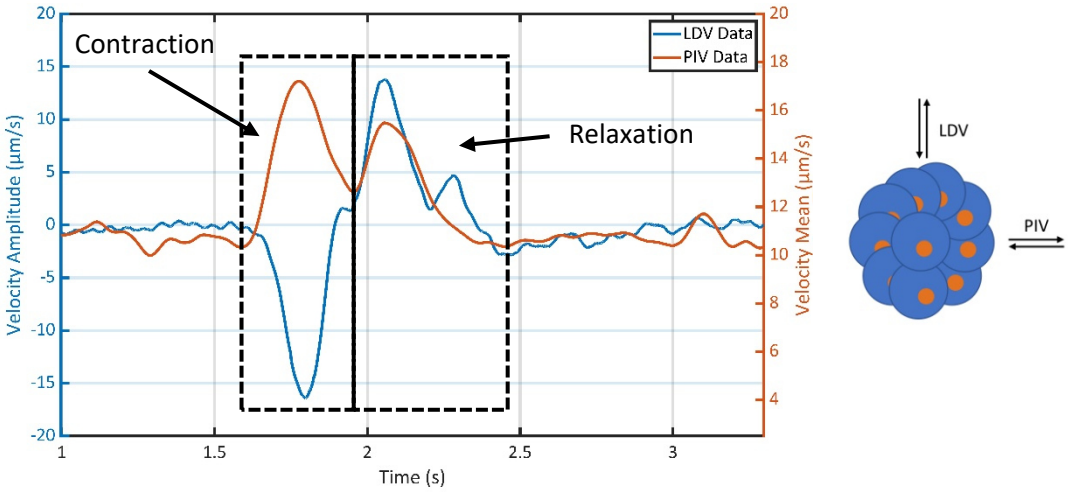

Figure 49 | Direct comparison of LDV and PIV data. *Both LDV and PIV data show contraction and relaxation phases measured from different areas of the spheroid. The PIV algorithm averages the amount of all data collected in one ROI window and tracks the horizontal movement in its absolute amount. Contraction and relaxation phases can be determined well.*

By applying isoprenaline, it was investigated whether an influence on the contractility by a drug could be detected. Before applying the drug, a basic contraction rate of approximately 15 BPM was determined with both methods. After the application of isoprenaline (also isoproterenol), which increases cardiac activity in patients and also in cardiomyocytes [233, 237, 238], a significant increase in the BPM rate was observed (see Figure 50 a)). PIV data could only be reliably evaluated up to the 24th contraction since the following contractions could not be clearly determined because the required repeating peaks (see Figure 48 a)) could not be identified. By plotting the BPM against its temporal course, the effects of the drug can be observed. The BPM rate reaches a maximum at about 45 BPM and returns to the basic contraction value of around 15 BPM after 90 seconds (see Figure 50 b)). However, it should be taken into account that the contraction of the spheroid without nutrient supply and temperature control will probably return to the baseline value faster than it would be the case under physiological conditions.

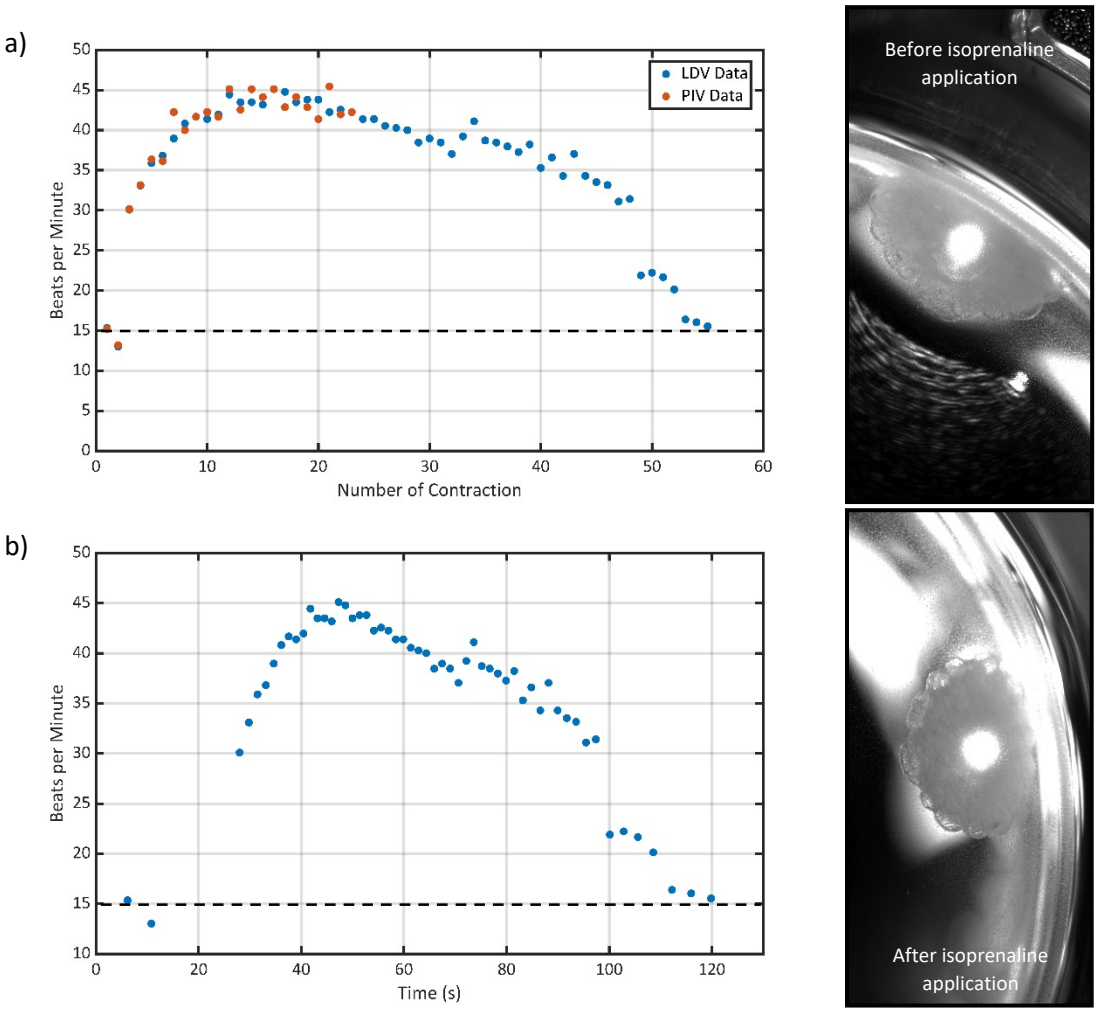

Figure 50 | Application of isoprenaline as a drug. a) *BPM values calculated from LDV and PIV data plotted against the number of contractions.* ***b)*** *Time-dependent effect of isoprenaline on BPM values calculated from the LDV data plotted against the time data. On the right side, the contraction observation window and data extraction region are shown. After the pipetting of the isoprenaline solution, the spheroid was shifted in its position (right images), and therefore the image position had to be relocated. Here, only LDV data is used for the calculation since PIV data could not be analyzed over the whole measurement time.*

6.6. Native cartilage tissue measurement

Tissues are an intricate composition between ECM and cells. Pathological processes change this composition and thus altering their mechanical properties, which LDV possibly could detect. The pathological process of osteoarthritis in cartilage tissue, the increasing disintegration of the cartilage layer, and its collagen network can be simulated using an enzymatic digestive system. To evaluate the application of LDV to such samples, a bovine cartilage plug was gradually digested enzymatically, and its mechanical properties were probed using indentation measurement. For the LDV measurement, a piezo was contacted from above on the cartilage surface, and in the immediate vicinity, several points were measured with the LDV device, which allowed the transmissibility to be calculated (see Figure 51).

It was not possible to measure the complete sample area since through the piezo stack, and the fixation clamp around a third of the sample was covered. Therefore, the input signal could only be measured on the cartilage itself and not from the tip of the indentation geometry, which would be the better input signal for calculating the transmissibility. Consequently, only measurement points on the cartilage and a section of the sample holder's rim have been placed (see Figure 51). After each measurement run, the sample was characterized in its elastic properties using the indentation tester and an indenter with the same geometry as it was used for the piezo. No loosening of the cartilage plug glued to the sample holder could be detected during the complete measurement. For further analysis, input and output locations were defined onto the cartilage, as shown in Figure 51, required for transmissibility calculation.

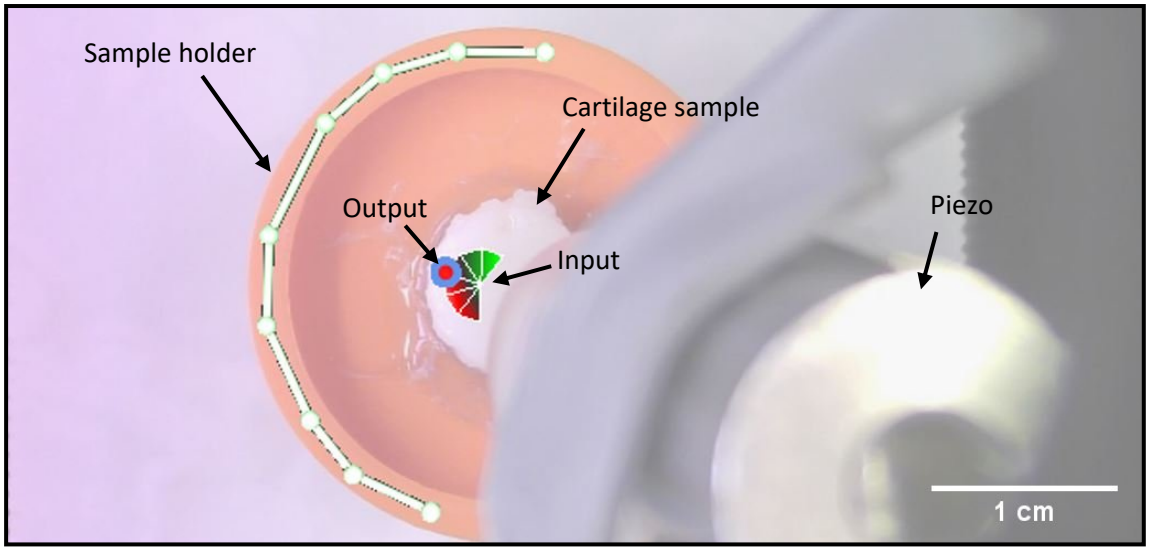

Figure 51 | Experimental setup. *The picture shows the view of the LDV device taken with the built-in camera. The piezo stack is contacted from above onto the cartilage surface, consequently covering around 40% of the sample surface, making a measurement of the complete sample and investigation of mode-shapes impossible. Thus, measurement grids could only be positioned partially on the sample holder (orange) and cartilage sample.*

Data taken from the cartilage shows a good signal quality, and dynamics can be recognized (see Figure 52). Following this result, the non-labeled cartilage surface can be analyzed using a 1550 nm LDV device. Despite the partially covered surface by the piezo stack, no mode shape could be identified in the data. Comparing the input and output signal (see Figure 52), certain differences can be detected, but mainly in the amplitude and not in a

shift of the resonance frequencies, indicating a potential change in the sample's Young's modulus. Calculation of the transmissibility (see Figure 52) nearly cancels out all resonance curves and suggests that no change of the structure's mechanical properties between the two measurement points occurred due to the enzymatic treatment. On the first look, the assumption of changed mechanical properties due to the collagenase treatment cannot be confirmed.

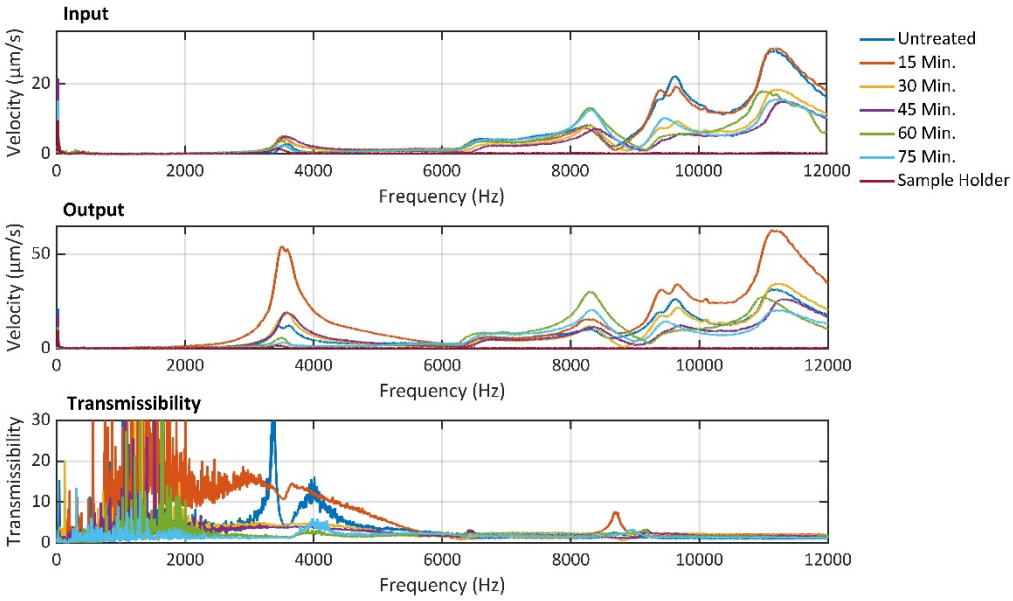

Figure 52 | Input and output signal and resulting transmissibility. *Input and output data show the same resonances located at the same frequencies but with different velocity amplitudes. This difference can be attributed to the different locations on the sample surface. Calculating the transmissibility (output signal / input signal) does not result in clearly identifiable resonance curves and, therefore, detectable changes among the different digestion times of the cartilage with collagenase enzyme.*

Among all the results, the amplitude of the resonance curve located at 8.23 kHz seems to be well suited for further analysis since this resonance can be identified for all samples. Therefore, the amplitude of the output signal is divided by the input, isolating the properties of the path between both of them. Plotting these against the treatment time, no significant change can be recognized (see Figure 53). The same accounts for the measured Young's modulus. The assumption of a change in the Young's modulus with increasing treatment time cannot be confirmed [205, 239]. Comparing both the LDV data and the indentation data, a slight similarity in the data can be observed, further suggesting no change in the cartilage's Young's modulus due to the enzymatic digestion.

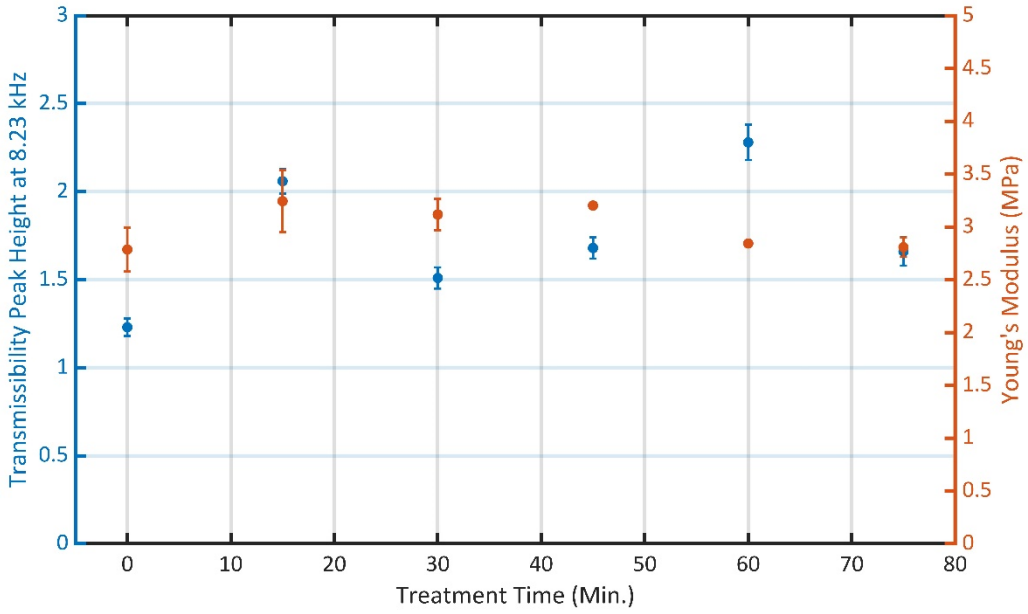

Figure 53 | Transmissibility of the peak height at 8.23 kHz and the measured Young's modulus. *Over digestion times up to 75 minutes, the Young's modulus of the cartilage sample was measured. Samples were treated with a 500 µg/ml collagenase. Results show no significant change in elastic properties with increasing treatment time. The same effect accounts for the peak height.*

A possible reason for the missing change in the measured values from the indentation measurement could be the lack of sensitivity to small stiffness changes. If this would be the case, changes in the force curve profiles should be observable. However, taking the average force-displacement curves (see Figure 54), no significant differences can be seen, and no systematic change of the curves due to the collagenase treatment occurs. For example, a change in only the uppermost layer would show a delayed rise of the curve since a softer material would generate fewer opposing forces due to the local compression of the indentation. Calculating the Young's modulus from different indentation depths underlines this finding and also shows no change in the Young's modulus among the different treatment times (see Supplementary Figure 6).

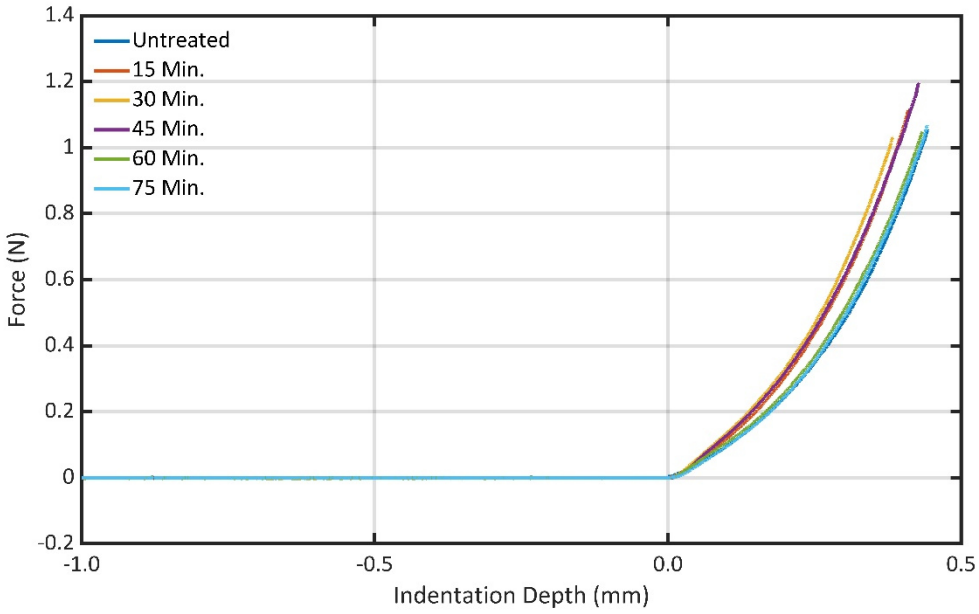

Figure 54 | Indentation curves taken after different treatment times. *Averaged force-displacement curves (n = 5) of the MACH-1™ indentation measurement for different collagenase treatment times. No significant differences between the single curves can be seen, suggesting no effect of the enzymatic digestion.*

6.7. Engineered tissue measurement

After the fabrication process, engineered tissue relies on further cultivation and maturation steps for achieving full functionality. During this maturation phase, the tissue will undergo changes in its morphology and mechanical properties (see Figure 55). Here, LDV could be a versatile tool for monitoring those properties and identifying whether the maturation process is still in progress, already finished or if something went wrong. All of these aspects need to be done without contact, non-destructive, and in a sterile environment. For this purpose, an engineered tissue construct has been manufactured using the in-house developed biomolding approach (see Chapter 5.8). Over the cultivation period, a change in morphology can be detected (see Figure 55), also suggesting a change in the tensional forces since a tearing off in thinner regions can be observed from time to time. To evaluate this potential application of LDV, a manufactured artificial tissue with a straight suspension (see Figure 55, lower left) was fabricated and placed in a specially designed measuring chamber (see Figure 56). The tissue can be measured with the LDV device through the transparent cover of the chamber, while the vibration excitation is realized from below using a piezo.

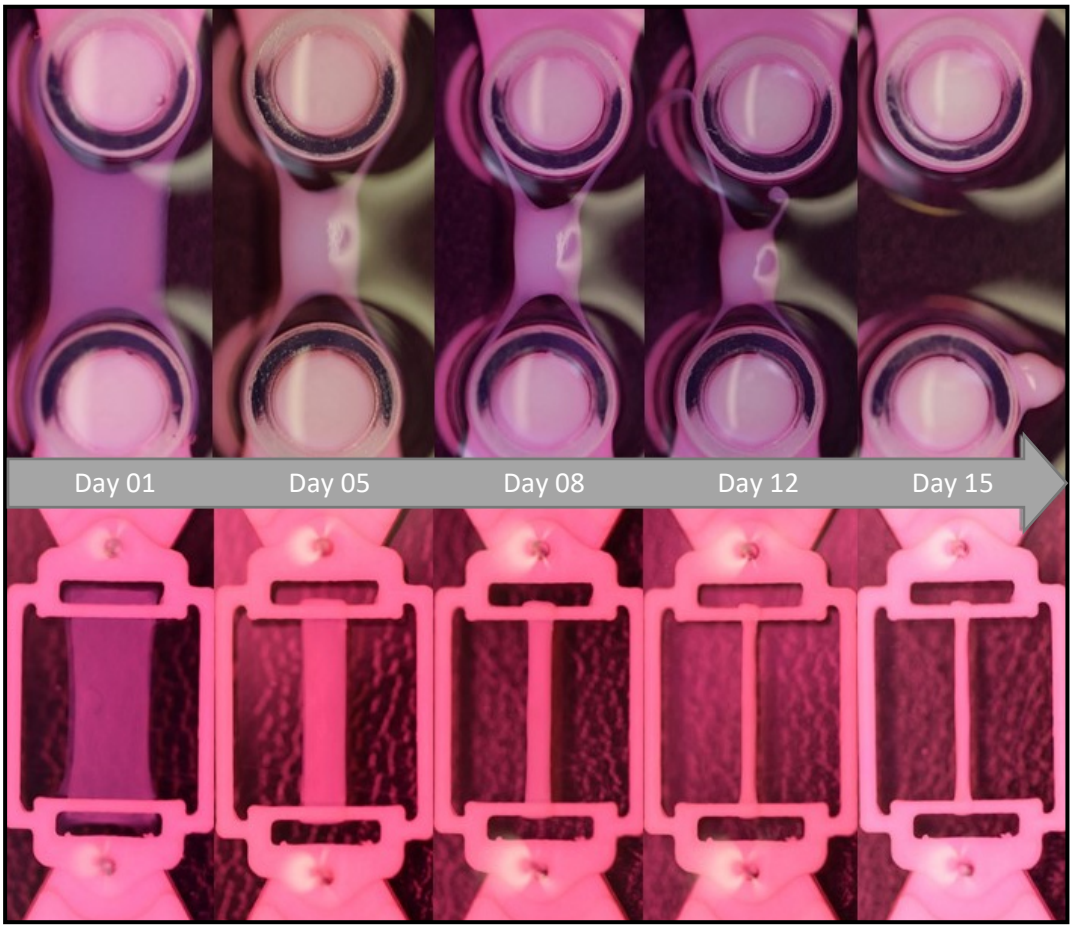

Figure 55 | Change of sheet morphology over multiple days of cultivation. *Engineered tissue constructs were fabricated using the self-developed biomolding approach. As a building material, collagen type I hydrogel with incorporated hMSC's was used. Depending on the fixation geometry, the sheet morphology changes over a longer period of cultivation. The construct shrinks towards its center, and outer areas get thinner and thinner for a round fixation geometry, eventually tearing off. A uniform shrinkage can be observed for a straight fixation geometry. Because of this shrinkage process, mainly caused by the embedded cells, the samples become denser, changing their mechanical properties.*

To prevent contamination and ensure physiological conditions during engineered tissue testing, an enclosure unit with a transparent measurement window was developed and built (see Figure 56). A silicon layer was placed under the cover for damping out possible undesired vibrations during testing since a vibrating cover would influence measurement results (see Figure 56 b), turquoise rectangles). After the experiments, the engineered tissue constructs could be further cultivated, demonstrating the feasibility of a sterile and non-destructive measurement.

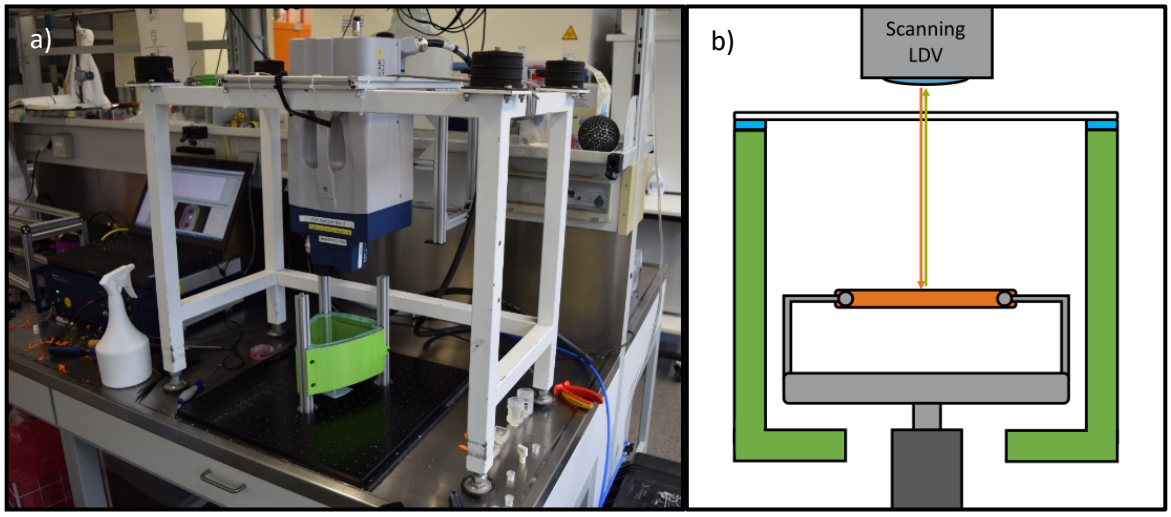

Figure 56 | Experimental setup and schematic view of the setup. a) *Using mounting support, the LDV device was positioned perpendicular over the sample in the measurement chamber.* ***b)*** *Engineered tissue (orange) positioned in the measurement chamber (green). On top of the chamber, a transparent cover (grey) is placed and decoupled from vibrations using a soft silicone layer (turquoise).*

Before measuring a sample in the measuring chamber, it was evaluated whether the chamber and its transparent cover are excited through the vibration introduced by the piezo. Thus, only the piezo and afterward the piezo in the chamber without and with a cover were investigated (see Figure 57 a) and b)). Excitation was realized using a periodic chirp signal ranging from 0 to 2.5 kHz (linear sweep with 1.56 Hz frequency resolution, 640 ms sweep time, 3906.25 Hz/s sweep speed). The resulting data reveals almost identical signals, indicating that the chamber and its cover do not alter dynamics measured from the tip of the piezo (see Figure 57 c)). Thus, a decoupling of the entire chamber from the excitation source can be assumed. However, around 20 Hz, a very high amplitude can be seen in the lower frequency range, resulting from the piezo's dynamics, and can be found in each measurement point.

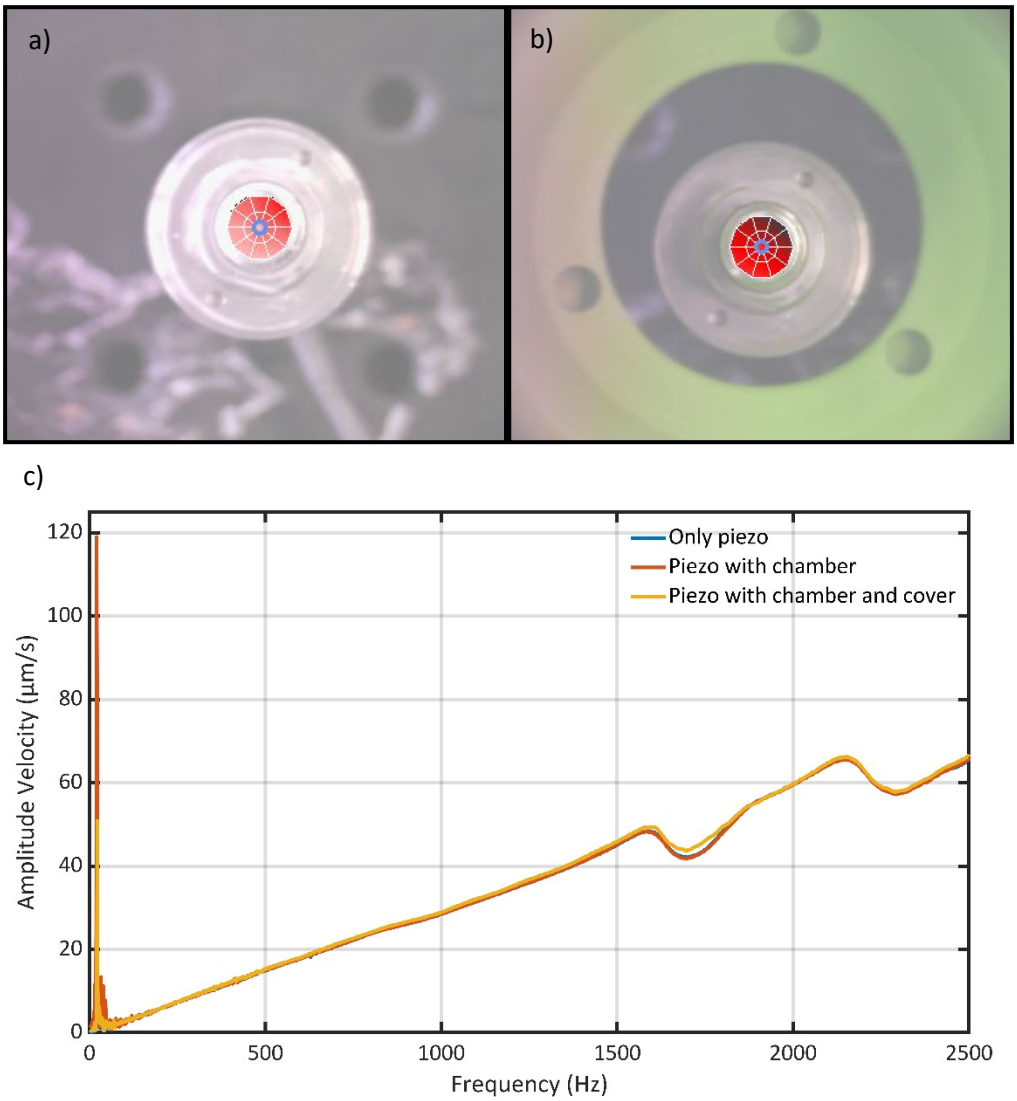

Figure 57 | Influence of the measurement chamber and its transparent cover. a) *Tip of the piezo measured outside of the chamber.* ***b)*** *Characterization of the piezo's dynamics in the chamber and through the transparent cover.* ***c)*** *A comparison of all acquired amplitude velocities shows no significant difference indicating no influence from the chamber and cover on measurement results. Peaks around 20 Hz occur due to the piezo's dynamics and can be observed in every data point.*

Using the LDV software interface, a measuring grid was defined on the sample, including the collagen type I sheet laden with hMSCs, the sample holder, and the magnets fixing the sample (see Figure 58). A periodic chirp sweep signal from 0 to 2.5 kHz (linear sweep with 1.56 Hz frequency resolution, 640 ms sweep time, 3906.25 Hz/s sweep speed) was used as an excitation signal generated by the built-in signal generator and amplified before it was sent to the piezo. The sheet was spanned between PLA beams and only supported on its lateral sides. Even though the sample was quite soft and fragile, sheet tension was sufficient to maintain structural integrity outside the culture medium. With this tension, a free-hanging setup can be realized, similar to the measurement with the gelatin disks in chapter 5.1.1.

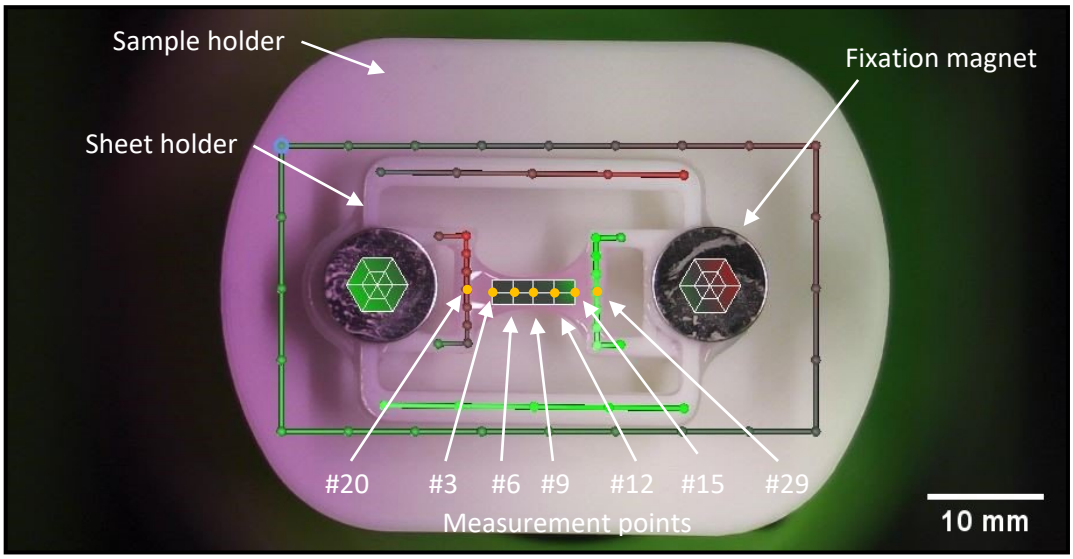

Figure 58 | Experimental setup for the LDV analysis of cell-laden collagen type I sheets. *The scanning feature of the LDV device enables the user to place a measurement point on each relevant structure. Stated are the numbers of the measured points of the scanning grid considered for further data analysis (orange points).*

In Figure 59, several resonances can be observed between 0 and 2.5 kHz. Due to its filigree geometry, the sheet holder itself vibrates significantly. In addition, the magnets for the fixation of the sheet and the sample holder itself do possess dynamics in the examined frequency range. Those dynamics are not surprising and were not eliminated by an experimental redesign since the experimental design was optimized for realizing the biomolding approach and not specifically for the vibration analysis. Evaluating the usability of LDV in the first step was done without changing the sheet holder's design. Analyzing the engineered tissue dynamics was done using the measurement points along the longitudinal middle-axis of the sample (see Figure 58, measurement points #20, #3, #6, #9, #12, #15, and #29). Both measurement points #20 and #29 can be seen as the position where the excitation energy enters the structure as input. The measurement point #9 in the middle of the sheet was used as the output signal for calculating the transmissibility. As shown in Figure 59 a), the two fixation points of the sheet (purple #29 and blue line #20) show the largest amplitudes. The higher frequency resonances, observable at the suspensions, are not present in the center of the collagen type I sheet. Looking only at the data from the middle of the sheet (see Figure 59 b), measurement point #9), the velocity amplitude from the input point at the resonance frequency of the support structure located at 992 Hz has decreased from 507.00 µm/s for the left fixation point #20 and 1636.90 µm/s for the right fixation point #29 down to 31.14 μm/s, which is only a fraction of the original velocity amplitude entering the engineered tissue. Looking into more detail at the lower frequency range of measurement point #9 reveals a resonance at 43.8 Hz (see Figure 59 c)). Taking the low-frequency resolution of 1.56 Hz into account, experiments should be redone with a higher frequency resolution and a smaller sweep range.

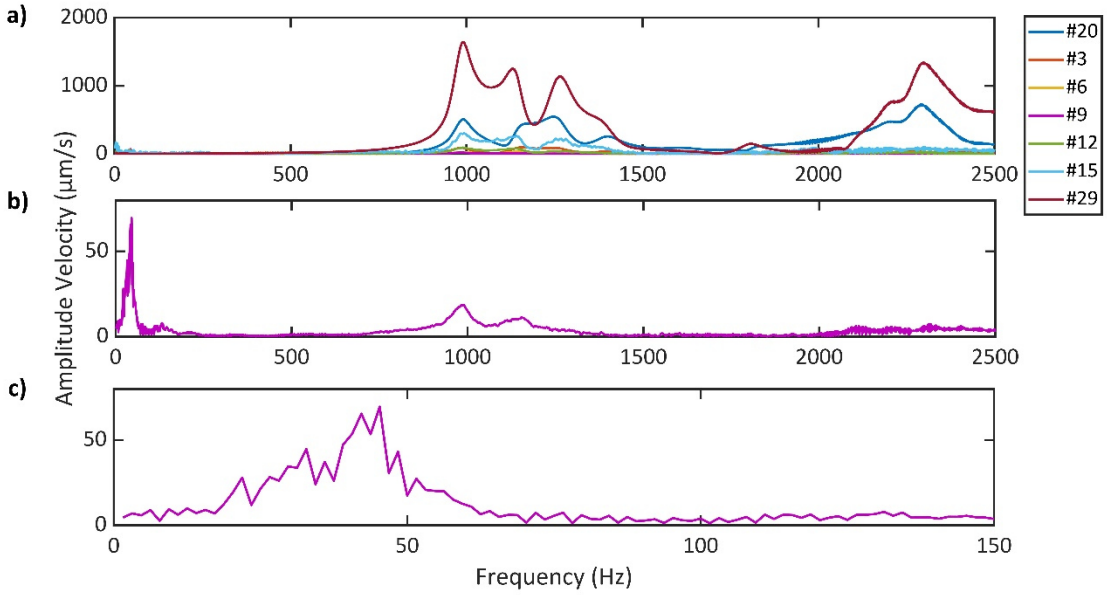

Figure 59 | The results for various data points measured alongside the sheet (a)) and the center location (b) and c)). a) *Amplitude velocity measured across the center of the sheet, from the fixation point to the fixation point. Amplitudes are becoming smaller the closer the measuring point is located to the center of the sample.* ***b)*** *In the overall measurements results shown in a), the obtained amplitude velocities of measurement point #9, the center of the sheet, can not be recognized. Only plotting results from measurement point #9 show the resonance around 1000 Hz but also reveals new dynamics in the lower frequency range.* ***c)*** *Zooming into the lower frequency range between 0 and 150 Hz shows a roughly recognizable resonance peak at 43.8 Hz, which can be attributed to the first mode shape of the engineered tissue sample, as shown at the top of Figure 60.*

A closer look at the lower frequency range (see Figure 59 b), purple line) reveals two peaks. The resonance at 43.8 Hz can be correlated to the first bending mode as a mode-shape (see Figure 60 a) and b)). This oscillation can be completely attributed to the sample since the surrounding sample holder structure does not possess significant dynamics at this low-frequency area. At 22.1 Hz, a second and rather hidden peak can be observed (see Figure 59 b)). Here the structure shows an uncoordinated amplitude distribution (see Figure 60), and this peak can also be observed in the characterization of the piezo shown in Figure 57 c).

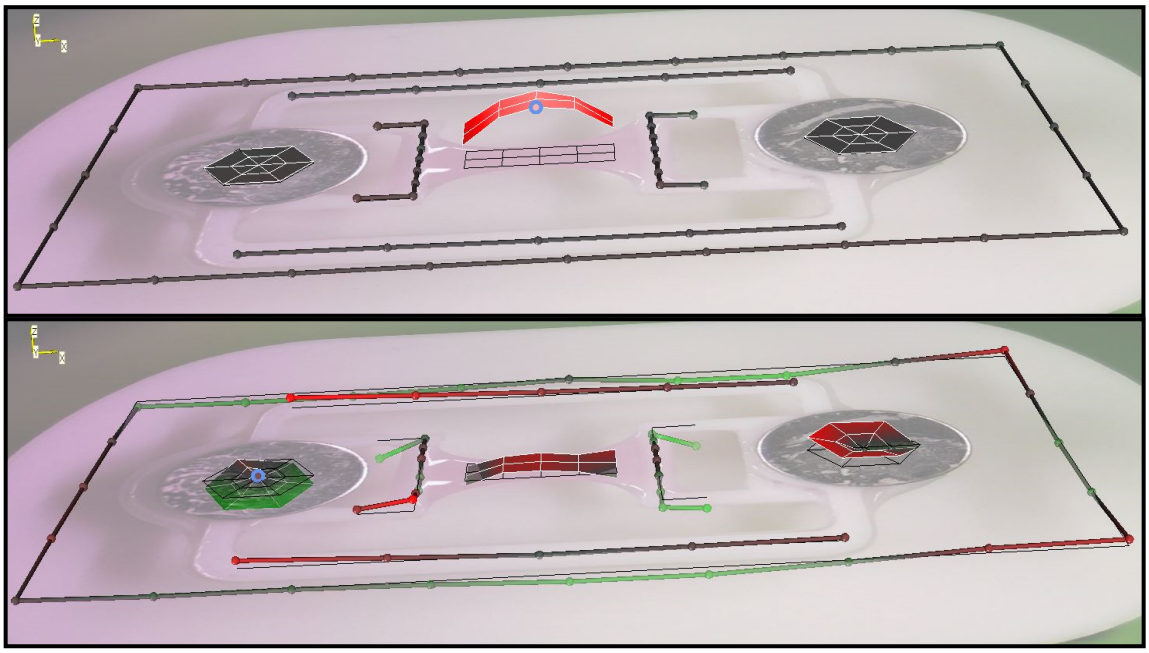

Figure 60 | Sheet motion at 43.8 Hz (top) and 22.1 Hz (bottom). Top: *At 43.8 Hz, the sample structure possesses its first resonance frequency, and a bending mode can be observed.* ***Bottom:*** *Around 20 Hz below the first resonance, some uncoordinated vibration patterns can be observed. This is possibly due to dynamics introduced by the piezo at the frequency of 22.1 Hz.*

In this experimental setup, the input energy enters the sample through two points, and the transmissibility can therefore be calculated for two transfer paths, one from the left and one from the right side (see Figure 61). In both transmissibility curves, resonances can be detected, but only the first resonance frequency around 44 Hz (43.75 Hz for the left side, 45.31 Hz for the right side) can be considered identical regarding frequency resolution of 1.56 Hz. Differences can be caused by various reasons, including geometrical variations and unequal mass distribution. For the transmissibility of the left side to the middle (point #20 to #9), a damping constant γ of 65.35 based on the FWHM and a damping ratio, ζ of 0.24 can be calculated. From the right side to the middle (point #29 to #9), a damping constant γ of 35.78 and a damping ratio ζ of 0.13 can be calculated. In this experiment, no mechanical testing could be done as it was done in the previous experiments since the sample is too fragile and sensitive. Here, LDV can have a great benefit by enabling a non-destructive sample analysis. Frequency data like resonance frequency and FWHM necessary for a later calculation of the Young's modulus using analytical models, as it was done in the gelatin disk experiment, can be measured. Since resonance frequencies and modal damping are both characteristics of the whole vibrating system, they should be equal for the left and right parts. Differences can be explained by looking first at the frequency resolution of 1.56 Hz, definitely too coarse for measuring at such a small frequency range of 150 Hz. Additionally, the rather high noise and filtering further affect the measurement results. Here, after a sweep for detecting the resonance frequency, the excitation frequency should have been adapted to this identified frequency range.

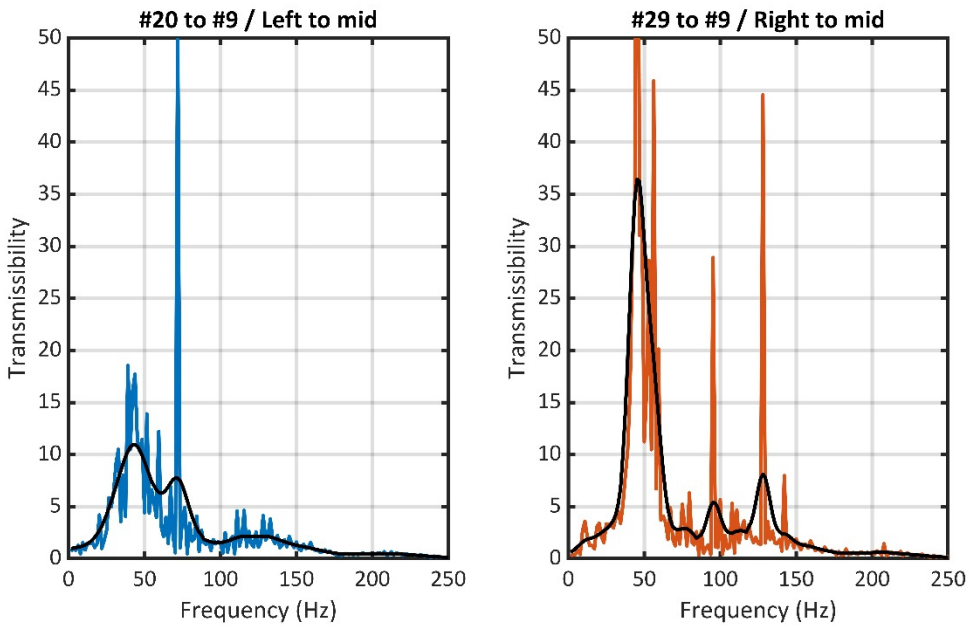

Figure 61 | Calculated transmissibility for the left and right energy transfer path. *In both signals, resonances can be observed, but only the one located around 44 Hz is present in both signals and can be attributed to the mode-shape shown in figure 60 a). The solid black lines represent the smoothed transmissibility using a Gaussian filter with a smoothing factor of 0.55.*

7

Discussion

Label-free LDV measurements of hydrogels:
Elastic properties of hydrogels can be characterized contactless and label-free.

Vibrational analysis of hydrogels can be challenging since these gels are often too fragile for using contact-based force or accelerations sensors. Optical methods like LDV can bypass this problem. However, due to the transparency and low reflectivity of most hydrogels, only a small percentage of the laser signal is reflected from the sample surface. Transmitted laser signal can be reflected at the backside of the sample or from surfaces behind the sample and superimpose with the relevant signal originating from the surface of interest.

In the past, this problem has been solved by increasing the signal reflected from the hydrogel by applying reflective particles and adhesive tapes to the hydrogel surface [16, 35] or by incorporating reflective structures inside the transparent samples [36, 37]. This exploratory study aimed to investigate the feasibility of label-free LDV measurements of transparent hydrogels and evaluate if their mechanical properties can be deduced from obtained LDV frequency data. An alternative approach to keep the signal to background ratio of LDV measurements of hydrogels in an acceptable range is to keep potential background signals as low as possible. This can be done using an infrared laser, like the 1550 nm laser used in this thesis. At this wavelength, the optical extinction coefficient κ of water is more than three orders of magnitude larger than at 633 nm of the commonly used helium-neon lasers ($9.86 \cdot 10^{-05}$ at 1550 nm, compared to $1.66 \cdot 10^{-08}$ at 633 nm [32]). This difference in the extinction coefficients leads to an absorption coefficient α, which is almost four orders of magnitude larger at 1550 nm than at 650 nm ($2.02 \cdot 10^{-08}$ at 1550 nm, compared to $8.13 \cdot 10^{-12}$ at 650 nm [30]). Additionally, the NIR-LDV device can operate with a higher power since it is still eye-safe at the wavelength of 1550 nm (8.92 mW) compared to the 633 nm helium-neon laser (<1 mW), consequently increasing the amount of reflected laser signal.

Testing the transmitted laser signal for different sample heights (see Figure 27), only a small fraction of applied laser energy passes the sample at a thickness of 3 mm. This thickness has proven to be optimal regarding the sample preparation process. For samples thinner than 3 mm, a detachment of the hydrogel from the sample holder's rim occurred. With increasing sample thickness, amplitudes and thus the measured output is reduced, making the investigation of sample dynamics more challenging.

The high signal-to-noise ratio (see Figure 30) and characterized mode shapes (see Supplementary Figure 1) suggest that the obtained measurement data originates from the sample's surface. As a homogenous material without incorporated particles, only scattering and no reflection of the applied laser energy are expected inside the gelatin material. The scattered fraction of the laser energy is too low for really being considered as a problem regarding interference with the reflected signal from the front surface of the sample. The next position where the signal could be reflected is the sample's backside at the interface between gelatin and air. Here, total internal reflection could be possible at the right angle since the light comes from the denser media. However, the signal reflected at this point must pass the sample twice, reducing the originally applied laser energy of 8.92 mW to 1.20 μW. The intensity of laser light reflected from the backside or behind the sample is therefore 7433 times lower than the signal originating from the sample surface, too low for dominating the recorded signal. It can be assumed that these measurement results are originating from the sample's surface. Note that the refractive index of water, determining the amount of light being reflected at the air-water interface, changes only marginally from 1.331 to 1.318 when changing the laser wavelength from 650 nm to 1550 nm. Consequently, the absorption properties of the tested material are crucial for a successful measurement

Based on the optical properties of the gelatin samples for an LDV laser wavelength of 1550 nm, it can be assumed that the measured frequency data actually originates from the sample surface. To investigate whether it is possible to characterize the elastic properties of the gelatin hydrogels, not only qualitatively but also to derive the respective Young's moduli from the LDV data, the obtained resonance spectra were first correlated with the Young's moduli obtained through IT-AFM measurements. Comparison between the square root of the Young's moduli and frequencies of the (0,1) mode shows a linear correlation (see Figure 33), as predicted for the (0,1) mode of a homogenous circular clamped disk by suitable analytical models (see Equation (18) and (19)) [179, 240].

Following the good qualitative agreement between the experimental data and elastic theory, in a second step, the possibility to quantitatively deduce the Young's modulus values from the LDV spectra was investigated. Calculating the Young's moduli based on the (0,1) mode frequencies with a thin disk elastic model (see Equation (18) to (21)) [179, 240] renders Young's moduli comparable to the IT-AFM data (see Figure 35, yellow and blue dots). However, the thin disk model is a good approximation only as long as the disk's aspect ratio (height/radius) remains much smaller than 0.1 [221]. For the aspect ratio of the gelatin disk used in the LDV experiment (height/radius = 3 mm/4.85 mm = 0.62), the thin disk approximation is no longer valid, and the shear effects across the thickness during bending have to be taken into account. When adapting the model to a thick disk, which can be accomplished by choosing an aspect ratio dependent prefactor (see Equation (22)) [221], the calculated Young's moduli increase and do fit better the data obtained from the unconfined compression testing (see Figure 35, green and red dots), rather than the IT-AFM data. Similarly, the Young's moduli calculated by modeling the vibrating gelatin disk with FEM agree much better with the Young's moduli obtained by unconfined compression testing (see Figure 35, orange dots) than with the IT-AFM data. Still, we have to note that this allows us not to directly link the applied elastic theories and the experimentally determined Young's moduli. Due to quasi-static testing and assuming linear elasticity for extracting the Young's modulus from the force-displacement curves during data analysis, the real material properties may not have been revealed, and more studies going deeper

into material property modeling are required to investigate further the trend indicated by the data shown in Figure 35.

Looking at the IT-AFM and unconfined compression testing results, the differences are quite reasonable: it is well known that biological materials, such as gelatin hydrogels, show non-linear elasticity with considerable strain stiffening [241-246]. Following this effect, small strains only stretch the curved fibrils between two cross-link points in the polymer network, probing the entropic elasticity. Further increasing the strain stretches the stiff polymer backbones of single filaments and therefore probes the enthalpic elasticity resulting in higher Young's moduli being measured. Nature developed this concept of semi-flexible filaments to prevent the damaging of biological materials when large deformations occur and still being soft at small strains and deformations. IT-AFM only probes a small area onto the sample as a surface-sensitive method, keeping the strains small and rendering smaller Young's moduli than methods, which compress the entire sample by several percent probing the bulk elastic modulus such as unconfined compression testing. FEM analysis and the model for a thick disk consider and account for deformations of the complete hydrogel structure. It should be noted that a strain stiffening effect can also be observed in the non-linear stress-strain curves of unconfined compression testing (see Figure 35 and Supplementary Figure 3). However, the Young's modulus values shown in Figure 35 were extracted at strain values between 10 and 15%, where the curves become nearly linear. Taken together, using either the thick disc analytical model or FEM analysis, the Young's moduli of the gelatin samples can be derived with good quantitative agreement from the (0,1) frequencies determined by LDV. The observed deviations between Young's moduli determined by LDV and theoretical modeling and unconfined compression testing are most likely caused by the variation in the sample thickness, which is difficult to determine exactly and enters the equations with the third power. Still, we have to consider that we use frequency data to calculate the elastic properties, more or less representing a dynamic Young's modulus, and compare it with a Young's modulus determined in a quasi-static manner. In the future, frequency-based mechanical testing methods such as DMA should also be taken into account when correlating LDV data with mechanical testing results.

In addition to their elastic properties, hydrogels frequently also show visco-elastic behavior. To also extract information about the hydrogel viscosity from the LDV data, the damping ratio ζ, which is directly proportional to the viscosity of a viscous fluid, can be used. The results presented in Supplementary Figure 2 show an exponential increase of the damping constant γ with increasing polymer concentration, which is in accordance with literature observations [227-229]. Because the viscosity of our samples was not directly determined, only a qualitative comparison with literature data can be made, and no quantitative viscosity values can be derived from the LDV data.

The experimental design for the direct mechanical characterization of hydrogel samples using LDV presented here can measure both the elastic and viscous properties of the hydrogel samples. The elastic parameters were compared to two different mechanical testing methods. A quantitative conclusion can be drawn using numerical and analytical models for calculating the elastic properties based on the measured frequency data, which agrees well with the experimental data, but this link needs to be investigated in more detail in future studies. Although viscosities of gelatin samples were not quantitatively determined in this study, the comparison with the literature shows that this should also be possible. This aspect should be further investigated in future experiments. This setup allows a comprehensive mechanical characterization of hydrogels using the LDV method label-free

without altering the mechanical properties due to possible coatings or markers. However, the elaborate sample preparation of the free-hanging samples renders this method only partly suitable for direct integration into existing biofabrication processes where continuous inline monitoring of the mechanical properties is mandatory.

Probing the mechanical hydrogel properties using a bi-clamped beam and LDV:
Qualitative characterization of the elastic hydrogel properties can be done using probing structures whose dynamics are measured by LDV.

Instead of directly measuring the surface of the transparent hydrogel sample and being dependent on its optical properties, a 3D-printed bi-clamped beam structure was used in this approach for probing mechanical sample properties. One advantage of this experimental design is the direct pouring of the liquid hydrogel sample onto the bi-clamped beam cantilever. The sample material can then solidify either through fibrillogenesis, cross-linking, or cooling. The beam dynamics changes because of the added hydrogel material and this change can be detected by focusing the LDV laser on its back surface. This setup eliminates the reflectivity and focusing problem when measuring transparent hydrogels since the beam's material, e.g., through surface metallization, can be adapted to the applied LDV laser wavelength. Furthermore, soft samples, which are too fragile for maintaining a free-hanging setup, can be measured. Compared to the clamped circular disk, this approach can be integrated into existing biofabrication processes.

Because of the additional mass added to the sample on top of the beam, one would expect an initial decrease in the resonance frequency (see Equation (6)) compared to the empty beam and an increase of the resonance frequency with rising Young's modulus of the hydrogel, due to the increased bending modulus (see Equation (19)). This assumption corroborates with the gelatin disk measurement results (see Chapter 6.2), showing an increase in the FWHM of the resonance curves and a shift of the resonances towards higher frequencies (see Figure 31). Results from the gelatin disk experiment do suggest an increase in damping and thus in the viscous properties of the material, which is also consistent with the literature [227-229]. In addition, the results of the FEM analysis (see Figure 43) allow for such a conclusion. However, these assumptions only apply for a permanent and fixed physical contact between the beam and the hydrogel sample, preventing the sliding of the two surfaces against each other. This seems not to be the case since the experimental results do not show a significant shift of the resonance frequency and FWHM between different hydrogel samples with varying polymer concentrations (see Figure 39), leading to the conclusion that the beam has no permanent physical fixed contact with the hydrogel, especially in plane. One explanation for the poor adhesion between the cantilever beam and the sample could be a thin water film between them, allowing the two materials to slide against each other. This means that the bending stiffness D of the cantilever would not be affected by the changing Young's moduli of the gelatin samples. Therefore, no change in the resonance frequencies and modal parameters could be expected. This hypothesis should be further investigated by conducting a suitable FEM study with a sliding contact between the beam and sample.

The only parameter that clearly and systematically changes for the different samples is the amplitude at the resonance frequency at 16.4 kHz (see Figure 39 and Supplementary Figure 4). The displacement amplitude of the unladen beam outside its resonances is only between

43 pm and 150 pm, increasing to 1.42 nm at 16.4 kHz. The displacement amplitude of the surrounding sample holder (see Figure 38, green points) lies between 50 pm and 70 pm outside of its resonances. This increased displacement amplitude of the cantilever leads probably to an interaction between the top of the beam and the bottom of the hydrogel in vertical direction, which can be observed looking at the decreasing amplitude at 16.4 kHz with increasing Young's modulus. The beam has to deform the hydrogel and experiences more resistance as the sample's Young's modulus increases, and thus, its amplitude is reduced (see Figure 40 and Supplementary Figure 4). Reducing the stiffness of the cantilever would make its dynamics less dominant compared to the hydrogel sample and more sensitive to the sample's elastic properties. Thus, the vibration of the beam can better be modulated by the mechanical properties of the sample placed on it. This is relevant for the concept of probing the mechanical properties of hydrogel samples through a cantilever, as proposed in this work.

In summary, no complete mechanical characterization of the hydrogel, comparable to the gelatin disk experiments, could be achieved with the bi-clamped beam probing structure. Nevertheless, the oscillation and velocity amplitudes of the resonance located at 16.2 kHz exhibit a clear negative correlation with the gelatin concentration, with a correlation factor of -0.82 for the velocity amplitude and the gelatin concentration. The positive correlation between gelatin concentration and Young's modulus depicted in Figure 41 implies a negative correlation between the velocity amplitude and the Young's modulus of the samples. It can therefore be assumed that the elastic modulus can be deduced from the measured amplitude. This experimental setup allows for the direct pouring of the sample into the testing geometry while still being viscous and thus allows for the investigation of a broad range of biological materials. Furthermore, the cantilever structure can be adapted and miniaturized according to the process in which it should be integrated, similar to what IBM™ demonstrated with its millipede approach [187].

Measurement of single mammalian cells:
Single cells being submersed in culture media cannot be characterized in their dynamics with a 532 nm LDV setup used in this thesis.

Besides the characterization of hydrogels as possible building materials for the fabrication of engineered tissue, the investigation of living cells as the essential tissue component is of great interest. Their mechanical properties can provide information about their developmental stage and if a pathological progression is present. Current state-of-the-art cell culture is predominantly done in Petri dishes as a 2D culture. The challenge for the LDV measurement of such adherent cells is the analysis of microscopic structures submersed in a culture medium. For this reason, an LDV integrated into a microscope (λ = 532 nm) combined with a water-immersion objective has been used for this experimental setup. Using a water immersion objective allows measuring directly in the culture medium. A sound transducer mounted on the microscope stage was used for excitation. The FRF transmissibility was calculated between a measurement point on the non-overgrown Petri dish bottom and the apical cell surface.

In an adherent 2D-culture, the cells spread mainly in-plane and assume a flat morphology. This makes the finding of a proper focus value for such a transparent sample challenging. Furthermore, it is more likely that the signal reflected from behind the sample is

superimposing with the signal originating from the cell's surface and alters or even dominates the results. Calculating the relative amount of laser intensity R_1 reflected from the cell's surface and R_2 reflected from the Petri dish renders a 23 fold higher reflectivity at the polystyrene Petri dish surface than at the cell surface:

$$R_1 = \left|\frac{n_1 - n_2}{n_1 + n_2}\right|^2 = 0.00034 \mid 0.034\% \qquad (27)$$

$$R_2 = \left|\frac{n_1 - n_3}{n_1 + n_3}\right|^2 = 0.00792 \mid 0.792\% \qquad (28)$$

Refractive index water / culture media: $n_1 = 1.33$ [32]

Refractive index cell[5]: $n_2 = 1.38$ [247]

Refractive index polystyrene: $n_3 = 1.59$ [248]

Comparing R_1 and R_2 clearly shows, the main part of the reflected signal originates from the Petri dish right below the measured cell area. With the setup presented here, the dynamics of living mammalian cells could not be studied. Using a confocal setup or enhancing the reflectivity of the cell surface could improve the results. This will be further discussed in the recommendations chapter (see Chapter 9). A further aspect of those measurements is whether the dynamics of such thin samples are distinguishable compared to the growth substrate.

Contraction analysis of contracting cardiomyocyte spheroids:
Contractions and changes due to drug-induced effects can be investigated if spheroids are partly exposed to air.

Spontaneous contraction of cardiomyocytes can be detected as displacement amplitude using an LDV device. The previous experiment with murine fibroblasts showed no characterization of the cells was possible using an LDV wavelength of 532 nm. Consequently, the setup with a wavelength of 1550 nm is used, which was already successfully tested in the gelatin disk experiments. Because water strongly absorbs light at this wavelength, cell spheroids with a diameter of around 900 μm were used and partly exposed to air, enabling surface movement detection.

The results recorded on the contracting cardiomyocyte spheroids show a high signal-to-noise ratio, and contraction events can be determined in nearly all experiments (see Figure 47, Figure 48, and Supplementary Figure 7). Despite the lack of culture medium and thus reducing the contraction rate and amplitude over time, all spheroids survived the LDV

[5] 1.34 near the membrane of the cell and 1.38 near cell nucleus [219]

measurement and could be further cultivated afterward. Monolayers of cardiomyocytes could not be characterized by LDV, probably due to the thin layer of culture medium left on the cell layer. However, small elevations resulting from cell clusters within the cell monolayer were large enough to allow for a successful LDV measurement (see Figure 47 b), orange dashed circle). This is probably due to the fact that the thin water film on this cell cluster is not present or thinner. Because the cardiomyocytes usually synchronize their contraction in such a dense culture, the contraction activity of these clusters can be considered representative of the whole culture [249, 250]. The reaction of the cells to the application of drugs, such as isoprenaline, could also be successfully analyzed (see Figure 50). In addition to the maximum BPM rate induced by the drug, also the duration of the drug influence on the spheroids could be determined (see Figure 50 a) and b)). It should be noted that in these experiments, the changes in contraction frequency and amplitude must partly be attributed to exhaustion of the cells caused by the lack of nutrient supply and physiological conditions. Eliminating this exhaustion effect from measurement data is an important aspect to be addressed in future experiments.

A more detailed look into the PIV analysis of the contracting cardiomyocyte monolayer and the signal-to-noise ratio of the PIV data reveals that the recorded image sequences are sometimes not perfectly suited for the PIV algorithm. The available speckle pattern is often insufficient, and the PIV algorithm cannot follow and analyze the contraction movement. The main reason for this is the thickness of the cellular aggregates and, due to their high cellular density, only a little light can pass the sample. This can be confirmed by comparing results from spheroid (see Figure 48) and monolayer (see Figure 47) measurements. In the area of the pilot laser spot, which was used to determine the measurement location of the NIR LDV laser, only white pixels can be identified, and therefore, the PIV algorithm cannot detect any movement within this spot. For future experiments, the pilot laser should be dimmed down or completely turned off during the measurement, even when the information of the exact measurement location is lost. Here, the problem of poor speckle patterns due to overexposure was solved by shifting the PIV analysis window until the results had sufficient quality for further data analysis and BPM value calculation. Nevertheless, this data analysis procedure is quite time-consuming compared to the LDV because it requires several runs of the PIV algorithm before a result with sufficient quality is obtained. In comparison, data acquisition and processing are much faster and more robust with LDV. Additionally, the LDV device measures the relevant parameter, i.e., displacement amplitude of the cell surface in the vertical direction, while the PIV algorithm determines the lateral velocity by a complex image analysis algorithm from an image sequence. Thus, the PIV analysis results could be more susceptible to errors due to this additional analysis step, but this has not been proven or further investigated in this study.

During the measurements, a clear shift of the spheroids along the rim of the well on the remaining thin water film was observed. This can be prevented in future experiments by fixing the spheroids in suitable fixing geometries and will be further discussed in the recommendations chapter 9.

Despite the lack of physiological conditions and air contact during the measurement, the contraction activity could be analyzed for nearly all samples. Comparing the results of the PIV and LDV analysis, the advantages of the LDV method become apparent. The high sensitivity and the direct measurement of the out-of-plane movement from the sample surface make the LDV method independent of sample illumination conditions. For small spheroids and thin engineered tissues, a sufficient amount of light can pass the sample, but

in the future, such fabricated tissue constructs will get thicker for reaching a relevant size compared to the target organ, resulting in less light being transmitted, consequently reducing the contrast of the speckle pattern. However, the spheroid's partial exposure to air is a significant drawback and does not allow extended measurement times or measurements under truly physiological conditions. This diminishes the viability and usability of the living samples. However, despite the encouraging results obtained on cell spheroids, with the approaches followed here, the LDV method is not suitable for the mechanical characterization of single cells completely submersed in culture media. For contracting and larger cell systems, such as cardiomyocyte spheroids, the contraction can be characterized using a NIR LDV device when the samples are partly exposed to air. However, one cell monolayer is too small, and the chosen approach works best with spheroids. As an optical microscopy-based method, PIV depends on the right illumination conditions but can be performed with most existing microscope setups in laboratories without purchasing additional devices and allowing for the measurement under physiological conditions.

Experiments on native cartilage tissue:
Surface dynamics of bovine cartilage plugs can be investigated using a NIR-LDV device.

As already discussed, for mammalian cells, a change in the mechanical properties of natural or engineered tissues is one of the key markers for their proper functionality. This is particularly the case with tissues of the musculoskeletal system such as cartilage [128, 251-254]. Like the complete cartilage, also its uppermost superficial layer mainly consists of collagen fibers, proteoglycans, and hyaluronic acid, creating a composite material capable of absorbing mechanical loads and forces [255]. In diseases such as osteoarthritis, there is a gradual degradation of both proteoglycans and collagen, leading to a disintegration of the cartilage layer, resulting in altered mechanical properties. This thesis evaluated whether this effect and changes in the mechanical properties can be detected with LDV. A cylindrical bovine cartilage plug was used as a sample, and the disease progression was simulated by enzymatic digestion of the collagen fibers. In the previously described experiments, it could already be shown that vibration analysis works best for freely suspended samples such as the gelatin disk described in chapter 6.2. However, such an experimental setup cannot be realized for the cartilage plugs, and therefore, the vibrational excitation was realized locally with a piezo probe contacting the cartilage surface. Multiple LDV measurement positions have been selected near this contact point, and finally, the transmissibility between the two positions was calculated. This was done for the initially undigested, native cartilage and after enzymatic digestion with different treatment times. In addition, the elastic properties of the sample have been determined using indentation measurement for the native sample and the different treatment times in order to correlate the LDV results with the elastic parameters.

Based on the high-signal-to-noise ratio of the LDV data, it can be assumed that the LDV signal originates from the sample surface and that the excitation amplitude was sufficient (see Figure 52). Nevertheless, the dynamics introduced by the piezo and the indentation geometry could not directly be measured since the LDV device was positioned above the sample, and the piezo itself conceals the contact point. This renders the extraction of the sample's inherent dynamics and mechanical properties impossible, and it is unclear whether resonances originate from the piezo with the indenter or from the sample. With the methods

used in this study, indentation testing and LDV, no influences of the collagenase treatment could be detected. It is unclear and was not checked if the used enzyme still was functional, which should have been evaluated before the experiment. At the same time, it becomes apparent how challenging experiments with biological samples can be. Possibly, not only the area of interest, the small cartilage layer, but also the complete bone beneath it, are excited by the piezo, consequently contributing to the measured oscillations. If the bone is not altered in its mechanical properties due to the enzymatic digestion but dominates the vibration, then no change in the system's response can be expected. To verify if and how the bone layer is excited and involved in the measured vibration response of the cartilage, its dynamics should be measured too.

Future experiments must change the design and scan the whole sample surface during a measurement, allowing for the analysis of the mode shapes, helping to identify the resonance frequencies. Instead of contacting the piezo from above, it could be contacted laterally in a horizontal orientation not covering the cartilage surface. Although in these experiments, no clearly assignable dynamics caused by mechanical properties of the superficial cartilage layer could be measured, and consequently, no change of these mechanical properties could be observed, nevertheless, they show that the oscillation of the cartilage surface can be measured label-free with a 1550 nm LDV laser wavelength. However, if only the surface is significantly altered by the digestion and not the whole sample, it can be quite difficult to spot the change by a global measurement such as transmissibility or vibration modes. Looking at the wave propagation at the sample surface could be a more promising approach [33, 34, 159-161]. In order to make a reliable statement about the mechanical tissue properties based on the measured frequency data, the enzymatic digestion and the indentation measurement should have worked properly. Here, further control experiments are missing and need to be included in future experiments.

Experiments on engineered tissue:
The first mode of a freely suspended rectangular-shaped engineered tissue can be determined when the sample is exposed to air.

In addition to measuring the mechanical properties of native tissue, the investigation of engineered tissues with LDV was investigated. These tissues must first mature into a fully functional tissue equivalent by various maturation steps after their fabrication. During this phase, growth and reformation processes lead to a change of the mechanical properties, which can be detected using LDV. In the initial experiment, the engineered tissue was used directly after the biomolding process, i.e., a thin sheet fixed on a support geometry. To ensure a sterile environment, the measurement was performed in a chamber with a transparent cover. Using the scanning feature of the LDV device, it was first examined whether the vibration of the tissue could be analyzed at all and whether parameters such as resonance frequencies and damping constant could be deduced from the obtained frequency data.

During the measurement, the construct was not damaged at all, and due to the magnetic fixation, it was possible to remove the engineered tissue out of the measuring chamber back into cultivation damage-free. During subsequent cultivation and maturation of the tissue, no contamination could be observed. This is a prerequisite regarding future experiments

involving living tissue fabricated by a cost and time-intensive process. Around 20 Hz, a noise peak can be observed, which is also present in the measurement of the hydrogel disks (see Figure 35), could originate either from the HiFi amplifier used for amplification of the excitation signal, from the piezo actuator, or like in the cardiomyocyte experiment, from a nearby fan. In these experiments, no fan or similar device was present in the experimental setup or its vicinity. A closer look into the differences between data generated by the LDV signal generator and its amplification showed no disturbance around 20 Hz. Therefore, this effect must be attributed to the piezo actuator.

Following the LDV data, the first resonance frequency and its mode shape can be determined. Within the resolution limit of 1.56 Hz, the same resonance frequency could be measured on both the left and right fixation points. Like the experiments with the hydrogel disk, the sample is also fixed in a way so it can oscillate without restrictions. Still, these resonance frequencies have been identified using a sweep excitation and should have been remeasured after the sweep using a single frequency excitation to gain more insight into the sample's dynamics. Identical to the gelatin disk experiments, here also resonance frequencies and damping ratios could be determined. Nevertheless, the damping constants γ and the damping ratios ζ from the left and right sides differ by a factor of two, possibly originating from the noise, data-smoothing, and thin water film, further affecting measurement results. This thin water film on the sample surface, which already could be observed during the measurement, cannot completely be removed since this would affect the viability of cells due to humidity loss but is also a non-negligible factor due to the high absorbance of water at the used laser wavelength of 1550 nm.

Regarding the stiffness of the fibrillated 4 mg/ml collagen hydrogel used for the engineered tissue fabrication, different values can be found in literature ranging from 60 Pa to 300 Pa, as it was found here, seems reasonable [256-258]. Nevertheless, this only allows to roughly estimate the mechanical properties of the collagen hydrogel at the beginning of maturation and growth processes and not after a longer period of cultivation. Because the exact geometries of the sheets are difficult to determine, it was not possible to directly derive the elastic parameters from the acquired LDV data using elastic theory or FEM modeling, as was the case for the gelatin disks described in chapter 6.2.

Geometry and fixation of the tissue sheets used in the LDV experiments have been optimized for the biomolding method, and the LDV method can be readily integrated into the biofabrication workflow. As a result, the filigree sheet holder possesses many own resonances, and thanks to the transmissibility calculation, the engineered tissue's inherent dynamics could be isolated. As in the experiments with the cardiomyocyte spheroids, the short exposure of the engineered tissue to air is not optimal and does not pose a major problem. Using this experimental setup, the vibrations of engineered tissue constructs could be measured using a NIR-LDV laser wavelength device. However, at the current status, the mechanical parameters of the tissue constructs could not be directly derived from the LDV data. This is because the exact geometry of the tissue sheets is not known, and the mechanical properties have not yet been tested with an established mechanical testing method and for several constructs with different cultivation times. Again, the advantages of the LDV method, such as contactless and non-destructive data acquisition and its flexibility, proved to be highly beneficial in these experiments. In this study, only one construct was investigated using NIR-SLDV directly after its fabrication. Experiments with multiple engineered tissues at different cultivation time steps were not feasible due to time limitations.

8

Conclusion

Can LDV be used for the label-free and contactless mechanical characterization of biological materials? This question can be answered with yes. The presented results show that LDV can be used to characterize hydrogels, living cells, engineered, and native tissues to a certain extent. Nevertheless, the LDV method does not outperform the already established methods, like IT-AFM, indentation, and unconfined compression testing. The advantages of the LDV method are the high sensitivity and the capability of fast, contactless measurements. However, all biomaterials used in this study could only be measured when being exposed to air. Consequently, physiological conditions cannot be guaranteed during the characterization of living samples, and this aspect has to be investigated closer in the future.

The elastic and viscous properties of gelatin samples could be determined, and for a well-defined disk geometry, the elastic parameters could be deduced from the LDV spectra. This is a significant advantage for biological materials, which often have viscoelastic material properties due to their high water content. Furthermore, already established contact-based methods do pose the risk of harming these often-fragile samples during testing. A comparison between the experimental LDV data and the results of established test methods like IT-AFM and unconfined compression testing was performed successfully and laid the foundation for further studies. For the indirect measurements of gelatin samples using a bi-clamped beam structure, it could be shown that the beam dynamics are modulated by the material properties of the sample. However, when determining the cantilever's first resonance frequency, there was no frequency shift, as expected, but instead a reduced velocity amplitude at the resonance frequency with increasing Young's modulus of the sample could be observed. This is possibly due to a water layer or slippage between the top of the beam and the bottom of the gel. Therefore, only in the vertical direction, an interaction is present, not because of adhesion but due to contact when the beam locally compresses the hydrogel during its resonance. Consequently, the vibration amplitude is decreased at this resonance frequency regarding the increasing Young's modulus of the gelatin sample due to the higher compression resistance. Numerical modal analysis for a permanently fixed contact between the two layers predicts a change in resonance frequency and FWHM of the beam's dynamics with changing sample material properties. The hypothesis assuming a non-fixed contact between the beam and sample should be further investigated with a suitable FEM model in the next step.

Adherent living cells growing as a monolayer on a Petri dish surface could not be analyzed due to the poor reflectivity of the cell membrane at the used LDV laser wavelength of 532 nm. However, contracting cell aggregates, here cardiomyocyte spheroids, could be measured successfully using a 1550 nm LDV laser when they were partially emerged from the culture medium. Detecting their response to the application of isoprenaline was possible with LDV and an increase in the contraction activity was observed. With the experimental setup presented here for characterizing native tissue, a bovine cartilage sample could be excited via a piezo, and the response to this excitation could be measured with the LDV device. However, practically no difference between excitation and response signal could be observed, which could be an indicator that the modification of the mechanical properties by enzymatic digestion was not successful since no significant change could be detected after the treatment, both with LDV and with indentation testing. Still, the experiment should be redone with a more sensitive measurement method such as IT-AFM to evaluate the effect of the enzymatic digestion. For engineered tissue, the first resonance of a three-dimensional, cell-laden collagen type I construct could be successfully determined. The measurement was realized through a transparent, sterile enclosure without affecting or altering the results.

Taken together, the experiments conducted in this exploratory study clearly show that LDV can be used in the field of TE. It is not only possible to investigate individual tissue components such as hydrogels and cells but also more complex, living structures like engineered tissues. Similar to the experiments shown in this study, future tests will still require a contact-based test method to correlate vibration data with the mechanical parameters. However, through the systematic creation of a database, a calibration of the experimental LDV can be realized, gradually reducing the need for the mechanical, contact-based test method.

Take-home messages[6]:

Building materials: *In a free-hanging setup gelatin hydrogels can be characterized and their mechanical parameters can be deduced from obtained frequency data without labeling. This approach can now be extended to other hydrogels and soft materials.*

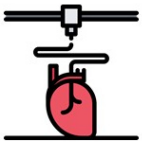

Fabrication processes: *The presented concept enables the monitoring of mechanical material properties during processes like bioprinting via cantilever geometries. In the current setup, the Young's modulus can only be analyzed qualitatively and not quantitatively from the measured frequency data.*

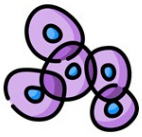

Living cells: *A monolayer of cells is too small for investigating them with a NIR-LDV device (1550 nm) and poor reflectivity at the wavelength of 532 nm makes measurements challenging despite the structures were analyzed using a microscopic LDV setup. Other wavelengths have not been investigated yet.*

Cardiomyocyte spheroids: *Due to their increased size compared to single cells or a cell monolayer, cellular aggregates can be measured using a NIR-LDV device when they are partially exposed to air. Furthermore, their contraction activity and the effect of drugs modulating the contraction activity can be analyzed. Compared to the PIV method, this approach is more robust and allows investigating comparatively thick samples, but does currently not enable a measurement under complete physiological conditions.*

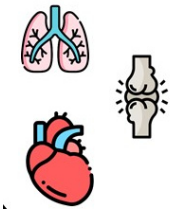

Native tissue: *With the measurement surface exposed to air, the superficial layer of a cartilage plug can be analyzed in its dynamics using a NIR-LDV device, but no conclusions can be made about the mechanical properties. Often native tissues represent a complex, anisotropic composition of different biomaterials, making the investigation of specific areas challenging.*

Engineered tissue: *Initial tests proved the feasibility of characterizing engineered tissues and their vibrational parameters like first resonance frequency and damping ratio, using LDV. Also here a NIR-LDV device was used and the sample was exposed to air during the experiment.*

[6] The single pictures have been taken from the image database *flaticon* [86].

9

Future research directions

Still, to be addressed, open issues in the experimental designs can be identified following the results of this exploratory study. Regarding the direction of future research, those open issues should be addressed and further investigated to reveal the currently unknown of this research topic: the application of LDV for the mechanical characterization of biological materials.

Hydrogel experiments have shown that LDV can characterize the mechanical properties of gelatin disks. This approach can now be extended not only to other hydrogels relevant for TE and biofabrication but also to hydrogels used in the food industry and other applications such as the production of contact lenses and wound dressings. The concept of using a climate chamber for the measurement of engineered tissue should also be applied to the measurements of hydrogels in order to minimize evaporation effects. Through inlets and outlets in the developed chamber (see Figure 56), air with suitable humidity and temperature and CO2 can be supplied from the outside, ensuring a stable, cell-friendly environment. This allows for extending the measurement time, frequency and reproducibility, and could even enable continuous measurements or time-lapse experiments during tissue maturation.

For the indirect measurement of hydrogels via a probing geometry, such as the bi-clamped beam, the setup should be miniaturized. This would allow for multiple such structures to be installed in the same area and used in parallel. Such miniaturization of the setup could be achieved, for example, by using silicon microfabrication technology. In doing so, entire arrays of cantilevers could be produced in parallel, comparable to IBM's millipede technology in the 90s [187, 259, 260]. Already using silicon microfabrication technologies, the LDV device is not necessarily required since data readout can be realized by using a micro-electro-mechanical approach, but LDV measurements in an aqueous environment could be realized. After such a size reduction, direct process integration could be evaluated. Here, bioprinting could be a suitable first application (see Figure 9).

Trying to characterize **adherent living mammalian cells** was challenging, and only the Petri dish bottom dynamics have been measured. One approach for improving the measurement of cells could be to integrate the LDV device into a confocal microscope setup, restricting the detection volume to the size of the point spread function of the microscope objective. Such a setup would eliminate signals from outside the focal plane, such as the Petri dish's surface below the apical cell membrane [261-263].

It should also be noted that although the LDV measurements of single cells were not successful, reflection interference contrast microscopy uses comparable wavelengths near 532 nm to determine the distance between a cell membrane and a glass substrate based on light reflected from the cell membrane [247, 264, 265]. These findings further underline the proposal to redo the measurements on single cells using an LDV device integrated into a confocal microscope.

The cardiomyocyte spheroid experiment results reveal the influence of pharmaceuticals applied on the spheroid's surface and could be promising for future scientific applications. Nevertheless, throughout the experiments, a slight shift of the spheroid's position can be observed. Such a slipping must be restricted without influencing the spheroid's contraction movement. By integrating microscopic wells or rings for spheroid positioning and fixation, slipping would be prevented, especially during the water level changing or the addition of substances.

During the measurements of the spheroids, exhaustion of cells was observed caused by the lack of nutrient supply and non-physiological conditions. This cellular reaction must be kept minimal in future experiments, affecting the cell reaction to any added medication. External vibration sources possibly exciting the spheroid, as it was observed in this study with the cooler fan, must be avoided to further increase the signal-to-noise ratio. In addition to the previously mentioned fixation for the spheroids, automated control of the fluid level should be integrated to minimize the time when an insufficient nutrient supply is present. This would also contribute to the automation of the entire setup enabling higher measurement rates and future high-throughput experiments.

With the 1550 nm LDV setup, **native cartilage tissue** could be analyzed at its surface with good signal quality. However, the piezo not only excited the superficial cartilage layer of interest, but also the entire sample, including the stiffer bone material below the cartilage layer. Exciting a defined area or point at the sample surface could be realized using focused ultra-sound [266, 267]. Furthermore, the photoacoustic effect could be useful in future experiments, to avoid this problem, since it can be used to locally excite a well-defined small area of the cartilage. Studies have already shown a good usability of the photoacoustic effect for non-invasive in-vivo imaging and tumor tissue analysis in mice and humans [166, 167]. Both photoacoustic effect and LDV are laser-based technologies and can also be applied via optical fibers. This makes this whole approach capable of being integrated into an arthroscopic setup, enabling minimally invasive measurement in patients, such as in the joint gap of the knee.

Engineered tissue has been successfully analyzed using a NIR-LDV device, and as described in the methods section, the modular design of the measuring chamber for engineered tissues allows for the connection to an incubation unit. This can provide a controlled environment inside the chamber. Under such physiological conditions, including temperature, pH value, O_2, and CO_2 concentration, measurements could be conducted over a longer period without the risk of reduced cell viability. If engineered tissue constructs are cultivated over multiple days, a change in their morphology can be observed (see Figure 61). This is a well-known effect when working with hMSCs embedded in collagen type I [196-199]. The constructs shrink perpendicular to the fixation and become denser and denser, as it was observed in own experiments (see Figure 55) and in the literature [197-199, 268], leading to the assumption that their mechanical properties change over the time of cultivation and that this change could be measured using the LDV method. Especially here, LDV is a reasonable alternative to already established mechanical testing methods for testing soft samples. LDV

tests on engineered tissue have shown that this material can be analyzed with LDV if the investigated surface is exposed to air during the measurement. In such a case, it was also possible to measure the contractions of cardiomyocyte clusters and spheroids. Both systems survived this short exposure to air and could be further cultivated after the experiments. A future experiment could examine the already investigated sheet geometry, but this time not loaded with hMSCs, but with contracting cardiomyocytes. In such a setup, the contraction of the cells could be investigated and monitored in parallel. With such an experimental design, the extensive testing of new drugs in a 3D environment would be possible. Testing the engineered tissue showed that a global excitation strategy like it was used in this experimental design can be quite problematic since all structures are excited and not only the region of interest. Therefore, more sophisticated techniques using the radiation force of focused ultrasound can also be realized [267].

In summary, it was quite unclear before this study if the suggested approaches could successfully be realized with LDV at all. After initial ideas have been evaluated and the first experimental setups have been realized, more complex ideas and applications can be investigated in future experiments.

In natural sciences and especially in biological sciences, standardization, decoupling, and abstraction are the three basic engineering principles for gaining a better understanding of biological systems and the development of new applications [269]. In the future, biofabrication will emerge towards a new industry, and for realizing this goal, especially the standardization of fabricated tissue equivalents needs to be ensured. Upcoming applications will be animal-free meat fabrication, in vitro 3D tissue models of human diseases, drug toxicity, and drug discovery assays, as well as eventually the development of human tissues and organs for implantation [270, 271][73,259][73, 272-274]. Without the standardization of such future products, no trust in their benefit will be created, consequently reducing innovation acceptance. Additionaly, after standardization of such fabrication processes, personalization towards each patient's requirement needs to be tackled. The author can envision a future scenario in which LDV is used as a non-destructive, contactless, and non-intrusive monitoring method in intelligent automated tissue fabrication processes which are guided and performed by collaborative robots in combination with artificial intelligence. LDV can and potentially will become a characterization tool enabling standardization and further innovation in this field, helping to speed and scale up the research and development as well as the manufacturing of tissue equivalents reaching clinically relevant sizes.

10

Appendices

10.1. Experimental materials

A

AFM silicon nitride cantilever, MLCT cantilever E, Bruker, Mannheim, Germany

B

Bioprinting slicing software, Simplify 3D™, version 4.1.2, Simplify 3D, Cincinnati Ohio, USA

C

CAD Software, SolidWorks™ Version 2018 – 2019, Dassault Systèmes, Vélizy-Villacoublay, France

Close-up unit for SLDV, PSV-A-410, Polytec GmbH, Waldbronn, Germany

Collagen type I G1 solution, 5 mg/ml stock solution, Matrix Biosciences GmbH, Mörlenbach, Germany

Collagenase type II, 17101015, lot-activity: 250.00 units/mg, Thermo Fisher Scientific Inc., Massachusetts, USA

COMSOL Multiphysics FEM software, version 4.3b, COMSOL AB, Stockholm, Sweden

Curing station Formlabs CURE, Formlabs, Sommerville, Massachusetts, USA

D

DMEM, Dulbecco's Modified Eagle Medium, F0445, Biochrom, Berlin, Germany

E

Electrodynamic exciter EX 30 S 8 Ohm, 4532, Visaton GmbH & Co.KG, Haan, Germany

F

FCS, fetal calf serum, S0115, Biochrom GmbH, Berlin, Germany

Form 2 3D printer (SLA), Formlabs, Sommerville, Massachusetts, USA

Framegrabber card, AS-FBD-1xCLD-2PE8, Active Silicon, Iver Heath, United Kingdom

G

Gelatin, 4308.1, Carl Roth GmbH & Co. KG, Karlsruhe, Germany

GlutaMax, 5050-038, Gibco/Thermo Fisher Scientific, Waltham, USA

H

HEPES buffer solution, Sigma Aldrich / Merck KGaA, Darmstadt, Germany

HiFi-Amplifier, AV-235IS, electronic Toys Trading GmbH, Braunschweig, Germany

High-temperature *Volcano* PLA, 2.85 mm diameter, Formfutura, Nijmegen, Netherlands

Hystoacryl tissue glue. 938104, B. Braun Melsungen AG, Melsungen, Germany

J

JPK Data Processing software, version 6.1.42, JPK Instruments AG, Berlin, Germany

M

MatLab™, version R2020b, The Mathworks Inc., Natick, Massachusetts, USA

Mechanical tester MACH-1 v500cs, MA003, Biomomentum Inc., Laval, Canada

μ-Manager camera software, version 1.4.22 [216, 217]

Micro-System-Analyzer MSA 600 vibrometer, Polytec GmbH, Waldbronn, Germany

Microscope camera, ORCA-Flash 4.0, C11440, Hamamatsu Photonics GmbH, Herrsching am Ammersee, Germany

Microscope system Zeiss Axio Observer Z1, Carl Zeiss AG, Jena, Germany

Multiple-axis load cell (70 N), MA235, Biomomentum Inc., Laval, Canada

N

Nano Wizard I AFM, JPK Instruments AG, Berlin, Germany

Neodymium magnets, 3 mm in diameter and 1.5 mm in height, SM-03x1.5-N, magnets4you GmbH, Lohr am Main, Germany

Non-essential amino acids, 11140050, Gibco, Life Technologies, Carlsbad, California, USA

P

Parafilm™, IDL GmbH & Co. KG, Nidderau, Germany

Phosphate-buffered-saline, PBS, Dulbecco's PBS, Biochrom GmbH, Berlin, Germany

Penicillin/Streptomycin, A2212, Biochrom, Berlin, Germany

Petri dish, TC dish 60 standard, Sarstedt, Nümbrecht, Germany

Pluronic™ F127 powder, Sigma Aldrich / Merck KGaA, Darmstadt, Germany

Polylactide FDM printing filament, 2.85 mm diameter, Ultrafuse, BASF, Ludwigshafen am Rhein, Germany

Printing nozzles for printing the casting molds, standard nozzle orange, inner diameter 0.33 mm, Vieweg GmbH, Kranzberg, Germany

S

Scanning Laser-Doppler vibrometer, PSV-500, Polytec GmbH, Waldbronn, Germany

Silicone MoldStar™, Smooth-On, Macungie, Pennsylvania, USA

Sorbothane dampening sheet, Thorlabs GmbH, Bergkirchen, Germany

Stacked-Piezo system, P844.10, Physik Instrumente, Karlsruhe, Germany

T

Thermopile Sensor PS10, Coherent Inc., Santa Clara, California, USA

Transparent printing resin for SLA, clear resin v4, Formlabs, Sommerville, Massachusetts, USA

Trypsin/Ethylenediaminetetraacetic solution (0.25%/0.02% weight/volume), Biochrom GmbH, Berlin Germany

U

Ultimaker 2+™ 3D printer (FDM), Geldermalsen, Netherlands

Ultimaker 3™ 3D printer (FDM), Geldermalsen, Netherlands

W

Washing station Formlabs Form wash, Formlabs, Sommerville, Massachusetts, USA

Water immersion lens (25 x magnification), 420852-9871, Carl Zeiss AG, Jena, Germany

10.2. Supplementary Information

Supplementary Table 1 | Resonance frequencies, damping constants, and measured Young's moduli of the gelatin disks. *Experimentally determined frequencies of the (0,1)-mode of the different samples, together with the damping constants, damping ratios, and the corresponding Young's moduli.*

Gelatin concentration (g/ml)	1st resonance frequency (Hz)	Damping constant γ (Hz)	Damping ratio ζ	Young's modulus AFM (kPa)	Young's modulus confined compression (kPa)
0.100	144	30	0.033	2.06	8.70
0.150	197	56	0.045	7.55	22.63
0.200	223	70	0.050	12.79	34.76
0.250	291	112	0.061	22.40	59.80
0.300	323	128	0.063	26.13	118.69
0.350	359	171	0.076	34.88	91.51
0.400	486	275	0.090	33.95	168.76

Supplementary Table 2 | Theoretical modeling data. *Gelatin density used for theoretical modeling, and Young's moduli derived from LDV data using an elastic model for a thin and thick disk and FEM analysis.*

Gelatin concentration (g/ml)	Gelatin density ρ (kg/m^3)	Young's modulus thin disk model (kPa)	Young's modulus thick disk model (kPa)	Young's modulus FEM (kPa)
0.10	1005	4.40	12.63	14.75
0.15	1017	8.35	23.98	28.02
0.20	1028	10.87	31.22	36.48
0.25	1040	18.63	53.51	62.52
0.30	1051	23.32	66.98	78.27
0.35	1063	29.18	83.82	97.95
0.40	1074	54.01	155.63	181.31

***Supplementary Table 3** | Experimental results of the cantilever-assisted hydrogel measurement presented in chapter 6.3.*

Concentration (g/ml)	**Resonance frequency (Hz)**	**FWHM (sqr-FRF) (Hz)**	**Damping constant γ**	**Damping ratio ζ**	**Young's modulus (kPa)**	**Peak Displacement (pm)**
Empty	15861.00	456.70	1434.77	0.0143	N/A	1422
0.10	15829.00	339.14	1065.44	0.0107	5.48	569
0.15	15804.00	345.42	1085.17	0.0109	13.27	428
0.20	15804.00	339.27	1065.85	0.0107	27.23	390
0.25	15791.00	377.76	1186.77	0.0119	47.62	439
0.30	15804.00	364.09	1143.82	0.0115	60.49	424
0.35	15804.00	371.01	1165.56	0.0117	80.60	409
0.40	15753.00	412.75	1296.69	0.0131	68.23	306
0.45	15776.00	378.39	1188.75	0.0120	93.93	348
0.50	15739.00	376.30	1182.18	0.0120	125.35	229

***Supplementary Table 4** | Calculated BPM values.*

	LDV	**PIV**
Organoid without Cover	30.46 ±5.80 (n=29)	30.46 ±5.80 (n=29)
Organoid with Cover	14.79 ±0.85 (n=11)	14.66 ±0.38 (n=14)
Application of Isoprenaline	41.11 ±3.90 (n=24)	41.26 ±3.96 (n=24)
Cell Layer	N/A	14.9 ±2.66 (n=13)
Blob in Cell Layer	9.19 ±3.35 (n=6)	9.24 ±3.39 (n=6)

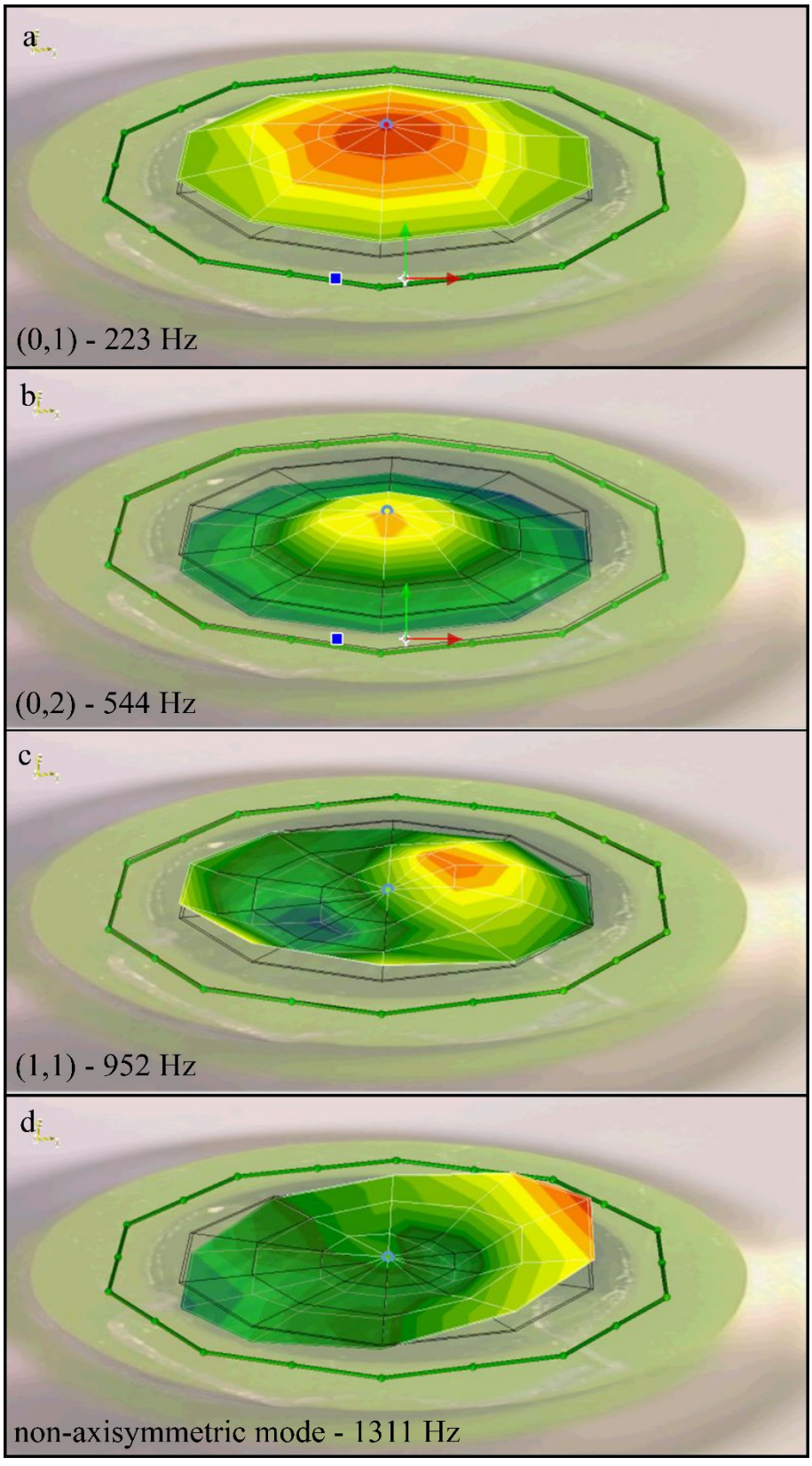

Supplementary Figure 1 | Mode shapes of a gelatin disk. *Mode shapes associated with the first four resonance frequencies of the 0.20 g/ml gelatin sample shown in Figure 30, blue line.*

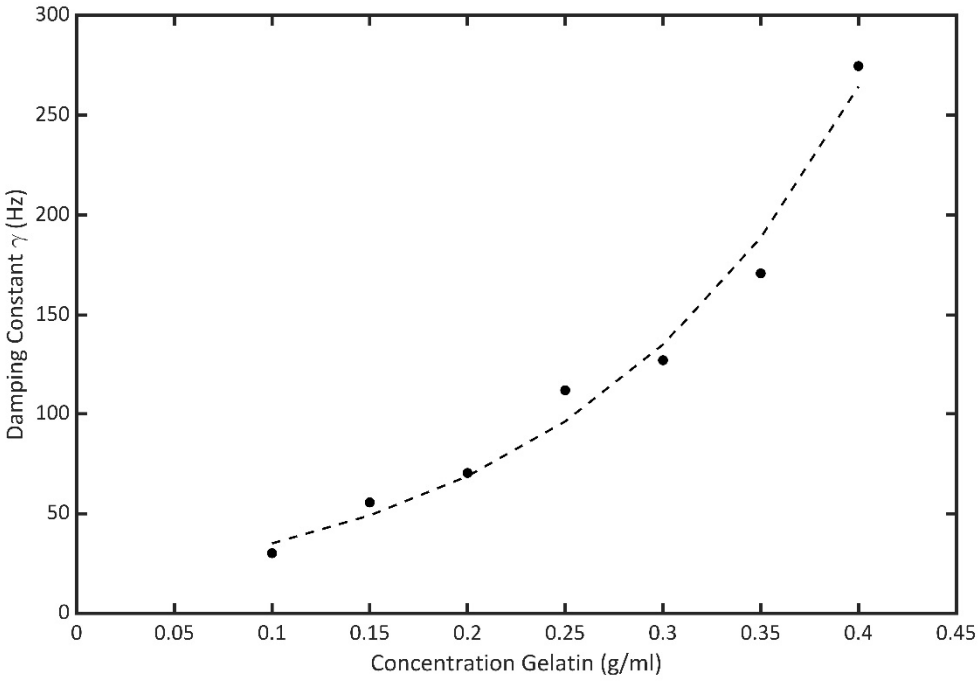

Supplementary Figure 2 | Damping constant γ for different gelatin concentrations. *With an increasing polymer concentration, an exponential increase of the damping constant* ***γ*** *can be observed.*

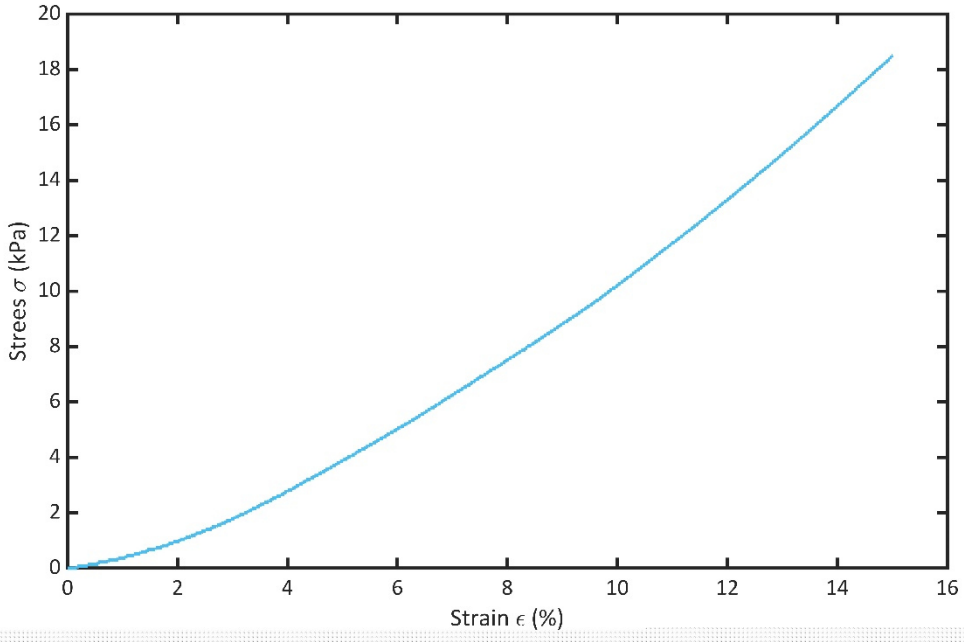

Supplementary Figure 3 | Exemplary stress-strain curve for a 0.40 g/ml gelatin hydrogel obtained with the unconfined compression testing. *Here, the compressing speed was set to 139 µm/s (10 µm/s for IT-AFM measurement), resulting in a strain rate of 2.3 %/s.*

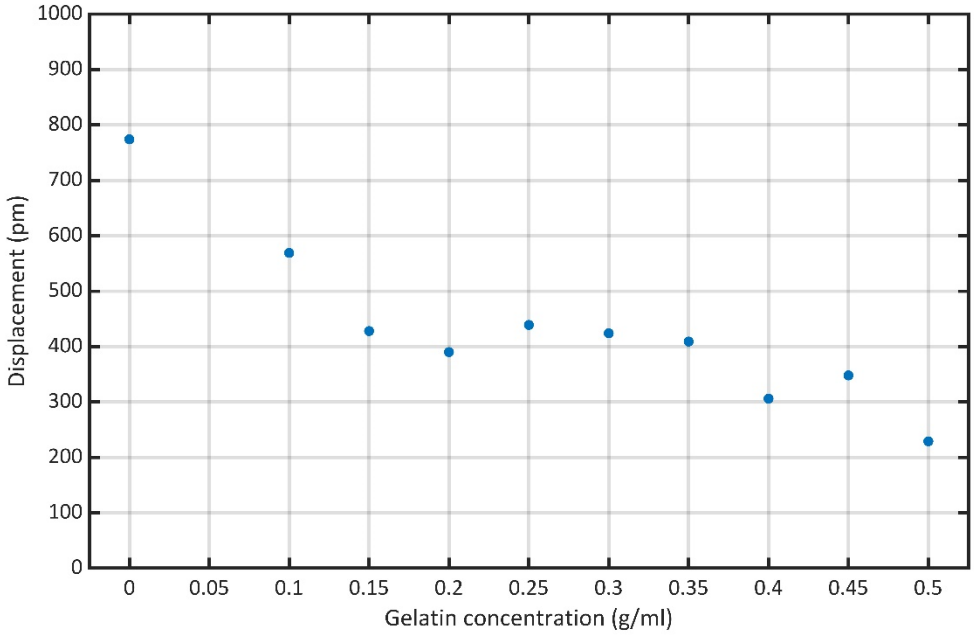

Supplementary Figure 4 | Displacement amplitude for the mid of the beam geometry at the frequency of 16.4 kHz.

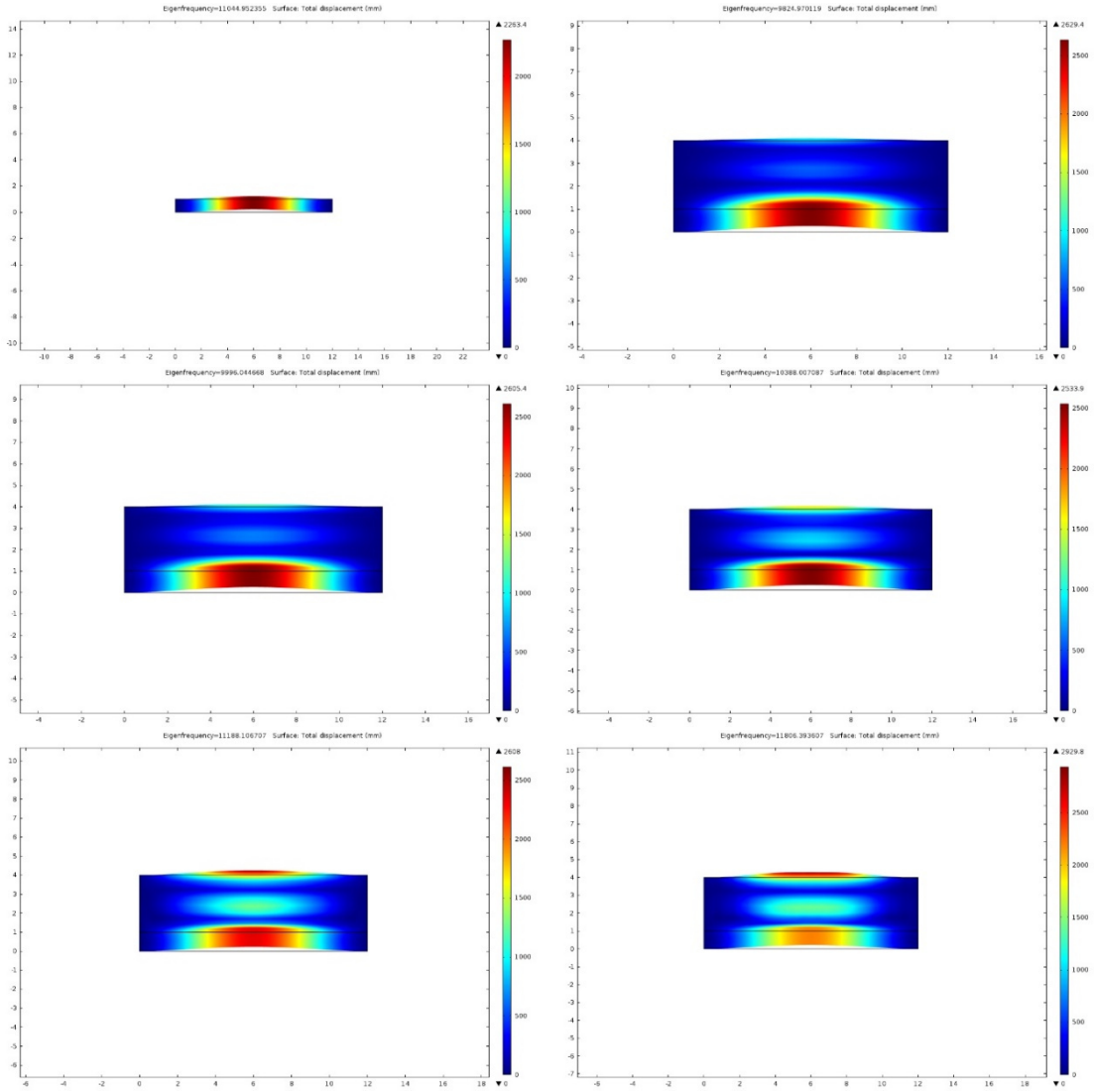
Eigenfrequency=11044.952355 Surface: Total displacement (mm)
Eigenfrequency=9824.970119 Surface: Total displacement (mm)
Eigenfrequency=9996.044668 Surface: Total displacement (mm)
Eigenfrequency=10388.007087 Surface: Total displacement (mm)
Eigenfrequency=11188.106707 Surface: Total displacement (mm)
Eigenfrequency=11806.393607 Surface: Total displacement (mm)

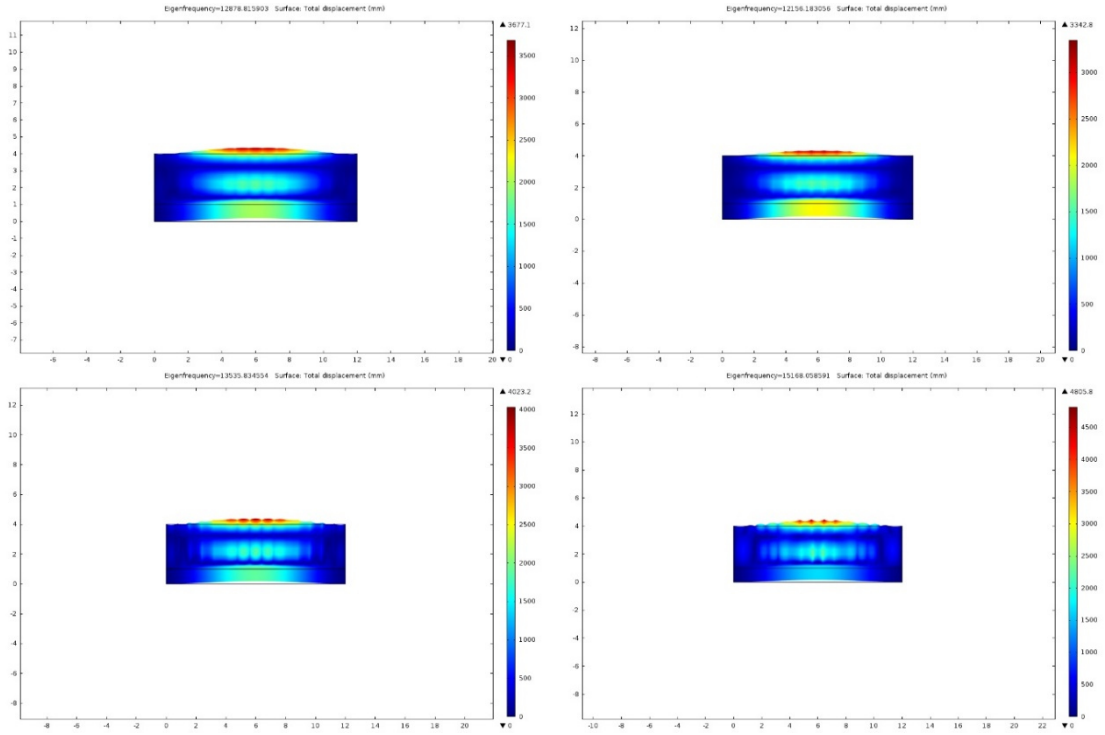

Supplementary Figure 5 | Mode-shapes from the FEM modal analysis for the cantilever bi-clamped beam geometry. *Shown are the resulting mode shapes for the non-laden beam, 0.10 g/ml, 0.15 g/ml, 0.20 g/ml, 0.25 g/ml, 0.30 g/ml, 0.35 g/ml, 0.40 g/ml, 0.45 g/ml and 0.50 g/ml.*

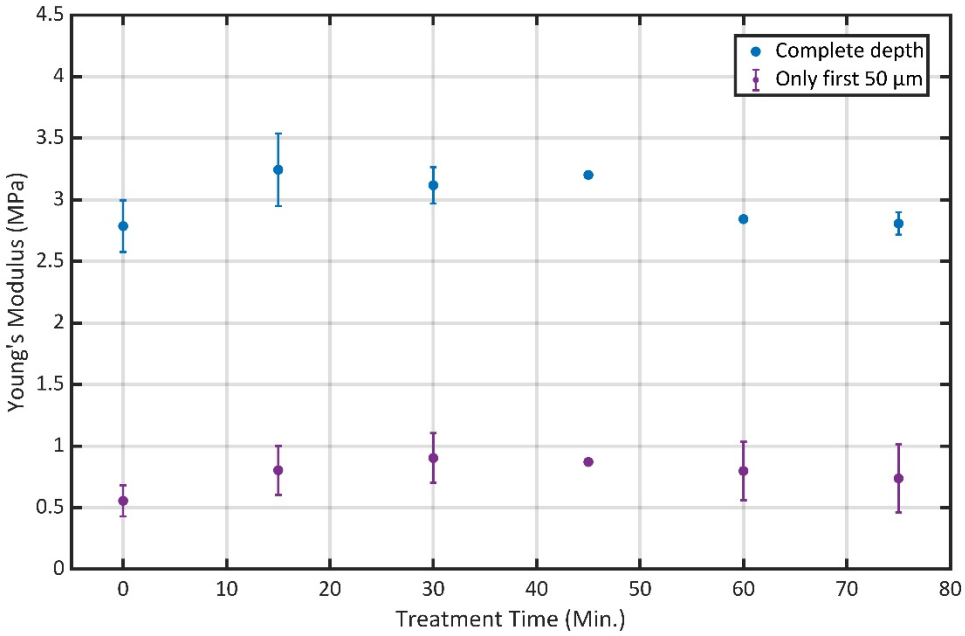

Supplementary Figure 6 | Resulting Young's modulus of the MACH-1™ data, when the first 50 µm and the complete indentation depth are analyzed. *A change in the Young's modulus can be seen between the two indentation depths, but not in behavior regarding the different treatment times.*

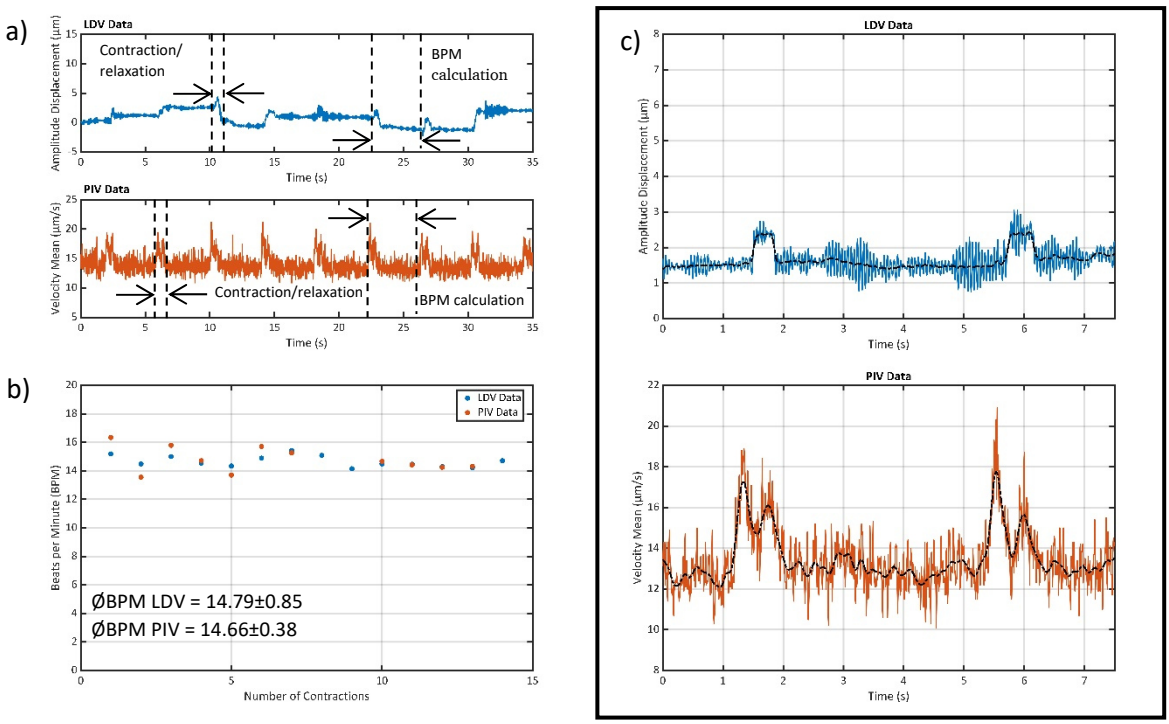

Supplementary Figure 7 | Comparison of LDV and PIV data with a multiwell plate cover. a) *Similar to the data shown in Figure 48, Both LDV data (top) and PIV data (bottom) show repetitive patterns allowing to determine the contraction and relaxation phases of each contraction event. Furthermore, the time between two contractions can be extracted for calculating the BPM values.* ***b)*** *For each time interval between two consecutive contractions, the contraction rate in one minute was calculated (beats per minute, BPM). Since this experiment was done after the measurement without a multiwell plate cover, no decrease in the contraction rate can be observed, and it seems as a stable contraction rate is reached here.* ***c)*** *Zooming into the data reveals the same disturbing vibration as shown in Figure 30, with a frequency of around 20 Hz is present. The black dashed line represents the measurement data smoothed by a Gaussian filter (factor 0.20 for the LDV data, factor 0.50 for the PIV data).*

11

Bibliography

[1] O. A. Bauchau and J. J. Craig, *Structural Analysis - With Applications to Aerospace Structures*, 1st ed. Springer Science+Business Media B.V., 2009.

[2] B. Junge, *Experiences with scanning laser vibrometry in automotive industries* (Vibration Measurements by Laser Techniques: First International Conference). SPIE, 1994.

[3] M. Ozbek and D. J. Rixen, "Aero-elastic Parameter Estimation of a 2.5 MW Wind Turbine Through Dynamic Analysis of In-Operation Vibration Data," *ENEFM2013,* pp. 279-285, 2014.

[4] J. Hancox, B. C. Staples, and R. J. Parker, "The Application of Scanning Laser Doppler vibrometry in Aero-Engine Development," *Proceedings of the Institution of Mechanical Engineers, Part G: Journal of Aerospace Engineering,* vol. 209, no. 1, pp. 35-42, 1995, doi: 10.1243/pime_proc_1995_209_268_02.

[5] r. H. Lyon, *Machinery Noise and Diagnostics*, 1 ed. Butterworth-Heinemann, 1987.

[6] A. Pouliezos and G. S. Stavrakakis, *Real Time Fault Monitoring of Industrial Processes*. Springer Netherlands, 1994.

[7] Y. Fujino, K. Kaito, and M. Abe, *Detection of structural damage by ambient vibration measurement using laser Doppler vibrometer* (6th Annual International Symposium on NDE for Health Monitoring and Diagnostics). SPIE, 2001.

[8] N. Muramatsu *et al.*, "Remote sensing of fruit textural changes with a laser Doppler vibrometer," (in English), *J Am Soc Hortic Sci,* vol. 125, no. 1, pp. 120-127, Jan 2000, doi: 10.21273/Jashs.125.1.120.

[9] S. Terasaki, N. Sakurai, J. Zebrowski, H. Murayama, R. Yamamoto, and D. J. Nevins, "Laser Doppler vibrometer analysis of changes in elastic properties of ripening 'La France' pears after postharvest storage," (in English), *Postharvest Biol Tec,* vol. 42, no. 2, pp. 198-207, Nov 2006, doi: 10.1016/j.postharvbio.2006.06.007.

[10] S. Terasaki, N. Wada, N. Sakurai, N. Muramatsu, R. Yamamoto, and D. J. Nevins, "Nondestructive Measurement of Kiwifruit Ripeness Using a Laser Doppler Vibrometer," *Transactions of the ASAE,* vol. 44, no. 1, pp. 81-87, 2001, doi: https://doi.org/10.13031/2013.2291.

[11] G. Kastberger, F. Weihmann, and T. Hoetzl, "Social waves in giant honeybees (Apis dorsata) elicit nest vibrations," *Naturwissenschaften,* vol. 100, no. 7, pp. 595-609, 2013/07/01 2013, doi: 10.1007/s00114-013-1056-z.

[12] W. H. Kirchner, "Hearing in honeybees: the mechanical response of the bee's antenna to near field sound," *Journal of Comparative Physiology A,* vol. 175, no. 3, pp. 261-265, 1994/09/01 1994, doi: 10.1007/BF00192985.

[13] M. Hrncir, C. Maia-Silva, and W. M. Farina, "Honey bee workers generate low-frequency vibrations that are reliable indicators of their activity level," *Journal of Comparative Physiology A,* vol. 205, no. 1, pp. 79-86, 2019/02/01 2019, doi: 10.1007/s00359-018-1305-x.

[14] B. Aicher, H. Markl, W. M. Masters, and H. L. Kirschenlohr, "Vibration transmission through the walking legs of the fiddler crab,Uca pugilator (Brachyura, Ocypodidae) as measured by Laser Doppler Vibrometry," *Journal of comparative physiology,* vol. 150, no. 4, pp. 483-491, 1983/12/01 1983, doi: 10.1007/BF00609574.

[15] "Teeth Mobility Measurement: A Laser Vibrometry Approach," *Journal of Clinical Laser Medicine & Surgery,* vol. 16, no. 5, pp. 269-272, 1998, doi: 10.1089/clm.1998.16.269.

[16] N. Constanze *et al.*, "Development and Validation of Bone Models using Structural Dynamic Measurement Methods," (in English), *Current Directions in Biomedical Engineering,* vol. 5, no. 1, pp. 343-345, 2019, doi: https://doi.org/10.1515/cdbme-2019-0086.

[17] T. Schuurman, D. J. Rixen, C. A. Swenne, and J. W. Hinnen, "Feasibility of Laser Doppler Vibrometry as potential diagnostic tool for patients with abdominal aortic aneurysms," (in English), *J Biomech,* vol. 46, no. 6, pp. 1113-1120, Apr 5 2013, doi: 10.1016/j.jbiomech.2013.01.013.

[18] U. Morbiducci, L. Scalise, M. De Melis, and M. Grigioni, "Optical Vibrocardiography: A Novel Tool for the Optical Monitoring of Cardiac Activity," *Annals of Biomedical Engineering,* vol. 35, no. 1, pp. 45-58, 2007/01/01 2007, doi: 10.1007/s10439-006-9202-9.

[19] N. E. Conza, D. J. Rixen, and S. Plomp, "Vibration testing of a fresh-frozen human pelvis: The role of the pelvic ligaments," *J Biomech,* vol. 40, no. 7, pp. 1599-1605, 2007/01/01/ 2007, doi: https://doi.org/10.1016/j.jbiomech.2006.07.001.

[20] G. Revel, A. Scalise, and L. Scalise, *Noncontact dynamic analysis of mechanical behavior of tendons by optical techniques* (BiOS 2001 The International Symposium on Biomedical Optics). SPIE, 2001.

[21] G. M. Revel, A. Scalise, and L. Scalise, "Measurement of stress–strain and vibrational properties of tendons," *Measurement Science and Technology,* vol. 14, no. 8, pp. 1427-1436, 2003/07/21 2003, doi: 10.1088/0957-0233/14/8/332.

[22] P. Ferris and P. J. Prendergast, "Middle-ear dynamics before and after ossicular replacement," (in English), *J Biomech,* vol. 33, no. 5, pp. 581-590, May 2000, doi: 10.1016/S0021-9290(99)00213-4.

[23] J. J. Rosowski, R. P. Mehta, and S. N. Merchant, "Diagnostic utility of laser-Doppler vibrometry in conductive hearing loss with normal tympanic membrane," (in eng), *Otol Neurotol,* vol. 24, no. 2, pp. 165-175, 2003, doi: 10.1097/00129492-200303000-00008.

[24] H. Tang, P. Razavi, N. Maftoon, J. J. Rosowski, C. Furlong, and J. T. Cheng, "Comparative Modal Analysis of the Tympanic Membrane Mechanics Between Normal and Experimentally Simulated Pathological Ears," in *Mechanics of Biological Systems and Materials & Micro-and Nanomechanics, Volume 4*, Cham, M. E. Grady, Ed., 2020// 2020: Springer International Publishing, pp. 63-71.

[25] A. M. Huber, F. Ma, H. Felix, and T. Linder, "Stapes Prosthesis Attachment: The Effect of Crimping on Sound Transfer in Otosclerosis Surgery," *The Laryngoscope,* vol. 113, no. 5, pp. 853-858, 2003, doi: 10.1097/00005537-200305000-00015.

[26] A. M. Huber, G. R. Ball, D. Veraguth, N. Dillier, D. Bodmer, and D. Sequeira, "A New Implantable Middle Ear Hearing Device for Mixed Hearing Loss: A Feasibility Study in Human Temporal Bones," *Otology & Neurotology,* vol. 27, no. 8, pp. 1104-1109, 2006, doi: 10.1097/01.mao.0000244352.49824.e6.

[27] B. Waldmann, H. Maier, and R. Leuwer, "Indicators for efficient coupling of the Otologics MET ossicular stimulator," in *3rd symposium of middle ear mechanics in research and otology.*, Matsuyama, Ehime, Japan, K. Gyo and H. Wada, Eds., 2003.

[28] H. Tabatabai, D. E. Oliver, J. W. Rohrbaugh, and C. Papadopoulos, "Novel Applications of Laser Doppler Vibration Measurements to Medical Imaging," *Sensing and Imaging: An International Journal,* vol. 14, no. 1, pp. 13-28, 2013/06/01 2013, doi: 10.1007/s11220-013-0077-1.

[29] P. Tipler A. and G. Mosca, *Physik*, 8 ed. Springer, 2019.

[30] D. Meschede, *Gerthsen Physik*, 25 ed. Springer, 2015.

[31] Polytec. "Grundlagen der Vibrometrie." https://www.polytec.com/de/vibrometrie/technologie/ (accessed 28.10.2020)

[32] G. M. Hale and M. R. Querry, "Optical Constants of Water in the 200-nm to 200-µm Wavelength Region," *Applied Optics,* vol. 12, no. 3, 1973.

[33] S. Kazemirad and L. Mongeau, "Rayleigh wave propagation method for the characterization of a thin layer of biomaterials," *The Journal of the Acoustical Society of America,* vol. 133, no. 6, pp. 4332-4342, 2013/06/01 2013, doi: 10.1121/1.4804318.

[34] S. Kazemirad, H. K. Heris, and L. Mongeau, "Viscoelasticity of hyaluronic acid-gelatin hydrogels for vocal fold tissue engineering," *Journal of Biomedical Materials Research Part B: Applied Biomaterials,* vol. 104, no. 2, pp. 283-290, 2016/02/01 2016, doi: 10.1002/jbm.b.33358.

[35] A. B. Zerdoum *et al.*, "Regulation of Stem Cell Function in an Engineered Vocal Fold-Mimetic Environment," *Regenerative Engineering and Translational Medicine,* vol. 6, no. 2, pp. 164-178, 2020/06/01 2020, doi: 10.1007/s40883-019-00142-1.

[36] G. Xu, C. Wang, T. Feng, D. E. Oliver, and X. D. Wang, "Non-contact Photoacoustic Tomography with a Laser Doppler Vibrometer," (in English), *Proc Spie,* vol. 8943, 2014, doi: 10.1117/12.2040290.

[37] M. W. Urban, G. T. Silva, M. Fatemi, and J. F. Greenleaf, "Multifrequency vibro-acoustography," (in English), *Ieee T Med Imaging,* vol. 25, no. 10, pp. 1284-1295, Oct 2006, doi: 10.1109/Tmi.2006.882142.

[38] R. Langer and J. P. Vacanti, "Tissue engineering," *Science,* vol. 260, pp. 920-926, 1993.

[39] R. Lanza, R. Langer, and J. Vacanti, "Principles of Tissue Engineering," in *Principles of Tissue Engineering*, R. Lanza, R. Langer, and J. Vacanti Eds., 3rd ed. Burlington: Academic Press, 2007, p. xxxi.

[40] B. Alberts, D. Bray, J. Lewis, M. Raff, K. Roberts, and J. D. Watson, *Molecular Biology of the Cell*, 3rd ed. Garland Publishing, Inc. New York & London.

[41] R. O. Hynes and K. M. Yamada, *Extracellular matrix biology*. Cold Spring Harbor Laboratory Press, 2012.

[42] D. A. Cisneros, C. Hung, C. M. Franz, and D. J. Muller, "Observing growth steps of collagen self-assembly by time-lapse high-resolution atomic force microscopy," *Journal of Structural Biology,* vol. 154, no. 3, pp. 232-245, 2006/06/01/ 2006, doi: https://doi.org/10.1016/j.jsb.2006.02.006.

[43] B. Brodsky, J. A. Werkmeister, and J. A. M. Ramshaw, "Collagens and Gelatins," *Biopolymers Online,* 2005/01/15 2005, doi:10.1002/3527600035.bpol8006

[44] B. R. G. Williams, R. A., D. C. Poppke, and K. A. Piez, "Collagen Fibril Formation: optimal in vitro conditions and preliminary kinetic results," *The Journal of biological Chemistry,* vol. 253, no. 18, pp. 6578-6585, September 25th 1978.

[45] K. E. Kadler, A. Hill, and E. G. Canty-Laird, "Collagen fibrillogenesis: fibronectin, integrins, and minor collagens as organizers and nucleators," *Current Opinion in Cell Biology,* vol. 20, no. 5, pp. 495-501, 2008/10/01/ 2008, doi: https://doi.org/10.1016/j.ceb.2008.06.008.

[46] F. Marga, A. Neagu, I. Kosztin, and G. Forgacs, "Developmental biology and tissue engineering," *Birth Defects Research Part C: Embryo Today: Reviews,* vol. 81, no. 4, pp. 320-328, 2007.

[47] N. A. Campbell and J. B. Reece, *Biologie*, 6th ed. Spektrum Akademischer Verlag Heidelberg, Berlin, 2003.

[48] I. J. Haug and K. I. Draget, "5 - Gelatin," in *Handbook of Food Proteins*, G. O. Phillips and P. A. Williams Eds.: Woodhead Publishing, 2011, pp. 92-115.

[49] D. L. Cohen, "Additive manufacturing of functional constructs under process uncertainty.," ed. Cornell University, 2010.

[50] L. Liu, Y. Fan, and W. Li, "Viscoelastic shock wave in ballistic gelatin behind soft body armor," *Journal of the Mechanical Behavior of Biomedical Materials,* vol. 34, pp. 199-207, 2014/06/01/ 2014, doi: https://doi.org/10.1016/j.jmbbm.2014.02.011.

[51] M. D. Alley, B. R. Schimizze, and S. F. Son, "Experimental modeling of explosive blast-related traumatic brain injuries," *NeuroImage,* vol. 54, pp. S45-S54, 2011/01/01/ 2011, doi: https://doi.org/10.1016/j.neuroimage.2010.05.030.

[52] S. Malekzadeh, M. J. Pfisterer, B. Wilson, H. Na, and M. K. Steehler, "A Novel Low-Cost Sinus Surgery Task Trainer," *Otolaryngology–Head and Neck Surgery,* vol. 145, no. 4, pp. 530-533, 2011/10/01 2011, doi: 10.1177/0194599811413373.

[53] C. E. Mendez-Probst, M. Vanjecek, H. Razvi, and P. A. Cadieux, "Ordnance gelatine as an in vitro tissue simulation scaffold for extracorporeal shock wave lithotripsy," *Urological Research,* vol. 38, no. 6, pp. 497-503, 2010/12/01 2010, doi: 10.1007/s00240-010-0329-7.

[54] S. A. Irvine *et al.*, "Printing cell-laden gelatin constructs by free-form fabrication and enzymatic protein crosslinking," *Biomedical Microdevices,* vol. 17, no. 1, p. 16, 2015/02/01 2015, doi: 10.1007/s10544-014-9915-8.

[55] M. O. Culjat, D. Goldenberg, P. Tewari, and R. S. Singh, "A Review of Tissue Substitutes for Ultrasound Imaging," *Ultrasound in Medicine & Biology,* vol. 36, no. 6, pp. 861-873, 2010/06/01/ 2010, doi: https://doi.org/10.1016/j.ultrasmedbio.2010.02.012.

[56] H. Yang, C. A. Carrascal, H. Xie, V. Shamdasani, and B. W. Anthony, "2-D Ultrasound Shear Wave Elastography With Multi-Sphere-Source External Mechanical Vibration: Preliminary Phantom Results," *Ultrasound in Medicine & Biology,* 2020/06/06/ 2020, doi: https://doi.org/10.1016/j.ultrasmedbio.2020.03.009.

[57] J. A. Hubbell, "Biomaterials in Tissue Engineering," *Bio/Technology,* vol. 13, no. 6, pp. 565-576, 1995/06/01 1995, doi: 10.1038/nbt0695-565.

[58] R. L. Reis, N. M. Neves, J. F. Mano, M. E. Gomes, A. P. Marques, and H. S. Azevedo, *Natural-based polymers for biomedical applications*. Elsevier, 2008.

[59] P. Bianco and P. G. Robey, "Stem cells in tissue engineering," *Nature,* vol. 414, no. 6859, pp. 118-121, 2001/11/01 2001, doi: 10.1038/35102181.

[60] R. Lanza, R. Langer, and J. Vacanti, *Principles of Tissue Engineering*, 3rd ed. 2007.

[61] D. Shi, *Biomaterials and Tissue Engineering*. Springer Berlin Heidelberg New York, 2004.

[62] K. Takahashi *et al.*, "Induction of Pluripotent Stem Cells from Adult Human Fibroblasts by Defined Factors," *Cell,* vol. 131, no. 5, pp. 861-872, 2007/11/30/ 2007, doi: https://doi.org/10.1016/j.cell.2007.11.019.

[63] I. Apsite, J. M. Uribe, A. F. Posada, S. Rosenfeldt, S. Salehi, and L. Ionov, "4D biofabrication of skeletal muscle microtissues," *Biofabrication,* vol. 12, no. 1, p. 015016, 2019/12/11 2019, doi: 10.1088/1758-5090/ab4cc4.

[64] D. W. Hutmacher, M. Sittinger, and M. V. Risbud, "Scaffold-based tissue engineering: rationale for computer-aided design and solid free-form fabrication systems," *Trends in Biotechnology,* vol. 22, no. 7, pp. 354-362, 2004/07/01/ 2004, doi: https://doi.org/10.1016/j.tibtech.2004.05.005.

[65] M. Sittinger, D. W. Hutmacher, and M. V. Risbud, "Current strategies for cell delivery in cartilage and bone regeneration," *Current Opinion in Biotechnology,* vol. 15, no. 5, pp. 411-418, 2004/10/01/ 2004, doi: https://doi.org/10.1016/j.copbio.2004.08.010.

[66] T. Weigel, G. Schinkel, and A. Lendlein, "Design and preparation of polymeric scaffolds for tissue engineering," *Expert Review of Medical Devices,* vol. 3, no. 6, pp. 835-851, 2006/11/01 2006, doi: 10.1586/17434440.3.6.835.

[67] A. Atala, S. B. Bauer, S. Soker, J. J. Yoo, and A. B. Retik, "Tissue-engineered autologous bladders for patients needing cystoplasty," *The Lancet,* vol. 367, no. 9518, pp. 1241-1246, 2006/04/15/ 2006, doi: https://doi.org/10.1016/S0140-6736(06)68438-9.

[68] P. Macchiarini *et al.*, "Clinical transplantation of a tissue-engineered airway," *The Lancet,* vol. 372, no. 9655, pp. 2023-2030, 2008/12/13/ 2008, doi: https://doi.org/10.1016/S0140-6736(08)61598-6.

[69] J. M. Wallis *et al.*, "Comparative Assessment of Detergent-Based Protocols for Mouse Lung De-Cellularization and Re-Cellularization," *Tissue Engineering Part C: Methods,* vol. 18, no. 6, pp. 420-432, 2012/06/01 2011, doi: 10.1089/ten.tec.2011.0567.

[70] A. B. Daly *et al.*, "Initial Binding and Recellularization of Decellularized Mouse Lung Scaffolds with Bone Marrow-Derived Mesenchymal Stromal Cells," *Tissue Engineering Part A,* vol. 18, no. 1-2, pp. 1-16, 2012/01/01 2011, doi: 10.1089/ten.tea.2011.0301.

[71] S. F. Badylak, D. Taylor, and K. Uygun, "Whole-Organ Tissue Engineering: Decellularization and Recellularization of Three-Dimensional Matrix Scaffolds," *Annual Review of Biomedical Engineering,* vol. 13, no. 1, pp. 27-53, 2011/08/15 2011, doi: 10.1146/annurev-bioeng-071910-124743.

[72] L. Moroni *et al.*, "Biofabrication: A Guide to Technology and Terminology," *Trends in Biotechnology,* vol. 36, no. 4, pp. 384-402, 2018/04/01/ 2018, doi: https://doi.org/10.1016/j.tibtech.2017.10.015.

[73] V. Mironov, T. Trusk, V. Kasyanov, S. Little, R. Swaja, and R. Markwald, "Biofabrication: a 21st century manufacturing paradigm," *Biofabrication,* vol. 1, no. 2, p. 022001, 2009/06/01 2009, doi: 10.1088/1758-5082/1/2/022001.

[74] M. Fritz *et al.*, "Flat pearls from biofabrication of organized composites on inorganic substrates," *Nature,* vol. 371, no. 6492, pp. 49-51, 1994/09/01 1994, doi: 10.1038/371049a0.

[75] H. Fong, S. N. White, M. L. Paine, W. Luo, M. L. Snead, and M. Sarikaya, "Enamel Structure Properties Controlled by Engineered Proteins in Transgenic Mice," *Journal of Bone and Mineral Research,* vol. 18, no. 11, pp. 2052-2059, 2003/11/01 2003, doi: 10.1359/jbmr.2003.18.11.2052.

[76] S. Masuda, T. Shimizu, M. Yamato, and T. Okano, "Cell sheet engineering for heart tissue repair," *Advanced Drug Delivery Reviews,* vol. 60, no. 2, pp. 277-285, 2008/01/14/ 2008, doi: https://doi.org/10.1016/j.addr.2007.08.031.

[77] J. Yang *et al.*, "Reconstruction of functional tissues with cell sheet engineering," *Biomaterials,* vol. 28, no. 34, pp. 5033-5043, 2007/12/01/ 2007, doi: https://doi.org/10.1016/j.biomaterials.2007.07.052.

[78] Y. Kobayashi *et al.*, "Tailored cell sheet engineering using microstereolithography and electrochemical cell transfer," *Sci Rep-Uk,* vol. 9, no. 1, p. 10415, 2019/07/18 2019, doi: 10.1038/s41598-019-46801-9.

[79] B. C. Isenberg, C. Williams, and R. T. Tranquillo, "Small-Diameter Artificial Arteries Engineered In Vitro," *Circulation Research,* vol. 98, no. 1, pp. 25-35, 2006, doi:10.1161/01.RES.0000196867.12470.84.

[80] P. S. Robinson, S. L. Johnson, M. C. Evans, V. H. Barocas, and R. T. Tranquillo, "Functional Tissue-Engineered Valves from Cell-Remodeled Fibrin with Commissural Alignment of Cell-Produced Collagen," *Tissue Engineering Part A,* vol. 14, no. 1, pp. 83-95, 2008, doi: 10.1089/ten.a.2007.0148.

[81] J. S. Miller *et al.*, "Rapid casting of patterned vascular networks for perfusable engineered three-dimensional tissues," *Nature Materials,* vol. 11, no. 9, pp. 768-774, 2012/09/01 2012, doi: 10.1038/nmat3357.

[82] N. E. Putra *et al.*, "Extrusion-based 3D printed biodegradable porous iron," *Acta Biomaterialia,* 2020/11/20/ 2020, doi: https://doi.org/10.1016/j.actbio.2020.11.022.

[83] A. J. Melchiorri *et al.*, "3D-Printed Biodegradable Polymeric Vascular Grafts," *Advanced Healthcare Materials,* vol. 5, no. 3, pp. 319-325, 2016/02/01 2016, doi: https://doi.org/10.1002/adhm.201500725.

[84] I. T. Ozbolat, *3D bioprinting: fundamentals, principles and applications*. Academic Press, 2016.

[85] A. Ovsianikov, J. Yoo, and V. Mironov, *3D printing and biofabrication*. Springer, 2018.

[86] *Nikita Golubev, prettycons, Freepik, Smashicons, Eucalyp, Surang, Kiranshastry, Darius Dan, Those Icons,* "Flaticon Image Database", www.flaticon.com (accessed 28.10.2020)

[87] I. T. Ozbolat and M. Hospodiuk, "Current advances and future perspectives in extrusion-based bioprinting," *Biomaterials,* vol. 76, pp. 321-343, 2016/01/01/ 2016, doi: https://doi.org/10.1016/j.biomaterials.2015.10.076.

[88] J. Malda *et al.*, "25th Anniversary Article: Engineering Hydrogels for Biofabrication," (in English), *Adv Mater,* vol. 25, no. 36, pp. 5011-5028, Sep 2013, doi: 10.1002/adma.201302042.

[89] N. Paxton, W. Smolan, T. Bock, F. Melchels, J. Groll, and T. Jungst, "Proposal to assess printability of bioinks for extrusion-based bioprinting and evaluation of rheological properties governing bioprintability," (in English), *Biofabrication,* vol. 9, no. 4, Dec 2017, doi: 10.1088/1758-5090/aa8dd8.

[90] S. Khalil and W. Sun, "Bioprinting Endothelial Cells With Alginate for 3D Tissue Constructs," *Journal of Biomechanical Engineering,* vol. 131, no. 11, 2009, doi: 10.1115/1.3128729.

[91] R. Censi *et al.*, "A Printable Photopolymerizable Thermosensitive p(HPMAm-lactate)-PEG Hydrogel for Tissue Engineering," *Advanced Functional Materials,* vol. 21, no. 10, pp. 1833-1842, 2011, doi: 10.1002/adfm.201002428.

[92] C. M. Smith *et al.*, "Three-Dimensional BioAssembly Tool for Generating Viable Tissue-Engineered Constructs," *Tissue Engineering,* vol. 10, no. 9-10, pp. 1566-1576, 2004/09/01 2004, doi: 10.1089/ten.2004.10.1566.

[93] A. Tirella, A. Orsini, G. Vozzi, and A. Ahluwalia, "A phase diagram for microfabrication of geometrically controlled hydrogel scaffolds," *Biofabrication,* vol. 1, no. 4, p. 045002, 2009/10/30 2009, doi: 10.1088/1758-5082/1/4/045002.

[94] S. J. Bryant and K. S. Anseth, "Hydrogel properties influence ECM production by chondrocytes photoencapsulated in poly(ethylene glycol) hydrogels," *Journal of Biomedical Materials Research,* vol. 59, no. 1, pp. 63-72, 2002/01/01 2002, doi: 10.1002/jbm.1217.

[95] G. D. Nicodemus and S. J. Bryant, "Cell Encapsulation in Biodegradable Hydrogels for Tissue Engineering Applications," *Tissue Engineering Part B: Reviews,* vol. 14, no. 2, pp. 149-165, 2008/06/01 2008, doi: 10.1089/ten.teb.2007.0332.

[96] T. J. Hinton *et al.*, "Three-dimensional printing of complex biological structures by freeform reversible embedding of suspended hydrogels," *Science Advances,* vol. 1, no. 9, p. e1500758, 2015, doi: 10.1126/sciadv.1500758.

[97] S. Rhee, J. L. Puetzer, B. N. Mason, C. A. Reinhart-King, and L. J. Bonassar, "3D Bioprinting of Spatially Heterogeneous Collagen Constructs for Cartilage Tissue Engineering," *ACS Biomaterials Science & Engineering,* vol. 2, no. 10, pp. 1800-1805, 2016/10/10 2016, doi: 10.1021/acsbiomaterials.6b00288.

[98] K. K. Moncal, V. Ozbolat, P. Datta, D. N. Heo, and I. T. Ozbolat, "Thermally-controlled extrusion-based bioprinting of collagen," *Journal of Materials Science: Materials in Medicine,* vol. 30, no. 5, p. 55, 2019/04/30 2019, doi: 10.1007/s10856-019-6258-2.

[99] J. J. Senior, M. E. Cooke, L. M. Grover, and A. M. Smith, "Fabrication of Complex Hydrogel Structures Using Suspended Layer Additive Manufacturing (SLAM)," *Advanced Functional Materials,* vol. 29, no. 49, p. 1904845, 2019/12/01 2019, doi: 10.1002/adfm.201904845.

[100] M. Au - Müller, J. Au - Becher, M. Au - Schnabelrauch, and M. Au - Zenobi-Wong, "Printing Thermoresponsive Reverse Molds for the Creation of Patterned Two-component Hydrogels for 3D Cell Culture," *JoVE,* no. 77, p. e50632, 2013/07/10/ 2013, doi:10.3791/50632.

[101] H.-W. Kang, S. J. Lee, I. K. Ko, C. Kengla, J. J. Yoo, and A. Atala, "A 3D bioprinting system to produce human-scale tissue constructs with structural integrity," *Nature Biotechnology,* vol. 34, no. 3, pp. 312-319, 2016/03/01 2016, doi: 10.1038/nbt.3413.

[102] I. M. Diniz *et al.*, "Pluronic F-127 hydrogel as a promising scaffold for encapsulation of dental-derived mesenchymal stem cells," *Journal of Materials Science: Materials in Medicine,* vol. 26, no. 3, p. 153, 2015.

[103] A. V. Vashi *et al.*, "Adipose differentiation of bone marrow-derived mesenchymal stem cells using Pluronic F-127 hydrogel in vitro," *Biomaterials,* vol. 29, no. 5, pp. 573-579, 2008/02/01/ 2008, doi: https://doi.org/10.1016/j.biomaterials.2007.10.017.

[104] Y. Morimoto, S. Mori, F. Sakai, and S. Takeuchi, "Human induced pluripotent stem cell-derived fiber-shaped cardiac tissue on a chip," *Lab on a Chip,* 10.1039/C6LC00422A vol. 16, no. 12, pp. 2295-2301, 2016, doi: 10.1039/C6LC00422A.

[105] S. Itai, H. Tajima, and H. Onoe, "Double-layer perfusable collagen microtube device for heterogeneous cell culture," *Biofabrication,* vol. 11, no. 1, p. 015010, 2018/11/30 2018, doi: 10.1088/1758-5090/aaf09b.

[106] D. B. Kolesky, K. A. Homan, M. A. Skylar-Scott, and J. A. Lewis, "Three-dimensional bioprinting of thick vascularized tissues," *Proceedings of the National Academy of Sciences,* vol. 113, no. 12, p. 3179, 2016, doi: 10.1073/pnas.1521342113.

[107] N. Diamantides, C. Dugopolski, E. Blahut, S. Kennedy, and L. J. Bonassar, "High density cell seeding affects the rheology and printability of collagen bioinks," *Biofabrication,* vol. 11, no. 4, p. 045016, 2019/08/22 2019, doi: 10.1088/1758-5090/ab3524.

[108] B. Gao, T. Konno, and K. Ishihara, "Quantitating distance-dependent, indirect cell–cell interactions with a multilayered phospholipid polymer hydrogel," *Biomaterials,* vol. 35, no. 7, pp. 2181-2187, 2014/02/01/ 2014, doi: https://doi.org/10.1016/j.biomaterials.2013.11.060.

[109] Y. Song *et al.*, "Microfabrication of a tunable collagen/alginate-chitosan hydrogel membrane for controlling cell–cell interactions," *Carbohydrate Polymers,* vol. 153, pp. 652-662, 2016/11/20/ 2016, doi: https://doi.org/10.1016/j.carbpol.2016.07.058.

[110] A. N. Mehesz *et al.*, "Scalable robotic biofabrication of tissue spheroids," *Biofabrication,* vol. 3, no. 2, p. 025002, 2011/05/12 2011, doi: 10.1088/1758-5082/3/2/025002.

[111] V. Mironov, R. P. Visconti, V. Kasyanov, G. Forgacs, C. J. Drake, and R. R. Markwald, "Organ printing: Tissue spheroids as building blocks," *Biomaterials,* vol. 30, no. 12, pp. 2164-2174, 2009/04/01/ 2009, doi: https://doi.org/10.1016/j.biomaterials.2008.12.084.

[112] G. Y. Lee, P. A. Kenny, E. H. Lee, and M. J. Bissell, "Three-dimensional culture models of normal and malignant breast epithelial cells," *Nature Methods,* vol. 4, no. 4, pp. 359-365, 2007/04/01 2007, doi: 10.1038/nmeth1015.

[113] E. O. Mosaad, K. F. Chambers, K. Futrega, J. A. Clements, and M. R. Doran, "The Microwell-mesh: A high-throughput 3D prostate cancer spheroid and drug-testing platform," *Sci Rep-Uk,* vol. 8, no. 1, p. 253, 2018/01/10 2018, doi: 10.1038/s41598-017-18050-1.

[114] A. Scalzone, A. M. Ferreira, C. Tonda-Turo, G. Ciardelli, K. Dalgarno, and P. Gentile, "The interplay between chondrocyte spheroids and mesenchymal stem cells boosts cartilage regeneration within a 3D natural-based hydrogel," *Sci Rep-Uk,* vol. 9, no. 1, p. 14630, 2019/10/10 2019, doi: 10.1038/s41598-019-51070-7.

[115] M. J. Kratochvil, A. J. Seymour, T. L. Li, S. P. Paşca, C. J. Kuo, and S. C. Heilshorn, "Engineered materials for organoid systems," *Nature Reviews Materials,* vol. 4, no. 9, pp. 606-622, 2019/09/01 2019, doi: 10.1038/s41578-019-0129-9.

[116] K. Jakab, A. Neagu, V. Mironov, and G. Forgacs, "Organ printing: Fiction or science," *Biorheology,* vol. 41, pp. 371-375, 2004.

[117] K. Jakab *et al.*, "Tissue Engineering by Self-Assembly of Cells Printed into Topologically Defined Structures," *Tissue Engineering Part A,* vol. 14, no. 3, pp. 413-421, 2008/03/01 2008, doi: 10.1089/tea.2007.0173.

[118] J. M. Pérez-Pomares and R. A. Foty, "Tissue fusion and cell sorting in embryonic development and disease: biomedical implications," *BioEssays,* vol. 28, no. 8, pp. 809-821, 2006, doi: 10.1002/bies.20442.

[119] T. D. Brown, "Techniques for mechanical stimulation of cells in vitro: a review," *J Biomech,* vol. 33, no. 1, pp. 3-14, 2000/01/01/ 2000, doi: https://doi.org/10.1016/S0021-9290(99)00177-3.

[120] C. A. Powell, B. L. Smiley, J. Mills, and H. H. Vandenburgh, "Mechanical stimulation improves tissue-engineered human skeletal muscle," *American Journal of Physiology-Cell Physiology,* vol. 283, no. 5, pp. C1557-C1565, 2002/11/01 2002, doi: 10.1152/ajpcell.00595.2001.

[121] S. D. Waldman, C. G. Spiteri, M. D. Grynpas, R. M. Pilliar, and R. A. Kandel, "Long-Term Intermittent Compressive Stimulation Improves the Composition and Mechanical Properties of Tissue-Engineered Cartilage," *Tissue Engineering,* vol. 10, no. 9-10, pp. 1323-1331, 2004/09/01 2004, doi: 10.1089/ten.2004.10.1323.

[122] D. Seliktar, R. M. Nerem, and Z. S. Galis, "Mechanical Strain-Stimulated Remodeling of Tissue-Engineered Blood Vessel Constructs," *Tissue Engineering,* vol. 9, no. 4, pp. 657-666, 2003/08/01 2003, doi: 10.1089/107632703768247359.

[123] J. T. Shearn *et al.*, "Mechanical Stimulation of Tendon Tissue Engineered Constructs: Effects on Construct Stiffness, Repair Biomechanics, and Their Correlation," *Journal of Biomechanical Engineering,* vol. 129, no. 6, pp. 848-854, 2007, doi: 10.1115/1.2800769.

[124] C. Fischer *et al.*, "Long-term functional and structural preservation of precision-cut human myocardium under continuous electromechanical stimulation in vitro," *Nat Commun,* vol. 10, no. 1, p. 117, 2019/01/10 2019, doi: 10.1038/s41467-018-08003-1.

[125] A. W. Holle *et al.*, "Cell-Extracellular Matrix Mechanobiology: Forceful Tools and Emerging Needs for Basic and Translational Research," (in English), *Nano Lett,* vol. 18, no. 1, pp. 1-8, Jan 2018, doi: 10.1021/acs.nanolett.7b04982.

[126] F. Guilak, D. M. Cohen, B. T. Estes, J. M. Gimble, W. Liedtke, and C. S. Chen, "Control of Stem Cell Fate by Physical Interactions with the Extracellular Matrix," *Cell Stem Cell,* vol. 5, no. 1, pp. 17-26, 2009/07/02/ 2009, doi: https://doi.org/10.1016/j.stem.2009.06.016.

[127] A. J. Engler, F. Rehfeldt, S. Sen, and D. E. Discher, "Microtissue Elasticity: Measurements by Atomic Force Microscopy and Its Influence on Cell Differentiation," in *Methods in Cell Biology*, vol. 83: Academic Press, 2007, pp. 521-545.

[128] C. Prein, N. Warmbold, Z. Farkas, M. Schieker, A. Aszodi, and H. Clausen-Schaumann, "Structural and mechanical properties of the proliferative zone of the developing murine growth plate cartilage assessed by atomic force microscopy," (in English), *Matrix Biol,* vol. 50, pp. 1-15, Mar 2016, doi: 10.1016/j.matbio.2015.10.001.

[129] D. E. Discher, L. Smith, S. Cho, M. Colasurdo, A. J. Garcia, and S. Safran, "Matrix Mechanosensing: From Scaling Concepts in 'Omics Data to Mechanisms in the Nucleus, Regeneration, and Cancer," (in English), *Annu Rev Biophys,* vol. 46, pp. 295-315, 2017, doi: 10.1146/annurev-biophys-062215-011206.

[130] J. Swift *et al.*, "Nuclear Lamin-A Scales with Tissue Stiffness and Enhances Matrix-Directed Differentiation," (in English), *Science,* vol. 341, no. 6149, Aug 30 2013, doi: 10.1126/science.1240104.

[131] M. Vishwakarma, J. Di Russo, D. Probst, U. S. Schwarz, T. Das, and J. P. Spatz, "Mechanical interactions among followers determine the emergence of leaders in migrating epithelial cell collectives," (in English), *Nat Commun,* vol. 9, Aug 27 2018, doi: 10.1038/s41467-018-05927-6.

[132] F. A. Gegenfurtner *et al.*, "Micropatterning as a tool to identify regulatory triggers and kinetics of actin-mediated endothelial mechanosensing," (in English), *J Cell Sci,* vol. 131, no. 10, May 15 2018, doi: 10.1242/jcs.212886.

[133] D. E. Koser *et al.*, "Mechanosensing is critical for axon growth in the developing brain," (in English), *Nat Neurosci,* vol. 19, no. 12, pp. 1592-1598, Dec 2016, doi: 10.1038/nn.4394.

[134] E. Moeendarbary *et al.*, "The soft mechanical signature of glial scars in the central nervous system," (in English), *Nat Commun,* vol. 8, Mar 20 2017, doi: 10.1038/ncomms14787.

[135] R. Reuten *et al.*, "Structural decoding of netrin-4 reveals a regulatory function towards mature basement membranes," (in English), *Nat Commun,* vol. 7, Nov 30 2016, doi: 10.1038/ncomms13515.

[136] D. Rüdiger, K. Kick, A. Goychuk, A. M. Vollmar, E. Frey, and S. Zahler, "Cell-Based Strain Remodeling of a Nonfibrous Matrix as an Organizing Principle for Vasculogenesis," *Cell Rep,* vol. 32, no. 6, p. 108015, 2020/08/11/ 2020, doi: https://doi.org/10.1016/j.celrep.2020.108015.

[137] B. Yang *et al.*, "Stopping transformed cancer cell growth by rigidity sensing," *Nature Materials,* 2019/10/28 2019, doi: 10.1038/s41563-019-0507-0.

[138] A. Palamidessi *et al.*, "Unjamming overcomes kinetic and proliferation arrest in terminally differentiated cells and promotes collective motility of carcinoma," (in English), *Nature Materials,* vol. 18, no. 11, pp. 1252-+, Nov 2019, doi: 10.1038/s41563-019-0425-1.

[139] D. T. Butcher, T. Alliston, and V. M. Weaver, "A tense situation: forcing tumour progression," *Nature Reviews Cancer,* vol. 9, no. 2, pp. 108-122, 2009/02/01 2009, doi: 10.1038/nrc2544.

[140] R. Reuten *et al.*, "Basement membrane stiffness determines metastases formation," *Nature Materials,* 2021/01/25 2021, doi: 10.1038/s41563-020-00894-0.

[141] M. Ventre and P. A. Netti, "Controlling Cell Functions and Fate with Surfaces and Hydrogels: The Role of Material Features in Cell Adhesion and Signal Transduction," *Gels,* vol. 2, no. 12, 2016.

[142] A. Hoffman, "Hydrogels for biomedical applications," *Adv. Drug Delivery Rev,* vol. 43, pp. 1-12, 2002.

[143] M. Ahearne, Y. Yang, and K. Liu, "Mechanical characterisation of hydrogels for tissue engineering applications," *Topics in tissue Engineering,* vol. 4, no. 12, pp. 1-16, 2008.

[144] M. L. Oyen, "Mechanical characterisation of hydrogel materials," *International Materials Reviews,* vol. 59, no. 1, pp. 44-59, 2014/01/01 2014, doi: 10.1179/1743280413Y.0000000022.

[145] D.-H. Kim, P. K. Wong, J. Park, A. Levchenko, and Y. Sun, "Microengineered Platforms for Cell Mechanobiology," *Annual Review of Biomedical Engineering,* vol. 11, no. 1, pp. 203-233, 2009/08/01 2009, doi: 10.1146/annurev-bioeng-061008-124915.

[146] S. Kiderlen, C. Polzer, J. O. Radler, D. Docheva, H. Clausen-Schaumann, and S. Sudhop, "Age related changes in cell stiffness of tendon stem/progenitor cells and a rejuvenating effect of ROCK-inhibition," (in English), *Biochem Bioph Res Co,* vol. 509, no. 3, pp. 839-844, Feb 12 2019, doi: 10.1016/j.bbrc.2019.01.027.

[147] S. Lv, D. M. Dudek, Y. Cao, M. M. Balamurali, J. Gosline, and H. B. Li, "Designed biomaterials to mimic the mechanical properties of muscles," (in English), *Nature,* vol. 465, no. 7294, pp. 69-73, May 6 2010, doi: 10.1038/nature09024.

[148] D. Alsteens, D. J. Muller, and Y. F. Dufrene, "Multiparametric Atomic Force Microscopy Imaging of Biomolecular and Cellular Systems," (in English), *Accounts Chem Res,* vol. 50, no. 4, pp. 924-931, Apr 2017, doi: 10.1021/acs.accounts.6b00638.

[149] P. K. V. Babu, C. Rianna, U. Mirastschijski, and M. Radmacher, "Nano-mechanical mapping of interdependent cell and ECM mechanics by AFM force spectroscopy," (in English), *Sci Rep-Uk,* vol. 9, Aug 23 2019, doi: 10.1038/s41598-019-48566-7.

[150] J. D. Menczel and R. B. Prime, *Thermal Analysis of Polymers - Fundamentals and Applications*. Wiley, 2009.

[151] K. P. Menard and N. Menard, "Dynamic Mechanical Analysis," *Encyclopedia of Analytical Chemistry,* pp. 1-25, 2017/09/15 2017, doi:10.1002/9780470027318.a2007.pub3

[152] R. A. Horch, D. F. Gochberg, J. S. Nyman, and M. D. Does, "Non-invasive predictors of human cortical bone mechanical properties: T(2)-discriminated H NMR compared with high resolution X-ray," (in eng), *PLoS One,* vol. 6, no. 1, pp. e16359-e16359, 2011, doi: 10.1371/journal.pone.0016359.

[153] G. C. Stael, M. C. G. Rocha, M. Sônia Maria Cabral de, J. R. M. d'Almeida, and N. M. d. S. Ruiz, "Analysis of the mechanical properties and characterization by solid state 13C NMR of recycled EVA copolymer/silica composites," *Materials Research,* vol. 8, pp. 269-273, 2005. [Online]. Available: http://www.scielo.br/scielo.php?script=sci_arttext&pid=S1516-14392005000300008&nrm=iso.

[154] E. D. Williams *et al.*, "The design and validation of a magnetic resonance imaging–compatible device for obtaining mechanical properties of plantar soft tissue via gated acquisition," *Proceedings of the Institution of Mechanical Engineers, Part H: Journal of Engineering in Medicine,* vol. 229, no. 10, pp. 732-742, 2015/10/01 2015, doi: 10.1177/0954411915606150.

[155] K. F. Kvåle *et al.*, "Detection of Tissue Fibrosis using Natural Mechanical Wave Velocity Estimation: Feasibility Study," *Ultrasound in Medicine & Biology,* 2020/06/04/ 2020, doi: https://doi.org/10.1016/j.ultrasmedbio.2020.04.022.

[156] A. Manduca *et al.*, "Magnetic resonance elastography: Non-invasive mapping of tissue elasticity," *Medical Image Analysis,* vol. 5, no. 4, pp. 237-254, 2001/12/01/ 2001, doi: https://doi.org/10.1016/S1361-8415(00)00039-6.

[157] J. Ophir, I. Céspedes, H. Ponnekanti, Y. Yazdi, and X. Li, "Elastography: A Quantitative Method for Imaging the Elasticity of Biological Tissues," *Ultrasonic Imaging,* vol. 13, no. 2, pp. 111-134, 1991/04/01 1991, doi: 10.1177/016173469101300201.

[158] B. G. Wood, M. E. Ireson, M. W. Urban, and I. Z. D. Nenadic, "Attenuation measuring ultrasound shearwave elastography as a method for evaluating pancreatic viscoelasticity," *Biomedical Physics & Engineering Express,* vol. 5, no. 6, p. 065016, 2019/10/18 2019, doi: 10.1088/2057-1976/ab4c05.

[159] A. V. Astaneh, M. W. Urban, W. Aquino, J. F. Greenleaf, and M. N. Guddati, "Arterial waveguide model for shear wave elastography: implementation and in vitro validation," *Physics in Medicine & Biology,* vol. 62, pp. 5473 - 5494, 2017.

[160] S. S. Yengul, P. E. Barbone, and B. Madore, "Dispersion in Tissue-Mimicking Gels Measured with Shear Wave Elastography and Torsional Vibration Rheometry," *Ultrasound in Medicine & Biology,* vol. 45, no. 2, pp. 586-604, 2019/02/01/ 2019, doi: https://doi.org/10.1016/j.ultrasmedbio.2018.07.002.

[161] Y. Wang and J. Jiang, "Influence of Tissue Microstructure on Shear Wave Speed Measurements in Plane Shear Wave Elastography: A Computational Study in Lossless Fibrotic Liver Media," *Ultrasonic Imaging,* vol. 40, no. 1, pp. 49-63, 2018/01/01 2017, doi: 10.1177/0161734617719055.

[162] A. H. Henni, C. Schmitt, and G. Cloutier, "Shear wave induced resonance elastography of soft heterogeneous media," *J Biomech,* vol. 43, no. 8, pp. 1488-1493, 2010/05/28/ 2010, doi: https://doi.org/10.1016/j.jbiomech.2010.01.045.

[163] M. Hossain, C. J. Moore, and C. M. Gallippi, "Acoustic Radiation Force Impulse-Induced Peak Displacements Reflect Degree of Anisotropy in Transversely Isotropic Elastic Materials," *IEEE Transactions on Ultrasonics, Ferroelectrics, and Frequency Control,* vol. 64, no. 6, pp. 989-1001, 2017, doi: 10.1109/TUFFC.2017.2690223.

[164] A. Hadj Henni *et al.*, "Hyper-frequency viscoelastic spectroscopy of biomaterials," *Journal of the Mechanical Behavior of Biomedical Materials,* vol. 4, no. 7, pp. 1115-1122, 2011/10/01/ 2011, doi: https://doi.org/10.1016/j.jmbbm.2011.03.020.

[165] A. Alizad, M. Fatemi, L. E. Wold, and J. F. Greenleaf, "Performance of vibro-acoustography in detecting microcalcifications in excised human breast tissue: a study of 74 tissue samples," *Ieee T Med Imaging,* vol. 23, no. 3, pp. 307-312, 2004, doi: 10.1109/TMI.2004.824241.

[166] V. Ntziachristos, "Going deeper than microscopy: the optical imaging frontier in biology," *Nature Methods,* vol. 7, no. 8, pp. 603-614, 2010/08/01 2010, doi: 10.1038/nmeth.1483.

[167] A. Taruttis and V. Ntziachristos, "Advances in real-time multispectral optoacoustic imaging and its applications," *Nature Photonics,* vol. 9, no. 4, pp. 219-227, 2015/04/01 2015, doi: 10.1038/nphoton.2015.29.

[168] M. Raffel, C. E. Willert, F. Scarano, C. J. Kähler, S. T. Wereley, and J. Kompenhans, *Particle image velocimetry: a practical guide*. Springer, 2018.

[169] T. Chu, W. Ranson, and M. A. Sutton, "Applications of digital-image-correlation techniques to experimental mechanics," *Experimental mechanics,* vol. 25, no. 3, pp. 232-244, 1985.

[170] S. Yoneyama and G. Murasawa, "Digital image correlation," *Experimental mechanics,* vol. 207, 2009.

[171] S. J. Rothberg *et al.*, "An international review of laser Doppler vibrometry: Making light work of vibration measurement," (in English), *Opt Laser Eng,* vol. 99, pp. 11-22, Dec 2017, doi: 10.1016/j.optlaseng.2016.10.023.

[172] D. Goyal and B. S. Pabla, "The Vibration Monitoring Methods and Signal Processing Techniques for Structural Health Monitoring: A Review," *Archives of Computational Methods in Engineering,* vol. 23, no. 4, pp. 585-594, 2016/12/01 2016, doi: 10.1007/s11831-015-9145-0.

[173] I. A. Sever, A. B. Stanbridge, and D. J. Ewins, "Turbomachinery blade vibration measurements with tracking LDV under rotation," in *Proc.SPIE*, 2006, vol. 6345, doi: 10.1117/12.693172. [Online]. Available: https://doi.org/10.1117/12.693172

[174] P. Castellini, M. Martarelli, and E. P. Tomasini, "Laser Doppler Vibrometry for Structural Dynamic Characterization of Rotating Machinery," *Applied Mechanics and Materials,* vol. 415, pp. 538-543, 2013, doi: 10.4028/www.scientific.net/AMM.415.538.

[175] T. Miyashita and M. Nagai, "Vibration-based Structural Health Monitoring for Bridges using Laser Doppler Vibrometers and MEMS-based Technologies," 2009.

[176] T. L. Schmitz and K. S. Smith, *Mechanical Vibrations - Modeling and Measurement*. New-York: Springer, 2012, p. 378.

[177] Z.-F. Fu and J. He, *Modal analysis*. Elsevier, 2001.

[178] P. Avitabile, *Modal testing: a practitioner's guide*. John Wiley & Sons, 2017.

[179] M. Géradin and D. J. Rixen, *Mechanical Vibrations - Theory and Applications to Structural Dynamics*, 3 ed. John Wiley & Sons, 2015.

[180] H. Dresig and F. Holzweißig, *Maschinendynamik*. Springer-Verlag, 2013.

[181] G. H. Banwell, J. R. Roberts, B. J. Halkon, S. J. Rothberg, and S. Mohr, "Understanding the Dynamic Behaviour of a Tennis Racket under Play Conditions," *Experimental Mechanics,* vol. 54, no. 4, pp. 527-537, 2014/04/01 2014, doi: 10.1007/s11340-013-9803-9.

[182] J. M. Montalvao e Silva and N. M. M. Maia, *Modal Analysis and Testing* (Nato Science Series E, no. 363). Springer Netherlands, 1999.

[183] G. D'Emilia, C. Santolini, and E. P. Tomasini, "Comparison among Modal Analyses of Axial Compressor Blade using Experimental Data of Different Measuring Systems," in *Modern Practice in Stress and Vibration Analysis*, J. E. Mottershead Ed.: Pergamon, 1989, pp. 191-199.

[184] N. Contessi Negrini, N. Celikkin, P. Tarsini, S. Farè, and W. Święszkowski, "Three-dimensional printing of chemically crosslinked gelatin hydrogels for adipose tissue engineering," *Biofabrication,* vol. 12, no. 2, p. 025001, 2020/01/16 2020, doi: 10.1088/1758-5090/ab56f9.

[185] H. Lee, J. Kim, Y. Choi, and D.-W. Cho, "Application of Gelatin Bioinks and Cell-Printing Technology to Enhance Cell Delivery Capability for 3D Liver Fibrosis-on-a-Chip Development," *ACS Biomaterials Science & Engineering,* vol. 6, no. 4, pp. 2469-2477, 2020/04/13 2020, doi: 10.1021/acsbiomaterials.9b01735.

[186] S. Schwarz *et al.*, "Contactless Vibrational Analysis of Transparent Hydrogel Structures Using Laser-Doppler Vibrometry," *Experimental Mechanics,* 2020/07/13 2020, doi: 10.1007/s11340-020-00626-0.

[187] P. Vettiger *et al.*, "The “Millipede”—More than thousand tips for future AFM storage," *IBM Journal of Research and Development,* vol. 44, no. 3, pp. 323-340, 2000, doi: 10.1147/rd.443.0323.

[188] S. Schwarz, B. Hartmann, R. Moerl, S. Sudhop, H. Clausen-Schaumann, and D. Rixen, "Vibrational Analysis of Biopolymer-Based Hydrogels Using 3D-Printed Test Structures for Applications in Bioprinting," in *Mechanics of Biological Systems and Materials & Micro- and Nanomechanics, Volume 4*, Cham, M. E. Grady, Ed., 2020// 2020: Springer International Publishing, pp. 29-35.

[189] S. Schwarz, S. Kiderlen, R. Moerl, S. Sudhop, H. Clausen-Schaumann, and D. J. Rixen, "Investigating the Feasibility of Laser-Doppler Vibrometry for Vibrational Analysis of Living Mammalian Cells," in *Rotating Machinery, Optical Methods & Scanning LDV Methods, Volume 6*, Cham, D. Di Maio and J. Baqersad, Eds., 2020// 2020: Springer International Publishing, pp. 31-36.

[190] F. Bronner and M. C. Farach-Carson, *Bone and Osteoarthritis* (Topics in Bone Biology). Springer, 2007.

[191] N. Arden and M. C. Nevitt, "Osteoarthritis: Epidemiology," *Best Practice & Research Clinical Rheumatology,* vol. 20, no. 1, pp. 3-25, 2006/02/01/ 2006, doi: https://doi.org/10.1016/j.berh.2005.09.007.

[192] B. Hartmann *et al.*, "Early Detection of Cartilage Degeneration: A Comparison of Histology, Fiber Bragg Grating-Based Micro-Indentation, and Atomic Force Microscopy-Based Nano-Indentation," *International Journal of Molecular Sciences,* vol. 21, no. 19, p. 7384, 2020. [Online]. Available: https://www.mdpi.com/1422-0067/21/19/7384.

[193] S. Grenier, M. M. Bhargava, and P. A. Torzilli, "An in vitro model for the pathological degradation of articular cartilage in osteoarthritis," *J Biomech,* vol. 47, no. 3, pp. 645-652, 2014/02/07/ 2014, doi: https://doi.org/10.1016/j.jbiomech.2013.11.050.

[194] M. Stolz, R. Raiteri, A. U. Daniels, M. R. VanLandingham, W. Baschong, and U. Aebi, "Dynamic elastic modulus of porcine articular cartilage determined at two different levels of tissue organization by indentation-type atomic force microscopy," (in English), *Biophys J,* vol. 86, no. 5, pp. 3269-3283, May 2004, doi: 10.1016/S0006-3495(04)74375-1.

[195] M.-I. Pastrama *et al.*, "Combined enzymatic degradation of proteoglycans and collagen significantly alters intratissue strains in articular cartilage during cyclic compression," *Journal of the Mechanical Behavior of Biomedical Materials,* vol. 98, pp. 383-394, 2019/10/01/ 2019, doi: https://doi.org/10.1016/j.jmbbm.2019.05.040.

[196] A. J. Hughes *et al.*, "Engineered Tissue Folding by Mechanical Compaction of the Mesenchyme," *Developmental Cell,* vol. 44, no. 2, pp. 165-178.e6, 2018/01/22/ 2018, doi: https://doi.org/10.1016/j.devcel.2017.12.004.

[197] Y. Y. Li, K. L. Lam, A. D. Chen, W. Zhang, and B. P. Chan, "Collagen microencapsulation recapitulates mesenchymal condensation and potentiates chondrogenesis of human mesenchymal stem cells – A matrix-driven in vitro model of early skeletogenesis," *Biomaterials,* vol. 213, p. 119210, 2019/08/01/ 2019, doi: https://doi.org/10.1016/j.biomaterials.2019.05.021.

[198] M. Younesi, V. M. Goldberg, and O. Akkus, "A micro-architecturally biomimetic collagen template for mesenchymal condensation based cartilage regeneration," *Acta Biomaterialia,* vol. 30, pp. 212-221, 2016/01/15/ 2016, doi: https://doi.org/10.1016/j.actbio.2015.11.024.

[199] T. Takebe *et al.*, "Vascularized and Complex Organ Buds from Diverse Tissues via Mesenchymal Cell-Driven Condensation," *Cell Stem Cell,* vol. 16, no. 5, pp. 556-565, 2015/05/07/ 2015, doi: https://doi.org/10.1016/j.stem.2015.03.004.

[200] W. Zhang *et al.*, "Maturation of human embryonic stem cell-derived cardiomyocytes (hESC-CMs) in 3D collagen matrix: Effects of niche cell supplementation and mechanical stimulation," *Acta Biomaterialia,* vol. 49, pp. 204-217, 2017/02/01/ 2017, doi: https://doi.org/10.1016/j.actbio.2016.11.058.

[201] M. Walker, P. Rizzuto, M. Godin, and A. E. Pelling, "Structural and mechanical remodeling of the cytoskeleton maintains tensional homeostasis in 3D microtissues under acute dynamic stretch," *Sci Rep-Uk,* vol. 10, no. 1, p. 7696, 2020/05/06 2020, doi: 10.1038/s41598-020-64725-7.

[202] J. L. Hutter and J. Bechhoefer, "Calibration of Atomic-Force Microscope Tips (Vol 64, Pg 1868, 1993)," (in English), *Rev Sci Instrum,* vol. 64, no. 11, pp. 3342-3342, Nov 1993, doi: 10.1063/1.1144449.

[203] I. N. Sneddon, "The relation between load and penetration in the axisymmetric boussinesq problem for a punch of arbitrary profile," *International Journal of Engineering Science,* vol. 3, no. 1, 1965.

[204] W. Böcker *et al.*, "Introducing a single-cell-derived human mesenchymal stem cell line expressing hTERT after lentiviral gene transfer," *J Cell Mol Med,* vol. 12, no. 4, pp. 1347-1359, 2008/08/01 2008, doi: 10.1111/j.1582-4934.2008.00299.x.

[205] A. J. Kalahrodi, G. Marchi, J. Möller, S. Nolte, and J. Roths, "2D stiffness mapping for localizing osteoarthritic degenerated cartilage by using a fast indentation system based on fiber Bragg gratings," in *Proc.SPIE*, 2019, vol. 11199, doi: 10.1117/12.2539252.

[206] Y. Jin, W. Chai, and Y. Huang, "Fabrication of Stand-Alone Cell-Laden Collagen Vascular Network Scaffolds Using Fugitive Pattern-Based Printing-Then-Casting Approach," *ACS Applied Materials & Interfaces,* vol. 10, no. 34, pp. 28361-28371, 2018/08/29 2018, doi: 10.1021/acsami.8b09177.

[207] A. W. Justin, R. A. Brooks, and A. E. Markaki, "Multi-casting approach for vascular networks in cellularized hydrogels," *Journal of The Royal Society Interface,* vol. 13, no. 125, p. 20160768, 2016/12/31 2016, doi: 10.1098/rsif.2016.0768.

[208] M. G. McCoy, B. R. Seo, S. Choi, and C. Fischbach, "Collagen I hydrogel microstructure and composition conjointly regulate vascular network formation," *Acta Biomaterialia,* vol. 44, pp. 200-208, 2016/10/15/ 2016, doi: https://doi.org/10.1016/j.actbio.2016.08.028.

[209] M. G. McCoy, J. M. Wei, S. Choi, J. P. Goerger, W. Zipfel, and C. Fischbach, "Collagen Fiber Orientation Regulates 3D Vascular Network Formation and Alignment," *ACS Biomaterials Science & Engineering,* vol. 4, no. 8, pp. 2967-2976, 2018/08/13 2018, doi: 10.1021/acsbiomaterials.8b00384.

[210] N. L'Heureux, L. Germain, R. Labbé, and F. A. Auger, "In vitro construction of a human blood vessel from cultured vascular cells: A morphologic study," *Journal of Vascular Surgery,* vol. 17, no. 3, pp. 499-509, 1993/03/01/ 1993, doi: https://doi.org/10.1016/0741-5214(93)90150-K.

[211] S. D.;, N. R. M.;, and G. Z. S.;, "Mechanical Strain-Stimulated Remodeling of Tissue-Engineered Blood Vessel Constructs," *Tissue Engineering,* vol. 9, no. 4, pp. 657-666, 2003, doi: 10.1089/107632703768247359.

[212] C. Weinberg and E. Bell, "A blood vessel model constructed from collagen and cultured vascular cells," *Science,* vol. 231, no. 4736, pp. 397-400, 1986, doi: 10.1126/science.2934816.

[213] D. D. Allison, K. R. Braun, T. N. Wight, and K. J. Grande-Allen, "Differential effects of exogenous and endogenous hyaluronan on contraction and strength of collagen gels," *Acta Biomaterialia,* vol. 5, no. 4, pp. 1019-1026, 2009/05/01/ 2009, doi: https://doi.org/10.1016/j.actbio.2008.11.013.

[214] S. Tang and M. Spector, "Incorporation of hyaluronic acid into collagen scaffolds for the control of chondrocyte-mediated contraction and chondrogenesis," *Biomedical Materials,* vol. 2, no. 3, pp. S135-S141, 2007/07/30 2007, doi: 10.1088/1748-6041/2/3/s10.

[215] L. Adrian, R. J. Adrian, and J. Westerweel, *Particle image velocimetry* (no. 30). Cambridge university press, 2011.

[216] A. Edelstein, N. Amodaj, K. Hoover, R. Vale, and N. Stuurman, "Computer Control of Microscopes Using μManager," *Current Protocols in Molecular Biology,* vol. 92, no. 1, pp. 14.20.1-14.20.17, 2010/10/01 2010, doi: 10.1002/0471142727.mb1420s92.

[217] A. D. Edelstein, M. A. Tsuchida, N. Amodaj, H. Pinkard, R. D. Vale, and N. Stuurman, "Advanced methods of microscope control using μManager software," *2014,* high-speed imaging, high-content screening, localization microscopy, Micro-Manager, open-source microscopy 2014, doi: 10.14440/jbm.2014.36
 Fatal error: Call to undefined method PublishedArticle::getStartingPage() in /home/jbm/public_html/cache/t_compile/%%5F^5F4^5F4CE8DE%%citation.tpl.php on line 47
.

[218] W. Thielicke, "The Flapping Flight of Birds - Analysis and Application.," Phd, Rijksuniversiteit Groningen, 2014. [Online]. Available: http://irs.ub.rug.nl/ppn/382783069

[219] W. Thielicke and E. J. Stamhuis, "PIVlab – Towards User-friendly, Affordable and Accurate Digital Particle Image Velocimetry in MATLAB.," *Journal of Open Research Software,* vol. 2, no. 1, 2014, doi: http://dx.doi.org/10.5334/jors.bl.

[220] T. William and J. S. Eize, *PIVlab - Time-Resolved Digital Particle Image Velocimetry Tool for MATLAB*. 2014.

[221] D. Zhou, F. T. K. Au, Y. K. Cheung, and S. H. Lo, "Three-dimensional vibration analysis of circular and annular plates via the Chebyshev–Ritz method," *International Journal of Solids and Structures,* vol. 40, no. 12, pp. 3089-3105, 2003/06/01/ 2003, doi: https://doi.org/10.1016/S0020-7683(03)00114-8.

[222] N. Yang, K. K. H. Wong, J. R. de Bruyn, and J. L. Hutter, "Frequency-dependent viscoelasticity measurement by atomic force microscopy," *Measurement Science and Technology,* vol. 20, no. 2, p. 025703, 2008/12/30 2008, doi: 10.1088/0957-0233/20/2/025703.

[223] D. Koblar and M. Boltežar, "Evaluation of the frequency-dependent Young's modulus and damping factor of rubber from experiment and their implementation in a finite-element analysis," *Experimental Techniques,* vol. 40, no. 1, pp. 235-244, 2016.

[224] V. V. Tsukruk, V. V. Gorbunov, Z. Huang, and S. A. Chizhik, "Dynamic microprobing of viscoelastic polymer properties," *Polymer International,* vol. 49, no. 5, pp. 441-444, 2000/05/01 2000, doi: https://doi.org/10.1002/(SICI)1097-0126(200005)49:5

[225] N. Taberlet, J. Ferrand, E. Camus, L. Lachaud, and N. Plihon, "How tall can gelatin towers be? An introduction to elasticity and buckling," (in English), *Am J Phys,* vol. 85, no. 12, pp. 908-914, Dec 2017, doi: 10.1119/1.5009667.

[226] A. Karimi and M. Navidbakhsh, "Material properties in unconfined compression of gelatin hydrogel for skin tissue engineering applications," (in English), *Biomed Eng-Biomed Te,* vol. 59, no. 6, pp. 479-486, Dec 2014, doi: 10.1515/bmt-2014-0028.

[227] S. Suzuki and Y. Ikada, "Sealing effects of cross-linked gelatin," (in English), *J Biomater Appl,* vol. 27, no. 7, pp. 801-810, Mar 2013, doi: 10.1177/0885328211426491.

[228] E. Niehues and M. G. N. Quadri, "Spinnability, Morphology and Mechanical Properties of Gelatins with Different Bloom Index," (in English), *Braz J Chem Eng,* vol. 34, no. 1, pp. 253-261, Jan-Mar 2017, doi: 10.1590/0104-6632.20170341s20150418.

[229] Z. H. Bai, J. M. M. Reyes, R. Montazami, and N. Hashemi, "On-chip development of hydrogel microfibers from round to square/ribbon shape," (in English), *J Mater Chem A,* vol. 2, no. 14, pp. 4878-4884, 2014, doi: 10.1039/c3ta14573e.

[230] C. R. Archer, R. Sargeant, J. Basak, J. Pilling, J. R. Barnes, and A. Pointon, "Characterization and Validation of a Human 3D Cardiac Microtissue for the Assessment of Changes in Cardiac Pathology," *Sci Rep-Uk,* vol. 8, no. 1, p. 10160, 2018/07/05 2018, doi: 10.1038/s41598-018-28393-y.

[231] A. J. S. Ribeiro *et al.*, "Contractility of single cardiomyocytes differentiated from pluripotent stem cells depends on physiological shape and substrate stiffness," *Proceedings of the National Academy of Sciences,* vol. 112, no. 41, p. 12705, 2015, doi: 10.1073/pnas.1508073112.

[232] W. Dorn Gerald and D. Molkentin Jeffery, "Manipulating Cardiac Contractility in Heart Failure," *Circulation,* vol. 109, no. 2, pp. 150-158, 2004/01/20 2004, doi: 10.1161/01.CIR.0000111581.15521.F5.

[233] T. Hayakawa *et al.*, "Image-based evaluation of contraction–relaxation kinetics of human-induced pluripotent stem cell-derived cardiomyocytes: Correlation and complementarity

with extracellular electrophysiology," *Journal of Molecular and Cellular Cardiology,* vol. 77, pp. 178-191, 2014/12/01/ 2014, doi: https://doi.org/10.1016/j.yjmcc.2014.09.010.

[234] T. Hayakawa *et al.*, "Noninvasive Evaluation of Contractile Behavior of Cardiomyocyte Monolayers Based on Motion Vector Analysis," *Tissue Engineering Part C: Methods,* vol. 18, no. 1, pp. 21-32, 2012/01/01 2011, doi: 10.1089/ten.tec.2011.0273.

[235] B. Sabass, M. L. Gardel, C. M. Waterman, and U. S. Schwarz, "High Resolution Traction Force Microscopy Based on Experimental and Computational Advances," *Biophys J,* vol. 94, no. 1, pp. 207-220, 2008/01/01/ 2008, doi: https://doi.org/10.1529/biophysj.107.113670.

[236] M. Maddah *et al.*, "A Non-invasive Platform for Functional Characterization of Stem-Cell-Derived Cardiomyocytes with Applications in Cardiotoxicity Testing," *Stem Cell Reports,* vol. 4, no. 4, pp. 621-631, 2015/04/14/ 2015, doi: https://doi.org/10.1016/j.stemcr.2015.02.007.

[237] C. R. Cleaveland, R. E. Rangno, and D. G. Shand, "A Standardized Isoproterenol Sensitivity Test: The Effects of Sinus Arrhythmia, Atropine, and Propranolol," *Archives of Internal Medicine,* vol. 130, no. 1, pp. 47-52, 1972, doi: 10.1001/archinte.1972.03650010035007.

[238] C. F. George, M. E. Conolly, T. Fenyvesi, R. Briant, and C. T. Dollery, "Intravenously Administered Isoproterenol Sulfate Dose-Response Curves in Man," *Archives of Internal Medicine,* vol. 130, no. 3, pp. 361-364, 1972, doi: 10.1001/archinte.1972.03650030041010.

[239] S. Park, S. B. Nicoll, R. L. Mauck, and G. A. Ateshian, "Cartilage Mechanical Response under Dynamic Compression at Physiological Stress Levels Following Collagenase Digestion," *Annals of Biomedical Engineering,* vol. 36, no. 3, pp. 425-434, 2008/03/01 2008, doi: 10.1007/s10439-007-9431-6.

[240] L. D. Landau and E. M. Lifshitz, *Theory of Elasticity. Course of Theoretical Physics*, 3rd ed. Butterworth-Heinemann, 1986.

[241] M. L. Gardel, J. H. Shin, F. C. MacKintosh, L. Mahadevan, P. Matsudaira, and D. A. Weitz, "Elastic Behavior of Cross-Linked and Bundled Actin Networks," *Science,* vol. 304, no. 5675, p. 1301, 2004, doi: 10.1126/science.1095087.

[242] L. Martikainen, K. Bertula, M. Turunen, and O. Ikkala, "Strain Stiffening and Negative Normal Force of Agarose Hydrogels," *Macromolecules,* vol. 53, no. 22, pp. 9983-9992, 2020/11/24 2020, doi: 10.1021/acs.macromol.0c00601.

[243] S. Motte and L. J. Kaufman, "Strain stiffening in collagen I networks," *Biopolymers,* vol. 99, no. 1, pp. 35-46, 2013/01/01 2013, doi: https://doi.org/10.1002/bip.22133.

[244] D. A. Fletcher and R. D. Mullins, "Cell mechanics and the cytoskeleton," *Nature,* vol. 463, no. 7280, pp. 485-492, 2010/01/01 2010, doi: 10.1038/nature08908.

[245] C. Storm, J. J. Pastore, F. C. MacKintosh, T. C. Lubensky, and P. A. Janmey, "Nonlinear elasticity in biological gels," *Nature,* vol. 435, no. 7039, pp. 191-194, 2005/05/01 2005, doi: 10.1038/nature03521.

[246] G. H. Koenderink *et al.*, "An active biopolymer network controlled by molecular motors," *Proceedings of the National Academy of Sciences,* vol. 106, no. 36, p. 15192, 2009, doi: 10.1073/pnas.0903974106.

[247] G. Kim *et al.*, "Measurements of three-dimensional refractive index tomography and membrane deformability of live erythrocytes from Pelophylax nigromaculatus," *Sci Rep-Uk,* vol. 8, no. 1, p. 9192, 2018/06/15 2018, doi: 10.1038/s41598-018-25886-8.

[248] N. Sultanova, S. Kasarova, and I. Nikolov, "Dispersion proper ties of optical polymers," *Acta Physica Polonica-Series A General Physics,* vol. 116, no. 4, p. 585, 2009.

[249] K. Ronaldson-Bouchard *et al.*, "Advanced maturation of human cardiac tissue grown from pluripotent stem cells," *Nature,* vol. 556, no. 7700, pp. 239-243, 2018/04/01 2018, doi: 10.1038/s41586-018-0016-3.

[250] Y. Wang *et al.*, "Optogenetic Control of Heart Rhythm by Selective Stimulation of Cardiomyocytes Derived from Pnmt+ Cells in Murine Heart," *Sci Rep-Uk,* vol. 7, no. 1, p. 40687, 2017/01/13 2017, doi: 10.1038/srep40687.

[251] M. Hudelmaier *et al.*, "Age-related changes in the morphology and deformational behavior of knee joint cartilage," *Arthritis & Rheumatism,* vol. 44, no. 11, pp. 2556-2561, 2001/11/01 2001, doi: https://doi.org/10.1002/1529-0131(200111)44:11

[252] R. U. Kleemann, D. Krocker, A. Cedraro, J. Tuischer, and G. N. Duda, "Altered cartilage mechanics and histology in knee osteoarthritis: relation to clinical assessment (ICRS Grade)," *Osteoarthritis and Cartilage,* vol. 13, no. 11, pp. 958-963, 2005/11/01/ 2005, doi: https://doi.org/10.1016/j.joca.2005.06.008.

[253] J. S. Day, M. Ding, J. C. van der Linden, I. Hvid, D. R. Sumner, and H. Weinans, "A decreased subchondral trabecular bone tissue elastic modulus is associated with pre-arthritic cartilage damage," *Journal of Orthopaedic Research,* vol. 19, no. 5, pp. 914-918, 2001/09/01/ 2001, doi: https://doi.org/10.1016/S0736-0266(01)00012-2.

[254] T. Gronau *et al.*, "Forced exercise-induced osteoarthritis is attenuated in mice lacking the small leucine-rich proteoglycan decorin," (in English), *Ann Rheum Dis,* vol. 76, no. 2, pp. 442-449, Feb 2017, doi: 10.1136/annrheumdis-2016-209319.

[255] A. J. Sophia Fox, A. Bedi, and S. A. Rodeo, "The Basic Science of Articular Cartilage: Structure, Composition, and Function," *Sports Health,* vol. 1, no. 6, pp. 461-468, 2009/11/01 2009, doi: 10.1177/1941738109350438.

[256] M. Miron-Mendoza, J. Seemann, and F. Grinnell, "The differential regulation of cell motile activity through matrix stiffness and porosity in three dimensional collagen matrices," *Biomaterials,* vol. 31, no. 25, pp. 6425-6435, 2010/09/01/ 2010, doi: https://doi.org/10.1016/j.biomaterials.2010.04.064.

[257] Y.-L. Yang, L. M. Leone, and L. J. Kaufman, "Elastic moduli of collagen gels can be predicted from two-dimensional confocal microscopy," (in eng), *Biophys J,* vol. 97, no. 7, pp. 2051-2060, 2009, doi: 10.1016/j.bpj.2009.07.035.

[258] C. B. Raub, A. J. Putnam, B. J. Tromberg, and S. C. George, "Predicting bulk mechanical properties of cellularized collagen gels using multiphoton microscopy," (in eng), *Acta biomaterialia,* vol. 6, no. 12, pp. 4657-4665, 2010, doi: 10.1016/j.actbio.2010.07.004.

[259] E. Eleftheriou *et al.*, "Millipede - a MEMS-based scanning-probe data-storage system," *IEEE Transactions on Magnetics,* vol. 39, no. 2, pp. 938-945, 2003, doi: 10.1109/TMAG.2003.808953.

[260] U. Dürig *et al.*, "“Millipede” – an AFM data storage system at the frontier of nanotribology," *Tribology Letters,* vol. 9, no. 1, pp. 25-32, 2000/12/01 2000, doi: 10.1023/A:1018844124754.

[261] C. Rembe and A. Drabenstedt, "Laser-scanning confocal vibrometer microscope: Theory and experiments," (in English), *Rev Sci Instrum,* vol. 77, no. 8, Aug 2006, doi: 10.1063/1.2336103.

[262] S. M. Khanna, C. J. Koester, and S. M. Netten, "Integration of the Optical Sectioning Microscope and Heterodyne Interferometer for Vibration Measurements," *Acta Oto-*

Laryngologica, vol. 108, no. sup467, pp. 43-49, 1989/01/01 1989, doi: 10.3109/00016488909138320.

[263] J. Willemin, S. Khanna, and R. Dandliker, *Heterodyne Interferometer For Submicroscopic Vibration Measurements In The Inner Ear* (OE LASE'87 and EO Imaging Symposium). SPIE, 1987.

[264] J. Rädler and E. Sackmann, "Imaging optical thicknesses and separation distances of phospholipid vesicles at solid surfaces," *Journal de Physique II,* vol. 3, no. 5, pp. 727-748, 1993.

[265] G. Wiegand, K. R. Neumaier, and E. Sackmann, "Microinterferometry: three-dimensional reconstruction of surface microtopography for thin-film and wetting studies by reflection interference contrast microscopy (RICM)," *Applied optics,* vol. 37, no. 29, pp. 6892-6905, 1998.

[266] N. Roozen, P. Nuij, and H. Nijmeijer, "Sonic excitation by means of ultrasound: an experimental illustration of acoustic radiation force," in *Proceedings of Forum Acusticum*, 2011.

[267] A. Sabato, S. Chen, P. Avitabile, and C. Niezrecki, "Modal analysis of a beam structure excited by the ultrasound radiation force," *Journal of Physics: Conference Series,* vol. 1149, p. 012001, 2018/12 2018, doi: 10.1088/1742-6596/1149/1/012001.

[268] L. Zhang, T. Yuan, L. Guo, and X. Zhang, "An in vitro study of collagen hydrogel to induce the chondrogenic differentiation of mesenchymal stem cells," *Journal of Biomedical Materials Research Part A,* vol. 100A, no. 10, pp. 2717-2725, 2012/10/01 2012, doi: https://doi.org/10.1002/jbm.a.34194.

[269] D. Endy, "Foundations for engineering biology," *Nature,* vol. 438, no. 7067, pp. 449-453, 2005/11/01 2005, doi: 10.1038/nature04342.

[270] Z. F. Bhat and B. Hina, "Animal-free meat biofabrication," *American Journal of Food Technology,* vol. 6, no. 6, pp. 441-459, 2011.

[271] Z. F. Bhat, S. Kumar, and H. Fayaz, "In vitro meat production: Challenges and benefits over conventional meat production," *Journal of Integrative Agriculture,* vol. 14, no. 2, pp. 241-248, 2015/02/01/ 2015, doi: https://doi.org/10.1016/S2095-3119(14)60887-X.

[272] L. Moroni *et al.*, "Biofabrication strategies for 3D in vitro models and regenerative medicine," *Nature Reviews Materials,* vol. 3, no. 5, pp. 21-37, 2018/05/01 2018, doi: 10.1038/s41578-018-0006-y.

[273] J. Groll *et al.*, "Biofabrication: reappraising the definition of an evolving field," *Biofabrication,* vol. 8, no. 1, p. 013001, 2016/01/08 2016, doi: 10.1088/1758-5090/8/1/013001.

[274] A. M. Holmes, A. Charlton, B. Derby, L. Ewart, A. Scott, and W. Shu, "Rising to the challenge: applying biofabrication approaches for better drug and chemical product development," *Biofabrication,* vol. 9, no. 3, p. 033001, 2017/07/19 2017, doi: 10.1088/1758-5090/aa7bbd.